Cyclic behaviour of laterally loaded (mono)piles in sand

With emphasis on pile driving effects

Kementzetzidis, E.

DOI
10.4233/uuid:36b8a133-2a5a-49b3-9701-f75f102bbe3d

Publication date
2023

Document Version
Final published version

Citation (APA)
Kementzetzidis, E. (2023). *Cyclic behaviour of laterally loaded (mono)piles in sand: With emphasis on pile driving effects*. [Dissertation (TU Delft), Delft University of Technology].
https://doi.org/10.4233/uuid:36b8a133-2a5a-49b3-9701-f75f102bbe3d

Cyclic behaviour of laterally loaded (mono)piles in sand

With emphasis on pile driving effects

Cyclic behaviour of laterally loaded (mono)piles in sand

With emphasis on pile driving effects

Dissertation

for the purpose of obtaining the degree of doctor
at Delft University of Technology
by the authority of the Rector Magnificus Prof.dr.ir. T.H.J.J. van der Hagen,
chair of the Board for Doctorates
to be defended publicly on
Monday 27 February 2023 at 12:30 o'clock

by

Evangelos Kementzetzidis

Master of Science in Civil Engineering,
Delft University of Technology, Netherlands
born in Thessaloniki, Greece

This dissertation has been approved by the promotors

Composition of the doctoral committee:

Rector Magnificus,	chairperson
Prof. dr. A. V. Metrikine	Delft University of Technology, promotor
Dr. F. Pisanò	Delft University of Technology, copromotor

Independent members:

Prof.dr.ing. M. Achmus	Leibniz University Hannover, Germany
Prof.dr.ing. B. Bienen	The University of Western Australia, Australia
Prof.dr. K. Gavin	Delft University of Technology
Prof.dr. D. White	University of Southampton, United Kingdom
Dr. ir. A. Elkadi	Deltares, Netherlands
Prof.dr. M. A. Hicks	Delft University of Technology, reserve member

This work is part of the GDP research project (GROW joint research programme), which is (partly) financed by the *Topsector Energiesubsidie van het Ministerie van Economische Zaken* under grant number TEHE117100.

Keywords: monopiles, cyclic loading, cyclic $p-y$ modelling, monopile installation (effects), GDP driving
Printed by: Gildeprint – Enschede

ISBN 978-94-6419-699-3

An electronic version of this dissertation is available at
https://repository.tudelft.nl/.

ζώον δίπουν άπτερον – 'we are just' featherless bipeds

Plato

Contents

Summary

At the end of 2019, the European Union (EU) put forward the European Green Deal to facilitate the technological progress necessary to achieve CO_2-neutrality by 2050. Such a monumental achievement would require massive investments in infrastructure for the harvesting, storage and the transnational transportation of green energy. To date, the more mature of the scalable (cf. to hydroelectric) green-energy resources is offshore wind, with joint academic and industry efforts allocated to reduce its capital expenditure. Approximately 13-37% of the required investment for offshore wind farms is currently expended on the design, manufacturing, and installation of the substructure. Further reduction in the cost of offshore wind can be achieved by addressing the main technical challenges associated with the predominant offshore wind foundation, i.e., the monopile. The main challenges typically relate to its lifetime operations, namely, (i) the identification of the wind turbine's fundamental frequencies, which are strongly dependent on the monopile-soil interaction, (ii) and the prediction of the lifetime foundation tilt, but also the current installation technology (impact driving); the current norm in the offshore industry. In particular, impact driving is associated with (i) long installation times, especially in the presence of competent soils, (ii) excessive use of construction material (steel) to avoid pile damage under many hammer blows, and (iii) costly underwater noise mitigation measures to reduce noise the levels of installation-borne noise emissions harmful to marine life.

In an attempt to accelerate the growth of offshore wind, the Netherlands, country of origin of this study, has supported several research initiatives to reduce the engineering and manufacturing costs for the prevalent offshore wind foundation in the country (the monopile). This study elaborates upon the experimental findings of two major research projects, namely the DISSTINCT (2014-2018) and the Gentle Driving of Piles (2018-2022) projects, each designed to address specific technical uncertainties associated with the foundation concept. The DISSTINCT project (launched in 2014) aimed to improve the understanding of the natural frequency of installed monopiles as well as the engineering procedures used in the identification thereof. By conducting experiments at full scale on a monopile installed in the IJsselmeer lake in the Netherlands, the experimental campaign produced invaluable data on the dynamic response of monopiles during small amplitude lateral vibrations. Later, the GDP project (launched in 2018) was designed to propose, engineer, and demonstrate a novel monopile installation procedure, foreseen to alleviate most of the aforementioned installation-related challenges; the Gentle Driving of Piles (GDP) method. Moreover, the project would provide answers to questions concerning the long-term response of (mono)piles in sandy soils, relative to the installation method. For these reasons, an extensive experi-

mental campaign was conducted in the port of Rotterdam (Maasvlakte II), where a total of 9 piles were driven into the sandy Maasvlakte soil via different driving procedures, namely with the established impact hammering, the traditional axial vibro-driving, and the new GDP method. Subsequently, the cyclic lateral performance for four of these piles (which were heavily instrumented), was evaluated via an elaborate 82,000 load cycle (≈42 hours) loading programme of slow (0.1 Hz) high amplitude, and fast (0.1 - 4 Hz) low amplitude cyclic force applied to the (mono)piles' head.

This study elaborates and builds upon experimental findings from the above-mentioned test campaigns. These measurements were first carefully examined, and later interpreted using a variety of modelling tools (both 1D and 3D FE modelling) formulated and adapted to meet the particular geotechnical and loading challenges of the examined fieldwork. Enabled by the diversity of the field and numerical work performed, this study addresses a number of engineering challenges and knowledge gaps related to the design of monopiles, namely i) their post-installation resonance frequency, ii) the long-term response to environmental loading, and iii) the impact of the installation method on the long-term operations. In particular, 3D FE modelling was adopted to successfully simulate the dynamic response of the examined monopile in the DISSTINCT project. The modelling efforts enabled the interpretation of the field test measurements, and in turn, inspired confidence in the suitability of available simulation tools to identify the resonance frequencies of monopile foundations, and accurately calculate dynamic soil-monopile interactions. For the interpretation of the GDP field test data, 1D FE modelling was employed. In the field, the elaborate lateral loading programme returned a fairly complex cyclic pile response, with pronounced differences in the performance of piles installed by different installation methods. The particular geotechnical conditions at the GDP site, i.e., site inhomogeneity and the 4 m deep unsaturated topsoil, prevented the direct comparison of the installation methods. This was later achieved through the formulation of a cyclic soil reaction $p - y$ model able to simulate soil ratcheting and gapping effects. The results provided rich insights into the impact of relevant installation effects on the cyclic pile response on many loading cycles and indicated that the GDP-installed piles performed excellent overall in lateral cyclic loading.

Samenvatting

Eind 2019 heeft de Europese Unie (EU) de Europese Green Deal voorgesteld om de technologische vooruitgang te bevorderen die nodig is om CO_2-neutraliteit te bereiken in 2050. Een dergelijke immense prestatie vertgt enorme investeringen in de infrastructuur voor het opwekken, opslaan en internationaal transporteren van groene energie. Op dit moment is offshore-windenergie de meest volwassen schaalbare (in vergelijking tot hydro-elektrische) groene energiebron, waarvan de academische wereld en het bedrijfsleven gezamenlijk probeert om de uitgaven te beperken. Ongeveer 13 tot 37% van de vereiste investering voor offshore-windmolenparken wordt momenteel besteed aan het ontwerp, de fabricage en de installatie van de funderingsconstructie. De kosten van offshore-windenergie kunnen verder worden teruggedrongen door de belangrijkste technische uitdagingen aan te pakken die verband houden met de meest gebruikte funderingstype voor offshore-windmolens, namelijk de monopaal. Die uitdagingen hebben vooral betrekking op de levensduur van de monopaal, namelijk:(i) de identificatie van de resonantiefrequenties van de fundering, die sterk afhankelijk is van paal-grond interactie en (ii) de voorspelling van de rotatie van de fundering tijdens de levensduur. Tevens hebben zijn er uitdagingen die betrekking hebben op de huidige installatietechnologie (heien met een slaghamer); de huidige norm in de offshore-industrie. In het bijzonder wordt heien geassocieerd met (i) lange installatietijden, vooral in bodems die veel weerstand bieden, (ii) buitensporig gebruik van constructiemateriaal (staal) om paalbeschadiging onder vele hamerslagen te voorkomen, en (iii) dure geluidsisolerende maatregelen om geluidsemissies te beperken die schadelijk zijn voor het leven op zee.

In een poging om de groei van offshore windenergie te versnellen, heeft Nederland, het land van herkomst van deze studie, verschillende onderzoeksinitiatieven gesteund om de constructie- en fabricagekosten van de in ons land gangbare offshore windfundatie (de monopaal) te verlagen. Deze studie borduurt voort op de experimentele bevindingen van twee grote door de TU Delft geleide projecten, namelijk het DISSTINCT-project (2014-2018) en het Gentle Driving of Piles-project (2018-2022), die elk zijn ontworpen om specifieke technische onzekerheden in verband met het funderingstype aan te pakken. Het DISSTINCT project (gestart in 2014) had tot doel het inzicht van de geo-gemeenschap in de natuurlijke frequentie van monopalen te verbeteren, evenals de engineeringprocedures die worden gebruikt bij de identificatie daarvan. Door experimenten op ware grootte uit te voeren op een monopaal die in het IJsselmeer in Nederland was geïnstalleerd, leverde de experimentele campagne gegevens van onschatbare waarde op over de dynamische reactie van monopalen bij zijwaartse trillingen met een kleine amplitude. Later werd het GDP-project (gelanceerd

in 2018) ontworpen om een nieuwe installatiemethode voor monopalen te introduceren, ontwikkelen en demonstreren, die de meeste van de eerdergenoemde installatie gerelateerde uitdagingen zou moeten verhelpen; de Gentle Driving of Piles (GDP)-methode. Bovendien zou het project antwoorden verschaffen op vragen betreffende de langetermijnsreactie van (mono)palen in zandige bodems, in verhouding tot de bestaande installatiemethode. Om deze redenen werd een uitgebreide experimentele campagne uitgevoerd in de haven van Rotterdam (Maasvlakte II), waar in totaal 9 palen in de zandige Maasvlakte werden geheid via verschillende heiprocedures, namelijk met de gevestigde slaghamer, het traditionele axiale trillen, en de nieuwe GDP-methode. Vervolgens werd de cyclische laterale prestatie voor vier van deze zwaar geïnstrumenteerde palen geëvalueerd door het uitvoeren van 82.000 belastingscyclussen (≈42 uur). De belasting werd aan de bovenkant van de (mono)palen toegepast volgens een programma toegepast bestaande uit langzame (0.1 Hz) hoge amplitude cyclische krachten en snelle (0.1 - 4 Hz) lage amplitude cyclische krachten.

In deze studie wordt voortgebouwd op de experimentele bevindingen van bovengenoemde testcampagnes. De metingen werden eerst zorgvuldig onderzocht, en later geïnterpreteerd met behulp van een verscheidenheid aan modelleergereedschappen (zowel 1D als 3D FE-modellering), die werden geformuleerd en gebaseerd op de specifieke geotechnische en belastingsuitdagingen van het onderzochte veldwerk. Dankzij de diversiteit van het veldwerk en het uitgevoerde numerieke werk kunnen in deze studie een aantal technische uitdagingen en kennishiaten met betrekking tot het ontwerp van monopalen worden aangepakt, namelijk i) hun resonantiefrequentie, ii) de langetermijnreactie op omgevingsbelasting, en iii) de invloed van de installatiemethode op de langetermijnsgebruik. In het kader van het DISSTINCT-project is met name gebruik gemaakt van 3D FE-modellering om de dynamische reactie van de onderzochte monopaal met succes te simuleren. De modellering maakte interpretatie van de metingen bij veldproeven mogelijk en gaf vertrouwen in de geschiktheid van de beschikbare simulatie instrumenten om de resonantiefrequenties van monopaal fundering vast te stellen en de dynamische grond-paal interacties nauwkeurig te berekenen. Voor de interpretatie van de BBP-veldtestgegevens is gebruik gemaakt van 1D FE-modellering. In het veld leverde het uitgebreide laterale belastingsprogramma een vrij complexe cyclische paalrespons op, met uitgesproken verschillen in de prestaties van palen die volgens verschillende installatiemethoden zijn geïnstalleerd. De bijzondere geotechnische omstandigheden op de GDP-locatie, d.w.z. de inhomogeniteit van het terrein en de 4 m diepe onverzadigde bovengrond, maakten een directe vergelijking van de installatiemethoden onmogelijk. Dit werd later bereikt door de formulering van een cyclisch grondreactie p–y model dat in staat is om cyclische kruip en holtevorming tussen paal en grond te simuleren. De resultaten verschaften een rijk inzicht in de cyclische paalreactie bij vele belastingscyclussen en toonden aan dat de met GDP geïnstalleerde palen over het algemeen genomen uitstekend presteerden bij zijdelingse cyclische belasting.

Preface

This document contains the Ph.D. dissertation of Evangelos Kementzetzidis (me), which studies the behaviour of large-diameter monopiles embedded in soils while subjected to cyclic lateral loading at the pile head. After four years of doing research, both in the field and in the home/office (a considerable amount of the Ph.D. time coincided with the recent Coronavirus pandemic), I am almost elated that this experience is nearing its conclusion. Admittedly, though I am thrilled and eager to move forward to new challenges, I already feel some post-doctoral melancholy now that this unique, didactic process is coming to an end.

Although this was a solo project, this study would not have been possible without the help and contributions of various people that deserve to be acknowledged.

Foremost, my supervisor Dr. Federico Pisanó. Federico, almost six years ago, you proposed to me to do my M.Sc. thesis under your supervision. Who would have known that we'd get this far? I sometimes contemplate whether that moment was a bifurcation point in my life's trajectory. I would like to express my gratitude for your help and guidance during the past years, and for your expertise. I also want to thank you for all the faith you put in me. While working together, under your supervision, I learned much more besides the intricacies of research. I wish you the brightest future possible, also in the newly opened chapter in your life as a father.

Deep appreciation also goes to my promotor Prof. dr. Andrei V. Metrikine. Andrei, your support and guidance have been crucial for my research. During my presence in the group, I have seen numerous people express their admiration for the depth of your theoretical knowledge. While the admiration is certainly justified, I wanted to express my admiration for the group of people that you have assembled around you and the code of conduct within the group, which from what I see is inspired by you.

Furthermore, I would like to express my gratitude to Dr. José Abell from Universidad de los Andes. José, thank you so much for accepting me in Chile, and for your mentorship during the Southern Hemisphere's winter months (May-August) of 2019. Your profound knowledge of computational geomechanics, combined with your expertise in programming, equipped me with valuable tools. Thank you so much for all your help. I really hope that we can collaborate again in the future, and I'm looking forward to visiting you in Chile once more. I would also like to thank Dr. ir. Hayo Hendrikse, the expert on ice-structure interaction from our group, who sponsored my trip to Chile. Hayo, you are an excellent colleague and I sincerely appreciate your kind gesture and the fact that you offered to help without hesitation.

I would also like to thank Dr. ir. Pim Versteijlen. Pim, thank you for all your interest in my work, and also for granting me access to the measurements from the DISSTINCT project. The latter resulted in the first paper of my Ph.D. which was also awarded by ICE as the best (offshore) paper of 2022. I hope to see you for celebrations at the award ceremony in London.

I would further like to thank Dr. ir. Ahmed Elkadi from Deltares and ir. Kees van Beek from TU Delft, for their help on the GDP experiments, especially concerning post-installation lateral pile loading. The GDP post-installation tests had a big impact on the trajectory of my research, and Ahmed and Kees among many others helped a lot in making that part of the campaign go as smoothly as possible.

The Ph.D. process would have been far less enjoyable if I could not share the struggles with other candidates, PostDocs, and friends, for instance, my current roommates Thanasis and Timo. Guys, the very interesting discussions at the office have been great, they will be missed in the future. Andrei(s), Cody, Barbara, Fransesca, Giouli, Haoyuan, Huan, Jan, Joao, Mamin, Marco, Peter, Poni, Ponni, Sergio, Stavros, Tim, Vaibhav, Valentina, Xiangcou, Zheng, I wish you all a very bright future.

Besides friends/colleagues, I would like to express my gratitude to the whole DISSTINCT consortium (project number TKIW02001) for allowing full access to field data.

For funding and enabling my research, I would like to thank all the people behind the GROW joint research program. The presented study was funded by *Topsector Energiesubsidie van het Ministerie van Economische Zaken* under grant number TEHE117100. Financial/technical support from the following partners is gratefully acknowledged: Royal Boskalis Westminster N.V., CAPE Holland B.V., Deltares, Delft Offshore Turbine B.V., Delft University of Technology, ECN, Eneco Wind B.V., IHC IQIP B.V., RWE Offshore Wind Netherlands B.V., SHL Offshore Contractors B.V., Shell Global Solutions International B.V., Sif Netherlands B.V., TNO, and Van Oord Offshore Wind Projects B.V.

In conclusion, I would like to express my gratitude to my family and friends. Thank you, Alex G., Lauren, Alex P., Foti, Ioanna, Ira, Nancy, Niko, Saranto, Thanasi K., and Thanasi T. among many others for your support and friendship. To my parents (Pavlo and Sonia) and my sister Sophia, who have always supported my decisions and for the faith they had in me from my early years. Thank you for all your love, I love you unconditionally! Finally, to my companion in life, Anastasia. Thank you for always being there for me, and for your patience during the past four years; they would be so much duller without you.

Evangelos Kementzetzidis
Delft, August 2022

I

Introduction

From the beginning of the industrial revolution (mid-18 century), the footprint of humanity on the planet has substantially increased. The industrial revolution fostered the unprecedented growth of global economies and population size witnessed in the 20th century ((IMF), 2000). For the general public, this era marked a substantial yet 'delayed' improvement in the standard of living (Feinstein, 1998), and was facilitated by the currency of economic/population growth – energy –, which even to date is primarily obtained by combustion of fossil fuels. In an attempt to limit the footprint of humankind on the environment (Figure I.1), governments from countries around the globe have ratified the following landmark agreements:

- Montreal Protocol, 1987 – a historic agreement intended to diminish substances harmful to the ozone layer;
- UN Framework Convention on Climate Change (UNFCCC), 1992 – the first global treaty explicitly addressing climate change;
- Kyoto Protocol, 2005 – the first legally binding climate treaty, which required developed countries to reduce harmful emissions;
- Paris Agreement, 2015 – a global agreement (ratified by 196 countries) that demands all countries to reduce harmful emissions, and aims for a climate neutral world by mid-century;

At the end of 2019, the European Union (EU) complemented these efforts by sanctioning the European Green Deal, the aim of which is to reduce the carbon footprint of its member states and achieve no-net greenhouse gases by 2050. To facilitate such an extraordinary

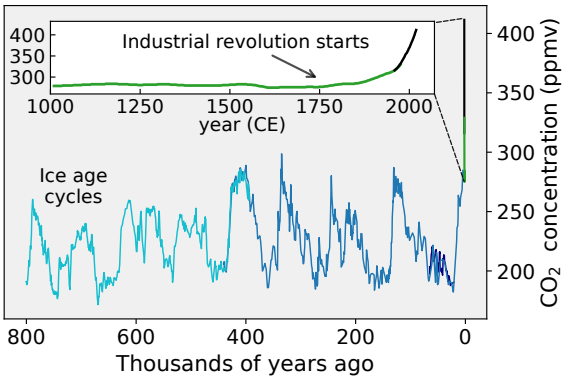

Figure I.1: CO_2 concentrations over the last 800,000 years as measured from ice cores (blue/green) and directly (black) light blue (Lüthi et al., 2008), Vostok core dark blue (Fischer et al., 1999), navy blue (Indermühle et al., 2000), green (Etheridge et al., 1998) and black (Keeling and Whorf, 1994). Figure (also found in Loucks, 2021), produced by Nijsse, 2018.

vision, massive investments are expected, among other areas, in the necessary infrastructure for the harvest and the transnational transportation of green renewable energy. To date, offshore wind energy, the more mature of the scalable green-energy resources (Esteban et al., 2011), [*] is expected to contribute substantially to this transition.

1. Offshore wind

Historically, the first European wind farm was erected onshore in 1982 on the Greek island of Kythnos (100 kW capacity). The transition from land to sea dates back to 1991 when the first offshore wind farm was built in Denmark (5 MW capacity). Since then, over 28 GW of offshore wind power have been developed in Europe (Komusanac et al., 2022) – a global capacity of 37 GW has been reported at the end of 2021 (Lee et al., 2021). To meet the ambitious goals of the European Green Deal, offshore wind capacity must scale up by 230-450 GW in the next 28 years (WindEurope, 2019).

In the coming thirty years, Asia is expected to lead the way in the development of installations for offshore wind harvesting, followed by Europe, North America, the Pacific (mainly Australia), South America, and Africa, with the global forecasted capacity reaching 2000 GW (Lee et al., 2021). To support this unprecedented energy transition, considerable research efforts are being devoted to closing knowledge gaps by promoting innovation in all areas of offshore wind science and engineering. Such areas include the installation (and future decommissioning) of ever larger offshore wind turbines (OWTs), which are currently approaching/exceeding a power output of 15 MW (Gaertner et al., 2020). Moreover, the remarkable fabrication costs for these enormous steel structures may only be alleviated by optimising the design of the whole OWT-foundation system. Currently, depending on the

[*] cf. (compared to e.g., hydroelectric energy for which suitable harvest locations are typically very limited)

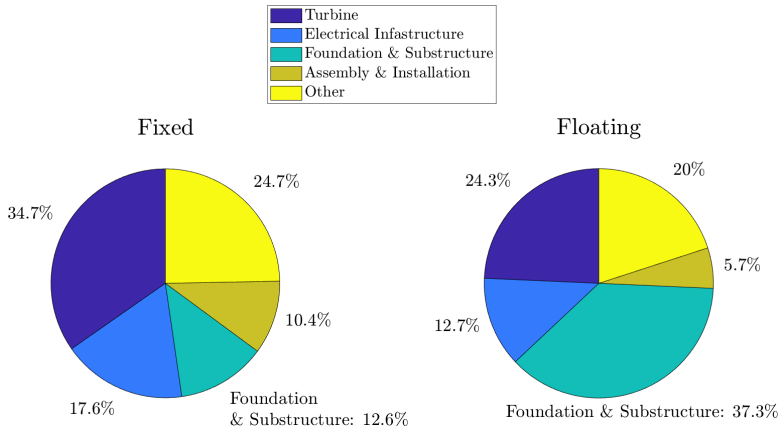

Figure I.2: Allocation of capital expenditure for bottom-fixed (monopile), and floating offshore wind turibes - modified after Stehly and Duffy, 2021.

foundation type, between 13-37% of the required investment for offshore wind turbines is expended on the design, manufacturing, and installation of the substructure (Stehly and Duffy, 2021), Figure I.2.

Large-diameter monopiles

Fostered by the relatively shallow coastline of the northern European countries, the large-diameter monopile (i.e., tubular steel piles with a diameter in the range from 5 to 11 m and a low ratio between embedded length and diameter typically between 3 and 6) is, to date, the most selected foundation option – currently supporting 80% of all European offshore wind turbines (Ramırez et al., 2021), more than 4600 in total. With such a vast number of monopile-supported OWTs installed and subsequently operated, the foundation concept has matured enough, for the engineering challenges to become apparent to the offshore wind industry. For offshore engineers, such challenges mainly relate to the phases of monopile installation and its lifetime operations.

The foreseen expansion of the offshore wind market, across the globe and evidently towards deeper waters, will require the adoption of alternative foundation types. For instance, gravity-based structures, jackets, and suction anchors for floating turbines, among others (Dıaz and Soares, 2020). Regardless of the future trajectory of offshore wind, the monopile is foreseen to remain an (ever-) popular foundation concept and is expected to expedite the expansion of offshore wind in the near future.

Monopile installation

To date, most monopiles are installed via impact hammering, a proven installation procedure that achieves gradual pile penetration via high amplitude hammer blows on the monopile head. Despite the wide adoption of the procedure due to its technical simplicity, the method

is associated with (i) lengthy installation times, especially in presence of competent soils (Achmus et al., 2020; Rodger and Littlejohn, 1980), (ii) use of excess steel (to avoid pile damage during driving) and (iii) with the adoption of costly soundproofing solutions to negate noise emissions that are harmful to marine life (Tsouvalas, 2020).

A promising alternative to impact piling is represented by traditional (axial) vibratory pile driving technologies. Vibratory driving methods, replace hammering impacts – the root cause of the installation-related concerns (Metrikine et al., 2020), with low(er) amplitude (axial) vibrations. The method is reported to achieve faster and quieter pile-driving compared to traditional impact piling (reported among others in Barkan, 1967; Lammertz, 2003; Mosher, 1987, 1990; Tsouvalas and Metrikine, 2016b). However, despite its assumed benefits, certification bodies still do not endorse its use for the construction of offshore wind farms, as is customary for any non-established (yet) engineering procedure. In particular, the process of vibro-driving is not yet well-understood, especially concerning the dynamic behaviour of the soil during vibro-driving (Mazza and Holeyman, 2019) and the effects of vibro-installation on the operational performance of the pile. Such effects are currently under investigation by an increasing number of geotechnical research teams (Achmus et al., 2020; Anusic et al., 2019; Heins and Grabe, 2017; Herwig and Gattermann, 2015; Kementzetzidis et al., 2023a,b; Labenski and Moormann, 2019; LeBlanc, 2014; Staubach, 2022; Tsetas et al., 2020, 2023), while for the important component of the post-installation lateral behaviour of monopiles, no consensus yet exists on the relative performance of the driving methods (impact- versus vibro piling).

Design requirements for the operation of monopile-supported OWTs

Monopile-supported offshore wind turbines are typically designed to withstand harsh storm events and remain operational through numerous but less severe loading cycles - $10^8 - 10^9$ during their lifetime. In the design against such environmental conditions, design standards are generally conservative due to knowledge gaps that prevent offshore engineers from calculating with certainty (i) the limit capacity of monopile foundations, (ii) their structural resistance to fatigue, (iii) the evolution of the lateral stiffness of the foundation, and (iv) the cyclic lateral deformations (e.g., at the monopile head) upon long-term environmental loading. The last two issues (shown schematically in Figure I.3), attract most of the attention in the geoengineering community. In part, out of (i) academic curiosity – they are driven by relatively unexplored geotechnical mechanisms, and also, (ii) by being the typical design drivers of these immense structures (monopiles), they contribute to a further rise in fabrication costs.

Concerning the aforementioned uncertainties, the lateral monopile stiffness (point iii) is a key design component for the so-called soft-stiff design approach (Kallehave et al., 2015a). Selected as the most economical option, at least for relatively shallow waters, a narrow frequency span is identified as serene from external loads (usually between f =0.2-0.3 Hz – see Figure I.4) and serves as the target range for the 1_{st} global natural frequency of the structure.

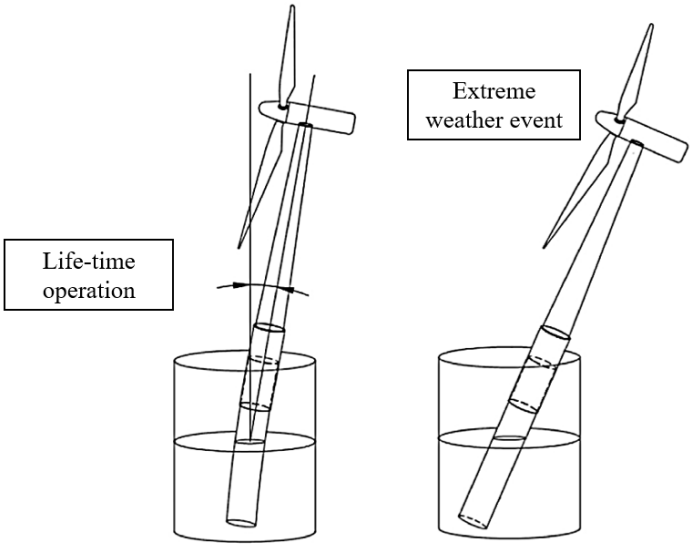

Figure I.3: Geotechnical risks for monopile-supported offshore wind turbines – modified after Arany et al., 2017b.

Adding to the complexity, field measurements (Kallehave et al., 2015b; Norén-Cosgriff and Kaynia, 2021) and experimental evidence (Abdullahi et al., 2022) support that the natural frequency of OWTs varies depending on the loading conditions (Kementzetzidis et al., 2019, 2018). Finally, the prediction of cyclic lateral deformations (point iv) is required in order for OWTs to meet strict SLS requirements, for instance, <0.5° cumulative monopile tilt over their operational life (DNVGL (Det Norske Veritas GL), 2016). Although treated separately, the evolution of the monopile stiffness and the accumulation of lateral deformations are coupled via the impressively complex cyclic behaviour of soils. To address the uncertainties mentioned above, a considerable amount of research has been carried out in recent years through experimental and numerical investigations.

Experimental testing, for the cyclic lateral loading of (mono)piles, usually involves testing model test piles at a small(er) scale, either at the lab or in the field. Laboratory testing is usually the most economical option (usually at 1:50 - 1:100 scale), offering a high degree of controllability over the test settings. Typically, laboratory testing is performed at 1g (Abadie, 2015a; Albiker et al., 2017; Frick and Achmus, 2019; LeBlanc et al., 2010; Richards, 2019) or augmented gravity (Fan et al., 2021a; Klinkvort, 2012; Klinkvort et al., 2010; Pisanò et al., 2022a; Richards et al., 2021; Rudolph et al., 2014; Truong et al., 2019; Wang et al., 2022; Wang et al., 2018a; Zhu et al., 2016), with the latter considered more representative of the prototype response. Finally, field experiments are performed, testing piles with dimensions much closer to the prototype (scale usually <1:10) (Achmus et al., 2020; Byrne et al., 2020a,b; Kementzetzidis et al., 2023a; Li et al., 2015), and are widely considered the epitome of experimental testing. Unfortunately, field tests are uncommon due to the very

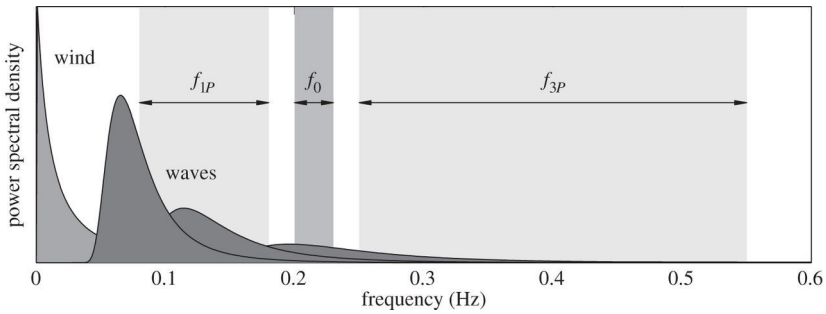

Figure I.4: Excitation frequencies for three bladed OWTs. Figure after Kallehave et al., 2015a.

high cost, complexity, and low controllability of the experimental settings – mostly concerning the foundation soil. Overall, such exercises had/have an immense contribution towards alleviating uncertainties associated with the monopile foundation, by expanding the understanding of the geo-community in the area of soil-monopile interactions, and by providing empirical data-driven relationships between the number of loading cycles and the associated monopile tilt, or even tangent stiffness. Unfortunately, the validity of such relationships outside the domain of the reference dataset is limited (Liu, 2020), and it is usually only achieved with numerical modelling.

In standard practice, 1D ($p-y$) or 3D finite element simulations are employed for the simulation of (mono)pile-soil interactions. 3D FE analysis provides the most accurate/realistic representation of the system's response, since they require smaller number of simplifying assumptions (c.f. to 1D $p-y$) in the modelling of the pile-soil system. Specifically, pile and soil are discretised by solid elements (for the pile, beam and cell elements are also employed), while the complex hydro-mechanical behaviour of soils is simulated by appropriate constitutive models reflecting on the scope of the selected work. The response of large-diameter monopiles under repetitive loading of considerable amplitude, has only lately been successfully simulated, (Kementzetzidis et al., 2019, 2018; Liu and Kaynia, 2022; Liu et al., 2021, 2022; Staubach and Machaček, 2019; Staubach et al., 2020; Staubach and Wichtmann, 2020; Staubach, 2022) allowed by recent developments in the constitutive modelling of sands (Corti et al., 2016; Dafalias and Manzari, 2004; Liu, 2020; Liu et al., 2019b; Niemunis et al., 2005). Finally, for loads of insufficient amplitude (to trigger any meaningful plasticity), such as the full-scale monopile testing for the DISSTINCT project (Versteijlen et al., 2016a; Versteijlen, 2018; Versteijlen et al., 2017a), the cyclic monopile response was successfully simulated by describing the soil as a linear elastic medium (Kementzetzidis et al., 2021). Although 3D FE analysis provides the most realistic and accurate simulation results, the method is seldom used in practice due to the high computational demands, especially in the simulation of soils with advanced constitutive models.

A more cost-effective alternative to the 3D FE analysis is the 1D $p-y$ approach, the de facto simulation procedure in engineering practice. The $p-y$ method is based on the

classical Winkler approach in which the (mono)pile-soil system is simulated via a set of beam elements (for the pile) supported horizontally by independent, usually non-linear elastic ($p-y$) springs, Figure I.5. Although conceptually simple, the challenge of the method lies in the appropriate selection of those $p-y$ relationships that describe the spring reaction p, with the pile/soil deflection y along the pile length. Established $p-y$ monotonic formulations were originally conceived (and proven in practice) for small-diameter, flexible piles used in the design of oil and gas platforms (API, 2011; DNVGL (Det Norske Veritas GL), 2016) which require, for calibration purposes, the inference of the peak friction angle ϕ from available site investigation data. The method is currently under "revision" as it has been found inaccurate for the design of large-diameter, stocky (non-flexible) monopiles (Byrne et al., 2019; Pisanò et al., 2022a), due to the disregard of reaction mechanisms deemed inconsequential for small-diameter flexible piles (Byrne et al., 2019; Davidson, 1982; Gerolymos and Gazetas, 2006; Lam and Martin, 1986). Figure I.5 shows the previously neglected reaction mechanisms, i.e., the shear traction at the pile shaft as well as the shear and moment reactions at the pile base – currently, calibration strategies for these reaction mechanisms are becoming available (Byrne et al., 2019; Pisanò et al., 2022a). Finally, the method is currently under further development, to allow straightforward CPT-based calibration strategies for its constitutive parameters (Dyson and Randolph, 1998; Li et al., 2014; Novello, 1999; Suryasentana and Lehane, 2016), and to enable the simulation of complex cyclic loading time histories (Beuckelaers et al., 2020; Choi et al., 2015; Kementzetzidis et al., 2022; Pisanò et al., 2022a; White et al., 2022).

2 . Motivation & Objectives

Motivated by the necessity to accelerate the expansion of offshore wind, this study focuses on the examination of the post-installation cyclic and dynamic lateral performance of (mono)piles in cyclic/dynamic loading, with additional considerations (when applicable) for the influence of selected pile-driving methods.

The majority of the previously identified knowledge gaps (relating to (mono)pile installation and lifetime operations), can be largely attributed to the complex soil-structure interaction mechanisms of laterally loaded OWTs, given the extremely complicated cyclic behaviour of (saturated) soils. This work aims to address these issues, via the careful inspection of measurements from two major experimental campaigns conducted as part of the DISSTINCT (Versteijlen, 2018), and the Gentle Driving of Piles (Metrikine et al., 2020) projects. Test results are later interpreted by incorporating state-of-the-art modelling tools of (mono)pile-soil interactions.

The DISSTINCT project

The DISSTINCT project was a 4-year (2014-2018) joint-industry project involving Siemens Gamesa Renewable Energy, TU-Delft, DNV-GL (currently DNV), Fugro, SWP, and MBO Offshore (currently GustoMSC). The project was designed to examine the lateral performance of

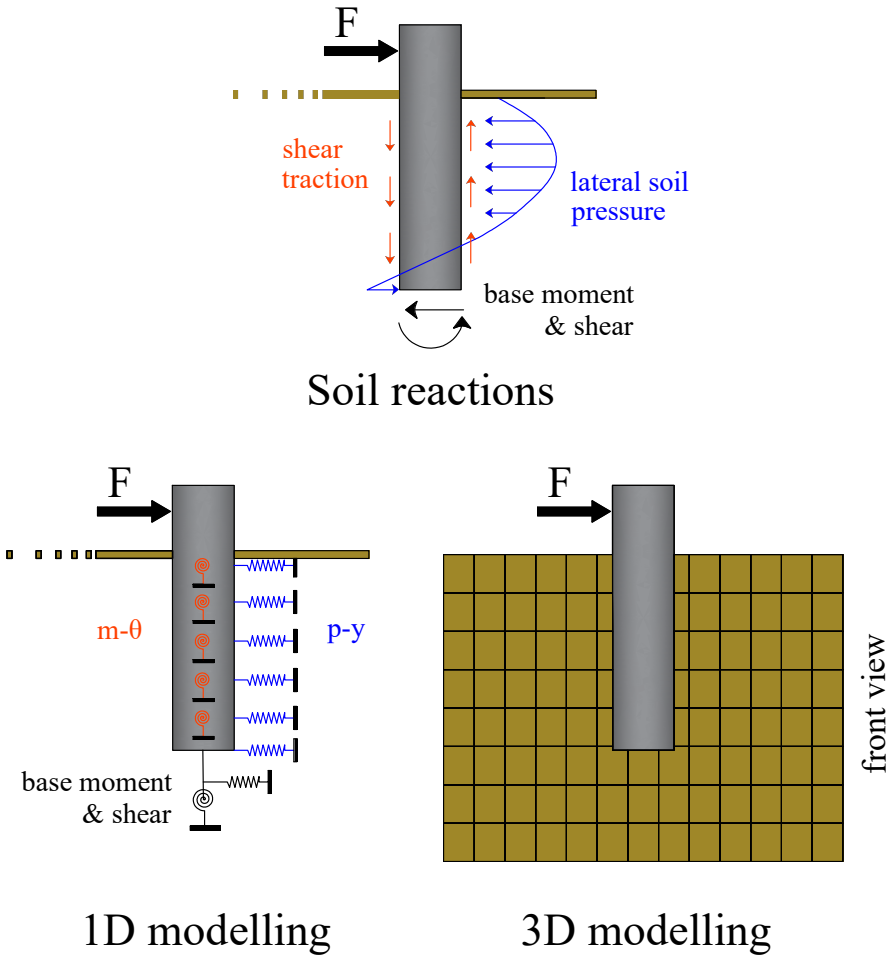

Figure I.5: Identified soil reaction mechanisms on lateral (mono)pile loading and the standard-practice numerical models.

Figure I.6: Aerial photo of the shaker on the monopile (MP45) tested as part of the DISSTINCT project in the Westermeerwind wind farm. Source: Versteijlen et al., 2016a

monopiles in offshore environments, in an attempt to improve the design tools for the identification of the monopile's post-installation resonance frequencies (Versteijlen et al., 2016b) on small amplitude lateral vibrations. For this reason, a vibrating device (henceforth referred to as "shaker" for brevity) was installed on the MP45 monopile (D =5 m, L_{emb} = 24.05 m) during the construction of the Westermeerwind wind farm on the eastern shore of the IJsselmeer lake in the Netherlands (Figure I.6). During testing, the shaker vibrated the monopile with small amplitude vibrations of increasing frequency (sweeps) in the range of 1-8 Hz (Figure I.7). For testing purposes, both MP45 and the surrounding soil were equipped with strain gauges (in the monopile), accelerometers, and pore water pressure sensors.

Chapter II presents the results of careful examination of the above experimental data, which provide valuable insight into the dynamic response of monopile foundations and the surrounding soil (at full scale) under lateral loading at variable frequencies. Such findings marked a great opportunity to test the reach of available modelling tools (3D poroelastic FE model for monopile-soil interaction), which were later employed to interpret the experimental measurements and successfully identify the foundation's resonance frequency – one of the key challenges in monopile foundation design. Additional/original material related to the DISSTINCT project can be found in Versteijlen, 2018; Versteijlen et al., 2016b, 2017a).

The Gentle Driving of Piles project

The Gentle Driving of Piles project (GDP), was a TU Delft-led 4-year (2018-2022) collaborative project involving Royal Boskalis Westminster N.V., CAPE Holland B.V., Deltares, Delft

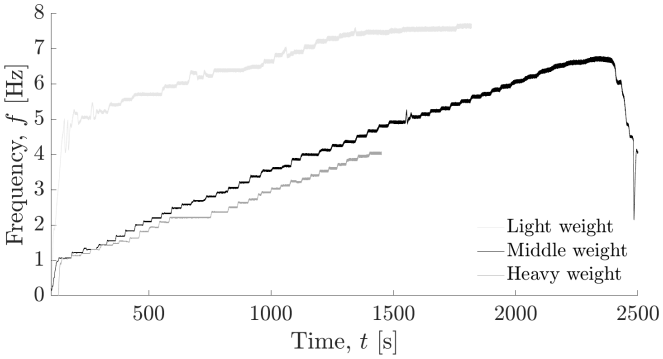

Figure I.7: Excitation frequency of the lateral loads applied at the pile head of MP45 (Figure I.6). Light, middle and heavy weight configurations relate to technical specifications of the shaker, discussed in detail in Chapter II.

Offshore Turbine B.V., Delft University of Technology, ECN, Eneco Wind B.V., IHC IQIP B.V., SHL Offshore Contractors B.V., Shell Global Solutions International B.V., Sif Netherlands B.V., TNO, and Van Oord Offshore Wind Projects B.V. The objective of the project was to further improve the existing (mono)pile installation technologies by proposing, engineering and demonstrating a novel pile-driving method. To test and prove the applicability of the newly proposed technology, its performance was compared against conventional installation methods, both in terms of driving performance and the lateral behaviour of the installed (mono)piles.

Enhanced (GDP) vibro-driving

Conceived in TU Delft, the Gentle Driving of Piles (GDP) installation method was proposed as an improvement on the traditional axial vibro-pile driving, by complementing the low-frequency axial (vibrations) with high-frequency torsional vibrations. Conceptually, the torsional vibrations are expected to consume the soil frictional resistance and reduce the pile radial expansion during driving, allowing for faster, and quieter pile driving.

To achieve a preliminary demonstration of the GDP technology, complemented with the comparative demonstration of its performance in both pile-driving and the post-installation pile performance, extensive medium-scale field tests were conducted in an inhomogeneous sand deposit at the Port of Rotterdam (site photo in Figure I.8a). A total of eight identical test piles ($D = 0.762$ m, $L_{emb} = 8$ m) were installed, using impact, traditional axial vibratory piling, and the GDP method. The test procedure consisted of two distinct stages; the first stage investigated the driving performance, and in the second phase, the cyclic lateral behaviour of the piles under repeated loading was studied with respect to the different installation methods. During the latter, the main test piles (with heavy instrumentation) were subjected to an elaborate loading programme (loading set-up in Figure I.8b) of $\approx 82 \times 10^3$ cycles, of variable amplitude and frequency, Figure I.9. Additional/original material

(a)

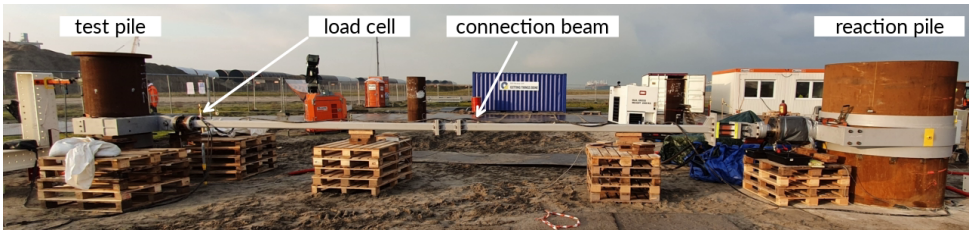

(b)

Figure I.8: Photos taken from the GDP site in the port of Rotterdam. In (a), an aerial photo of the GDP site, and in (b) the loading frame for the post-installation lateral loading tests, connected to a main test pile and the reaction pile.

for the GDP project can also be found (besides this study) in Metrikine et al., 2020; Tsetas et al., 2020.

Chapter III presents a careful inspection of the GDP experimental results (lateral pile response on the elaborate loading programme of Figure I.9), which provided considerable insight into the cyclic response of piles in (un)saturated sands. The observed response, motivated the development of a cyclic soil reaction model, presented in Chapter IV, which ultimately allowed the assessment of the main test piles' performance in the GDP field experiments (presented in Chapter V). The objective of this study was to understand the complex response of the tested piles in the GDP field, and finally to infer the impact of the installation method from the post-installation response.

The aforementioned experimental campaigns had a significant impact on the trajectory and a major contribution to the reach and scope of the presented work. These projects – designed independently to address (different) uncertainties associated with the (mono)pile foundation, provided the necessary material for this study to address the knowledge gap regarding i) the resonance frequency of wind turbines on monopile foundations, ii) the

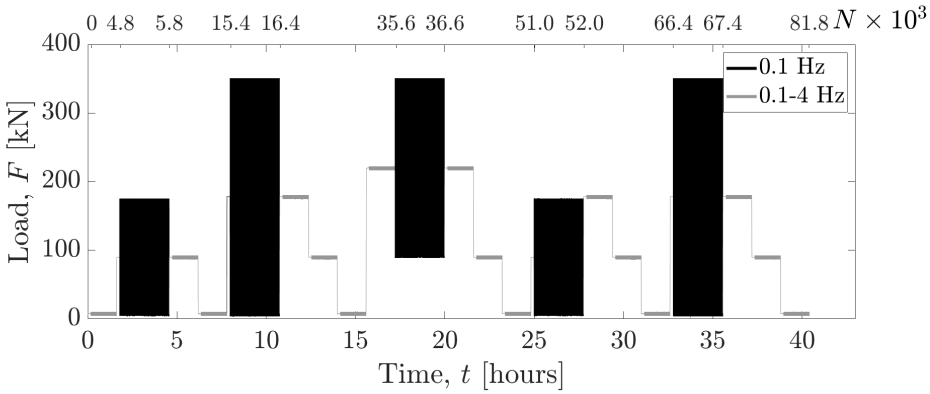

Figure I.9: The 40-hour loading programme (N = 82000 cycles), applied in the main test piles during the GDP field tests. Black and gray lines depict slow f =0.1 Hz loading with high amplitude, and fast f = 0.1 – 4 Hz loading with small amplitude (5kN) respectively.

dynamic interactions between monopile and soil, iii) the cyclic behaviour of (mono)piles under repetitive cyclic loads, iv) installation effects for conventional technologies and the novel GDP method, but also to validate and improve existing numerical approaches (both 1D and 3D FE modelling).

3 . Dissertation outline

The submitted dissertation is formatted as a collection of journal papers. Arranged in chronological order, the journal papers cover the main body of the research work conducted by the candidate during his doctoral studies. The thesis is comprised of a total of six chapters, namely i) the Introduction, ii) journal papers I-IV (four chapters) and iii) the Conclusions. The list of journal papers that compose this dissertation follows below.

Paper I

Published in Géotechnique, (2021), 71(9), pp. 812-825.
https://doi.org/10.1680/jgeot.19.TI.024

Frequency effects in the dynamic lateral stiffness of monopiles in sand: insight from field tests and 3D FE modelling

Evangelos Kementzetzidis, Andrei V. Metrikine, Willem G. Versteijlen, Federico Pisanò

Paper II

Published in Ocean Engineering, (2023), 270, 113452.
https://doi.org/10.1016/j.oceaneng.2022.113452

Gentle Driving of Piles (GDP) at a sandy site combining axial and torsional vibrations: Part II – cyclic/dynamic lateral loading tests

Evangelos Kementzetzidis, Federico Pisanò, Ahmed S. Elkadi, Apostolos Tsouvalas, Andrei V. Metrikine

Paper III

Published in Computers & Geotechnics, (2022), 148, 104810.
https://doi.org/10.1016/j.compgeo.2022.104810

A memory-enhanced py model for piles in sand accounting for cyclic ratcheting and gapping effects

Evangelos Kementzetzidis, Federico Pisanò, Andrei V. Metrikine

Paper IV

Under review for publication in the Journal of Geotechnical and Geoenvironmental Engineering.

Gentle Driving of Piles (GDP) at a sandy site combining axial and torsional vibrations: quantifying the influence of pile installation method on lateral behaviour

Evangelos Kementzetzidis, Federico Pisanò, Athanasios Tsetas, Andrei V. Metrikine

Figure I.10: Photograph from the ICE award ceremony in London, October 2022. Paper I of this dissertation was awarded as the best offshore paper of 2021. From left to right are Federico Pisanò, Evangelos Kementzetzidis, Ed McCann (ICE president 2021-2022) and Andrei Metrikine.

II

Paper I

Frequency effects in the dynamic lateral stiffness of monopiles in sand: insight from field tests and 3D FE modelling

Evangelos Kementzetzidis, Andrei V. Metrikine, Willem G. Versteijlen, Federico Pisanò

Géotechnique, (2021), 71(9), 812-825.

https://doi.org/10.1680/jgeot.19.TI.024

In 2022, this paper was awarded the prestigious David Hislop (offshore) award from ICE, the Institution of Civil Engineers.

https://www.icevirtuallibrary.com/page/awards/david-hislop

Abstract

With the offshore wind industry rapidly expanding worldwide, geotechnical research is being devoted to foundation optimisation – most intensively for large-diameter monopiles. The analysis and design of monopiles still suffers from significant uncertainties in relation to cyclic/dynamic loading conditions. This work aims to shed new light on dynamic soil-monopile interaction, based on the results of unique full-scale experiments performed at the Westermeerwind wind park (Netherlands). The response of a 24 m long, 5 m diameter monopile to harmonic lateral loading of varying amplitude and frequency is inspected. The analysis of original field measurements (soil accelerations and pore pressures) enables to link the lateral stiffness observed at the monopile head to dynamic effects occurring in the surrounding soil. The interpretation of measured data is supported by three-dimensional finite element studies, also looking at the influence of drainage conditions and monopile size. The set of presented results supports the need for dynamics-based monopile design as higher frequencies gain relevance in most recent offshore wind developments.

1. Introduction

In recent years renewable energy resources have gained increasing relevance worldwide in the fight against climate change, in order to free human development from polluting fossil fuels. Quite meaningful in this respect is the example of the Netherlands, where the Ministry of Economic Affairs has recently drawn a roadmap for CO_2-neutral energy supply by 2050 (Dutch Ministry of Economic Affairs, 2016). The transition to renewables is regarded as one of the pillars for achieving CO_2-neutrality, a goal towards which public agencies, industry and academia, are currently joining efforts.

The boom of the offshore wind market is continuing in Northern Europe and gradually expanding to other continents (Archer et al., 2017; Chancham et al., 2017; Mattar and Borvarán, 2016; Tsai et al., 2016). Technological improvements have enabled the growth in size and capacity of offshore wind turbines (OWTs), along with remarkable cost reduction – notable examples of new-generation OWTs are General Electric's Haliade-X 12 MW and Siemens Gamesa's 14 MW turbines, featuring a rotor diameter of 220 m and 222 m, respectively. The trend towards installations in deeper waters and harsher environments poses significant technical challenges, especially regarding support structures and foundations (Pisanò and Gavin, 2017; Versteijlen, 2018). To date, about 80% of all OWTs installed in Europe are founded on monopiles, tubular steel piles of large diameter. Although alternative structural concepts are also receiving attention (e.g., jacket-supported or floating OWTs – Arany and Bhattacharya, 2018; Bienen et al., 2018; Wang et al., 2018b), monopile-supported OWTs will continue to dominate the market in the foreseeable future as a low-risk solution (Kallehave et al., 2015a).

The uncertainties still associated with monopile design (Doherty and Gavin, 2012; Kallehave et al., 2012) have given rise to valuable research projects, such as PISA in the UK (Byrne et al., 2019), REDWIN in Norway (Skau et al., 2018) and, in the Netherlands, DISSTINCT (Versteijlen et al., 2017b). One of the main open questions in monopile design concerns the effects of installation on the operational performance. At present, most monopiles are driven into the soil by impact hammering, a method believed to highly influence the state of the soil around the monopile shaft and under the tip. Interesting steps towards grasping installation effects have been recently taken (Anusic et al., 2017; Fan et al., 2021b; Galavi et al., 2017; Tehrani et al., 2016), although with no wide consensus about long-term consequences. The above-mentioned DISSTINCT project used dynamic load tests on a full-scale, impact-driven monopile to address a number of interrelated questions (Versteijlen et al., 2017a): are (pre-installation) soil properties from site investigation relevant to (post-installation) soil-monopile interaction? Are existing prediction models adequate to capture such interaction as it occurs in the field? Would field tests on a single monopile provide sufficient insight into real dynamic behaviour, and enable cost optimisation at the wind park scale?

In the past decades, a number of authors have studied the dynamic interaction between soil and (slender) piles, originally in relation to vibrating machines, bridge piers, and earthquakes (Angelides and Roesset, 1981; Dobry and Gazetas, 1988; Gazetas and Dobry, 1984a; Kagawa and Kraft, 1980; Kuhlemeyer, 1979; Mylonakis and Gazetas, 1999; Novak, 1974; Shadlou and Bhattacharya, 2014). More recently, contributions about short monopiles and caissons for OWTs have also appeared in the literature (He et al., 2019; Houlsby et al., 2005, 2006; Shadlou and Bhattacharya, 2016). DISSTINCT added to this research thread through a field investigation on monopile behaviour under loading frequencies larger than currently considered in offshore design. Indeed, the range of relevant loading frequencies is gradually expanding beyond 0.5 Hz, mostly due to OWTs being built in seismically active regions, and/or exposed to 'breaking & slamming' sea waves in deeper waters (Paulsen et al., 2019). This paper dives deep into DISSTINCT field test results with support from three-dimensional (3D) finite element (FE) modelling (Pisanò, 2019). Focus is on the frequency-dependence of the lateral monopile stiffness as observed in the field during low-amplitude vibrations. Field data and numerical simulation results are critically compared to explore the role of relevant dynamic effects, such as structural resonance(s) in the embedded monopile and pore pressure variations in the surrounding soil.

2 . Full-scale field tests

The present work builds on the results of full-scale field tests performed in the framework of DISSTINCT (*Dynamic Interaction between Soil & Structures, Tools & Investigations using Numerical Calculation & Testing*), a 4-years collaborative project (2014-2018) involving TU Delft, Siemens Gamesa Renewable Energy, DNG-GL, Fugro, SWP and MBO Offshore. Methodology and main outcomes of the experimental programme are briefly overviewed in this section, while more details can be found in Versteijlen et al., 2017a and Versteijlen, 2018.

Dynamic load tests were executed on a monopile at the Westermeerwind wind farm, located in the Netherlands on the eastern shore of the IJsselmeer lake (Figure II.1). The monopile was 5 m in diameter and embedded under water in prevalently sandy soil for 24.05 m (L_{emb}) of its length ($L = 33.9$ m) – Figures II.2–II.3.

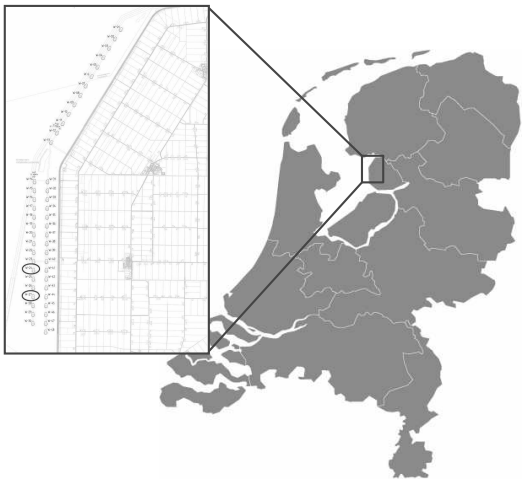

Figure II.1: Location of the Westermeerwind wind farm – modified after Versteijlen et al., 2017a.

2 .1. Site characterisation

The wind farm site was characterised by combining seismic cone penetration tests (SCPTs) and boreholes. Within the shallowest 30 m (cf. to $L_{emb} = 24.05$ m), in situ tests confirmed the presence of medium-dense to dense sand ($D_R \approx 60 - 85\%$), with interleaved thin layers of peat and stiff clay at about 1 m and 20 m height below the mudline, respectively – see Figure II.2 regarding the SCPT45 test performed at the monopile location. Additional information about soil permeability at the site was inferred by the results of two HPT-CPTs (Hydraulic Profiling Tests) and one slug test executed near the monopile. The results of these tests returned a continuous permeability profile, featuring average sand permeability of approximately 1.4×10^{-4} m/s.

At the IJsselmeer lake the Appelscha geological formation is known to create a rigid bedrock at depths ranging from 60 to 100 m. This information enables to estimate the multiple resonance frequencies associated with vertical shear wave propagation:

$$f_n = \frac{(2n-1)V_s}{4H} \tag{II.1}$$

where the n^{th} resonance frequency depends on the shear wave velocity V_s and the bedrock depth H. Inferring from Figure II.2 a representative V_s of 300 m/s, the first resonance of

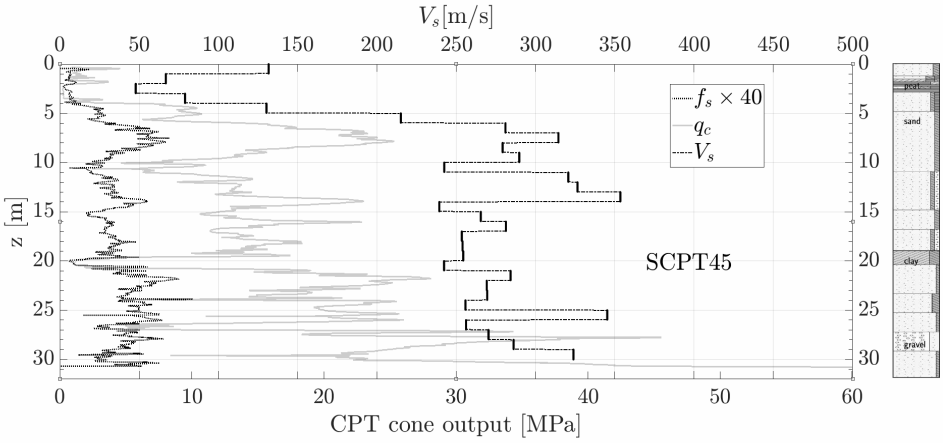

Figure II.2: Site characterisation near the monopile location based on SCPT tests (main plot) and borehole data (right side) – q_c: cone resistance, f_s: sleeve friction, V_s: shear wave velocity. Modified after Versteijlen et al., 2017a.

the sandy deposit is expected to lie in the range between 0.75 and 1.25 Hz (Versteijlen et al., 2017a).

2 .2. Field testing procedures and measurements

After impact pile driving, dynamic lateral load tests were executed by placing at the top of the monopile the vibratory device depicted in Figure II.3 – a shaker consisting of two hydraulically powered large cogwheels. The shaker was able to deliver a maximum hydraulic power of 50 kW and rotate at a maximum frequency of 8.6 Hz. Steel plates were attached over the cogwheels at varying radial distance, and three different weight setups were considered to study the influence of the loading amplitude. Detailed studies delivered accurate estimates of effective lever arm (R) and rotating mass (m_e) associated with each set-up (Versteijlen, 2018). The total force $F(t)$ applied to the monopile head can thus be calculated as a function of the angular frequency of mass rotation (Ω, [rad/s]):

$$F(t) = m_e \Omega^2 R \sin(\Omega t) \tag{II.2}$$

where t denotes time. Different load cases were set up, and especially relevant to this paper were those involving step-wise increase in excitation frequency. For each mass configuration, the duration of each frequency step was deemed sufficient to approach steady-state conditions. Three steel plates of different mass were used to generate the experimental scenarios summarised in Table II.1. It was also evaluated that DISSTINCT shaking tests loaded the pile with forces much lower than those to be later transmitted by the installed OWT, and therefore well below the lateral capacity of the foundation.

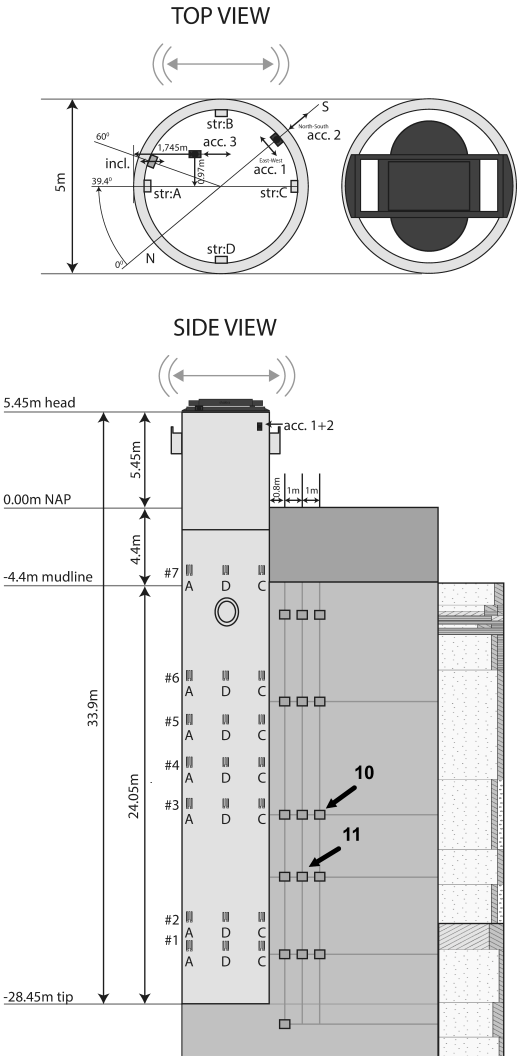

Figure II.3: Measurement setup. Depth values correspond with the NAP (Dutch equivalent of Mean Sea Level). Square markers in the soil region indicate locations of soil sensors, i.e. cones equipped with accelerometers and pore water pressuremetres. Numbering along the pile (e.g. #1, #2, etc.) refers to arrays of strain gauges. Structural accelerations were measured both at the pile head and at the shaker. The locations of pore water and soil acceleration sensors 10 and 11 are put in evidence by arrows – modified after Versteijlen et al., 2017a.

As illustrated in Figure II.3, the response of the monopile was recorded through sensors installed on the pile and in the soil (Versteijlen, 2018; Versteijlen et al., 2017a). Two Althen

Setup	$m_e \times R$ [mkg]	Frequency range [Hz]	Force range [kN]
Heavy weight	239.32	1.04 - 4.03	10.31 - 153.42
Middle weight	88.76	1.06 - 6.70	3.95 - 157.31
Light weight	32.08	5.04 - 8.68	32.15 - 95.40

Table II.1: Technical specifications for the DISSTINCT load cases considered in this study.

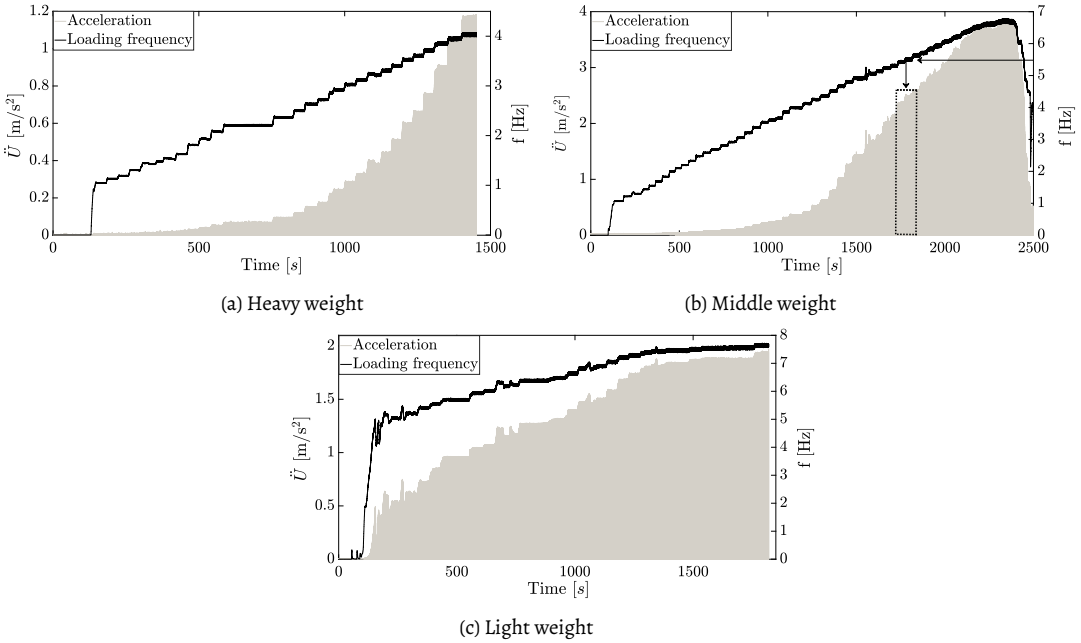

(a) Heavy weight

(b) Middle weight

(c) Light weight

Figure II.4: Time evolution of accelerations ($\ddot{U}$) recorded at the shaker and loading frequency (f) for the three loading scenarios in Table II.1. Only the positive side of acceleration diagrams are plotted for better readability. The dashed window in (b) highlights the response around 5.5 Hz.

AAA320 accelerometers where placed on the pile head and one on the shaker, together with strain gauges along the monopile shaft. The soil response around the pile was detected by measuring local accelerations and variations in pore water pressure. The soil motion was recorded via 16 AS28/5g accelerometers capable of measuring accelerations lower than 1 gal. Variations in pore water pressure were recorded by means of fully analogue, 4-20 mA pressure transmitters of ATM/N type, endowed with a Wheatstone bridge circuit with analogue amplifier. It was thus possible to detect 'practically infinitesimal' pore pressure variations (very high resolution), and record maximum values up to 500 kPa with a deviation no larger than 0.3 kPa.

2 .3. Experimental data

The analyses presented in this work are mainly based on acceleration data at the shaker and pore water pressure variations in the soil. Acceleration and pore pressure signals were post-processed by first removing their baseline (mean value), and then low-pass filtering at 10 Hz against high-frequency noise. All recorded data were interpreted by assuming the soil-monopile system to behave as a damped linear system at steady state for each frequency step. While the assumption of linearity was suggested by the weak loading amplitudes in Table II.1, the attainment of stationary conditions in each frequency step was supported by good agreement with numerical simulation results based on the same assumption – see later on. Overall, assuming steady-state linear response also justified the above-mentioned low-pass filtering of acceleration records. As free-vibration components would be eventually damped out, it seemed appropriate to focus on a relatively narrow frequency band around the main input spectrum (Table II.1), so as to exclude most of the noise in sensor records. Filtered acceleration signals from the shaker and varying mass rotation frequency (henceforth, 'loading frequency') are illustrated in Figure II.4 for the three test setups in Table II.1.

As (linear) steady state theoretically implies vibrations at the same frequency Ω of the loading (Equation II.2), it was possible to relate monoharmonic amplitudes of applied force $F(\Omega)$ and shaker displacement amplitudes ($\bar{U}$) from recorded data, with the latter obtained from acceleration amplitudes ($\ddot{\bar{U}}$) as:

$$\bar{U}(\Omega) = -\frac{\ddot{\bar{U}}(\Omega)}{\Omega^2} \tag{II.3}$$

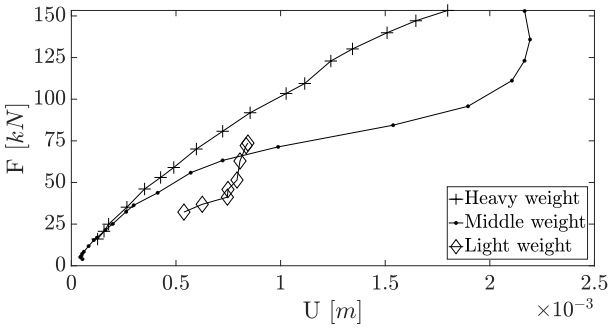

Figure II.5: Steady-state relationship between amplitude of the applied force (F) and displacement (U) at the shaker for the three loading scenarios in Table II.1.

Figure II.5 illustrates (steady-state) relationships between applied forces and displacement amplitudes for the three loading scenarios (heavy, middle, light) – with frequency-dependence implicitly embedded into data points. The same data in Figure II.5 are alternatively plotted in Figure II.6a in terms of absolute value of the lateral dynamic stiffness

($|K_{dyn}^{1dof}|$) against the loading frequency. Data-based $|K_{dyn}^{1dof}|$ values were obtained as the ratio between the amplitudes of applied force and displacement at steady state.

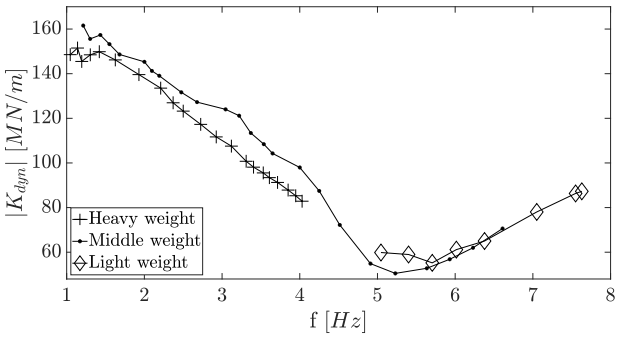

(a) from post-processing of field data for the three loading scenarios in Table II.1.

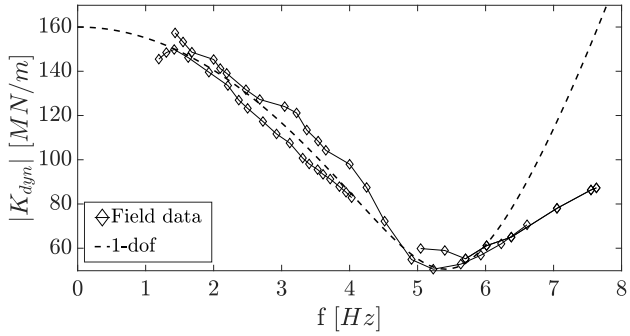

(b) 1dof fitting of field data – static stiffness: K_0^{1dof} =160 MN/m, damping: ζ^{1dof} = 16%, resonance frequency: f_{res}=5.56 Hz.

Figure II.6: Frequency-dependence of the dynamic lateral stiffness $|K_{dyn}^{1dof}|$ observed at the monopile head.

The comparison between Figures II.5 and II.6a hints that, under the low loads considered (Table II.1), the excitation frequency impacts the pile lateral stiffness more pronouncedly than the loading amplitude. The dynamic pile head stiffness in Figure II.6a appears clearly frequency-dependent, with a drop in $|K_{dyn}^{1dof}|$ of about 285% observed between 1-2 Hz and 5.3 Hz. As shown in Figure II.6b, experimental data were then re-interpreted as if they resulted from a one degree-of-freedom (1dof) mass-damper-spring oscillator, featuring (static) stiffness, mass and damping coefficient equal to K_0^{1dof} = 160 MN/m, M^{1dof} = 134 tons and C^{1dof} = 1.482 tons$\cdot s^{-1}$, respectively. Such settings in the equivalent 1dof system are associated with a resonance frequency of 5.5 Hz and a damping ratio ζ^{1dof} = 16%, whereas

the absolute value of the 1dof dynamic stiffness $|K_{dyn}^{1dof}|$ was derived from the absolute value of the frequency response function $G(\Omega) = U(\Omega)/F(\Omega)$:

$$|K(\Omega)_{dyn}^{1dof}| = 1/|G(\Omega)| = \sqrt{(K_0^{1dof} - M^{1dof}\Omega^2)^2 + (C^{1dof}\Omega)^2} \tag{II.4}$$

and then used to match the valley in experimental $|K_{dyn}^{1dof}|$ trends. The associated 1dof damping ratio of 16% may not be solely attributed to energy dissipation in the soil: generally, input energy will be dissipated through several physical mechanisms, including material damping (in the soil and in the monopile) as well as wave radiation. It should also be noted that 1dof fitting is fully adequate up to its resonance frequency, while $|K_{dyn}^{1dof}|$ is clearly over-predicted beyond that point. The physical nature of such resonance is discussed later on.

Interpretation of strain gauge data

Data from the strain gauges along the monopile supported the interpretation of the structural response during all shaking tests. For example, Figure II.7 reports 2 seconds of axial strains associated with the middle weight setup towards the end of the 5.5 Hz frequency step – the frequency at which the lowest $|K_{dyn}^{1dof}|$ is observed. Same as done for acceleration signals, strain data were also low-pass filtered at 10 Hz and corrected for mean offset. The strain time histories in Figure II.7 relate to sensors from 2A to 7A (Figure II.3). The highest pile bending moment is expected to occur where the highest axial strain is recorded, i.e. at sensor 6A. Importantly, all strain gauges recorded at 5.5 Hz simultaneous compressions and extensions along the same side of the monopile, meaning that the valley in the $|K_{dyn}^{1dof}|$ frequency-dependence is associated with the first bending mode.

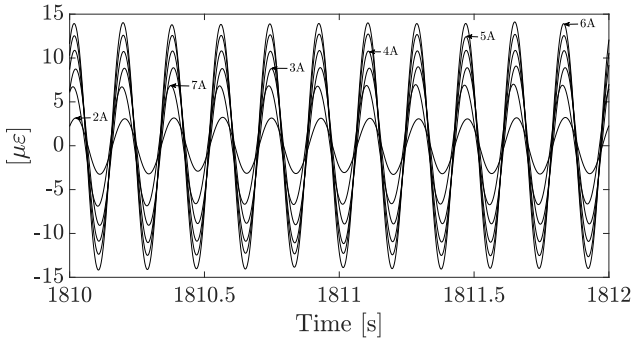

Figure II.7: Axial strains (ϵ) recorded along the monopile for the middle weight setup at the loading frequency of 5.5 Hz.

Assessment of soil measurements

As previously mentioned, an array of accelerometers and pore-pressure sensors were installed in the soil near the monopile. As for pore pressure measurements, most attention was devoted to transient variations (Δp_w) with respect to pre-shaking, hydrostatic values. Generally, low levels of soil acceleration ($\ddot{u}$) and pore pressure variations were recorded for the low-amplitude loads applied by the shaker, in the order of 0.1-0.2 m/s^2 and 0.5 kPa, respectively. Only pore pressure measurements in strong correlation with pile shaking were considered after selection based on the following procedure:

1. both soil acceleration and pore pressure signals were low-pass filtered at 10 Hz (see Figures II.8a-II.8b), then normalised with respect to their maxima;
2. cross-correlation functions were numerically determined for pairs of (normalised) acceleration and pore pressure signals, so as to objectively quantify signal similarity;
3. only pore pressure measurements highly correlated with soil motion were deemed reliable.

The above procedure led to 'approve' only those sensors ensuring high cross-correlation between pore pressure variation and acceleration. For the middle weight setup taken as main reference, this prerequisite was only fulfilled by sensors 10 and 11 in Figure II.8. For both sensors, correlations between pore pressure variations and horizontal accelerations were very similar regardless of the direction (x or y) – the cross-correlations shown in Figure II.8 relate to measured accelerations projected along the loading direction.

3 . 3D FE modelling

3D FE analysis is proving increasingly valuable to modern offshore wind developments, in that it can support the understanding of complex geotechnical mechanisms, as well as the conception of engineering design methods (Byrne et al., 2019; Kementzetzidis et al., 2019, 2018; Pisanò, 2019). 3D FE modelling was carried out through the OpenSees simulation platform (McKenna, 1997), however with no need for advanced, non-linear modelling of soil behaviour. As DISSTINCT field tests were performed by applying low-amplitude vibrations, the soil was idealised as a water-saturated, linear elastic, porous medium, with hydro-mechanical coupling effects possibly taking place depending on well-known governing factors (Zienkiewicz et al., 1999).

Numerical studies were conducted at two levels, aiming to investigate the response of soil-monopile system as a whole, but also the dynamics of the site prior to pile installation ('soil-only' analyses). The following three types of FE dynamic analyses were performed:

– soil deposit subjected to harmonic horizontal loading at the free surface;
– soil deposit subjected to harmonic vertical loading at the free surface;

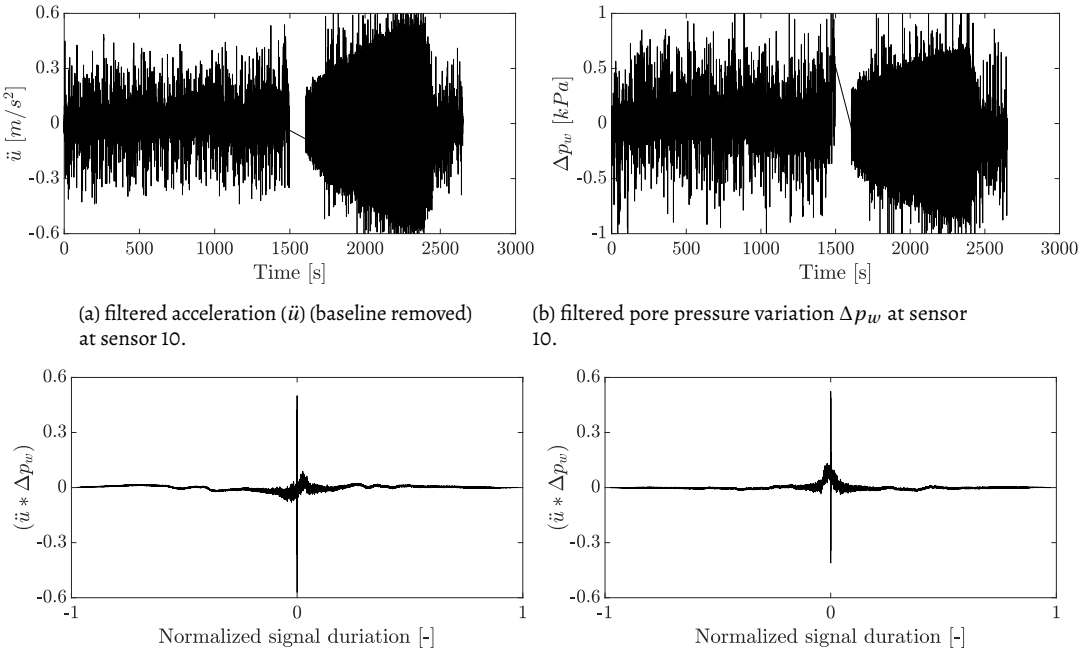

(a) filtered acceleration ($\ddot{u}$) (baseline removed) at sensor 10.

(b) filtered pore pressure variation Δp_w at sensor 10.

(c) acceleration-pressure cross-correlation for sensor 10.

(d) acceleration-pressure cross-correlation for sensor 11.

Figure II.8: Comparative assessment of soil acceleration and pore pressure variation data for the middle weight load setup in Table II.1. Data gaps in (a) and (b) around 1500 s were caused by partial corruption of original data files. (c) & (d) show the cross-correlation between acceleration-pore water pressure signals ($\ddot{u} * \Delta p_w$) for sensors 10 and 11.

– soil-monopile system subjected to harmonic horizontal loading at the monopile head as during the reference shaking tests.

In all cases sinusoidal point loads were applied until the attainment of steady state (total duration up to 120 seconds in some cases), with loading frequency ranging from 0 to 7.5 Hz and load application point shown in Figure II.10.

3 .1. Governing equations and space/time discretisation

The 3D FE model was built on the Biot-Zienkiewicz *u-p* coupled formulation described in Zienkiewicz et al., 1980, particularly in the simplified 'consolidation form' studied by Chan, 1988. Such formulation enabled to analyse with a single model the extreme hydromechanical bounds of fully drained and undrained response, by setting either very high or very low soil permeability in the coupled FE model. As shown in the Appendix, a *u-p* model of the mentioned kind produces results that are equivalent to the outcome of a one-phase/drained model as the permeability tends to infinity (i.e., to very high values). Given the assumption

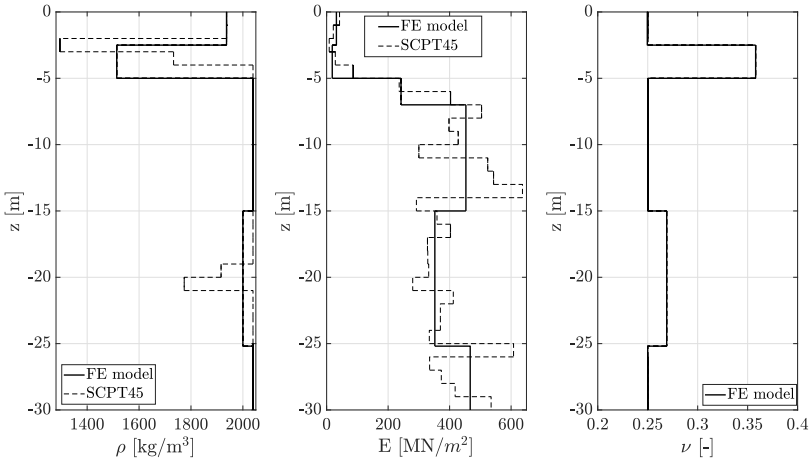

Figure II.9: Depth (z) profiles of saturated mass density (ρ) and elastic properties, Young's modulus (E) and Poisson's ratio ν, adopted in FE simulations.

of linear elastic behaviour, the properties of the soil skeleton were directly inferred from site investigation data (SCPT45, Figure II.2) to characterise the stratigraphy shown in Figure II.9. The typical value of $K_f = 2.2 \cdot 10^6$ kPa was assigned to the bulk modulus of the pore water. The geometrical/loading symmetry of the problem was exploited to build a less expensive half-model.

The soil domain was discretised using the eight-node H1-P1ssp stabilised elements developed by McGann et al., 2015, featuring equal-order, linear interpolation of both displacement and pore pressure unknowns. The benefits of H1-P1ssp elements in relation to soil-monopile simulations are described by Corciulo et al., 2017, and include the stabilisation of pore pressure instabilities as undrained conditions are approached. Space discretisation was set to ensure proper propagation of harmonics up to 8 Hz, so that no less than 7–8 elements per wavelength were guaranteed in that frequency range. The standard Newmark integration algorithm was selected for time marching, with integration parameters β and γ equal to 0.6 and 0.3025, respectively (Hughes, 1987). A time-step size of $\Delta t = 8.3 \times 10^{-4} s$ was found appropriate after numerical sensitivity studies (Watanabe et al., 2017) – not reported for brevity.

To alleviate computational costs, it was not attempted to model the real location of the bedrock at the IJsselmeer lake, about 100 m below the mudline. This choice was noted to affect the simulated dynamics of the soil deposit (and in turn of soil-monopile interaction), however with no serious impact on the general conclusions drawn later on in this study.

3 .2. Structural modelling of shaker and monopile

The embedded portion of the monopile was modelled as a 3D steel continuum and discretised by means of one-phase, eight-node ssp bricks (McGann et al., 2015). Conversely, the above-mudline part was modelled as an elastic beam and discretised through twenty Timoshenko beam elements (≈ 50 cm each), featuring consistent (non-diagonal) mass matrix. The mass of the shaker M_{sh} was lumped at the top of the monopile – see Figure II.10. Added mass effects associated with surrounding sea water were simplistically introduced in the form of nodal lumped masses evenly distributed along the water depth $H_w \approx 4.5$m (Figure II.3), and calculated as twice the water mass in the submerged OWT volume (Newman, 1977).

It was not attempted to include in the model a soil-pile interface with properties different from the surrounding/intact soil, nor with non-linear frictional behaviour. Although it is clearly unrealistic to assume perfect soil-pile bonding, this choice allowed to preserve the intended linearity of the analyses, and avoided the guess of interface parameters in the lack of specific experimental data. It was noticed, however, that interface properties may quantitatively affect dynamic soil-monopile interaction, especially at higher frequencies – this matter will receive further attention in future studies.

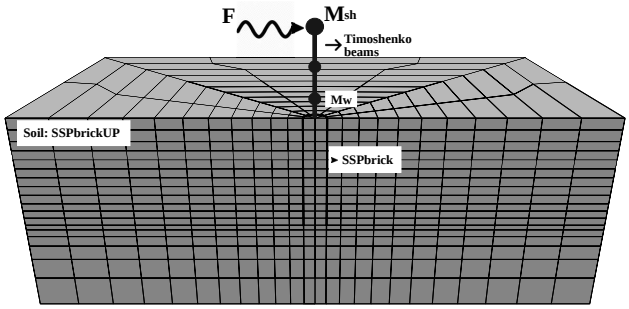

(a) shaker-monopile-soil

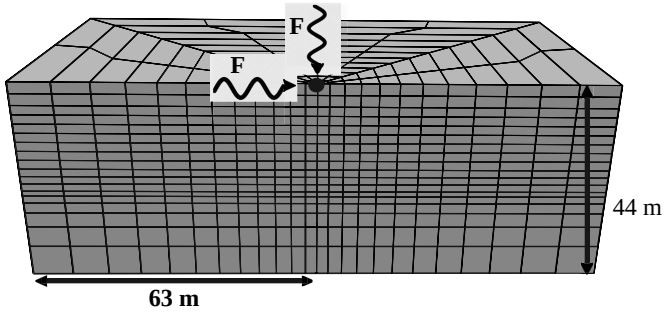

(b) soil-only

Figure II.10: Discretised soil domain and loading settings in complete and 'soil-only' FE analyses.

3 .3. Energy dissipation in the numerical model

Energy dissipation (damping) plays an essential role in dynamic soil-structure interaction. OWTs dissipate energy during operations in multiple ways, such as:

- aerodynamic damping due to interaction between wind and rotating blades;
- hydrodynamic damping associated with monopile-water interaction;
- damping in structural materials (steel) and connections;
- damping in the soil arising from material dissipation, hydro-mechanical effects and wave radiation – see also Kementzetzidis et al., 2019.

In all FE simulations, aerodynamic and hydrodynamic damping were neglected, since no actual OWT tower was present during the field tests in very shallow water depth (only 4.4 m above the mudline). It is also worth mentioning that:

- wave radiation through lateral domain boundaries was enabled based on the well-established approach by Lysmer and Kuhlemeyer, 1969;
- with the soil modelled as a linear elastic material, no damping in the solid skeleton was accounted for, in reasonable agreement with the small amplitude vibrations associated with the load cases in Table II.1. The use of Rayleigh damping to model dissipation in the soil skeleton at very small strains was not pursued, due to the lack of relevant data for calibration;
- (compressional) wave motion in saturated porous media is generally dissipative due to hydro-mechanical coupling effects – for instance, under the fully undrained conditions considered later on (Biot, 1956; Han et al., 2016);
- steel damping in the monopile was introduced according to Eurocode 1 BS EN, 1991, with (Rayleigh) damping ratio ζ_{steel} = 0.19% at the pivotal frequencies of 0.1 and 80 Hz;
- numerical damping spontaneously arises from Newmark's time integration algorithm set up as mentioned above. Nonetheless, algorithmic dissipation proved beneficial in attenuating high-frequency spurious oscillations in the simulated response (Kontoe et al., 2008).

4 . FE-based interpretation of field data

This section elaborates on the interpretation of field observations based on 3D FE results.

4 .1. 'Soil-only' simulations

Preliminary 'soil-only' simulations were performed to investigate the dynamics of the reduced soil model, and grasp its influence on the response of the shaker-monopile-soil system. The layered soil domain was subjected to mono-harmonic loading, either horizontal or vertical (Figure II.10), spanning the frequency range of interest from 0 Hz (static loading) to 8 Hz. Hydro-mechanical coupling effects were inhibited by setting an unrealistically high soil permeability of 10^6 m/s, i.e., sufficiently large to make the water-saturated soil behave as a one-phase porous medium of identical total mass density – see Appendix 5 . Horizontal/vertical soil responses at steady state are illustrated in Figure II.11 in terms of amplification factors $A = |\bar{u}_{dyn}|/u_{static}$ at the shaker location, and phase differences between applied load and predicted soil displacement – u_{static} represents the displacement computed under a static load of magnitude equal to the amplitude of the dynamic load.

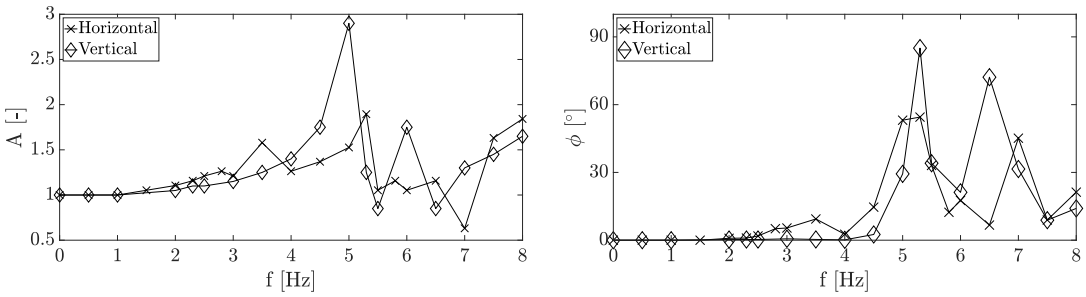

(a) Amplification factor (A)

(b) Phase difference (ϕ)

Figure II.11: Simulated steady-state responses of the soil deposit to horizontal and vertical point loading at varying loading frequency (f).

Phase difference trends in Figure II.11b show in-phase force-displacement oscillations until about 2.5 Hz and 4.5 Hz for horizontal and vertical loading, respectively. As is well-known, nil phase difference is indicative of a quasi-static response with no waves propagating in the domain. The frequencies numerically identified (2.5 Hz and 4.5 Hz) are usually referred to as 'cut-off' frequencies, and mark the transition from 'evanescent waves' (vibrations exponentially decaying along the distance from the source) to actual wave motion (Graff, 2012). Overcoming the cut-off frequency also determines the onset of radiation damping, primary source of energy dissipation in the FE soil models set up in this work. Previous studies on radiation damping in 3D continua pointed out its dependence on excitation frequency, geometrical settings and mechanical properties (Berger et al., 1977; Gazetas and Dobry, 1984a,b; Novak et al., 1978; O'Rourke and Dobry, 1982; Shadlou and

Bhattacharya, 2014). As mentioned above, the FE model is not fully representative of the real site configuration, where the rigid bedrock is quite deeper than in the model. The shallower bedrock set for faster FE computations implies cut-off frequencies higher than expected at the real site, and therefore later onset of radiation damping and some over-prediction of dynamic amplification levels.

4 .2. Dynamics of the shaker-monopile-soil system

Numerical eigenfrequency analysis

As a first step into understanding the response of the whole shaker-soil-monopile system, numerical eigenvalue analysis was carried out for the FE model in Figure II.10. Due to the many degrees of freedom in the discretised system, the analysis returned multiple closely-spaced eigenfrequencies, including the first eigenvalue at 1.59 Hz associated with 'soil-only resonance'. Among the numerous numerical modes found in proximity of relevant frequencies (e.g., near the resonance frequency observed in field test results – ≈ 5.5 Hz), it was not straightforward to identify real physical modes. A heuristic mode-sorting procedure was set up by selecting eigenvectors showing significant lateral displacement of the monopile at the shaker location. Accordingly, three modes near the resonance peak were isolated at 5.67, 5.71 and 5.87 Hz – see graphical representation in Figure II.12. In elastodynamics, each i^{th} mode contributes to the global response depending on the distance between external loading frequency Ω and related eigenfrequency ω_i, with a participation factor Γ_i that takes the following form for undamped multi-dof systems:

$$\Gamma_i = \frac{1}{\omega_i^2 - \Omega^2} \tag{II.5}$$

The above expression clarifies how the effect of the i^{th} mode on the global response vanishes for ω_i far from Ω.

Drained dynamic response

As for 'soil-only' simulations, the dynamic performance of the whole system was first analysed under fully drained conditions. Also in this case, pore pressure effects were prevented by setting high soil permeability ($k = 10^6$ m/s). There was no attempt to re-tune the soil properties in Figure II.9 to improve the numerical simulation of field measurements.

Time domain analyses were performed for different loading frequencies within the selected range (0-7.5 Hz), then steady-state displacement amplitudes at the shaker and load-displacement phase differences were extracted. Drained FE results are compared to experimental data in Figure II.13, and seem to capture well the overall frequency-dependence of the monopile stiffness. The minimum stiffness near 5.5 Hz is clearly reproduced, while simulations for frequencies lower than 2 Hz returned a gradual increase in dynamic stiffness as nearly static conditions are approached. On average, 3D FE results seem to slightly

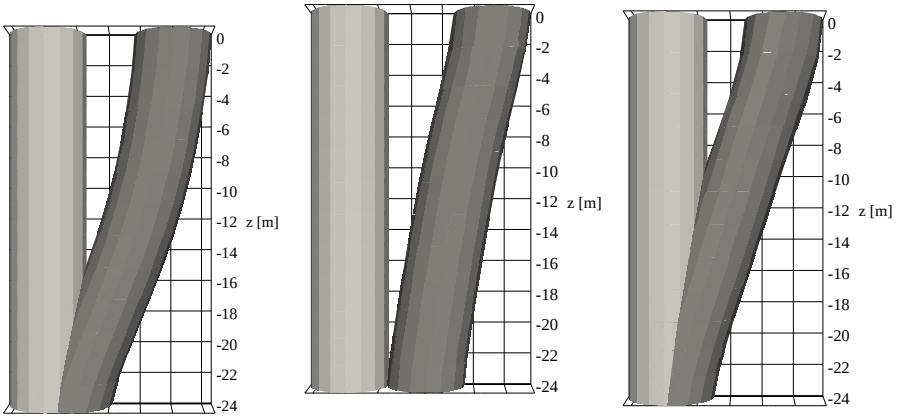

(a) 5.67 Hz (b) 5.71 Hz (c) 5.87 Hz

Figure II.12: Monopile (embedded) modal shapes for eigenvectors of the shaker-pile-soil system associated with eigenfrequencies close to experimental resonance (≈ 5.5 Hz).

over-predict experimental stiffness values, most probably as a consequence of simplifying modelling assumptions.

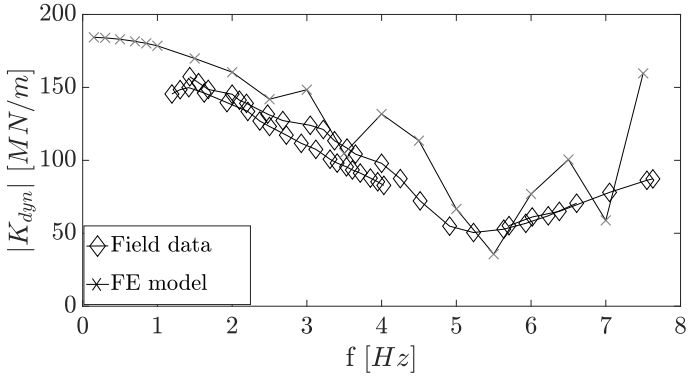

Figure II.13: Frequency dependence of monopile dynamic stiffness $|K_{dyn}|$ as emerging from field tests and FE modelling.

Some sharp 'outliers' appear in the numerical results in the form of local stiffness drops at 2.5, 3.5 and even 5.5. Hz. Such outliers, not visible in experimental data, may be directly related to soil-only amplification (see Gazetas, 1983), as hinted by Figure II.11a. In this respect, accurate modelling of the bottom rigid boundary would be key to improving numerical simulation results. Improved modelling of soil damping would also contribute to

the same goal, in that it would smoothen the sharp outliers in Figure II.13 (Gazetas, 1983). Although DISSTINCT data do not seem affected by pure soil resonance, it is worth noting that soil amplification in soft soils would likely be happening at frequencies lower than 0.5 Hz for bedrocks deeper than 100 m – i.e., within the frequency band considered in current design practice.

Further insight into FE results can be obtained by inspecting the phase difference between applied load and steady-state displacement at the shaker head. Figure II.15 reveals significant increase in phase difference in the vicinity of 5.5. Hz. This observation suggests an analogy with the response of the equivalent 1dof oscillator depicted in Figure II.6b, exhibiting a 90 phase shift at resonance. The agreement between FE and 1dof phase difference trends in Figure II.15 clarifies the physical nature of the 5.5 Hz stiffness valley, which can be now attributed to global resonance in the shaker-monopile-soil system. Besides, the smoothness of experimental stiffness curves leads to think that more energy dissipation occurred in field tests than reproduced by the FE model.

Also obtained from FE results is the steady-state deformed shape of the monopile at 5.5 Hz, resembling in Figure II.14 the typical shape of a cantilever loaded at the free end. This outcome is in full agreement with the strain measurements in Figure II.7. As none of the modes in Figure II.12 represents accurately the dynamic deformed shape, the influence of several participating modes is deduced.

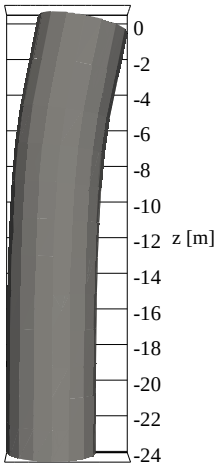

Figure II.14: Steady-state deformed shape of the monopile arising from 5.5 Hz FE calculations.

An additional conclusion about the dynamic stiffness of the monopile is inspired by 1dof-based arguments – refer to frequency-dependent, 1dof dynamic stiffness in Equation (2 .3). If damping is neglected as a first approximation, then mass is the main stiffness-reducing

factor (depending on Ω^2). Figure II.13 shows a decreasing stiffness branch at frequencies lower than 5.5 Hz, which is most likely due to monopile-shaker-soil mass effects.

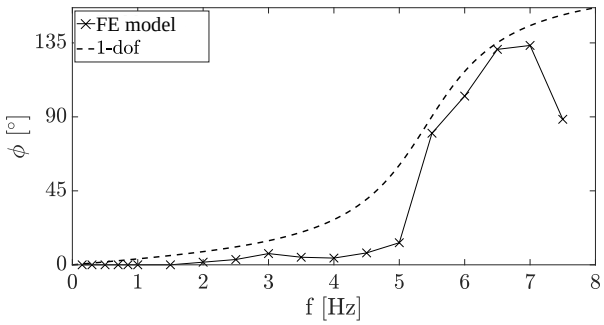

Figure II.15: Phase difference (ϕ) between applied load and steady-state shaker displacement from FE and equivalent 1dof results.

Undrained dynamic response

The FE results presented so far were obtained for fully drained conditions, i.e., by disregarding hydro-mechanical coupling effects in the soil. To assess the impact of such assumption, the response of the system in the opposite undrained limit was numerically explored by assigning a vanishing permeability ($k = 10^{-18}$ m/s) to the whole soil domain. Accordingly, it was possible to simulate pore pressure variations caused by hindered water drainage.

As in the drained case, 'soil-only' simulations were first performed to clarify how the undrained dynamics of the soil deposit can impact the response to lateral harmonic loading of the shaker-monopile-soil system. The same approach described above for drained conditions was followed, i.e., horizontal and vertical monoharmonic point loads were applied until steady-state over a frequency range from 0 to 8 Hz. Undrained trends of amplification factor and phase difference for both loading directions are reported in Figures II.16a–II.16b.

The undrained monopile-soil model was validated by comparing in Figure II.17 the steady-state amplitudes of pore pressure variations simulated for different loading frequencies to the measurements from sensors 10-11 (Figure II.3) associated with the middle weight load case. As done for the drained simulations, distinct mono-harmonic analyses were performed numerically until the attainment of steady-state; then, steady amplitudes of pore pressure variation were extracted (Figure II.17c) for comparison to measured data – it was assumed that also pore pressure variations reached a steady state in each frequency step during field tests. Numerical steady-state amplitudes (e.g., from Figure II.17c) were finally inserted in Figures II.17a–II.17b over time intervals corresponding with relevant frequency steps. Computed and measured pore pressure variations share same trends and reasonably similar values, confirming the suitability of the 3D FE model in its undrained version.

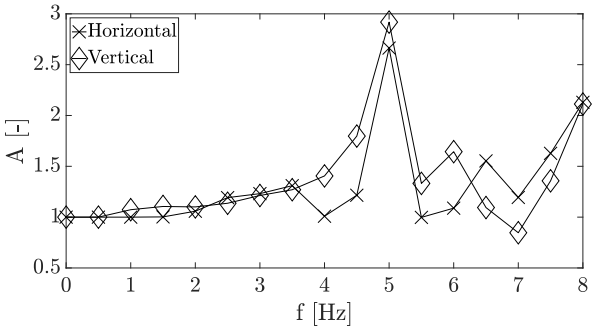

(a) Amplification factor (A)

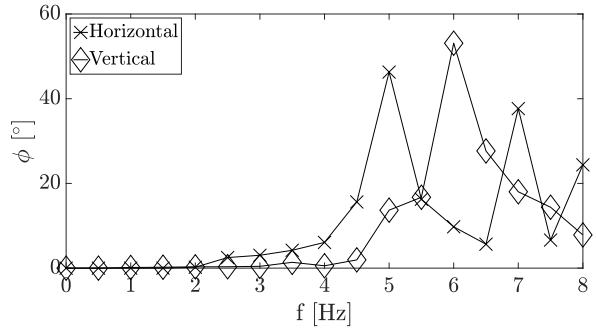

(b) Phase difference (ϕ)

Figure II.16: Simulated undrained steady-state responses of the soil deposit to horizontal and vertical point loading at varying loading frequency (f).

Figure II.17 suggests that pore pressure effects can be very weak under low operational loads, and yet the common assumption of fully drained response in sand not necessarily valid. The poro-elastic FE model enabled to evaluate the impact of hydro-mechanical coupling on the undrained dynamic stiffness of the monopile during small amplitude vibrations. Undrained model predictions are presented in Figure II.18 together with previous drained results and experimental data. Generally, undrained conditions do not seem to affect significantly the dynamic stiffness trend, especially until the 5.5 Hz resonance. Particularly, sharp 'outliers' characterise also the undrained response trend, for instance at 4 and 7 Hz, in a way that can be again attributed to the undrained 'soil-only' amplifications visible in Figure II.16a. Larger discrepancies among experimental, drained and undrained results arise in the post-resonance branch: such evidence hints that partial water drainage and relative soil-water accelerations may play a role in the monopile-soil interaction at sufficiently high frequencies. The investigation of such effects will require further refinement/generalisation of the *u-p*-based FE model adopted in this study.

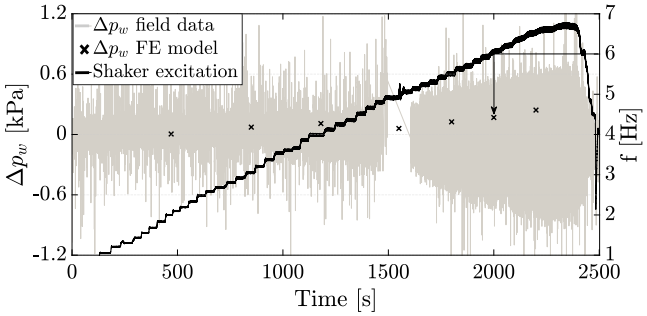

(a) measured pore pressure variations – sensor 10.

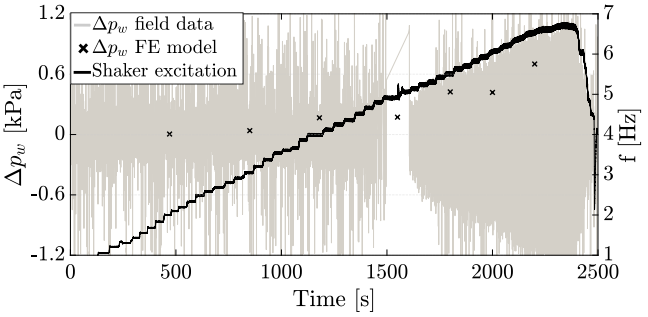

(b) measured pore pressure variations – sensor 11.

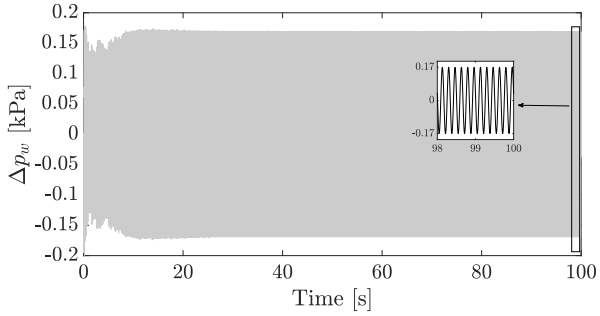

(c) simulation of pore pressure variation under 6 Hz harmonic loading at the location of sensor 10.

Figure II.17: Comparison between measured and simulated pore pressure variations (middle weight load case). The arrow in (a) points to a specific steady-state amplitude ($\Delta p_w = 0.17$ kPa), resulting from the numerical results illustrated in (c).

Influence of monopile diameter

Monopile diameter is normally tuned by designers to achieve desired dynamic performance in terms of OWT first natural frequency. Additional FE calculations were performed for a larger monopile of 6 m diameter, so as to shift the natural frequency of the global system beyond the 'soil-only' resonances previously discussed.

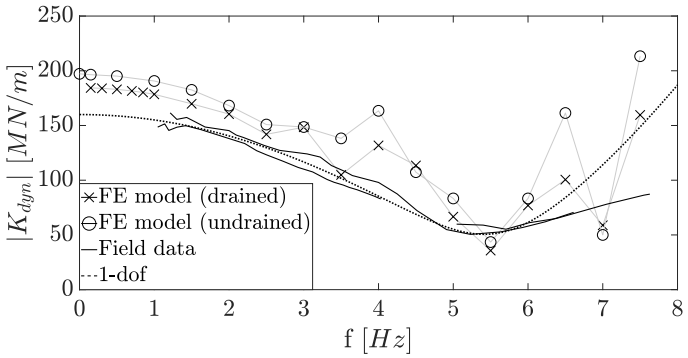

Figure II.18: Influence of drainage conditions on the monopile dynamic stiffness.

Frequency-dependent values of amplification factor, phase difference, and dynamic lateral stiffness are plotted in Figure II.19 for both diameters, 5 and 6 m. It is further confirmed that the amplification frequencies identified at 2.5 and 3.5 Hz are indeed of the 'soil-only' type (Figure II.11a), therefore not affected by mononopile diameter. Additionally, the highest amplification peak for the 6 m diameter monopile occurs at a frequency lower than 5 Hz, and should be compared to the 5.5 Hz resonance hit by the 5 m monopile. This seemingly counter-intuitive outcome (a stiffer monopile may be expected to resonate at a higher frequency) can be explained via the phase difference curves in Figure II.19b. Dynamic resonance is normally accompanied by input-output phase difference of 90 degrees, a circumstance that occurs at ≈ 5.6 Hz for the 5 m monopile, and near 6.8 Hz in the 6 m case – with an amplification peak lower than in the 5 m case. This observation leads to recognise that the 6 m pile undergoes structural resonance near 6.8 Hz, though with an amplification lower than at 5 Hz. Such difference can only be caused by 'soil-only' amplification effects at 5 Hz, whose quantitative influence remarks the importance of accurate domain modelling in dynamic soil-structure interaction problems.

5 . Concluding remarks

The results of full-scale, dynamic field tests on a stiff monopile were examined to investigate the frequency-dependence of soil-pile interaction at a sandy site. To support the interpretation of field data, 3D FE modelling was undertaken, with soil parameters derived from pre-installation site data.

For the weak vibrations induced by the pile-shaking device, the good agreement between experimental and numerical results supported the soundness of most simplifying assumptions, such as the idealisation of linear elastic soil skeleton. Low variations in pore pressures (with respect to hydrostatic values) were predicted when modelling fully undrained conditions – another outcome compatible with field measurements. The latter observation confirmed the suitability of neglecting pore pressure effects for weakly loaded monopiles in

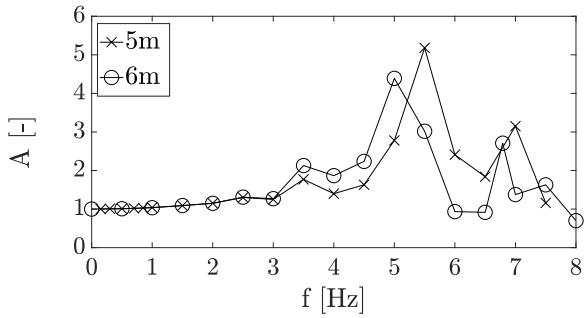

(a) Amplification factor (A)

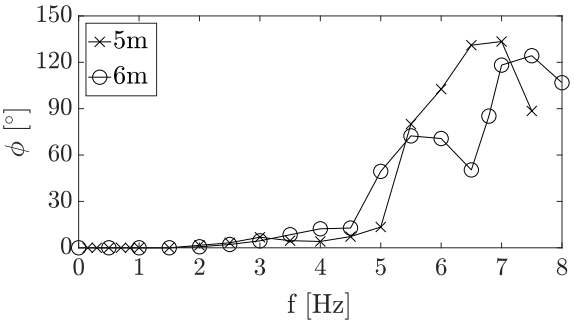

(b) Phase difference (ϕ)

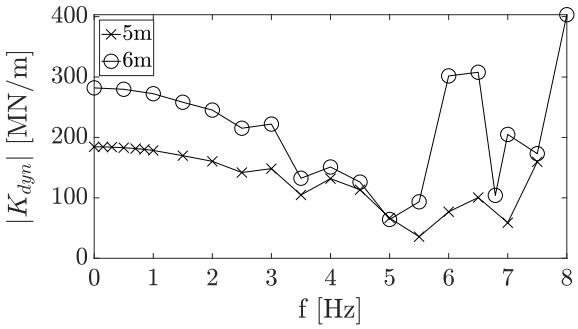

(c) Dynamic stiffness ($|K_{dyn}|$)

Figure II.19: Simulated steady-state responses of laterally loaded monopiles of 5 m and 6 m diameter.

sand; however, claiming that water drainage (and volume changes) are fully allowed in the soil around the pile may prove inaccurate in some cases. Obviously, the discussion about pore pressure effects will assume more relevance for higher load levels, under which soil non-linearity and cyclic effects weigh in more pronouncedly (Kementzetzidis et al., 2019; Liu et al., 2019a).

The dynamic response of the monopile exhibited remarkable frequency-dependence at loading rates higher than currently considered in design. Significant energy dissipation was also observed, with a global viscous damping ratio of about 16% deduced from field data. Wave radiation in the soil is believed to largely, but not exclusively, contribute to such dissipation.

The inspection of FE results at varying frequency, pile diameter and drainage conditions led to recognise the wide range of soil-monopile interaction scenarios caused by dynamic effects. As larger turbines are installed in more dynamically-active environments (deeper waters and/or seismic regions), considerations regarding wave motion in the surrounding soil will become increasingly relevant to geotechnical design.

Appendix

The dynamic response of a layered soil deposit has been studied throughout this work using a two-phase 3D FE model based on the well-known u-p formulation (Zienkiewicz et al., 1999). Compared to its original conception (Zienkiewicz et al., 1980), a simpler u-p formulation ('consolidation form') is adopted in the OpenSees FE software (Elgamal et al., 2002), so that fluid inertial terms (not only soil-fluid relative accelerations) are completely neglected (Chan, 1988). Using the same two-phase FE model, both drained and undrained conditions have been analysed by setting, respectively, very high or very low values of soil permeability. Obviously, a simpler one-phase model could be adopted for uncoupled drained analyses, as long as the saturated soil-fluid mass density is set to represent an underwater soil deposit.

3D one-phase and two-phase dynamic equations are compared in Table II.1 (Equations (II.1)-(II.4)), where ρ indicates the mass density of fluid-saturated soil, and $1/Q = n/K_f + (1-n)/K_s$ the overall compressibility of solid and fluid constituents (average of the corresponding bulk moduli, K_f and K_s, weighted on the porosity n) – all symbols are defined in the notation list. It is readily apparent that, if elastic, stress-independent behaviour is considered for the soil skeleton, then the u-p/consolidation model reduces exactly to the one-phase/drained model as the soil permeability k' tends to infinity. It should be noted that, in the dynamic version of the Darcy law, the hydraulic conductivity k' ([length]^3[time]/[mass]) is introduced in the relationship between (relative) discharge velocity and pore pressure gradient (instead of the hydraulic head gradient). The more usual permeability coefficient k ([length/time]) can be obtained as $k = k'\rho_f g$, where ρ_f and g stand for fluid density and gravity acceleration, respectively (Zienkiewicz et al., 1999).

The same conclusion is further corroborated in Table II.1 (Equations (II.5)-(II.7)) for the case of a 1D elastic soil column under forced harmonic motion. The steady-state eigenvalue problems associated with (II.5), both one-phase and two-phase/incompressible, are formulated in (II.6) and solved for the following boundary conditions: (i) free surface at the top, (ii) rigid/impervious bedrock at $y = H$, (iii) imposed harmonic motion at the bedrock, $u(H,t) = u_{inp}(\Omega)\exp\{(i\Omega t)\}$, with the amplitude u_{inp} possibly a function of the input circular frequency Ω. The two-phase eigenfunction $\bar{u}$ tends to its one-phase counterpart as $k' \to \infty$

Governing Equations	one-phase	two-phase	
mixture momentum balance	$\rho \ddot{u}_i = \sigma_{ij,j}$	$\rho \ddot{u}_i = \sigma_{ij,j} = \sigma'_{ij,j} - p_{w,i}$	(II.1)
elastic stress-strain law	$\sigma_{ij} = \frac{1}{2} D_{ijkl} \left(u_{k,l} + u_{l,k} \right)$	$\sigma'_{ij} = \frac{1}{2} D_{ijkl} \left(u_{k,l} + u_{l,k} \right)$	(II.2)
balance of fluid momentum and mass + Darcy law	—	$k' p_{w,ii} = \dot{u}_{i,i} + \frac{\dot{p}_w}{Q} = 0$	(II.3)
Combined form (A1)+(A2)+(A3)	$\rho \ddot{u}_{i,i} = \frac{1}{2} \left[D_{ijkl} \left(u_{k,l} + u_{l,k} \right) \right]_{,ji}$	$\rho \ddot{u}_{i,i} = \frac{1}{2} \left[D_{ijkl} \left(u_{k,l} + u_{l,k} \right) \right]_{,ji} - \frac{\dot{u}_{i,i} + \dot{p}_w / Q}{k'}$	(II.4)
1D elastic soil column under harmonic excitation			
1D governing equation	$\ddot{u} - \frac{\bar{E}}{\rho} u_{,yy} = 0$	$\left[\ddot{u} - \frac{\bar{E}}{\rho} u_{,yy} + \frac{1}{k'\rho} \left(1 + \frac{\bar{E}}{Q} \right) \dot{u} \right]_{,yy} - \frac{1}{Qk'} \dddot{u} = 0$	(II.5)
eigenvalue problem ($Q \to \infty$)	$\bar{u}_{,yy} + \frac{\rho \Omega^2}{\bar{E}} \bar{u} = 0$	$\left[\bar{u}_{,yy} + \left(\frac{\rho \Omega^2}{\bar{E}} - \frac{\Omega}{k' \bar{E}} i \right) \bar{u} \right]_{,yy} = 0$	(II.6)
eigenfunction $\bar{u}(y,\Omega)$ ($Q \to \infty$)	$\frac{\cos\left(\sqrt{\frac{\Omega^2 \rho}{\bar{E}}} y \right)}{\cos\left(\sqrt{\frac{\Omega^2 \rho}{\bar{E}}} H \right)} u_{inp}(\Omega)$	$\frac{\cos\left(\sqrt{\frac{\Omega^2 \rho}{\bar{E}} - \frac{\Omega}{k' \bar{E}} i} \, y \right)}{\cos\left(\sqrt{\frac{\Omega^2 \rho}{\bar{E}} - \frac{\Omega}{k' \bar{E}} i} \, H \right)} u_{inp}(\Omega)$	(II.7)

Table II.1: Dynamic soil modelling: 1-phase vs 2-phase (*u-p*/consolidation) formulations. Notation/conventions: (i) index notation for space derivatives, dots used for time differentiation; (ii) total and effective stresses denoted by σ_{ij} and σ'_{ij}, respectively; (iii) opposite sign conventions adopted for solid stresses (positive if tensile) and pore pressure (positive if compressive); (iv) the incompressible limit ($Q \to \infty$) is considered in (II.6)-(II.7) with no loss of generality.

(further details about the 1D two-phase solution available in Pisanò and Pastor, 2011), which re-confirms the legitimacy of using a *u-p*/consolidation model to recover fully drained conditions as a special case.

III

Paper II

Gentle Driving of Piles (GDP) at a sandy site combining axial and torsional vibrations:Part II - cyclic/dynamic lateral loading tests

Evangelos Kementzetzidis, Federico Pisanò, Ahmed S. L. Elkadi, Apostolos Tsouvalas, Andrei V. Metrikine

Ocean Engineering, (2023), 270, 113452.

https://doi.org/10.1016/j.oceaneng.2022.113452

Abstract

Gentle Driving of Piles (GDP) is a new technology for the vibratory installation of tubular (mono)piles. Its founding principle is that both efficient installation and low noise emission can be achieved by applying to the pile a combination of axial and torsional vibrations. Preliminary development and demonstration of the proposed technology are the main objectives of the GDP research programme. To this end, onshore medium-scale tests in sand have been performed on piles installed using both impact and vibratory driving methods (including GDP). While the results of the installation tests are presented by Tsetas et al., 2023, this work focuses on the post-installation performance of GDP-driven piles under a sequence of slow/large-amplitude (cyclic) and faster/low-amplitude (dynamic) load parcels. The field data point out the influence of onshore unsaturated soil conditions, which result in complex cyclic pile stiffness trends due to the interplay of pile-soil gapping and soil's fabric changes. The pile stiffness under small-amplitude vibrations is strongly correlated with the previous response to large load cycles, and noticeably frequency-dependent for load cycles with a period lower than 1 second. Overall, the post-installation performance of GDP-driven piles appears to be satisfactory, which encourages further development and demonstration at full scale.

1. Introduction

Ever more countries worldwide are working to shift their energy mix towards renewables. The Netherlands, country of origin of this study, is actively contributing to the European decarbonisation agenda (European Commission, 2020) by promoting the exploitation of renewable energy sources, both onshore and offshore (Minister of Economic Affairs and Climate Policy, 2020). In the country, recent policy updates require a substantial increase in offshore wind capacity to 4.5 GW by 2023 and to 21 GW by 2030 (Dutch Goverment, 2022). In this regard, offshore wind energy will continue to play an increasingly relevant role as an abundant, cost-effective resource (Esteban et al., 2011), on the condition that the pace of its technological development is further expedited. Presently, 15-24% of the investment for the construction of an offshore wind farm relates to the design, production, and installation of substructures (Stehly and Beiter, 2020). Continual improvement of engineering methodologies in this area is therefore key to achieving further cost reduction (Byrne et al., 2019; Page et al., 2019; Pisanò et al., 2022a; Wu et al., 2019).

As reported in the latest EWEA report (Ramırez et al., 2021), over 80% of the existing offshore wind turbines (OWTs) in European wind farms are founded on so-called monopile foundations, which are most commonly installed by means of impact hammering. The impact technology is to date very well established in the offshore industry (Kallehave et al., 2015a). However, impact installation in certain soil conditions (e.g., dense sands) may be slower than desired (Achmus et al., 2020; Rodger and Littlejohn, 1980), which causes

increased installation costs and, possibly, higher pile damage under many hammer blows (Meijers et al., 2018; Mosher, 1987). Moreover, the underwater noise emitted during pile installation is known to be harmful to marine life, and has motivated over the years the enforcement of strict regulations to limit its negative environmental effects (Tsouvalas, 2020). Such regulations include the adoption of costly soundproofing measures (Koschinski and Lüdemann, 2013; Tsouvalas and Metrikine, 2016a).

An interesting alternative to impact piling is provided by vibratory technologies, which can achieve quiet(er)/fast pile installation through the application of low-amplitude axial vibrations. The input excitation is induced through the harmonic rotation of eccentric masses, usually at a frequency no larger than 40 Hz. Vibratory pile hammers (or simply 'vibro-hammers') have been manufactured since the 1940s (Rodger and Littlejohn, 1980), and their benefits in terms of driving/noise performance already put in evidence by a number of previous studies (Barkan, 1967; Lammertz, 2003; Mosher, 1987, 1990; Tsouvalas and Metrikine, 2016b). The use of piling loads lower than in impact driving can effectively reduce both the damage and the radial expansion of the pile during driving – the latter (Poisson effect) is a major culprit for noise emission and larger soil resistance to driving (De Nicola and Randolph, 1993). Despite its obvious benefits, vibratory driving is not yet widely adopted for offshore piling. Its use is hindered by a number of factors, including the limited availability of field data. Major knowledge gaps also exist regarding the dynamic behaviour of the soil during vibro-driving (Mazza and Holeyman, 2019) and the effects of vibro-installation on the operational performance of the pile (Achmus et al., 2020; Anusic et al., 2019; Staubach et al., 2022; Tsetas et al., 2020).

To boost the improvement of vibro-piling methods, a new technology – Gentle Driving of Piles (GDP) – has been recently proposed in the Netherlands as core of a joint industry project led by the Delft University of Technology (TU Delft) (Metrikine et al., 2020). GDP targets enhanced piling performance and reduced noise emissions through the simultaneous application of low-frequency/axial and high-frequency/torsional vibrations. This thread of research was originally inspired by observing that torsional vibrations do not induce radial pile expansion during driving, which was foreseen to play in favour of both driving and acoustic performances. A preliminary demonstration of the proposed technology was pursued by performing medium-scale field tests on identical test piles installed using impact and vibratory driving methods, including GDP. The tests were performed in sandy soil at the Port of Rotterdam and comprised two distinct stages, the first to investigate the driving performance, and the second to explore installation effects in the response of the test piles to repeated lateral loading.

While the rationale and early development of the GDP technology is discussed in the companion paper by Tsetas et al., 2023, this paper focuses on the post-installation response of the test piles to cyclic/dynamic lateral loading. In particular, the behaviour observed for two GDP-driven piles is thoroughly discussed in light of the geotechnical conditions encountered at the test site. Selected field measurements are presented in the following to

(i) 'reassure' future users about the cyclic/dynamic performance of GDP-driven piles, and (ii) establish a conceptual framework for the interpretation of the whole field data set.

Although the GDP project was originally motivated by offshore wind developments, this paper provides experimental evidence and conceptual findings that are generally relevant to piled foundations, repeated lateral loading, and onshore sandy site conditions.

2 . Medium-scale field tests at the Maasvlakte II site

The response of piles to monotonic lateral loading has been researched since the 1960s (Matlock, 1970a; Matlock and Reese, 1962; McClelland et al., 1956; Poulos, 1971; Poulos and Davis, 1980; Reese et al., 1975). The interest for dynamic loading conditions was later motivated by earthquake engineering applications, and was initially limited to the derivation of dynamic impedance functions for slender piles (Angelides and Roesset, 1981; Dobry and Gazetas, 1988; Gazetas and Dobry, 1984a; Kagawa and Kraft, 1980; Mylonakis and Gazetas, 1999; Novak, 1974; Shadlou and Bhattacharya, 2014). Only more recently, this line of work has been extended to the case of short/stiff offshore units (monopiles and caissons) (He et al., 2019; Shadlou and Bhattacharya, 2016), though without considering relevant non-linear effects, such as gradual variations in lateral stiffness and cyclic accumulation of pile rotation (also termed 'tilt'). The latter aspect has attracted particular attention in the context of offshore wind research, since limiting the monopile tilt during the whole operational life has been recognised as an important design criterion (Arany et al., 2017b). A number of experimental studies have been performed to investigate the occurrence and evolution of cyclic monopile tilt, including small-scale tests under normal (1g) (Abadie, 2015b; Albiker et al., 2017; Frick and Achmus, 2019; LeBlanc et al., 2010; Richards, 2019) or augmented gravity (Klinkvort, 2012; Klinkvort et al., 2010; Richards et al., 2021; Rudolph et al., 2014; Truong et al., 2019; Wang et al., 2018a; Zhu et al., 2016), as well as medium-scale tests in the field (Byrne et al., 2020a,b; Li et al., 2015).

The GDP field tests were performed at the Maasvlakte II port site in Rotterdam, which comprises North Sea sand that was used to create a reclaimed/compacted site. Site location and access routes are shown in Figure III.1; the accessibility of the site and its proximity to logistic suppliers were relevant criteria in the site selection process.

2 .1. Test layout and site investigation

Geotechnical investigation activities at the Maasvlakte II site were carried out between June and September 2019 in two phases of *preliminary* and *detailed* site investigation – henceforth referred to as PSI and DSI, respectively. In October/November 2019, nine tubular steel piles were installed: eight test piles, and a larger/stiffer reaction pile for the post-installation loading tests (pile specifications in Table III.1). Four of the test piles, henceforth referred to as *Main Test Piles* (MTPs), were extensively instrumented, while the other four piles, labelled as *Auxiliary Test Piles* (ATPs), were installed uninstrumented for preliminary testing purposes. The four MTPs were installed and labelled after the corresponding driving method, namely

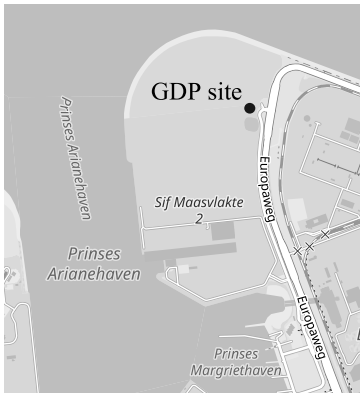

Figure III.1: GDP test site and its access routes – edited after (OpenStreetMap contributors, 2017).

impact hammering (IH), axial vibro-hammering (VH), and GDP-driving ($GDP_{1,2}$), whereas the ATPs were installed via impact hammering ($IH_{01,02}$) and GDP-driving ($GDP_{01,02}$). As shown in Figure III.2, the MTPs and the ATPs were installed around the reaction pile at a radial, centre-to-centre distance of 12 m and 16 m, respectively.

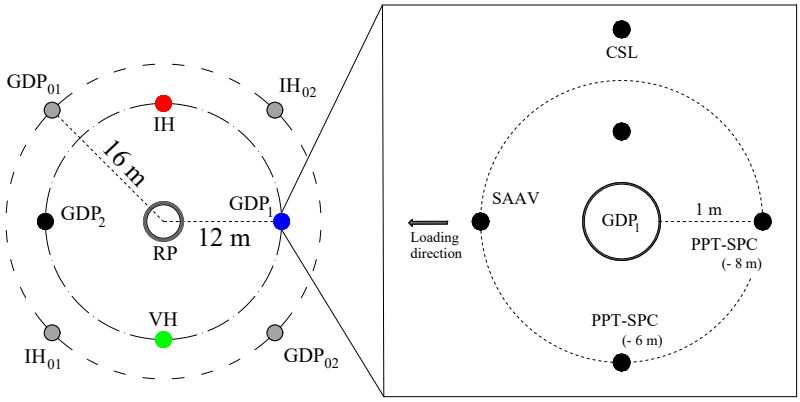

Figure III.2: Site layout (left – ATPs in grey) and soil monitoring around the MTPs (right). For better readability, the site layout on the left is shown with MTP diameters and distances from the central RP that are not to scale.

Relevant site investigation work is summarised in what follows, with further details provided by Tsetas et al., 2023. First, the PSI was performed to identify suitable locations for installing the test piles, mostly in light of site homogeneity and pile spacing considerations. During the PSI, 25 CPTu tests were performed down to a target depth of 10 m over a regular grid with a spacing of about 12.5 m. The PSI also enabled the identification of the water table depth – between 3.5 and 4.5 m below the ground surface, depending on the specific location.

After selecting the final pile locations (Figure III.2), the DSI was carried out around and at the centre of all piles. The DSI programme included:

- four CPTu tests at the ATP locations (target depth: 10 m);
- four Seismic CPTu (SCPTu) tests at the MPT locations (target depth: 10 m);
- four hydro-profiling tests with mini pump tests (HPT-MPT) around the MTPs (target depth: 15 m);
- borehole sampling around the MTPs, with a total of eight 10 m long boreholes (two per MTP);
- crosshole sonic logging (CSL) tests performed at MTP locations before and after pile driving (Tsetas et al., 2023).

Both PSI and DSI data confirmed the predominantly sandy nature of the soil deposit from the ground surface down to approximately 10 m below. The upper 5 m consist of the dredged material employed to create the Maasvlakte II site, which overlays a layer of sand and clayey/silty sand from the holocenic Naaldwijk formation (Vos, 2015). With reference to the locations of the MTPs and the GDP ATPs, the profiles in Figure III.3 of (a) cone resistance (q_c), (b) shear wave velocity (V_s), and (c) relative density (D_r) (based on Jamiolkowski et al., 2003) suggest the presence of medium-dense to very dense sand ($D_r = 60 - 100\%$) with an overall negative D_r depth-gradient. The same negative gradient is also exhibited by the corresponding SCPTu profiles of V_s (only available for the MTP locations). Profiles of hydraulic conductivity (k_h, horizontal component) are reported in Figure III.3d after HTP-MPT measurements close to the locations of the MTPs. The k_h values shown in the figure lie mostly in the range of 10^{-4}-10^{-3} m/s (average permeability of 4.45×10^{-4} m/s over the first 10 m.), which is typical for the sandy soil found at the Maasvlakte II site. Since the interpretation of HPT-MPT tests relies on the assumption of water-saturated soil, it was not attempted to infer k_h values for the unsaturated soil above the water table.

2 .2. Pile instrumentation, ground monitoring, and loading equipment

The mechanical response of the instrumented MTPs was recorded by means of the following sensors – technical specifications provided by Tsetas et al., 2023:

- fiber Bragg grating (FBG) sensors at multiple locations along the piles, to monitor strains in the longitudinal and two inclined directions, at angles of 60 and 120 degrees with respect to the horizontal axis;
- two triaxial accelerometers installed at diametrically opposite locations, to record the dynamic response of the piles during installation;
- one potentiometer transducer, to record the progress of pile penetration by measuring the vertical displacement;

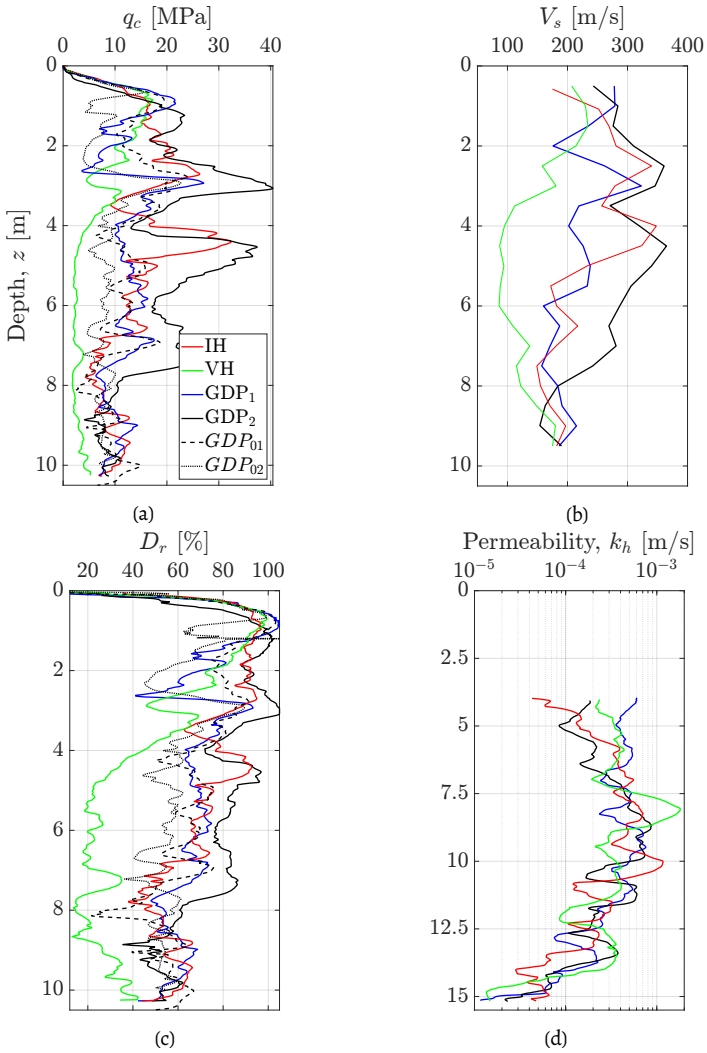

Figure III.3: Profiles of (a) cone resistance (q_c), (b) shear wave velocity (V_s), (c) relative density (D_r), and (d) horizontal hydraulic conductivity (k_h, 80 cm moving average plot). q_c and D_r obtained from CPTs performed on all piles while V_s and k_h available only at the MTP locations from in-situ SCPTu and HPT-MPT tests.

– one temperature sensor placed 40 cm above the pile tip.

Ground sensors were also installed to enable deeper understanding of pile-soil interaction mechanisms. Eight VWPC2100 *RST Instruments* sensors containing both soil pressure cells (SPCs) and pore water pressure transducers (PPTs) were deployed to simultaneously record the evolution in time of the total radial stress (σ_r) and the pore pressure (p_w), with accuracy and resolution of 5 kPa and 0.25 kPa, respectively. For each MTP and prior to pile driving,

the sensors were installed at two different depths (6 m and 8 m below the ground surface, see Figure III.2) and set to record with a sampling frequency of 100 Hz. All load test data were low-pass filtered at 12 Hz to remove high-frequency noise from the measurements.

The lateral loading tests, main subject of this paper, were performed using the loading frame illustrated in Figure III.4. The loading equipment included a TU Delft servo-hydraulic jack, which was able to impose load-controlled horizontal forcing by means of a closed-loop control system. The servo-hydraulic jack could load the test piles through the tension of the connection beam, i.e., by cyclically pulling test and reaction piles towards each other at a specified loading frequency. A custom-built load cell was also employed to ensure the application of desired load amplitudes regardless of the relative deflection of the opposite piles. The load cell provided highly repeatable load values over a selected range of 0.8 MN, with accuracy and resolution of 0.25 kN and 0.015 kN, respectively.

Since all test piles were installed to a target depth of 8 m, the remaining pile length allowed lateral loading with an eccentricity $e = 1$ m above the ground surface. During lateral loading, the deflection of all test piles was sampled and low-pass filtered at 6789 Hz and 70 Hz, respectively, via the displacement sensors (Gefran PY1, 100 mm stroke) shown in Figure III.5.

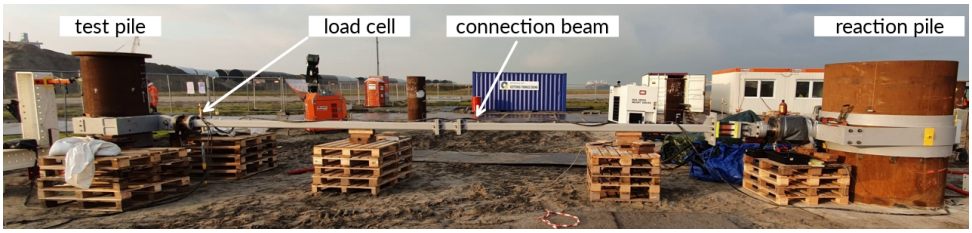

Figure III.4: The loading frame connecting a test pile (left) to the reaction pile (right). The wooden supports in the picture were used to counteract the vertical deflection of the connection beam under its own self-weight.

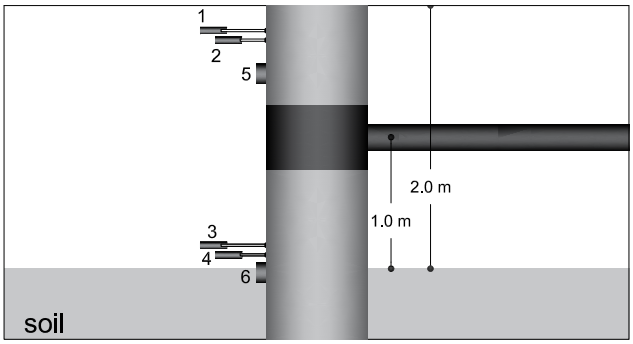

Figure III.5: Lateral pile motion monitoring by means of displacement sensors (1-2, 3-4) and inclinometers (5-6). The pile displacement at the ground surface was assumed to approximately coincide with the output of sensor 4 located for all piles approximately 15 cm above the ground.

As previously mentioned, four piles in total (GDP piles) were installed through the GDP vibratory method. The testing programme comprised monotonic loading on the non-instrumented GDP ATPs (GDP_{01} and GDP_{02} in Figure III.2) and multi-amplitude cyclic/dynamic loading on the four instrumented MTPs. Particularly, the latter tests were conceived to explore the lateral response of the test piles to combinations of slow/large-amplitude (cyclic) and fast(er)/small-amplitude (dynamic) loading. Henceforth, the terms 'cyclic' and 'dynamic' are used to distinguish these two types of loading parcels and the associated pile response.

2 .3. Preliminary monotonic tests

Preliminary monotonic tests were carried to support the definition of a cyclic loading programme compatible with the capabilities of the loading frame. Monotonic loading was applied to the two GDP ATPs as is shown on the right-hand side of Figure III.6a (load vs time), while the resulting force-displacement responses are reported on the left – the pile displacement at the ground level was assumed to coincide with the output of sensor 4 in Figure III.5. The load was kept constant on both ATPs after achieving the intended maximum value of 550 kN, while additional constant-load stages were introduced for GDP_{02} (at 325 kN and 400 kN) to allow for possible creep deformations. The presence of rate effects in the monotonic pile response was evaluated for GDP_{01} by varying the loading rate with respect to the main selected value of 0.05 kN/s. During the test on GDP_{01} the loading rate was increased twice to 70 kN/s, namely when the applied load lied in the ranges of 0-180 kN and 330-420 kN. The fastest loading rate of 70 kN/s was selected as representative of the average rate that the MTPs would later experience under the cyclic loading parcel of largest amplitude.

Due to technical limitations of the loading frame, it was not possible to load the two piles up to their (conventional) capacity – e.g., associated with a lateral deflection of $0.1D$ at the ground surface. Such a capacity was thus estimated by analytically extrapolating the monotonic response (see the dashed interpolation line in Figure III.6a). For instance, a conventional capacity of 1.46 MN was estimated for GDP_{01} and a loading rate of 0.05 kN/s.

The lateral response of GDP_{01} appears to be globally stiffer than GDP_{02}'s, which is consistent with the values of cone resistance at the two pile locations (cf. to Figure III.3). The clear presence of both rate effects and creep in the measured pile responses confirms that time effects can be significant even in sandy soil (Lazari et al., 2019). It should also be noted that the same field evidence might have been co-promoted by the occurrence of transient hydromechanical processes in the shallow unsaturated soil. While more field research on this subject is being carried out (Buckley et al., 2020), an influence of time effects is generally to be expected.

The same monotonic responses in Figure III.6a are re-plotted in Figure III.6b-left after normalising the applied load ($\tilde{F} = F/L_e^2 D\gamma'$) and the displacement ($\tilde{U} = U/D \cdot \sqrt{p_a/L_e\gamma'}$) as proposed by LeBlanc et al., 2010. Such a normalisation allows direct comparison to selected

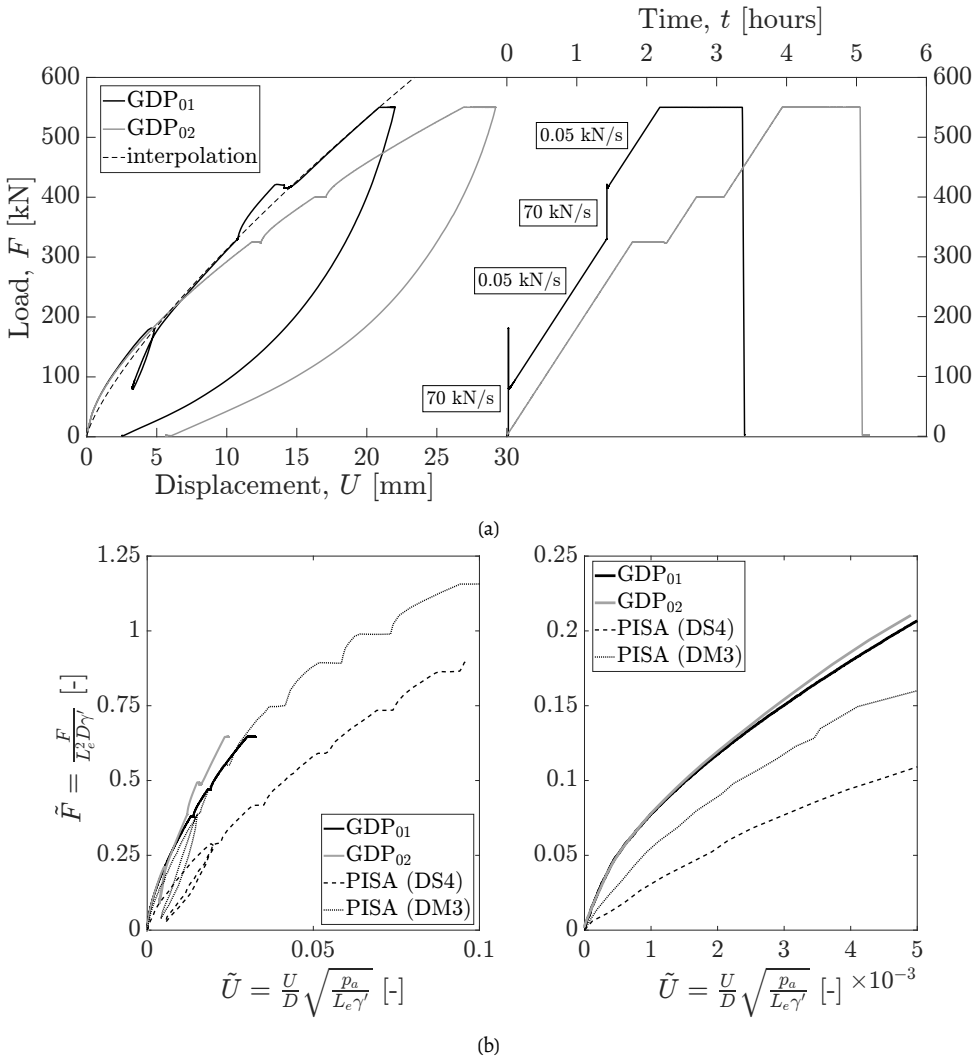

Figure III.6: (a) Monotonic loading test results for the ATPs GDP$_{01}$ and GDP$_{02}$; (b) comparison in terms of normalised load ($\tilde{F}$) and displacement ($\tilde{U}$) between the monotonic responses of GDP$_{01}$–GDP$_{02}$ and those of the piles DS4 ($L_e/D = 10$, $D = 0.273$ m, $h = 0.7$ cm) and DM3 ($L_e/D = 8$, $D = 0.762$ m, $h = 2.5$ cm) tested in the framework of the PISA project (McAdam et al., 2020): (left) full test view and (right) magnified view of the small-displacement range. p_a and γ' stand in the normalisation for atmospheric pressure and buoyant soil unit weight, respectively.

field test results from the PISA project (McAdam et al., 2020), particularly to those associated with the similar piles DS4 ($L_e/D = 10$, $D = 0.273$ m, $h = 0.7$ cm, $e = 10$ m) and DM3 ($L_e/D = 8$, $D = 0.762$ m, $h = 2.5$ cm, $e = 10$ m) – cf. to the GDP pile specifications in Table III.1. Despite the differences in soil conditions and load eccentricity, reasonable agreement between the two

sets of field data is observed – see also the magnified view around small displacements in Figure III.6b-right.

2 .4. Cyclic/dynamic loading programme

The cyclic/dynamic loading programme applied to the MTPs is illustrated in Figure III.7. Each cyclic/dynamic test lasted about 40 hours and included a total amount of $N = 82000$ loading cycles. Some of the cycles were applied with relatively large amplitude at constant/low frequency (black parcels in Figure III.7), with interleaved stages of small-amplitude loading at variable frequency (henceforth referred to as dynamic 'frequency sweeps' – grey parcels in Figure III.7). All load parcels were defined by combining a monoharmonic excitation of amplitude F_{cyc} and frequency f with an average load level F_{av}:

$$F(t) = F_{av} + F_{cyc} \times \sin(2\pi f t) \tag{III.1}$$

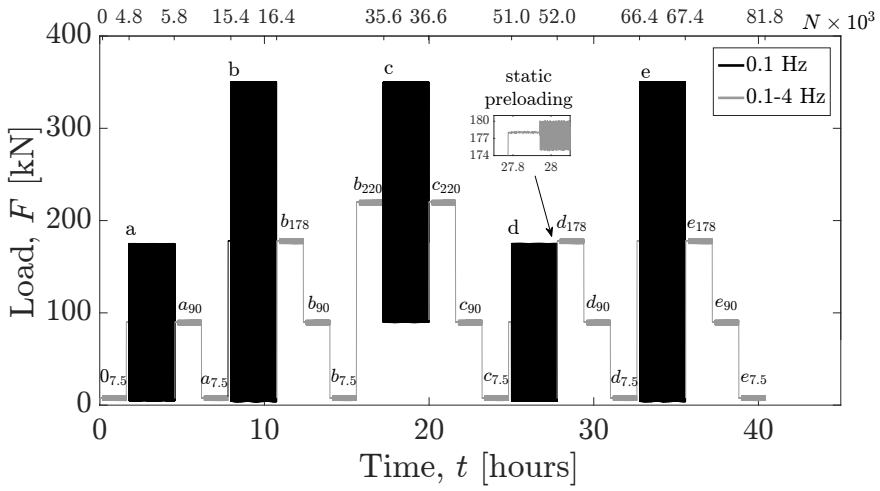

Figure III.7: Cyclic/dynamic loading programme. Load amplitudes are provided against time (bottom axis) and number of cycles (top axis). Cyclic load parcels ($a - e$) and dynamic f-sweeps ($a - e_{7.5,\ldots,220}$ are shown in black and grey, respectively – see loading specifications in Table III.2.

All the loading settings associated with Equation (IV.24) and Figure III.7 are summarised in Table III.2. Cyclic/dynamic loading was applied in all instances with $F_{av} > F_{cyc}$ ('one-way' loading), therefore with no risk of compression buckling for the connection beam in Fig. III.4. The stroke (displacement range) of the loading frame was limited by the capabilities of the hydraulic power unit, which finally allowed for a maximum load of 350 kN when applied at 0.1 Hz, and a maximum loading frequency of 4 Hz.

Each low-frequency cyclic parcels ($a - e$ in Figure III.7) comprised $N = 1000$ cycles. Taking GDP_{01}'s CPT profile as an average of the profiles at all MTPs locations, the aforementioned reference capacity of 1.46 MN was retained for both GDP-driven MTPs as a reasonable first

approximation. Accordingly, the maximum load magnitudes ($F_{av} + F_{cyc}$) imposed during the parcels $a - d$ and $b - c - e$ were, respectively, 12% and 24% of the reference capacity – these are representative of operational loading conditions for modern OWT monopiles (Kementzetzidis et al., 2019), and also sufficient to mobilise non-linear features of pile-soil interaction. Such features include, e.g., the cyclic accumulation of permanent pile displacement, which is closely related to the perturbation of the stress state and micro-structure of the surrounding soil (Cuéllar et al., 2009). In order to mitigate creep effects in the cyclic response, every change towards new F_{av}-F_{cyc} pairs was preceded by a 10 minutes stage of static preloading – see the magnified window in Figure III.7.

Dynamic frequency sweeps (or f-sweeps, for brevity) were interleaved between consecutive cyclic parcels (Figure III.7) to gain insight into the response of the test piles during weak vibrations and for different F_{av} values; the possible impact on the (dynamic) lateral stiffness of a varying loading frequency was also inspected in light of the full-scale observations discussed by Versteijlen et al., 2017a and Kementzetzidis et al., 2021. The 16 frequency sweeps featured $N = 4800$ cycles applied at a constant/low amplitude of $F_{cyc} = 2.5$ kN, while the loading frequency was increased from 0.1 Hz to 4 Hz with increments of 0.1 Hz every 120 cycles. Preliminary tests on the ATPs indicated that 120 cycles would be generally sufficient for the attainment of a steady-state response under the considered loading/site conditions.

In what follows, individual dynamic parcels are referred to as labelled in Figure III.7 – for example, $b_{7.5}$ denotes a frequency sweep applied after the cyclic parcel b around an average load of 7.5 kN, while 'f_b-sweeps' indicates the whole set of frequency sweeps between parcels b and c.

3 . Pile response to cyclic load parcels

This section elaborates on the results of the tests performed on the GDP MTPs, particularly on the response to slow/large amplitude load parcels ($a - e$ in Figure III.7).

3 .1. Impact of onshore soil conditions

As confirmed by previous field studies (Achmus et al., 2020; Li et al., 2015; McAdam et al., 2020), onshore tests are typically affected by the presence of shallow unsaturated soil. An important consequence of unsaturated soil conditions is the development of an apparent cohesion, even in otherwise cohesionless soils such as sands (Fredlund, 2006). Such a cohesion allows sand to self-support, and therefore enables the formation of a vertical soil-pile gap during lateral loading – see in Figure III.8a an example of soil-pile gap observed at the GDP site. Gapping introduces a geometrical non-linearity in the lateral behaviour of a pile, in that its embedment in the soil (in full contact) becomes a function of the lateral displacement (Figures III.8b-III.8c). The formation and evolution of the gap impacted significantly the cyclic/dynamic pile response during the whole loading programme, however in a manner not expected at offshore sandy sites – similar gapping behaviour is expected to manifest in cohesive soils both on and offshore (Bea et al., 1979; Ciavaglia et al., 2017) .

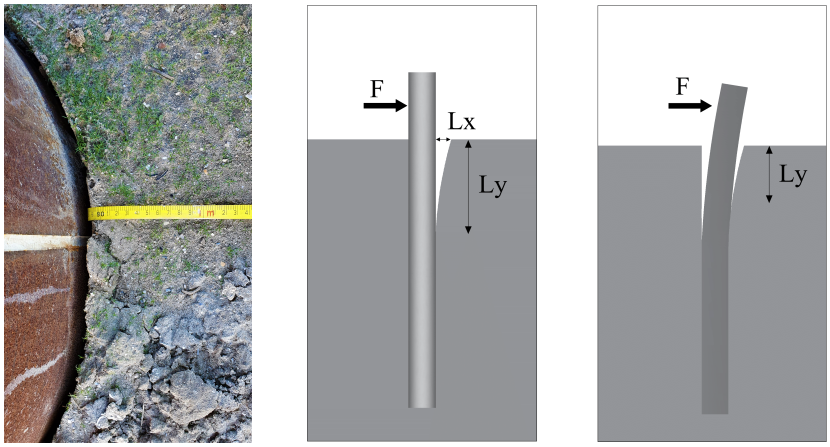

(a) (b) (c)

Figure III.8: (a) Pile-soil gap observed after loading monotonically an ATP; pile-soil contact patterns after first gap formation (i.e., for $N > 1$): (b) $F = 0$ (fully unloaded pile), and (c) $F > 0$ (during pile reloading).

Figure III.9a displays the cyclic load-displacement response of GDP_2 to the cyclic load parcel *a* in Figure III.7, with emphasis on N =1, 2, 1000. The effect of the gap emerges immediately from the comparison between the responses measured during the first two cycles: while a typical decrease in tangent stiffness with the load amplitude is observed during the former, an opposite (*locking*) behaviour is observed during the latter and magnified by prolonged cycling – cf. to $N = 1000$. This finding is further supported by Figure III.9b, which displays GDP_2's force-displacement response to the five cyclic load parcels (from *a* to *e*). The response during the first two cycles is qualitatively very similar for parcels *a* and *b*, whereas only a stiffening behaviour is observed for the following parcels *c* – *d* – *e* from the onset of loading. It may thus be inferred that the geometry of the gap mainly evolved during the first cycles of parcels *a* and *b*. In this respect, the interaction between lateral pile behaviour and gap formation/evolution can be simply conceptualised with the aid of Figure III.8, where L_y and L_x denote, respectively, the current depth and opening of the gap on one side of the pile (Figure III.9a). It may be argued that the maximum value of L_x, $L_{x,max}$, approximately coincides with the largest displacement ever experienced by the pile (minus the soil rebound caused by elastic unloading (Matlock et al., 1978)), which evolves in time depending on the specific features of the loading sequence (Figure III.7). Upon unloading (i.e., reversal of the load direction), the apparent soil cohesion allows soil-pile separation with a (nearly) vertical soil wall; upon the subsequent reloading, the pile regains contact with the self-standing soil wall after moving through the open gap. As the gap progressively recloses (i.e., L_x and L_y decrease), the deflection of the pile is resisted by an increasing mass of 'engaged' soil, which produces the gradual stiffening of lateral response (tangent stiffness) that is visible in Figure III.9a-III.9b for $N > 1$. Generally, the evolution in time of the gap size

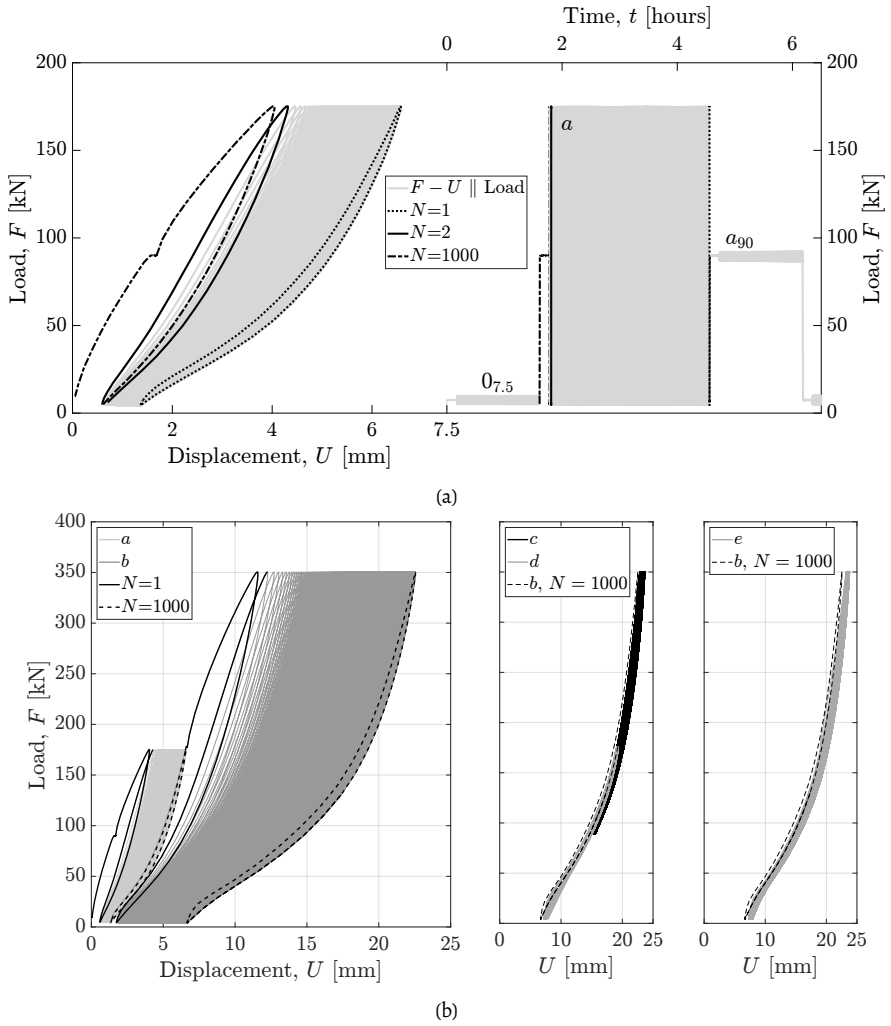

Figure III.9: (a) GDP_2's load-displacement response to the first cyclic load parcel (*a*) in Figure III.7 (left), and the corresponding load-time history (right); (b) GDP_2's load-displacement response to cyclic load parcels $a - b$ (left), $b - c - d$ (centre), and $b - e$ (right) – solid and dashed black lines highlight the first ($N = 1$) and the last ($N = 1000$) response cycles for parcels $a - b$.

is mainly determined by the magnitude of the capillary forces in the unsaturated soil and the maximum loading amplitude experienced by the pile, with only marginal gap enlargement caused by the cyclic lateral ratcheting of the pile. In conclusion, L_x and L_y are expected to vary substantially when the cyclic loading amplitude rises to a new maximum as suggested by Figure III.9b, III.11.

It is also apparent in Figure III.9b that, due to the gapping mechanism, the resulting cyclic response does not comply with the well-known Masing idealisation, which is at

variance with the experimental evidence normally associated with pile tests in either dry or water-saturated sand (Abadie, 2015b; Liu et al., 2021).

3 .2. Cyclic pile deflection and bending

Despite the differences in soil profile (Figure III.3), it is possible to draw a qualitative picture of the installation effects associated with different pile driving methods – more quantitative conclusions may only be obtained through numerical modelling work, e.g., using a cyclic p-y model accounting both for soil ratcheting and pile-soil gapping effects (Kementzetzidis et al., 2022). To this end, Figure III.10a shows for all MTPs the evolution in time of the lateral displacement in response to the whole cyclic/dynamic loading sequence. Overall, the GDP-installed piles experienced a smaller deflection than the other piles (cf. GDP_1 to IH considering their similar soil profiles), which reflects positively on the GDP method also from a post-installation perspective. In particular, GDP_2 displaced less than GDP_1, as one could have anticipated based on the respective CPT profiles. It is also worth noting that the VH-installed pile displaced less than the IH pile, which is rather surprising in light of the pre-installation soil conditions at the respective locations (Figure III.3) – see Tsetas et al., 2023. In this regard, previous studies on full scale monopiles (Achmus et al., 2020) in sand have shown that the installation settings of standard axial vibro-driving can drastically impact the post-installation lateral response in comparison to impact-hammered piles, which seems indeed consistent with the experimental findings of this field study.

It was qualitatively observed for all MPTs that, after the main gap-forming events (parcels *a*–*b*), cycling with a lower amplitude (e.g., parcel *d*) determined a motion of the piles that was entirely within the breadth of the gap (Figure III.8c) and, therefore, with a lower cyclic stiffness due to the reduced embedment. As a consequence, wider ranges of cyclic displacement were recorded for a given load parcel when applied under 'fully gapped' conditions – compare the pile responses to parcels *a* and *d* in Figure III.10a. With further reference to parcel *d*, some displacement relaxation was measured, which indicates a reversal in the direction of pile deflection. Such a mechanism, sometimes termed *self-healing* or *stabilisation*, was first documented in relation to small-scale 1g tests on monopiles (**theodorosgeotechnical**; Sturm et al., 2008), and later interpreted through 1D (Kementzetzidis et al., 2022) and 3D FE (Solf et al., 2010) numerical simulations, respectively. A similar self-healing mechanisms has also been observed during cyclic centrifuge tests on tripod bucket foundations (Wang et al., 2018a).

Pile deflection measurements are complemented by the ground monitoring data shown in Figure III.10 for the two GDP-driven MTPs. Figure III.10 displays the evolution of the total radial stress and the pore water pressure ($\Delta\sigma_r$ and Δp_w, increments with respect to post-installation values) at the soil locations and depths indicated in Figure III.2. There is evident correlation between the trends of radial soil stress and lateral pile displacement (Figure III.10a). Particularly, significant permanent variations in radial stress are associated with the load parcels of larger amplitude, which are also those causing the most significant

lateral pile deflection. Conversely, only modest pore pressure variations have been recorded throughout the loading sequence at the considered sensor locations under the water table, which is at variance with the substantial variations that occurred during pile installation (Tsetas et al., 2023).

The above observations regarding cyclic pile-soil interaction in the presence of a gap are largely confirmed by the GDP_2 moment profiles shown in Figure III.11 as an example. Such profiles were derived from the FBG strain sensor data – particularly, for the first ($N = 1$) and last ($N = 1000$) cycles of all cyclic parcels $a - e$ (at the corresponding maximum load level), and also for the static preloading stages preceding parcels a and e_{90} (a^{sp} and e_{90}^{sp} respectively, with $F = 90$ kN, see Figure III.11c); circular markers and solid lines are used for the experimental data and their 4th-order polynomial interpolations, respectively.

The moment profiles seem overall to confirm that no further gap enlargement/deepening took place after the application of parcel b. This statement is supported by the considerable evolution of the moment profile that may be observed through parcels a (Figure III.11a) and b (Figure III.11b), whereas very limited moment variations are associated with the other cyclic parcels. The major impact of the gap on the cyclic pile response clearly emerges from the comparison in Figure III.11b between the moment profiles associated with the static preloading stages a^{sp} and e_{90}^{sp}. These particular profiles were selected to highlight the difference between full and partial soil-pile contact on the passive soil side – it is indeed argued that the gap had not yet been opened for a^{sp}, while the previous parcels of larger amplitude did likely prevent full contact under the e_{90}^{sp}'s low load level ($F = 90$ kN). The latter conjecture is fully confirmed by the atypical moment distribution that is shown for e_{90}^{sp} in Figure III.11b: the moment values down to about 3.5 m are aligned along the same linear trend that one would obtain for the case of no soil reactions and with the real lateral load eccentricity that was held during the field tests. Such a depth of 3.5 m may be regarded as a close approximation of the maximum gap depth, which is also consistent with the field observations of McAdam et al., 2020.

3 .3. Evolution of the cyclic stiffness

The responses of GDP_1 and GDP_2 are further compared in Figure III.12 in terms of the load-displacement cycles associated with N =1, 1000 for the load parcel a. Comparison to the ATP monotonic curves in Figure III.6a is also included in the figure, which indicates good consistency in terms of (pre-gapping) pile response at the considered ATP/MTP locations. While the cyclic responses of GDP_1 and GDP_2 appear very similar in the first cycle, appreciable differences can be noticed after 1000 cycles.

The responses of both GDP piles to slow/cyclic loading were further processed to obtain quantitative information regarding the overall cyclic stiffness. Special attention to the effects of soil-pile gapping had to be devoted when processing the experimental force-displacement cycles, such as those in Figure III.9a. To distinguish material and geometrical non-linearity in the soil, three distinct definitions of the secant cyclic stiffness K_{cyc} were considered as

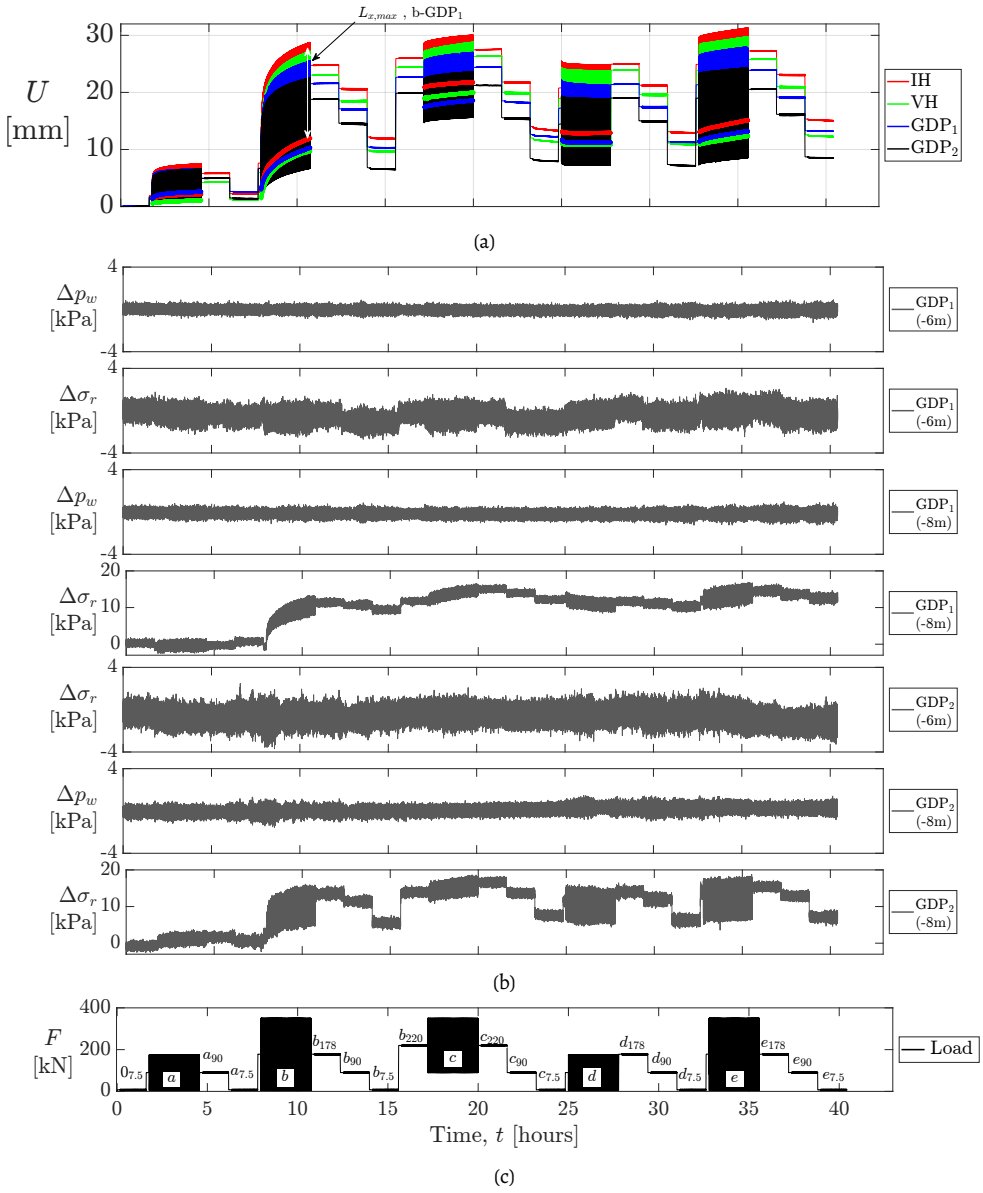

Figure III.10: Pile deflection and ground response recorded during the loading programme in Figure 7: (a) lateral displacement (U) of all MPTs (GDP$_{1,2}$, IH, VH) recorded at the ground surface – the single-head arrow points to the maximum displacement experienced by GDP$_1$ at the end of parcel b ($\approx L_{x,max}$: maximum gap-opening over the loading programme), while the double-head arrow spans the displacement range of the IH pile at the 1000th cycle of parcel b; (b) time increments of radial soil pressure ($\Delta\sigma_r$, total stress) and pore water pressure (Δp_w) with respect to the initial in-situ value for GDP$_1$ and GDP$_2$ ($\Delta\sigma_r$(t=0)=Δp_w (t=0)=0); (c) cyclic/dynamic loading programme.

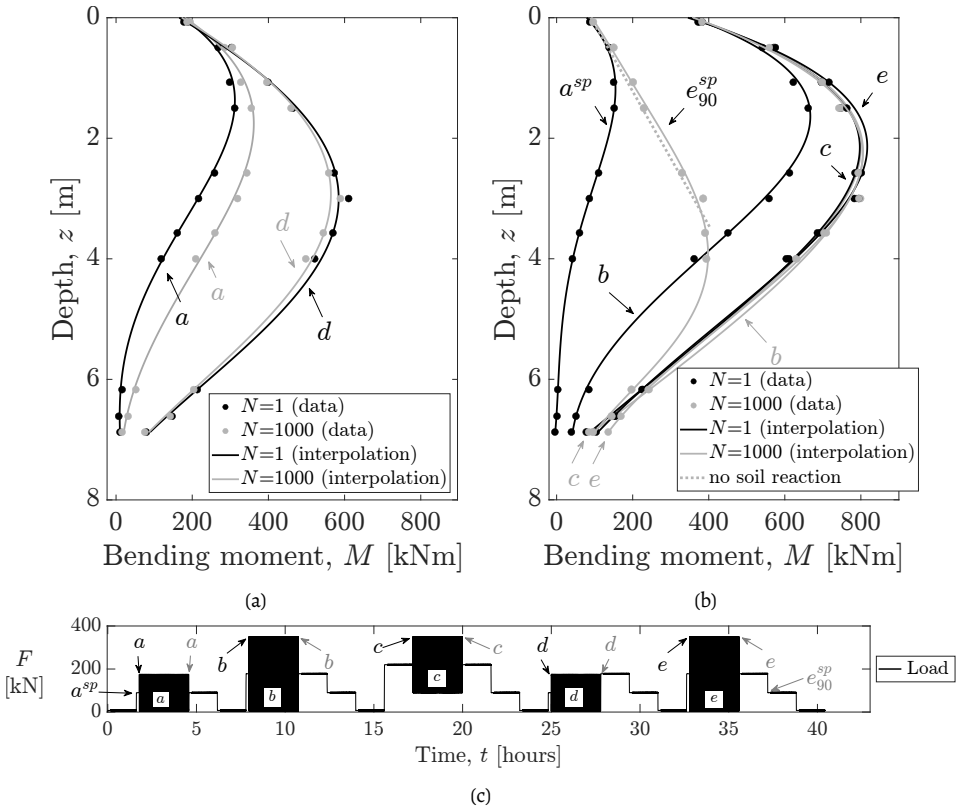

Figure III.11: (a-b) Selected GDP$_2$'s moment profiles from FBG strain sensor data and (c) their temporal correspondence with the cyclic/dynamic loading programme. Moment data (circular markers) and their 4th-order polynomial interpolations (solid lines) are plotted in (a-b) using the same colours adopted in (c).

per Figure III.13a, namely with respect to (i) the initial 0.5 mm of the cyclic deflection range (K_{cyc}^{og}, at minimum load), (ii) the final 0.5 mm (K_{cyc}^{cg}, at maximum load), and (iii) the whole load/deflection range (K_{cyc}^{av}) – it was found appropriate to determine K_{cyc}^{og} and K_{cyc}^{cg} with reference to cyclic displacement ranges of 0.5 mm (Figure III.13a), based on the observation that its further reduction would not alter the corresponding stiffness values. While K_{cyc}^{av} was defined to track an average secant stiffness affected both by soil plasticity and gapping (see results in Figure III.14a), K_{cyc}^{og} and K_{cyc}^{cg} were introduced to inspect the role of different conditions on the passive side of the pile-soil interface, i.e., in the presence of either open or (re)closed gap – hence the superscripts *og* and *cg* for 'open-gap' and 'closed-gap'.

As illustrated in Figure III.14a, the evolution of K_{cyc}^{av} against the number of cycles N clearly displays the influence of soil-pile gapping. During the main gap-opening parcels (*a-b*), a gradual decrease in average stiffness occurred due to the largest loading amplitudes being experienced by both GDP piles for the first time. Some slower decrease is also visible

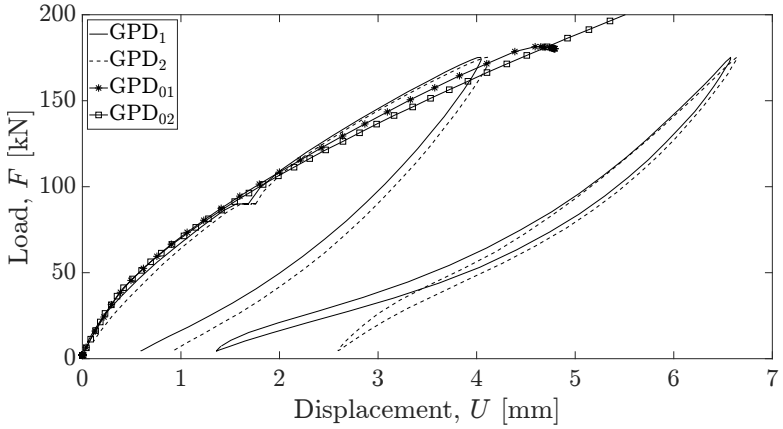

Figure III.12: GDP_1-GDP_2 load-displacement cycles associated with N =1, 1000 for the load parcel *a* in Figure III.7. Monotonic test results for GDP_{01}-GDP_{02} (from Figure III.6a) are also reported for comparison.

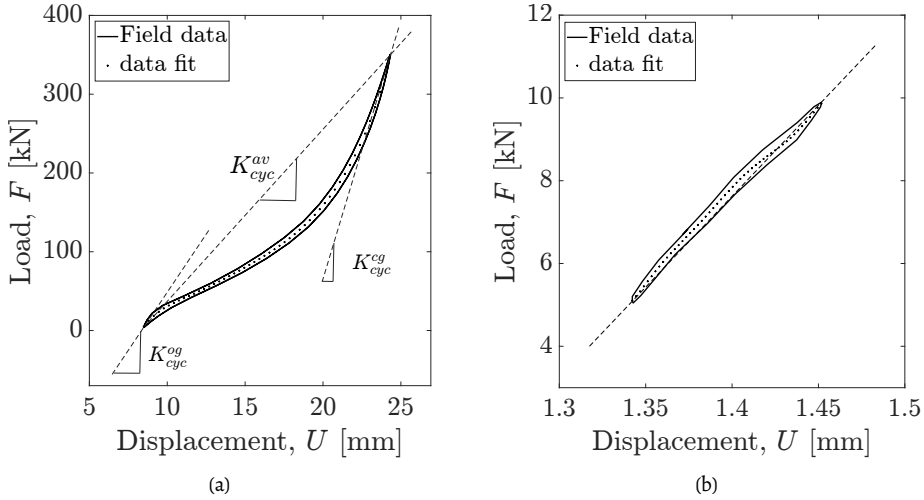

Figure III.13: Relevant definitions of (a) cyclic and (b) dynamic stiffness adopted in the discussion of pile response data.

for parcel *c*, during which there was presumably no further opening of the gap. When parcel *d* (equal to *a*) was applied, the piles experienced an overall unloading and responded to cyclic loading with a permanently open gap, which explains the drop in K_{cyc}^{av} as a consequence of lateral resistance being provided only by the soil below the gap. With no further gap opening, K_{cyc}^{av} gradually increased during cycling, in a way already reported in the literature based on small-scale pile tests in dry sand (i.e., without appreciable gapping effects) (Abadie et al., 2019; Abadie, 2015b; Klinkvort et al., 2010; LeBlanc et al., 2010; Richards, 2019).

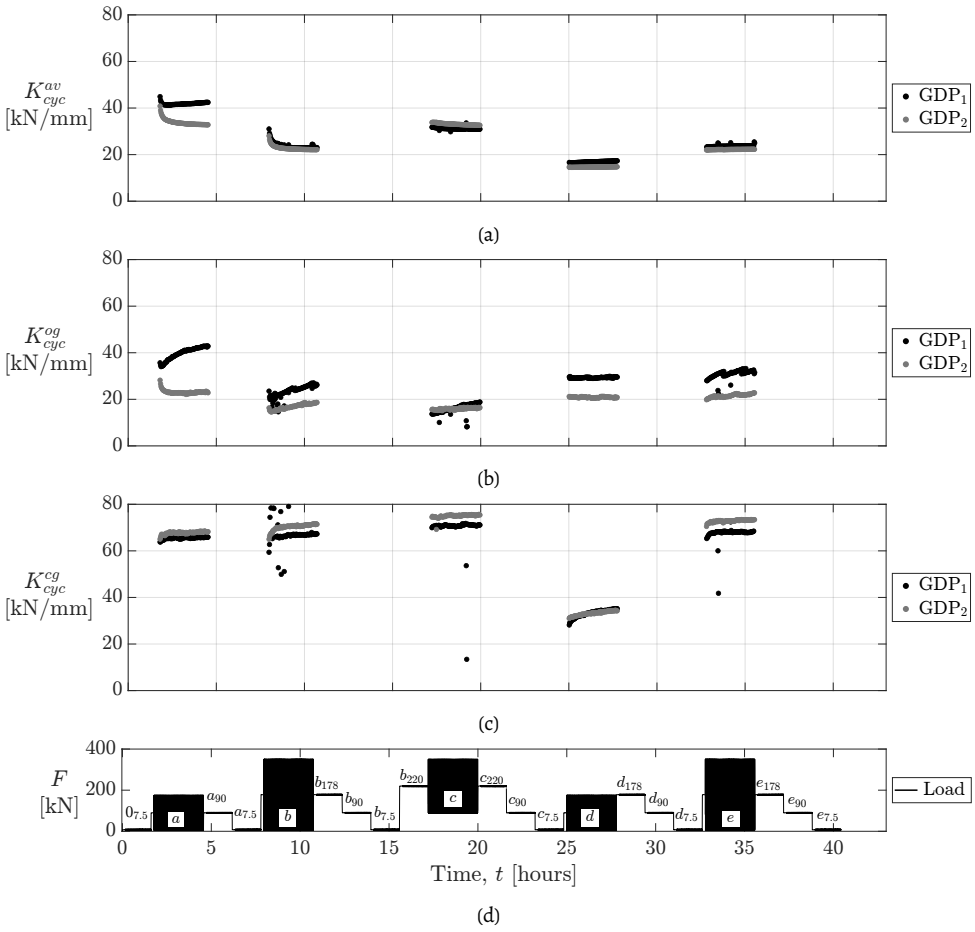

Figure III.14: Cyclic evolution vs time of the (a) average (K_{cyc}^{av}), (b) open-gap (K_{cyc}^{og}), and closed-gap (K_{cyc}^{cg}) lateral pile stiffness; (d) cyclic/dynamic loading programme.

To broaden the picture offered by Figure III.14a, cyclic trends both of K_{cyc}^{og} and K_{cyc}^{cg} are plotted in Figures III.14b–III.14c. K_{cyc}^{og} was previously introduced as representative of open-gap conditions, in which only the soil below the gap contributes to the lateral stiffness. After full formation of the gap, K_{cyc}^{og} values of approximately 27 kN/mm and 19 kN/mm may be observed at the end of parcel *b* and, very consistently, at the beginning of both parcels *d* and *e*. This outcome suggests to regard the pile-gap-soil system as a single entity in combination with the applied loading: its (current) geometrical configuration seems to determine the resulting open-gap stiffness K_{cyc}^{og}, which does explain why very similar K_{cyc}^{og} values are associated with comparable widths (L_x) of the gap. With reference to Figure III.10a, $L_{x,max}$ was estimated to approximately equal L_x at the end of parcel *b* (and also at the

beginning of parcels *d*-*e*), i.e., about 25.5 mm and 22.5 mm for GDP_1 and GDP_2, respectively (see Figure III.10a).

The same test results are re-elaborated in Figure III.14c also in terms of closed-gap stiffness K_{cyc}^{cg}, which was defined to filter gapping effects out of the global pile-soil response. It is argued that, with the only exception of parcel *d*, all the other parcels allowed both piles to achieve (nearly) full contact with the resisting passive soil. With reference to the 'full-contact parcels', (*a*, *b*, *c*, and *e*), the K_{cyc}^{cg} values seem to align along a trend always increasing with the number of cycles, in a manner that is consistent with the pile behaviour presented in the aforecited small-scall studies from the literature.

Overall, a good consistency between site investigation data and pile test results is confirmed by the response of GDP_2 featuring cyclic deflections (Figure III.10a) and closed-gap stiffness K_{cyc}^{cg} values (Figure III.14c) respectively lower and larger than GDP_1's, which reflects the larger soil density/stiffness at the GDP_2 location (Figure III.3).

4 . Pile dynamics under small-amplitude load parcels

As illustrated in Figure III.7, dynamic frequency sweeps of small amplitude (2.5 kN) were interleaved between cyclic parcels. Figures III.10a–III.14 suggest altogether that weak dynamic vibrations did not impact substantially the slow/cyclic response, regardless of the larger number of applied small cycles – for instance, $N = 17200$ cycles at four different values of F_{av} between parcels *b* and *c*. Generally, small-amplitude vibrations did not induce further pile deflection and gap opening.

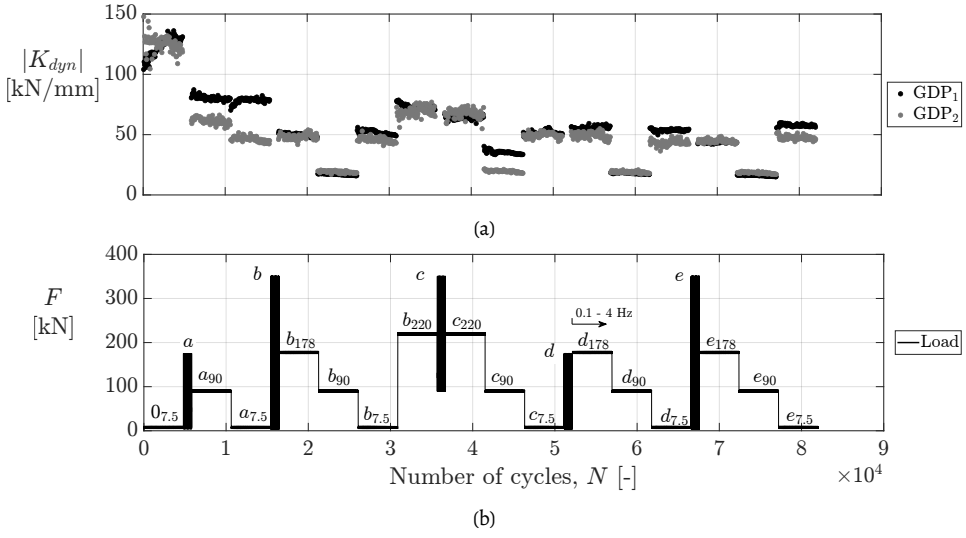

Figure III.15: (a) Absolute value of the dynamic stiffness $|K_{dyn}|$ vs number of cycles (bottom axis) during the dynamic f-sweeps; (b) cyclic/dynamic loading programme.

Figure III.15 displays the evolution of (the absolute value of) the dynamic pile stiffness $|K_{dyn}|$ during each frequency sweep. For each dynamic loading cycle, $|K_{dyn}|$ was obtained as the ratio between the ranges of applied load (5 kN in all cases) and displacement, as illustrated in Figure IV.11c. Although all associated with small-amplitude vibrations, $|K_{dyn}|$ values vary significantly along the sequence of f-sweeps. Particularly worth noting are the variations in $|K_{dyn}|$ during the f_b-sweeps: while $|K_{dyn}| \approx 20$ kN/mm when the pile was previously cycled around $F_{av} = 90$ kN in a_{90}, a significantly larger average load of 178 kN (b_{178}) determined a higher stiffness of about 50 kN/mm – similar conclusions also apply to the $|K_{dyn}|$ trends during the f_c-, f_d-, and f_e-sweeps.

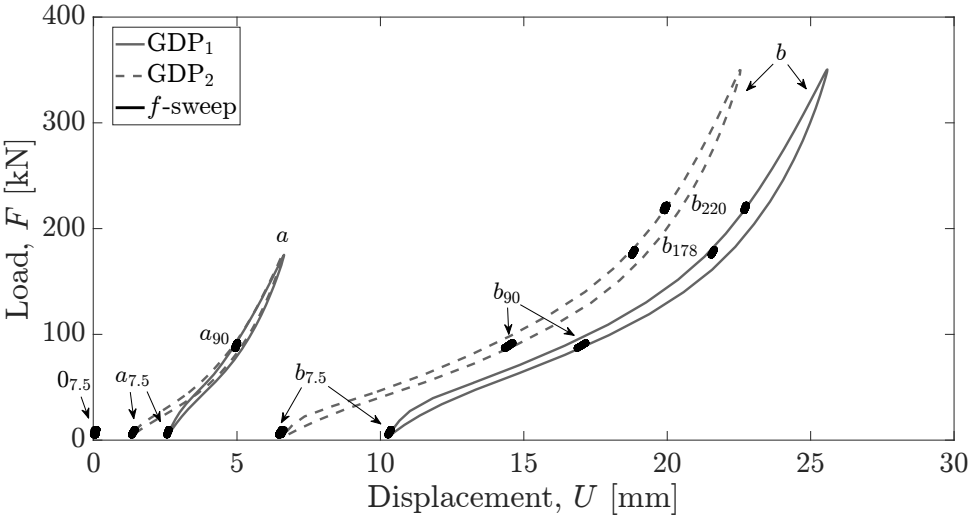

Figure III.16: Relationship between the cyclic (parcels a and b, 1000th cycles) and dynamic (f_a-f_b-sweeps) load-displacement responses for GDP_1 and GDP_2.

Figure III.16 helps to understand the observed non-monotonic relationship between $|K_{dyn}|$ and F_{av}. The figure displays the last (1000th) load-displacement cycle associated with the main gap-opening parcels a and b, together with the dynamic responses that resulted from the f_a- and f_b-sweeps. An interesting finding emerges clearly from Figure III.16: the dynamic stiffness during individual f-sweeps seems to be strongly correlated with the (tangent) cyclic stiffness K_{cyc}^{tan} around the same F_{av} level that characterises the preceding cyclic parcel. Such a finding is more quantitatively supported, for GDP_2, by Figure III.17, which shows on the left a magnified view of Figure III.15 around the f_b-sweeps and, on the right, the thousandth cycle recorded for parcel b. The cycle in Figure III.17b was also interpolated through a polynomial function (dotted line through the cycle), so that tangent stiffness values (K_{cyc}^{tan}, on the right axis) within the relevant range of F_{av} could be readily computed through differentiation.

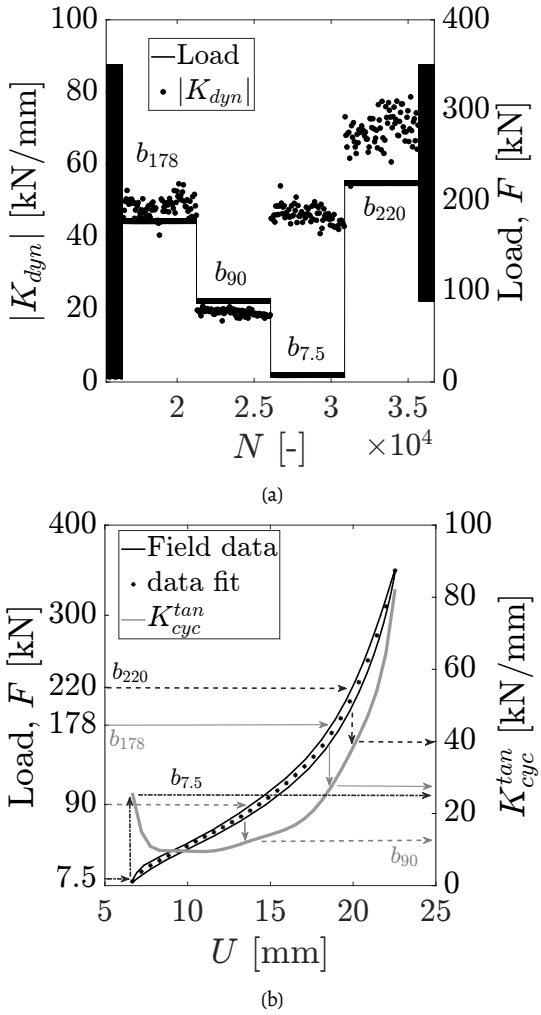

Figure III.17: Detailed comparison between GDP_2's cyclic and dynamic responses: (a) absolute value of the dynamic stiffness $|K_{dyn}|$ (left axis) vs number of cycles at different F_{av} levels (right axis) for the frequency sweeps $b_{7.5,90,178,220}$; (b) 1000^{th} load-displacement cycle (left axis) and corresponding interpolated tangent stiffness (right axis) at the end of parcel b.

The comparison between Figures III.17a and III.17b highlights the non-monotonic relationship between $|K_{dyn}|$ and F_{av}, in which the $|K_{dyn}|$ patterns in Figure III.15 follow consistently the sequence of applied F_{av} values. This observation leads to believe that a loading event of large magnitude (such as parcel b) may provide information relevant to predicting the behaviour under subsequent small-amplitude parcels within the same load range.

$|K_{dyn}|$ appears to be nearly unaffected by the loading frequency during most of the f-sweeps applied to both piles, with the exception of $0_{7.5}$, $a_{7.5}$, b_{220}, and $(b-e)_{90}$. While some of

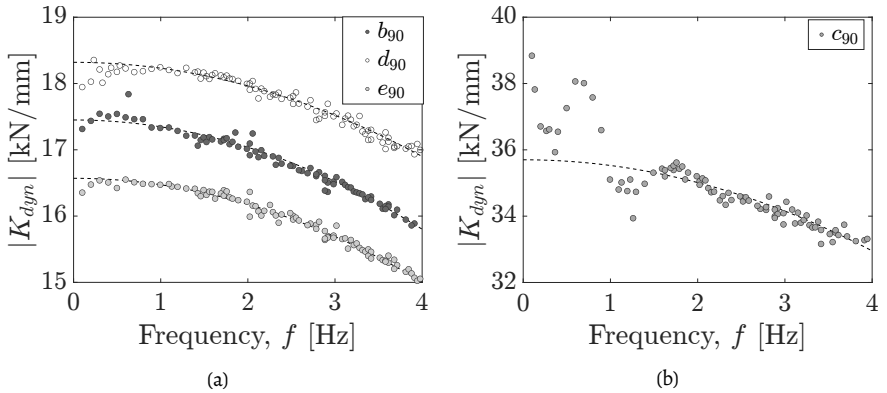

Figure III.18: Identification of the equivalent 1dof dynamic properties of the GDP$_1$-soil system during the $(b-e)_{90}$ f-sweeps.

these exceptions would not be easily explained (e.g., $0_{7.5}$, $a_{7.5}$, and b_{220}), the kind of frequency-dependence observed for $(b-e)_{90}$ has been recently interpreted by Kementzetzidis et al., 2021. Based on the results of full-scale dynamic tests, Kementzetzidis et al. showed that the low-frequency dynamics of a monopile in sand can be conveniently described through an equivalent linear visco-elastic macro-system with one degree of freedom (1dof), characterised by independent values of static stiffness (K_0), damping ratio (ξ), and undamped resonance frequency (f_{res}). In this regard, Figure III.18a shows for GDP$_1$ how the experimental $|K_{dyn}|-f$ trends emerged from $(b,d,e)_{90}$ can be used to identify the properties of the mentioned 1dof macro-system, based on the following expression of the dynamic stiffness:

$$|K_{dyn}(f)| = K_0\sqrt{\left[1-\left(\frac{f}{f_{res}}\right)^2\right]^2+\left[2\xi\frac{f}{f_{res}}\right]^2} \tag{III.2}$$

where f is the excitation frequency. The identified properties are summarised in Table III.3 for both GDP-driven piles and the selected f-sweeps. Overall, the values provided in the table suggest that: (i) the global dynamic properties of the system are quite similar for sweeps around the same F_{av} value – with the unclear exception of c_{90} for GDP$_1$ (see Figure III.18b); (ii) resonance-related valleys in the $|K_{dyn}|-f$ curves would have likely been found at significantly larger frequencies, expectedly in the order of 12-14 Hz (see identified f_{res} values in Table III.3). Such dynamic macro-properties could have been more reliably identified by spanning a wider frequency range in the loading tests (Kementzetzidis et al., 2021; Versteijlen et al., 2017a).

Finally, the field data were also post-processed to derive global values of foundation damping for all f-sweep stages. To this end, the following conventional definition of damping ratio (ξ) was adopted (Chopra, 1995; Jacobsen, 1960):

$$\xi = \frac{E_D}{4\pi E_S} \tag{III.3}$$

		Test piles	Reaction pile
Length	L	10 m	10 m
Embedded length	L_e	8 m	8 m
Outer diameter	D	0.762 m	1.6 m
Wall thickness	h	0.0159 m	0.02 m

Table III.1: Pile dimensions

-	F_{av} [kN]	F_{cyc} [kN]	f [Hz]	$N \times 10^3$
$0_{7.5}$	7.5	2.5	0.1-4	4.8
a	**90**	**85**	**0.1**	**1**
a_{90}	89.5	2.5	0.1-4	4.8
$a_{7.5}$	7.5	2.5	0.1-4	4.8
b	**177.5**	**172.5**	**0.1**	**1**
b_{178}	177.5	2.5	0.1-4	4.8
b_{90}	89.5	2.5	0.1-4	4.8
$b_{7.5}$	7.5	2.5	0.1-4	4.8
b_{220}	219.5	2.5	0.1-4	4.8
c	**220**	**130**	**0.1**	**1**
c_{220}	219.5	2.5	0.1-4	4.8

-	F_{av} [kN]	F_{cyc} [kN]	f [Hz]	$N \times 10^3$
c_{90}	89.5	2.5	0.1-4	4.8
$c_{7.5}$	7.5	2.5	0.1-4	4.8
d	**90**	**85**	**0.1**	**1**
d_{178}	177.5	2.5	0.1-4	4.8
d_{90}	89.5	2.5	0.1-4	4.8
$d_{7.5}$	7.5	2.5	0.1-4	4.8
e	**177.5**	**172.5**	**0.1**	**1**
e_{178}	177.5	2.5	0.1-4	4.8
e_{90}	89.5	2.5	0.1-4	4.8
$e_{7.5}$	7.5	2.5	0.1-4	4.8

Table III.2: Loading specifications for the cyclic/dynamic field tests – cf. to Figure III.7.

	GDP_1			GDP_2		
	K_0 [kN/mm]	f_{res} [Hz]	ξ [%]	K_0 [kN/mm]	f_{res} [Hz]	ξ [%]
a_{90}	84	-	-	63	-	-
b_{90}	17.45	12.98	5%	19.92	13.41	8%
c_{90}	35.70	14.23	11%	20.02	12.00	9%
d_{90}	18.32	14.31	6%	19.95	13.71	8%
e_{90}	16.57	12.91	9%	18.85	12.81	12%

Table III.3: Equivalent 1dof dynamic properties identified for GDP_1 and GDP_2 with respect to different f-sweeps around F_{av} = 90 kN (cf. to Figure III.18). Data associated with a_{90} did not allow the same kind of interpretation/processing – see Figure III.15.

where E_D and E_S denote the stored elastic energy and the plastic work (loop area) associated with individual force-displacement cycles (Yang et al., 2018). From a practical standpoint, the ξ values displayed in Figure III.19 were obtained after 'removing' the asymmetry introduced by the load bias F_{av} (i.e., by treating each load-displacement loop as if centred with respect to the load value $F = F_{av}$). There was no need to extend the calculation procedure to the case of a ratcheting cyclic response (as in Abadie, 2015b), given the negligible displacement accumulation that was recorded during the frequency sweeps.

The damping values obtained, cycle by cycle, for both GDP-driven piles are reported in Figure III.19. In general, relatively large damping values were found, in reasonable agreement with the values alternatively identified through the stiffness-frequency trends in Figure III.18 (cf. to Table III.3).

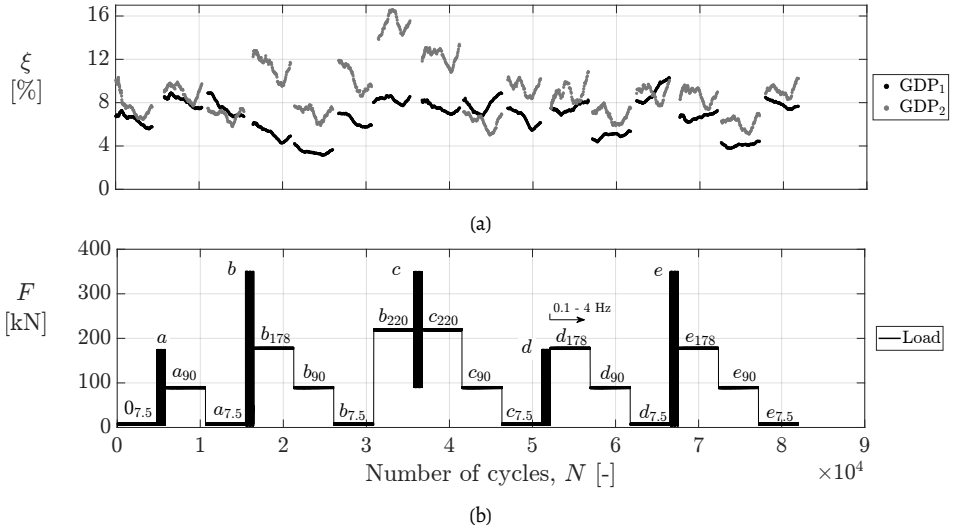

Figure III.19: Damping ratio values calculated for GDP_1 and GDP_2 from the f-sweep data.

5. Concluding remarks

Recent research related to the GDP project ('Gentle Driving of Piles') has been presented in this study, which complements the companion paper by Tsetas et al., 2023. GDP is a TU Delft-led joint industry project on the development of a new vibratory driving technology for monopiles. Its stepping stone is the idea that both efficient installation and low noise emission can be achieved by applying to the pile a combination of low-frequency/axial and high-frequency/torsional vibrations. To achieve a first demonstration of the GDP concept, medium-scale field tests were performed at the sandy Maasvlakte II site in Rotterdam. Such tests included installation experiments with different driving methods (impact hammering, axial vibro-driving, and GDP driving), followed by cyclic/dynamic loading of the same piles.

The soil inhomogeneity at the Maasvlakte II site has hindered a straightforward comparison of all loading test results, and led to focus on the cyclic/dynamic response of the two GDP-driven piles – except for cyclic pile deflection data, which have been reported and compared for all the instrumented test piles.

The main experimental evidence presented in this paper may be summarised as follows:

- the measured lateral pile responses have been found to be significantly affected by the onshore geotechnical conditions at the Maasvlaakte II site, especially by the occurrence of pile-soil gapping in the shallow unsaturated soil;
- the cyclic trends of lateral pile deflection have shown good compatibility with soil monitoring data, particularly with the variations in radial soil pressure that were recorded near the piles at different depths;
- while the expected pile displacement accumulation has been observed during most cyclic load parcels, both decreasing and increasing cyclic patterns have been documented for the average secant stiffness. The latter evidence has been attributed to the complex interplay of gap geometry and sand's fabric changes under multi-amplitude cyclic lateral loading;
- the lateral pile stiffness during small-amplitude frequency sweeps has been shown to be well correlated with the stiffness variations observed during the cyclic parcel of largest amplitude. The frequency sweep data have also exposed some frequency-dependence of the dynamic stiffness for loading frequencies larger than 1 Hz, and returned values of damping ratio that are broadly consistent with those alternatively inferred from dynamic stiffness-frequency trends.

In addition to the above geotechnical observations, the field campaign has preliminarily shown that not only GDP is an effective pile installation method (see companion paper), but also that it is unlikely to compromise a satisfactory post-installation response of the pile. More quantitative analysis of all loading test results will be presented in the future based on detailed numerical modelling work.

IV

Paper III

A memory-enhanced p-y model for piles in sand accounting for cyclic ratcheting and gapping effects

Evangelos Kementzetzidis, Federico Pisanò, Andrei V. Metrikine

Computers and Geotechnics, (2022), 148, 104810.

https://doi.org/10.1016/j.compgeo.2022.104810

Abstract

The analysis of cyclically loaded piles is acquiring ever greater relevance in the field of geotechnical engineering, most recently in relation to the design of offshore monopiles. In this area, predicting the gradual accumulation of pile deflection under prolonged cycling is key to performing relevant serviceability assessments, for which simplified pile-soil interaction models that can be calibrated against common geotechnical data are strongly needed. This study proposes a new cyclic $p-y$ model for piles in sand that takes a step further towards meeting the mentioned requirements. The model is formulated in the framework of memory-enhanced bounding surface plasticity, and extends to cyclic loading conditions the previous monotonic, CPT-based $p-y$ formulation by Suryasentana and Lehane, 2016; additionally, detailed modelling of pile-soil gapping is introduced to cope with the presence of unsaturated sand layers or, more generally, of cohesive soil behaviour. After detailed description of all model capabilities, field data from an onshore cyclic pile loading test are simulated using the proposed $p-y$ model, with the most relevant parameters calibrated against available CPT data. Satisfactory agreement is shown between experimental and numerical results, which supports the practical applicability of the model and the need for further studies on a fully CPT-based calibration.

1. Introduction

The use of piled foundations in civil engineering has evolved substantially over the past decades, with a number of new applications and design challenges driven by offshore energy developments (Kaynia, 2021). The viability of any piled foundation concept is closely related to the soundness and accuracy of the adopted analysis methods, especially for what concerns the interaction with the surrounding soil. For piles subjected to lateral loading, pile-soil interaction is most commonly analysed by resorting to the well-known $p-y$ method. The popularity of such approach is motivated by its simplicity and computational efficiency, in that it reduces the analysis of a 3D interaction problem to the study of a 1D foundation beam in the presence of distributed soil reactions (Winkler, 1867). In the $p-y$ framework, such soil reactions emerge from the constitutive behaviour of deformable soil spring elements, which yields a relationship between the lateral soil reaction (p) and corresponding pile deflection (y) at a given location (fully local approach). $p-y$ modelling approaches have significantly evolved in time with regard to mathematical formulation and calibration procedures, so as to accommodate a variety of geotechnical, geometrical, and loading conditions (API, 2011; Byrne et al., 2019; DNV, 2014; Suryasentana and Lehane, 2016).

The development of soil reaction models for cyclic loading conditions has been often associated with seismic design matters – see, e.g., the work of Boulanger et al., 1999; Brandenberg et al., 2013; Choi et al., 2015 for piles in sandy soil. More recently, modern offshore wind developments have given rise to new threads of soil-foundation interaction research, with focus on the impact of cyclic loading effects on the serviceability of offshore wind turbine

foundations. A notable instance is represented by the case of large-diameter monopile foundations, which must be designed to avoid undesired resonance under environmental and mechanical loads (Kementzetzidis et al., 2019, 2018), as well as prevent the accumulation of excessive lateral tilt during their whole operational life (Arany et al., 2017a). The prediction of such tilt requires thorough understanding of the role played by soil's ratcheting behaviour, especially when the pile at hand is subjected to asymmetric loading cycles (Cuéllar et al., 2009; Niemunis et al., 2005; Pisanò, 2019). In this respect, numerous experimental studies have been conducted in recent years – both in the laboratory (Abadie, 2015b; Albiker et al., 2017; Frick and Achmus, 2019; Klinkvort, 2012; Klinkvort et al., 2010; LeBlanc et al., 2010; Richards et al., 2021; Richards, 2019; Rudolph et al., 2014; Truong et al., 2019; Wang et al., 2018a; Zhu et al., 2016) and in the field (Byrne et al., 2020a,b; Kementzetzidis et al., 2023a; Li et al., 2015). The data from such studies have provided essential input to the improvement of cyclic modelling procedures, ranging from advanced 3D analyses (Achmus et al., 2009; Jostad et al., 2014; Kementzetzidis et al., 2021; Liu et al., 2021; Staubach and Wichtmann, 2020) to, more recently, 1D $p-y$ approaches (Beuckelaers et al., 2020; Pisanò et al., 2022a). However, there is still a substantial demand for enhanced cyclic $p-y$ models, since the majority of the existing cyclic formulations are typically unable to reproduce soil ratcheting effects and, therefore, the cyclic accumulation of pile deflection. This is the case, for example, of well-known $p-y$ formulations for monotonic loading (Byrne et al., 2019; DNV, 2014; Matlock, 1970b; Suryasentana and Lehane, 2016), even when their cyclic versions are obtained based on the well-known Masing rules (Pyke, 1979); on the other hand, existing $p-y$ models for seismic applications (Boulanger et al., 1998; Choi et al., 2015) will often tend to over-predict the accumulated displacement when used to tackle cyclic loading conditions that are commonly experienced by offshore (mono)piles.

The practical use of $p-y$ models is intimately related to the possibility of calibrating relevant parameters against simple, readily available geotechnical data – such as those from standard laboratory and/or in-situ tests. In this regard, the $p-y$ models for piles in sand associated with, e.g., the API industry guidelines (API, 2011) and the PISA design method (Burd et al., 2020), require as an input, respectively, the friction angle (ϕ) and the initial relative density (D_r) of the sand. Since such properties are typically inferred from in-situ CPT results, an intermediate step is necessary to translate the measured resistance to cone penetration (q_c) into ϕ or D_r values – which adds a further layer of uncertainty to the overall calibration procedure. An interesting alternative is offered by so-called CPT-based $p-y$ methods, where model parameters are directly correlated to the q_c values measured in-situ (Dyson and Randolph, 2001; Li et al., 2014; Novello, 1999; Suryasentana and Lehane, 2014b). Particularly worth mentioning is the work of Suryasentana and Lehane (Suryasentana and Lehane, 2014b, 2016), who proposed a CPT-based monotonic $p-y$ method that is applicable to piles of different cross-section shape and aspect ratio in (in)homogeneous sand profiles.

In the presence of cohesive soil behaviour, it is relevant to capture the occurrence and influence of pile-soil separation (also termed 'gapping'). Gapping is associated with formation

of a self-standing vertical soil surface as the pile is loaded away from a previous configuration with full pile-soil contact (Boulanger et al., 1999; Kementzetzidis et al., 2023a; Matlock et al., 1978; Suzuki and Nakai, 1985). A number of gapping $p-y$ models are already available in the literature (Boulanger et al., 1999, 1998; Brandenberg et al., 2013; Gerolymos and Gazetas, 2005a,b; Hededal, Klinkvort et al., 2010; Nogami et al., 1992), mostly in relation to seismic loading and clayey soil conditions. In the case of sandy soils, modelling pile-soil gapping may be relevant to simulating the effects of natural cementation and/or unsaturated conditions – in fact, most field testing campaigns about offshore monopiles have been recently carried out at onshore sites, and have returned measured pile responses that cannot be fully understood without considering the influence of gapping (Byrne et al., 2020a,b; Kementzetzidis et al., 2023a; Li et al., 2015).

Based on the above premises, this work aims to incorporate the following features into a new $p-y$ model for piles subjected to lateral cyclic loading in sand:

- hysteretic soil reaction behaviour, with controlled accumulation of lateral deflection under prolonged cyclic loading;
- modelling of pile-soil gapping effects under cyclic loading conditions;
- direct calibration of key $p-y$ model parameters against in-situ CPT data.

The proposed cyclic $p-y$ model is formulated in the framework of bounding surface plasticity (Dafalias, 1986), with the inclusion of an additional memory locus for the accurate modelling of lateral deflection accumulation under prolonged cycling (Corti et al., 2016; Liu et al., 2019a) – cyclic ratcheting soil behaviour. Further, the modelling of pile-soil gapping is inspired by the approach of Boulanger et al., 1998, who introduced a set of parallel springs to represent the physical mechanisms of ' frictional drag' and 'gap closure'. The proposed $p-y$ model builds directly on the work of Suryasentana and Lehane, 2016, in that it retains their original CPT-based philosophy to tackle cyclic loading conditions and pile-soil gapping effects.

After a detailed description of the mathematical formulation and its modelling implications, the suitability of the new $p-y$ model is finally assessed against original field data from recent medium-scale pile loading tests. In particular, the reference data describe the cyclic response of an instrumented tubular pile that was hammered into an inhomogenous sand deposit including a shallow unsaturated layer (Kementzetzidis et al., 2023a; Tsetas et al., 2023). While more data and further research will be necessary to further develop/validate the proposed CPT-based parameter calibration procedure, this paper demonstrates the remarkable capabilities and flexibility of the proposed $p-y$ model.

2 . Bounding surface p-y modelling with ratcheting control

This section describes the reformulation of the monotonic $p-y$ relationship by Suryasentana and Lehane, 2016 as a bounding surface model with kinematic hardening. An additional

ratcheting control mechanism is then introduced for more realistic simulation of pile deflection accumulation under prolonged cycling. The proposed model is applicable to one-directional cyclic loading scenarios with no substantial hydro-mechanical effects in the soil (i.e., drained conditions). Its implications are discussed in what follows both at the level of a single interaction element ($p-y$ spring) and global pile-soil interaction.

2.1. Reformulation of Suryasentana and Lehane's $p-y$ model

This section takes further the previous work of Suryasentana and Lehane, who proposed a monotonic $p-y$ relationship for piles in sand (henceforth referred to as *SL* model) along with a CPT-based parameter calibration procedure (Suryasentana and Lehane, 2014b, 2016). The *SL* model was developed after performing FE simulations of spherical cavity expansion and lateral pile loading, in order to establish quantitative relationships between simulated q_c values and lateral soil reactions for piles of different cross-section shape and aspect ratio – both in dry and water-saturated sand. The main outcome of Suryasentana and Lehane's work was a $p-y$ relationship between lateral soil reaction (p) and pile displacement (y), which (i) can be completely calibrated against in-situ q_c profiles, and (ii) has been successfully validated against the field test results by Anusic et al., 2019; Li et al., 2015; Suryasentana and Lehane, 2014a; Suryasentana and Lehane, 2016; Wang et al., 2022. In particular, the *SL* $p-y$ relationship reads as follows:

$$p = p_u\left[1-\mathrm{e}^{-\alpha(y/D)^m}\right] \Rightarrow y = D\left[-\frac{1}{\alpha}\ln\left(\frac{p_u-p}{p_u}\right)\right]^{1/m} \tag{IV.1}$$

In Equation (IV.1), p_u represents the ultimate soil reaction per unit length, D is the pile diameter, while α (>0) and m (>0) are dimensionless parameters that can be calibrated using the following CPT-based relationships (Suryasentana and Lehane, 2016):

$$\begin{cases} p_u = 2.4\sigma'_{v0}D\left(\dfrac{q_c}{\sigma'_{v0}}\right)^{0.67}\left(\dfrac{z}{D}\right)^{0.75} \le q_c D \\ \alpha = 8.9\left(\dfrac{z}{D}\right)^{-1.25}\left(\dfrac{\sigma_{v0}-u_g}{\sigma'_{v0}}\right)^{0.5} \\ m = 1 \end{cases} \tag{IV.2}$$

σ_{v0} and σ'_{v0} represent the in-situ total and effective vertical stresses at a depth z below the ground surface, while u_g is the hydrostatic pore water pressure at $z=0$.

In what follows, the *SL* model is reformulated as a bounding surface plasticity model with kinematic hardening, which is suitable to tackle one-directional cyclic loading conditions (Dafalias, 1986) – see also Choi et al., 2015. In the context of one-dimensional $p-y$ kinematic hardening plasticity, the following modelling ingredients are necessary to describe an incremental elasto-plastic response – for brevity, the terms 'stress' and 'strain' are used in lieu of 'soil reaction' (p, per unit length) and 'lateral displacement' (y):

(i) Elastic + plastic splitting of the strain increment

$$\mathrm{d}y = \mathrm{d}y_e + \mathrm{d}y_p \tag{IV.3}$$

where the subscripts e and p denote the elastic and plastic components of the total strain increment, respectively.

(ii) Elastic law

$$\mathrm{d}y_e = \frac{\mathrm{d}p}{K} \tag{IV.4}$$

where the stiffness K relates the corresponding increments of stress and elastic strain.

(iii) Translating yield locus (kinematic hardening)

$$f = |p - p_\alpha| - p_y = 0 \tag{IV.5}$$

Equation (IV.5) defines a translating locus in the 1D stress space, always centred around the (evolving) back-stress p_α with a total size equal to $2 \cdot p_y$. Under a given loading history, the back-stress is assumed to evolve with the plastic strain increment according to the following

(iv) Back-stress translation rule

$$\mathrm{d}p_\alpha = H \cdot \mathrm{d}y_p \tag{IV.6}$$

where H is the so-called plastic modulus. In the spirit of bounding surface plasticity, H is set to depend on the distance between the current stress p and its projection (along the loading direction) onto the

(v) Bounding locus

$$F = |p| - p_u = 0 \tag{IV.7}$$

which identifies the range of admissible stresses, i.e., $-p_u \le p \le p_u$.

(v) Flow rule

$$\mathrm{d}y_p = \mathrm{d}\lambda \cdot \mathrm{sgn}\left(p - p_\alpha\right) \tag{IV.8}$$

where sgn represents the signum function and the plastic multiplier $\mathrm{d}\lambda$ is obtained through the 'consistency condition' ($\mathrm{d}f = 0$) whenever the yield condition $f = 0$ is satisfied.

To enable perfect adherence to the original *SL* relationship, two further assumptions are embedded into the model formulation:

1. negligible elastic strains ($\mathrm{d}y_e = 0$), i.e., $K \to \infty$ and $\mathrm{d}y_p = \mathrm{d}y$;
2. plastic straining occurring from the very onset of loading, which coincides with the assumption of 'zero elastic range', i.e., $p_y \to 0$ (Borja and Amies, 1994; Dafalias and Popov, 1977; Dafalias and Taiebat, 2016; Pisanò and Jeremić, 2014).

Introducing the assumption 2 into Equation (IV.5) implies that

$$p = p_\alpha \Rightarrow \mathrm{d}p = \mathrm{d}p_\alpha \tag{IV.9}$$

which, in combination with the translation rule (IV.6), leads to the following 'hypoplastic' redefinition of the flow rule (IV.8):

$$\mathrm{d}y_p = \frac{\mathrm{d}p}{H} \tag{IV.10}$$

and, in light of assumption 1, to the final relationship between strain and stress increments below:

$$\mathrm{d}y = \frac{\mathrm{d}p}{H} \Rightarrow y = \int \frac{1}{H}\,\mathrm{d}p \tag{IV.11}$$

In conclusion, the performance (and accuracy) of the resulting model depends entirely on the choice of the hardening modulus H. In order to reproduce within the reference plasticity framework the monotonic $p-y$ relationship (IV.1), the following expression of H is derived using Equation (IV.11):

$$H = \frac{\alpha \cdot m}{D} \cdot |\bar{p}_u - p| \cdot \left| \frac{1}{\alpha} \ln\left(\frac{\bar{p}_u - p}{\bar{p}_u - p_0} \right) \right|^{\frac{m-1}{m}} \tag{IV.12}$$

which underlies a $p-y$ model suitable for the step-by-step analysis of cyclic pile-soil interaction problems in the time domain. In Equation (IV.12), $\bar{p}_u = p_u \cdot \mathrm{sgn}(\mathrm{d}p)$ with $\mathrm{d}p$ denoting the stress increment within the current calculation step; p_0 represents a stress projection centre that takes the current p value whenever a soil reaction reversal occurs (i.e., whenever $\mathrm{sgn}(\mathrm{d}p)$ changes*). For $0 < m < 1$, Equation (IV.12) complies with well-established bounding surface plasticity principles, in that $H \to 0$ when $p \to \bar{p}_u$ (nil plastic stiffness as the bounding locus is approached) and $H \to \infty$ when $p \to p_0$. The limit setting $m = 1$ suggested by Suryasentana and Lehane, 2016 (Equation (IV.2)) can be approximated as closely as desired by choosing values slightly lower than 1 (e.g., $m = 0.9999$), so as to preserve the aforementioned limiting properties of the plastic modulus – which would no longer hold for m strictly equal to 1.

Importantly, the bounding surface model resulting from Equation (IV.12) (with p_0 initialised to 0) can easily be proven to match the SL relationship for monotonic loading conditions – see Figure IV.2.

2 .2. Memory-enhancement for ratcheting control

As noted in the introduction, the study of soil-structure interaction in the presence of ratcheting soil behaviour is key to analysing the serviceability of offshore monopiles (Cuéllar et al., 2012; Liu et al., 2021; Wichtmann et al., 2010), and is at the core of the experimental studies cited above. The same subject has also been attracting the interest of numerical mod-

* The value of p_0 for each $p-y$ spring is usually initialised to 0, and then varies during the analysis as many times as the number of stress reversals

ellers, who have recently begun to propose $p-y$ approaches accounting for cyclic ratcheting effects – see, e.g., the work of Beuckelaers et al., 2020 in the framework of hyperplasticity.

Bounding surface models of the kind described in Section 2 .1 are known to be quantitatively inaccurate with regard to the simulation of cyclic ratcheting – particularly, they tend to overpredict the accumulation of ratcheting deformations under (asymmetric) cyclic loading. In order to overcome this drawback, the above bounding surface $p-y$ formulation is enriched with an additional 'memory locus', which can be exploited to keep track of the cyclic stress history and make the stiffness of the system evolve in agreement with relevant experimental evidence. The same approach has been recently developed for the constitutive modelling of (multiaxial) cyclic sand behaviour (Corti et al., 2016; Liu et al., 2019a), and is here applied for the first time to 1D $p-y$ modelling. The use of a memory locus (Equation (IV.13)) that keeps track of the previous loading history allows higher versatility than casting fabric change effects directly into the evolution of the bounding domain (Equation (IV.7)), particularly with regard to complex cyclic loading histories (Liu et al., 2022).

The memory-enhancement of the above bounding surface $p-y$ model requires the introduction of the following memory locus:

$$F_M = |p - p_{\alpha,M}| - p_M = 0 \tag{IV.13}$$

which can translate and change in size in the stress space through the evolution of the associated memory back-stress ($p_{\alpha,M}$) and domain size (p_M), respectively. The memory locus is used to introduce an additional metrics into the model, namely the distance b_M between the current stress p and its projection onto the memory locus ($\bar{p}_M$) along the loading direction ($\bar{p}_M = p_{\alpha,M} + \bar{p}_M$, with $\bar{p}_M = p_M \cdot \mathrm{sgn}(\mathrm{d}p)$):

$$b_M = |p - \bar{p}_M| \tag{IV.14}$$

The distance b_M is then exploited to upgrade the definition of the plastic modulus H in Equation (IV.12) as follows:

$$H_M = H \cdot \exp\left\{\mu_0 \left(\frac{b_m}{b_{ref}}\right)^2\right\} \tag{IV.15}$$

where μ_0 is a scalar ratcheting-control parameter, and $b_{ref} = 2p_u$ is introduced for normalisation purposes.

The role of the memory locus can be grasped through Equation (IV.15): when the current stress point satisfies $F_M = 0$, i.e., $b_M = 0$, then $H_M = H$ and the response is not affected by the memory mechanism – this situation is referred to as 'virgin loading conditions'; in contrast, $H_M > H$ whenever p lies inside the memory locus, which implies a stiffer response depending on the current value of b_M and the selected parameter μ_0. As is shown in the following, the addition of the memory locus can improve the modelling of cyclic ratcheting, after

introducing suitable evolution laws for the memory internal variables $p_{\alpha,M}$ and p_M (mixed isotropic-kinematic hardening). Herein, the same phenomenological approach described by Liu et al., 2019a is adapted to 1D $p-y$ modelling, which is summarised by the following two assumptions:

1. starting from an initial situation of virgin loading (i.e., $p=\tilde{p}_M$) with $p_M=0$, the evolution of p under first loading (and under any following virgin loading event) produces an expansion of the memory locus ($\mathrm{d}p_M>0$) along $\mathrm{d}p$, pivoting around the opposite boundary point of the locus itself;

2. the mathematical relationships derived based on the above assumption are held valid for any loading conditions (i.e., also for $p\neq\tilde{p}_M$).

These assumptions underlie the simple derivations reported in Section 5 , which lead to the following evolution laws for $p_{\alpha,M}$ and p_M:

$$\mathrm{d}p_{\alpha,M}=\tilde{H}_M\cdot\mathrm{d}y_p \tag{IV.16}$$

$$\mathrm{d}p_M=|\mathrm{d}p_{\alpha,M}| \tag{IV.17}$$

where $\tilde{H}_M$ is a 'dummy' hardening modulus related to a fictitious deformation mechanism built on the evolving memory locus (Corti et al., 2016; Liu et al., 2019b) – cf. to Equation (IV.6).

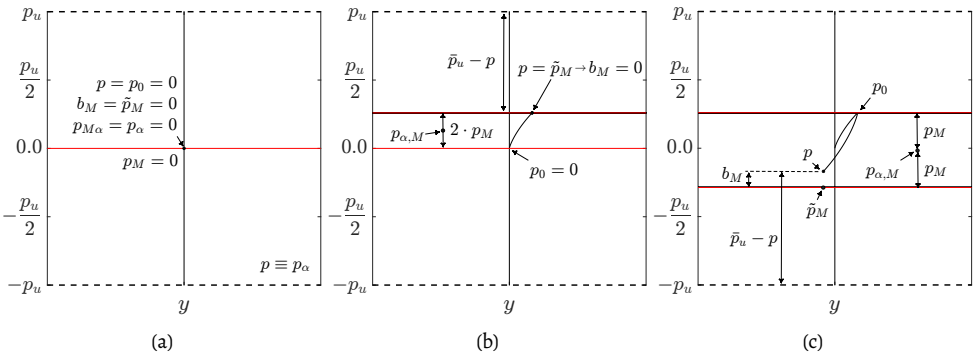

Figure IV.1: Location and evolution of the model loci in the proposed memory-enhanced bounding surface $p-y$ formulation.

Figure IV.1 illustrates the location and evolution of the different model loci during an arbitrary loading-unloading one-directional $p-y$ process, which determines the update of the projection centre p_0 upon load reversal (Equation (IV.12)) – also note that, due to the vanishing yield locus, $p\equiv p_\alpha$ (Equation (IV.9)). Given the phenomenological nature of the memory locus, its initialisation at the beginning of a $p-y$ analysis is generally such that

$p_{\alpha,M} = p_\alpha \equiv p(=0)$ and $p_M = 0$. Such assumption of 'initial virgin loading' may be relaxed by setting $p_M > 0$ at the onset of lateral loading, for instance to simulate the influence of pile installation effects on the lateral stiffness. Although appealing, this possibility will however require further studies on how to convert pile driving effects into a suitable initialisation of the memory locus for simplified $p-y$ analyses.

2 .3. From memory-enhanced $p-y$ model performance to cyclic pile response

The memory-enhanced $p-y$ model – as well as its extension allowing for pile-soil gapping (see Section 3) – was implemented as a material model for *ZeroLength* elements into the OpenSees Finite Element (FE) platform (McKenna, 2011). In all pile-soil interaction analyses presented herein, the step-by-step integration of the above $p-y$ equations was performed using a fourth-order Runge-Kutta integration scheme with adaptive time step and automatic error control – in which the local truncation error is estimated as the difference between sixth- and fifth-order solution estimates, as detailed by Sloan et al., 2001.

It is worth recalling that the memory-enhanced $p-y$ model features at the same time (i) a zero yield locus and (ii) infinite elastic stiffness. Although perfectly admissible from a theoretical standpoint, special care is required with regard to the impact of such features on numerical integration. In particular, a practical 'cut-off' (upper bound) was introduced on the theoretically infinite value of the unloading/reloading (elastic) stiffness, which was found to negligibly impact the intended *SL* monotonic backbone curve. Moreover, given the adopted bounding surface plasticity framework, the $p-y$ model suffers from the well-known 'overshooting' phenomenon, which can produce unrealistically large stiffness values upon unloading/reloading cycles of small amplitude – such occurrence was originally recognised by Dafalias, 1986 as an inherent shortcoming of the bounding surface plasticity theory. Herein, overshooting effects have been remedied following the methodology proposed by Dafalias and Taiebat, 2016.

Figure IV.2 illustrates the role of the memory mechanism in the response of a single $p-y$ spring in terms of normalised stress-strain variables (i.e., p/p_u vs y/y_{ref}, where y_{ref} denotes the spring deformation associated with the maximum p/p_u value attained monotonically for a given cyclic loading scenario – in Figure IV.2 y_{ref} is associated with $p/p_u = 0.5$). In particular, the behaviour under asymmetric/one-way (Figure IV.2a) and symmetric/two-way (Figure IV.2b) loading is exemplified for μ_0 =0, 50, 500 – $\mu_0 = 0$ implies $H_M = H$ (Equation (IV.15)) and, therefore, no memory effects. As expected, an increase in μ_0 determines a lower cyclic accumulation of the spring strain under one-way loading, while a decrease in the net lateral deformation is observed under a symmetric excitation. The one-way behaviour in Figure IV.2a appears to capture the gradual stiffening of the soil response under prolonged cyclic (in reality largely due to cyclic densification), which would not be possible to capture within the traditional bounding surface framework (Corti et al., 2016; Liu et al., 2019a). It should be noted that, in the proposed formulation, the memory locus does not influence the ultimate resistance associated with the local soil reactions – i.e., p_u is not altered by cyclic loading.

This modelling choice is consistent with experimental evidence from the literature (Abadie et al., 2019; Richards et al., 2021), showing that the monotonic capacity of a pile in sand is mostly unaffected by previous loading cycles of lower amplitude (and same direction). In Figures IV.2a, IV.2b, the first loading branch obtained through numerical integration can be seen to perfectly match, as intended, the *SL* $p-y$ relationship (black dashed line in the figure) (Suryasentana and Lehane, 2016). Importantly, since inelastic deformations accumulate as part of a single plastic strain component (y_p), there is no need to calibrate different model parameters for either monotonic or cyclic loading histories – that is a typical shortcoming of modelling the cyclic accumulated strain as an additional component of inelastic deformation (Beuckelaers et al., 2020).

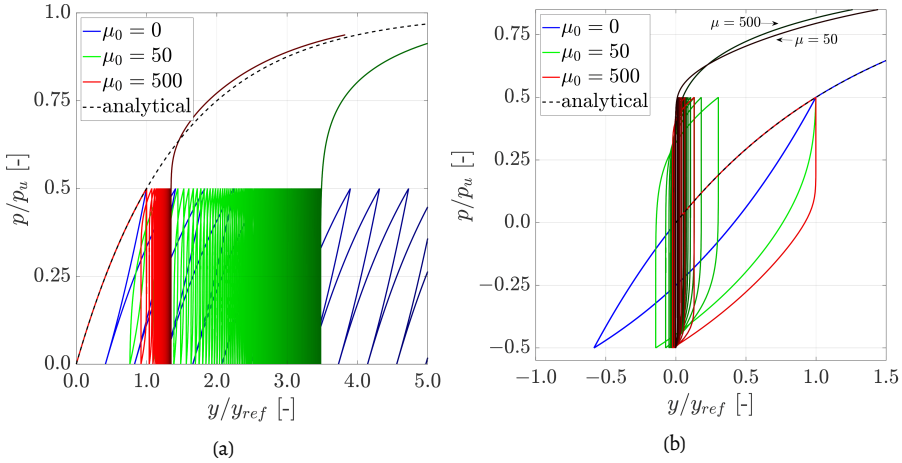

Figure IV.2: Cyclic performance of the memory-enhanced bounding surface $p-y$ model under (a) asymmetric/one-way cyclic loading ($N = 100$ cycles), and (b) symmetric/two-way loading ($N = 10$ cycles) for $\mu_0 = 0,\ 50,\ 500$. The black dashed line represents the SL analytical relationship in Equation IV.1; lines associated with $\mu_0 = 50,500$ gradually darken as the number of loading cycles increases. All model parameters calibrated based on Equation (IV.2) for a circular pile (diameter: $D = 0.762$ m) and a soil location characterised by: $z = 4$ m (soil depth), cone resistance $q_c = 17$ MPa, dry unit weight $\gamma_{dry} = 16$ kN/m^3).

The implications of the proposed model in scaling up from a single $p-y$ element to the global pile-soil system are exemplified with respect to the laterally loaded tubular pile in Figure IV.3a, featuring total and embedded lengths equal to $L = 9$ m and $L_e = 8$ m, diameter $D = 0.762$ m, and wall thickness $h = 1.59$ cm – the lateral load is applied with an eccentricity $e = 1$ m with respect to the ground surface ($z = 0$). In the corresponding OpenSees simulations of the pile subjected to one-way and two-way cyclic loading, the pile was uniformly discretised using 90 *ElasticTimoshenkoBeam* elements with typical elastic ($E = 210$ GPa, $\nu = 0.3$) and cross-sectional properties (Timoshenko shear coefficient: $\kappa = 0.57$, from Hutchinson, 2001), while nodal soil reactions compliant with the memory-enhanced $p-y$ model were introduced along the embedded pile length with a spacing of $\Delta z = 0.08$ m. A Newton-Raphson iteration scheme was adopted to solve the relevant system of non-linear equations, with a tolerance on

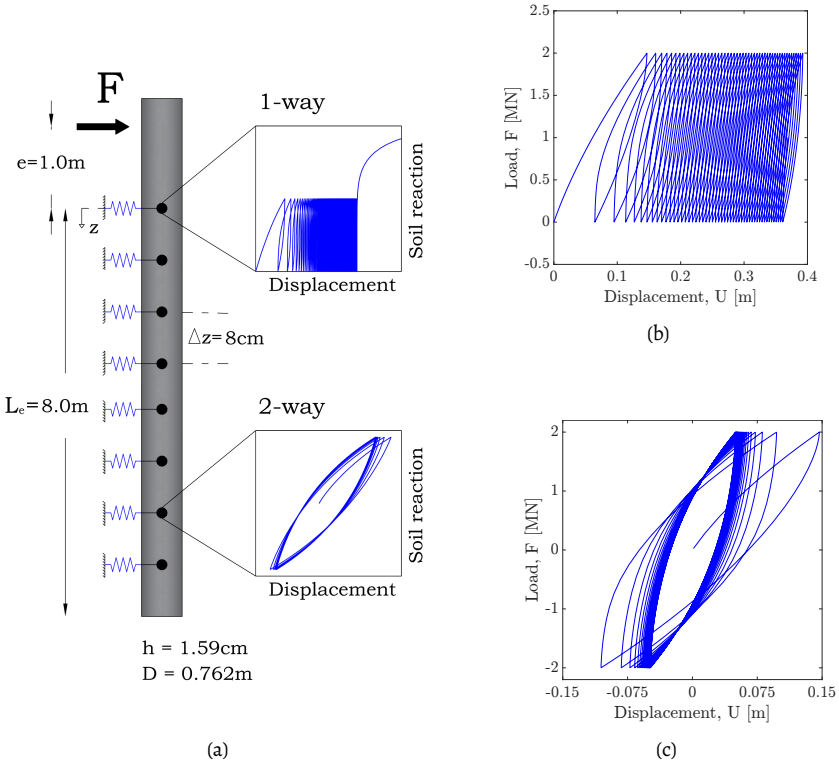

Figure IV.3: (a) Reference pile subjected to lateral cyclic loading: typical one-way vs two-way responses of the soil reaction springs in agreement with the proposed memory-enhanced $p-y$ formulation; simulated load-displacement pile response at ground surface to (b) one-way and (c) two-way cyclic loading ($N = 50$ loading cycles) with regard to the reference pile in (a).

the norm of the incremental displacement vector set as $\|\Delta \mathbf{y}\| \leq 10^{-10}$. Since this work focuses on lateral $p-y$ reactions, additional reaction mechanisms that may become prominent for lower L/D ratios – e.g., distributed moment, base shear resistance and moment fixity (Byrne et al., 2019; Davidson, 1982; Gerolymos and Gazetas, 2006; Lam and Martin, 1986) – were deliberately neglected in this first demonstration of the model's performance. A set of meaningful $p-y$ parameters was obtained for a fictitious cone resistance profile – namely $q_c[\text{MPa}] = 5 + 2z$, with z in metres – using the calibration procedure in Equation (IV.2) (with $m = 0.9999$ instead of $m = 1$), and setting $\mu_0 = 20$ for the ratcheting control mechanism.

Qualitatively, the resulting load-displacement response of the pile at the ground surface resembles in most respects the evidence emerging from the aforecited experimental studies on monopiles under lateral cyclic loading. For instance, in the case of one-way loading (Figure IV.3b), the typical gradual decrease in deflection accumulation rate is observed, along with an increase in the secant cyclic stiffness and a decrease in the cyclic loop area associated with subsequent response cycles (Abadie et al., 2019). Under symmetric/two-way

loading (Figure IV.3c), a net shift towards negative pile head deflection values is observed, which is consistent with recent observations from centrifuge experimental tests (Richards et al., 2021) and more advanced 3D FE simulations (Liu et al., 2021).

3 . Modelling of cyclic pile-soil gapping

Most onshore sites feature a phreatic level that is located at a certain depth below the ground surface, which determines a water saturation degree lower than 1 in the shallowest soil layers. As is well-known, unsaturated soils exhibit features of cohesive behaviour due to (transient) hydraulic suction effects, even in geomaterials that would otherwise be cohesionless – such as sands (Fredlund, 2006). The pseudo-cohesion of unsaturated sand can (temporarily) enhance the stability of relatively steep slopes, or enable the formation of a shallow gap with the soil in laterally loaded piles. In the latter case, cyclic soil reaction curves ($p-y$) are expected to assume a sort of S-shape, similar to that previously described for cohesive clayey soils – see Figure IV.4. Importantly, gapping effects under cyclic loading conditions are inherently displacement-dependent, as are the evolution of the gap depth and the alternation of 'contact'-'no-contact' stages between the pile and the soil. Pile-soil gapping mechanisms are more extensively described, e.g., by Boulanger et al., 1999; Kementzetzidis et al., 2023a; Matlock et al., 1978; Suzuki and Nakai, 1985.

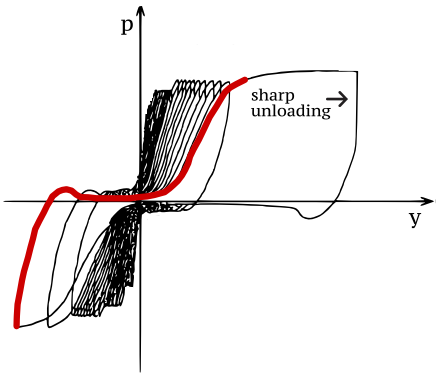

Figure IV.4: Cyclic $p-y$ curves for cohesive soils – modified after Randolph and Gourvenec, 2011, originally from Bea et al., 1979. The red line highlights the mentioned S shape of the last $p-y$ response cycle.

The memory-enhanced $p-y$ model described in the previous section is applicable to cyclically loaded piles in either dry or fully saturated sand. In order to reproduce gapping effects in unsaturated sand, an extension of the modelling framework is proposed hereafter. To this end, the overall soil reaction scheme (henceforth the gapping $p-y$ model) is extended as is shown in Figure IV.5, based on the following general principles:

– under one-directional cyclic loading, soil reactions must be modelled separately on the two sides – say, left (L) and right (R) – of the pile, due to the asymmetric configuration

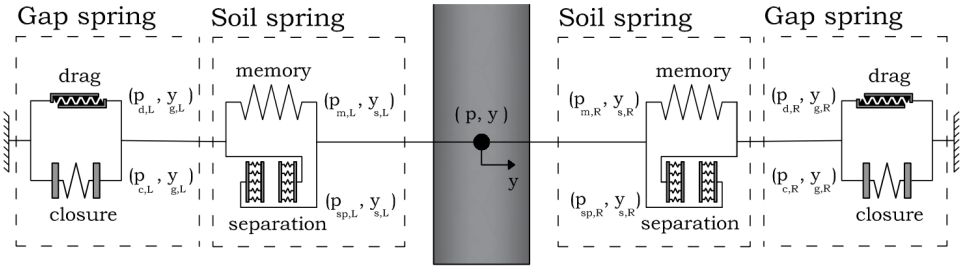

Figure IV.5: Proposed $p - y$ scheme allowing for cyclic ratcheting control and pile-soil gapping.

spring	reaction	deflection
soil	$p_m + p_{sp} = p_s$	$y_{sp} = y_m = y_s$
gap	$p_d + p_c = p_g$	$y_d = y_c = y_g$
left/right	$p_g = p_s = p_L \parallel p_R$	$y_g + y_s = y_R = y_L$
$p - y$	$p_L + p_R = p$	$y_R = y_L = y$

Table IV.1: Static and kinematic relationships for the spring elements included in the gapping $p - y$ model (Figure IV.5).

and evolution of the gap (Heidari et al., 2014). This is at variance with usual $p - y$ formulations, where soil reactions at a given depth represent the total integral along the perimeter of the foundation;

– on each side of the pile, a multi-component soil reaction scheme is introduced (Figure IV.5), including (i) the memory-enhanced $p - y$ mechanism described in Section 2 (henceforth the memory component) and three additional elements referred to as (ii) 'separation', (iii) 'closure', and (iv) 'drag' springs.

In particular, the memory component is connected in parallel to the separation spring to form a so-called 'soil element', which is in turn linked in series to a parallel combination of the closure and drag springs (altogether the 'gap ' spring). The resulting $p - y$ scheme combines the soil and gap elements, both including two distinct sub-components. In what follows, the static and kinematic variables associated with each soil reaction component are denoted by specific subscripts (memory spring → m; separation spring → sp; soil spring → s; drag spring → d; closure spring → c; gap spring → g; left component → L; right component → R), while typical relationships for the springs connected either in series or in parallel are reported in Table IV.1. For the sake of clarity, the physical motivation and mathematical formulation of each model component are first individually described in the following subsections; then, the global performance of the model is discussed in detail, particularly with respect to the cyclic lateral response of a pile embedded in a combination of unsaturated and saturated sand layers.

3 .1. Impact of gap modelling features on $p - y$ response

The model components displayed in Figure IV.5 are hereafter described in light of the following remarks:

- all relevant internal variables (such as the maximum displacement ever experienced at one location, y_{max}) are defined independently for each side of the pile, and denoted by above-mentioned subscripts L and R;
- at a given soil depth, the size of the gap opening is determined by the pile displacement history, and assumed to coincide with the interval $[y_{L,max}, y_{R,max}]$, which is updated every time either $y_{L,max}$ or $y_{R,max}$ varies;
- under general cyclic loading conditions, the gap spring is switched on/off depending on whether the pile and the soil are or are not in contact. On each side of the pile, pile-soil contact results in deactivation of the gapping spring, which is then re-activated when pile-soil separation occurs again (on the corresponding side).

Regarding the third item in the above list, the response of the gap spring is computed according to the following geometrical cases:

1. the pile and the soil are in contact on the right side (i.e., $y = y_{R,max}$ and the right gap spring is inactive), hence, upon rightward loading, the left side of the pile lies inside the gap while $y > y_{L,max}$;
2. the pile and the soil are in contact on the left side (i.e., $y = y_{L,max}$ and the left gap spring is inactive), hence, upon leftward loading, the right side of the pile lies inside the gap while $y < y_{R,max}$;
3. both sides of the pile are within the gap, i.e., $y_{L,max} < y < y_{R,max}$.

The interaction elements in Figure IV.5 are hereafter individually described in the following order: (i) separation spring, (ii) closure spring, and (iii) combination of drag and memory springs. Note that, although presented last in what follows, the (novel) features of the memory element are identical to those of the memory-enhanced $p - y$ model described in Section 2 for piles in dry or saturated sand – with only some minor differences related to the adjusted limit resistance p_u ($p_{u,m}$ in the gapping $p - y$ model) in the presence of the additional drag spring. Using the model requires the calibration of the nine parameters listed in Table IV.2, which is further discussed in the following section.

Separation spring

Due to the occurrence of pile-soil separation during gapping, soil reaction curves for piles in unsaturated sand are known to exhibit certain unique features, such as a sharp unloading branch in force-displacement plane – precisely at the onset of the separation stage (Figure

	Recommended values/range	Case example in Section 4	Units
CPT-based spring capacity			
p_u	$2.4\sigma'_{v0}D\left(\frac{q_c}{\sigma'_{v0}}\right)^{0.67}\left(\frac{z}{D}\right)^{0.75}$	$0.34\sigma'_{v0}D\left(\frac{q_c}{\sigma'_{v0}}\right)^{0.67}\left(\frac{z}{D}\right)^{0.75}$	[N/m]
memory spring			
$p_{u,m}$	$(1-C_d)p_u$		[N/m]
α	$8.9\left(\frac{z}{D}\right)^{-1.26}\left(\frac{\sigma_{v0}-u_g}{\sigma'_{v0}}\right)^{0.5}$		[-]
m	0.9999…99 → 1.0	0.5	[-]
μ_0	to be calibrated	$7.7\times10^4\exp\left\{6\frac{\bar{\sigma}'_0-\bar{\sigma}_{ref}}{\bar{\sigma}_{ref}}\right\}$	[-]
separation spring		(deactivated)	
α_{sp}	$0-5$	0	[-]
β_{sp}	$>10^6$	-	[-]
M_{sp}	$p_M^{cur}/p_{u,m}$	-	[-]
drag spring		(deactivated)	
C_d	0-1	0	[-]
$p_{u,d}$	$C_d p_u$	-	[N/m]
closure spring			
m_c	0.6	0.5	[-]
α_c	20	$-\ln(0.15)/(0.55)^{m_c}$	[-]

Table IV.2: Gapping $p-y$ model parameters along with their suggested range (for preliminary calibration) and calibrated values for the field test results in Section 4 – the recommended values in the second column for p_u, α, and m are based on Suryasentana and Lehane, 2016. $\bar{\sigma}'_0$ represents the in-situ mean effective stress, while $\bar{\sigma}_{ref}$ = 100 kPa is a reference pressure. For case example in Section 4 , identical memory spring parameters have been set both above (unsaturated soil) and below (saturated soil) the assumed water table depth.

IV.4). This kind of behaviour is enabled by the aforementioned pseudo-cohesion, which tends to limit displacement relaxation in the associated soil reaction curve upon load reduction. Sharper unloading branches are reproduced by the gapping $p-y$ model for unsaturated conditions via a dedicated separation spring that is set in parallel with the memory element, and stiffens during unloading (i.e., when $|y|$ decreases with respect to $|y_{max}|$) to induce a globally stiffer unloading-reloading response. From a mathematical standpoint, the separation spring stiffness K_{sp} is expressed as follows – recall that the separation and the memory elements share the same displacement y_s (Table IV.1) as parts of the combined 'soil spring':

$$K_{sp} = \begin{cases} 0 & y_s = y_{s,max} \\ M_{sp}\alpha_{sp}K_{50}\left[1 - \dfrac{1}{\beta_{sp}\left(\frac{y_{s,max}-y_s}{z}\right)^2 + 1}\right] & |y_s| < |y_{s,max}| \end{cases} \tag{IV.18}$$

where z is the soil depth, K_{50} is the stiffness of the parallel memory spring at $p = 0.5p_{u,m}$, while α_{sp}, M_{sp}, and β_{sp} are scalar factors to be calibrated.

In summary, the separation spring has only two possible response modes: (i) it is inactive when $y_s = y_{s,max}$, i.e., when the pile and the soil are (or go back to be) in contact; (ii) it stiffness progressively for increasing $|y_s - y_{s,max}|$ values (pile-soil separation) up to the limiting value of $K_{sp} = M_{sp}\alpha_{sp}K_{50}$. M_{sp} is a stiffness multiplier factor always larger than 1, which aims to preserve the same relative contribution to the soil reaction of the separation and memory springs during the whole loading history – note that the memory spring will gradually stiffen under repeated loading cycles. To this end, M_{sp} is given a value that represents the intensity of the memory mechanism (e.g., the current size of the memory locus normalised by the memory spring capacity – i.e., $p_M^{cur}/p_{u,m}$) each time that the separation spring is activated, which happens upon the transition from $y_s = y_{s,max}$ to $|y_s| < |y_{s,max}|$.

In addition to stiffening the unloading-reloading response of the soil element, the stiffness of the separation spring also works to limit the reaction force of the memory element when $|y_s| < |y_{s,max}|$ – i.e., when a certain side of the pile is moving inside the gap. With such a reaction limitation it is effectively possible to inhibit the evolution of the internal variables $p_{\alpha,M}$ and p_M associated with the memory mechanism (see Equations IV.17-IV.16)). This is in fact a desirable feature for this component of the soil reaction, since the soil fabric changes (e.g., densification) induced by cyclic loading – and phenomenologically described through the memory mechanism – are mostly driven by plastic straining, which evolves differently depending on whether the pile and the soil are or are not in contact.

The impact of the separation stiffness on the cyclic response of the soil element is illustrated in Figure IV.6a. The response of the soil spring for $\alpha_{sp} = 0$ is presented in blue, in which case the soil element reduces to the sole memory component; in contrast, the red curve represents the case of $\alpha_{sp} = 2$. Increasing values of α_{sp} lead to a stiffer soil spring response inside the gap, accompanied by a reduced contribution of the memory component

(red dotted line versus blue solid line). Under repetitive cycling, and depending on the selected μ_0 value, the unloading stiffness of the soil spring will naturally increase in time – see Figure IV.2 – up to reproducing the desired sharp unloading response that emerges from pile-soil gapping. In such cases, setting $\alpha_{sp} = 0$ may be assumed as an easier calibration option, considering though that memory effects will invariably develop regardless of pile-soil contact/separation.

Closure spring

The inclusion of the so-called closure spring is needed to simulate the peculiar shape (resembling an inverted S) of the stress-strain response cycles in the presence of cohesive soil behaviour (Boulanger et al., 1999) – also shown in Figure IV.4. To reproduce mathematically such a shape, the following function – similar to Equation IV.1 – is adopted to relate, in finite terms, the reaction component in the closure spring (p_c) to the corresponding displacement (y_g, i.e., the overall gap spring displacement):

$$p_c = p_{c,max}\left(e^{-\alpha_c\left|\frac{y_g - y_{g,0}}{y_{max}}\right|^{m_c}}\right) \tag{IV.19}$$

where m_c and α_c are dimensionless shape parameters, while $y_{g,0}$ assumes the current value of y_g every time the pile re-enters the gap from a new y_{max} ($y_g - y_{g,0} = 0$, when also $p_c = p_{c,max}$). On each side of the pile, y_g and p_c evolve independently, as implied by the sketch in Figure IV.5. Independent on each side is also the update of the internal variables ($y_{L-R,max}$, $y_{g,L-R,0}$, $p_{c,L-R,max}$), which occurs as follows when a cross-section of the pile at a given depth re-enters the gap (upon unloading) after the attainment of a new maximum y value, y_{max}:

$$\begin{aligned} &y_{g,R,0} = y_{g,R} \quad || \quad y_{g,L,0} = y_{g,L} && (a)\\ &y_{R,max} = y \quad || \quad y_{L,max} = y && (b)\\ &p_{c,R,max} = p_{g,R} \quad || \quad p_{c,L,max} = p_{g,L} && (c) \end{aligned} \tag{IV.20}$$

When re-entering the gap after a new maximum displacement y_{max}, also the reactions associated with the gap spring components (drag and separation) are re-initialized ($p_d = p_{sp} = 0$, $p_{c,max} = p_s = p_m$), where p_m is the reaction component in the memory element – this happens because an update of y_{max} alters the gap geometry and resets its constitutive description. As suggested from field data and discussed in Section 4 .3, Equation (IV.19) implies that the average closure spring stiffness decreases with increasing $|y_{max}|$; this feature can be easily overridden by replacing y_{max} with $y_{g,0}$ in the denominator of the exponent in Equation (IV.19). From an implementation standpoint, it is worth noting that the updated value of $p_{c,max}$ can be lower than its value in a previous geometrical configuration of the gap (i.e., with different value of $|y_{max}|$).

Typical reaction-deflection responses resulting from the series combination of the closure spring and the soil element is shown in Figure IV.6b for different values of the α_c and α_{sp} parameters and $\beta_{sp} = 10^5$. The formulation of the closure spring ensures that upon unloading from $p_c = p_{c,max}$, the closure spring reaches a nil asymptote ($p_c = 0$) as fast as enabled by the selected pair of m_c-α_c values, so as to reproduce the desired S-shape of the $p-y$ response. Ideally, the gap shape parameters should be identified against back-calculated cyclic $p-y$ curves from pile loading tests in soil exhibiting cohesive behaviour (e.g., due to unsaturated conditions). Values such as $m_c = 0.6$ and $\alpha_c = 20$ seem to provide a reasonable closure response for a sharp pile-soil separation, and can be henceforth considered as a first-guess parameter calibration.

Combined memory and drag springs

To properly capture cyclic pile-soil interaction in the presence of gapping, a $p-y$ model should also be able to reproduce the frictional resistance offered by the side soil wall when normal contact is lost on one or both sides of the pile – see in Figure IV.6d the relevant resisting mechanisms for a pile moving from $y_{L,max}$ towards $y_{R,max}$. Frictional drag (side pile-soil friction, introduced via the drag spring) resists pile motion regardless of the pile location and displacement direction within the gap area. Conversely, the passive soil resistance (from the memory spring) manifests itself only when the pile is acting to enlarge the gap – i.e., when the pile displacement y equals either $y_{L,max}$ (with $\dot{y} < 0$) or $y_{R,max}$ (with velocity $\dot{y} > 0$). Frictional drag is incorporated in the proposed model by setting the closure spring in parallel with a drag spring, in a fashion similar to that proposed by Boulanger et al., 1998.

In light of the chosen setup of the separation and gap springs, the resulting gapping $p-y$ model (left + right sides) will respond to, e.g., a rightward monotonic load as follows:

1. the $p-y$ element on the right opposes the pile deflection through the memory spring exclusively ($y_{R,max} = y_{max}$) – in fact, no additional resistance is offered by the (deactivated) gap and separation springs when the pile and the soil are in contact;

2. on the left side, the soil reaction is almost completely provided by the drag spring, since the flexibility of the overall soil element (memory + separation springs) is nearly nil when the separation spring is active (for rightward monotonic loading, when $y_{L,max} = 0 < y$). Additionally, the closure spring is practically inactive under these conditions, since the associated reaction already lies on its nil asymptote ($p_{c,max} = 0$).

In conclusion, for monotonic loading, the set of soil reactions in the presence of a gap includes the memory and drag reactions on the 'passive' and 'active' sides, respectively – clearly, the attribute of passive or active side depends on the direction of the external lateral load.

A desirable feature of the overall $p-y$ formulation is to ensure perfect compatibility between the model responses obtained with and without gap modelling. Such compatibility is ultimately guaranteed by combining, when gapping is enabled, the following monotonic

responses of the memory and drag springs, which is altogether equivalent to the original *SL* formulation – see Equation (IV.1):

$$p_d = p_{u,d}\left[1 - \mathrm{e}^{-\alpha\left(|y_g - y_g^r|/D\right)^m}\right] \tag{IV.21}$$

$$p_m = p_{u,m}\left[1 - \mathrm{e}^{-\alpha|y_s/D|^m}\right] \tag{IV.22}$$

where $p_{u,d} = C_d\, p_u$ and $p_{u,m} = (1 - C_d)\, p_u$, while $y_g^r = y_g$ is updated at every sign reversal of $\dot{y}_g$ (at the beginning of the analysis, the initialisation $y_g^r = y_g = 0$ is set). C_d is a scalar parameter that can be tuned between 0 and 1 to modulate the relative contribution of the drag reaction to the total lateral soil resistance. Since during monotonic rightward loading the two springs share the same displacement value (as discussed above, $y_{s,R} = y_{g,L} = y$), then Equation (IV.1) results exactly from the sum of the p_d and p_m reactions. The calibration of the drag and memory reaction parameters requires only the additional identification of C_d, since p_u, α, and m can be obtained through the CPT-based procedure proposed by Suryasentana and Lehane, 2016 (Equation(IV.2)). The impact of C_d on the response of the right/left spring component is illustrated in Figure IV.6c

The implications of the above modelling assumptions are visualised in Figure IV.7, which illustrates the response of the complete $p-y$ scheme in Figure IV.5 to displacement-controlled two-way loading (with $N = 2$ loading cycles). Figure IV.7d confirms that the monotonic response of the gapping $p-y$ model is coincident with the target *SL* formulation – see the performance of distinct model components in Figures IV.7a-IV.7b, where red/black solid lines and dots are used to illustrate the responses of the right/left soil and gap springs, respectively. When the maximum reaction value is achieved during the first monotonic loading branch (point A in Figure IV.7d), the component from the right soil spring is at the level A_R (Figure IV.7c), while the left drag and soil springs are at the levels $A_{d,L}$ and $A_{s,L}$, respectively. This outcome is in agreement with previous statements, i.e., no contribution from the right gap spring and left closure spring, plus minimal contribution from the left soil element. Finally, Figure IV.7c displays the contributions of the left and right spring components, which provide altogether ($y_L = y_R = y$ and $p_L + p_R = p$, Table IV.1) the unsaturated $p-y$ response shown in Figure IV.5.

After establishing suitable working principles for the memory and drag springs under monotonic loading, their extension to cyclic loading conditions is relatively straightforward. The cyclic response of the memory spring results from the evolution of the memory-enhanced hardening modulus in Equation (IV.15), according to the same bounding surface formulation described in Section 2 – the calibration of the ratcheting control parameter μ_0 is likewise required. On the other hand, the desired cyclic response of the drag element is shown in Figure IV.8 to exhibit some different features in comparison to the cyclic memory spring. The cyclic rules given below are applicable to both left and right drag springs, except for the signs of relevant inequalities (< or >) (they are opposite on the two sides of the

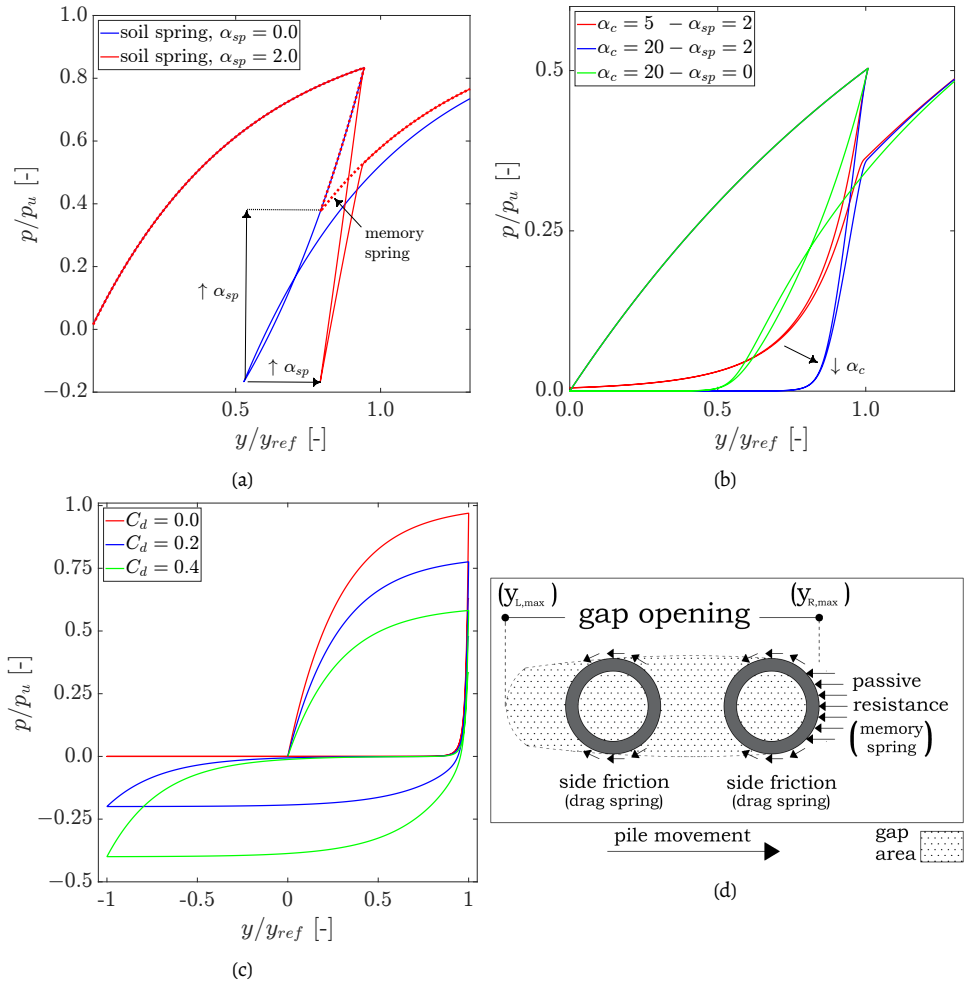

Figure IV.6: Impact of (a) the separation spring, (b) the closure spring, and (c) the drag spring on the cyclic soil reactions in the presence of pile-soil gapping. Spring calibration settings in (a), (b), and (c) are same as reported in Figure IV.2 unless mentioned otherwise. (a) shows the role of the separation spring – in parallel with the memory spring (Figure IV.5). Solid and dotted lines denote the (global) soil and (individual) memory spring responses, respectively – note that for $\alpha_{sp} = 0$, the soil component reduces to the soil memory spring ($\mu_0 = 0$, $\beta_{sp} = 10^5$). Arrows (↑) highlight the impact of an increasing α_{sp} value on the soil spring response; (b) illustrates the role of the closure spring – in series with the soil spring (Figure IV.5) for different values of α_c and α_{sp} ($m_c = 0.6$, $\mu_0 = 10$); (c) clarifies the influence of the C_d parameter on the gapping response of the $p - y$ model (either right or left component) under displacement-controlled cyclic loading ($\alpha_{sp} = 2$, $m_c = 0.6$, $\alpha_c = 20$, $\mu_0 = 10$); (d) depicts the soil resistance mechanisms against rightward motion (from $y_{L,max}$ to $y_{R,max}$) for a pile in unsaturated sand.

pile – for brevity, only the right drag spring is considered below). In Figure IV.8, the cyclic response of a drag spring (right side of the pile) is displayed starting from a configuration with pile-soil contact ($y_g - y_g^r = 0$), then under cyclic loading within the gap ($y_g - y_g^r < 0$), – e.g., ($y_g - y_g^r > 0$) for the left spring component, and finally towards gap re-closure ($y_g - y_g^r = 0$). A

IV

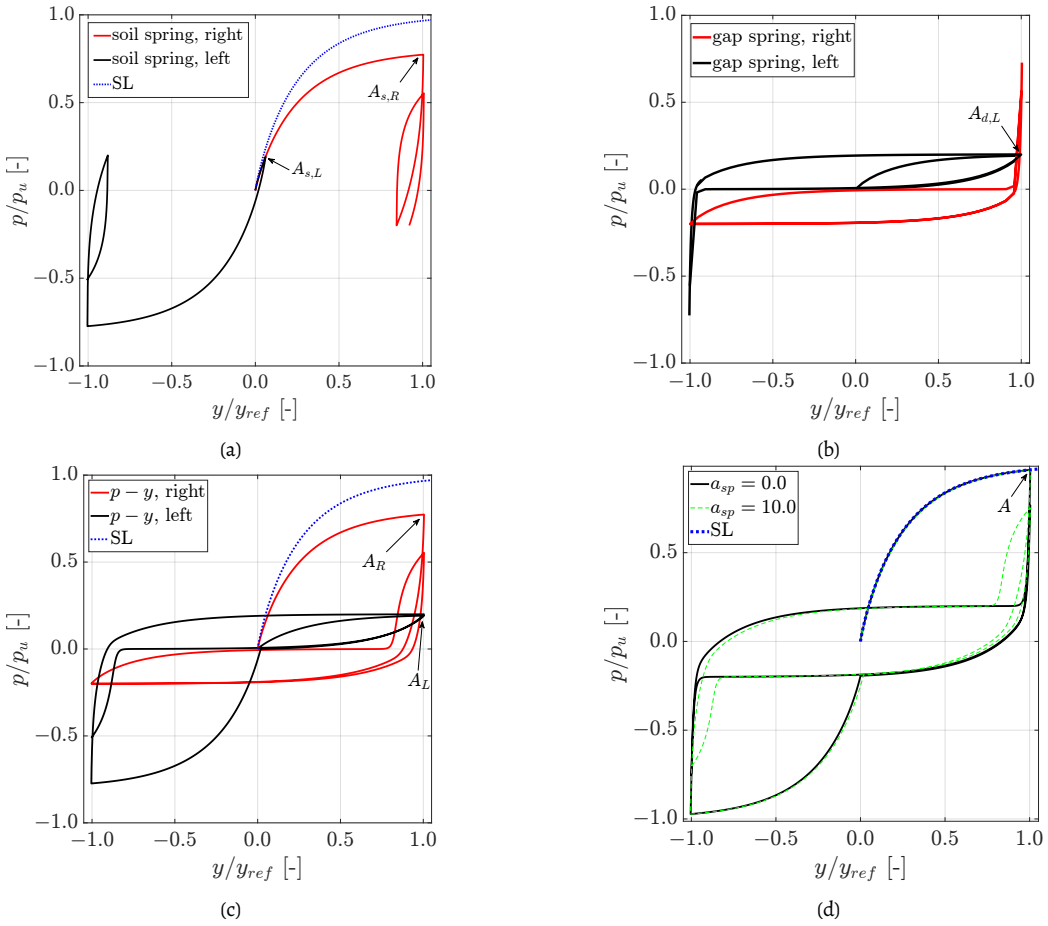

Figure IV.7: Force-displacement response to $N = 2$ displacement-controlled cycles. The unsaturated $p-y$ spring is presented in (d) after its sub-components in (a), (b), and (c). Black and red colours denote the response of the L and R interaction elements in Figure IV.5, while blue is used for the monotonic response of the overall $p-y$ spring with total capacity equal to p_u. In (d), the impact of the separation spring stiffness on the global response is shown in green. Points A denote the occurrence of the peak monotonic load in the global $p-y$ spring (d) and its sub-components (a-c). Relevant parameters are the same as reported for Figure IV.2, along with: $C_d = 0.2$, $\alpha_c = 60$, $\alpha_{sp} = 0$, $\mu_0 = 10$)

requirement introduced by separately modelling the left and right sides of the pile is the need for the drag reaction to precisely meet the values $p_d = 0$ and $y_g - y_g^r = 0$ upon complete re-closure – i.e., upon pile-soil contact the drag spring (on the contact side) does not oppose any resistance, while the closure spring resists with $p_c = p_{c,max}$. The described drag reaction mechanism (right spring component) can therefore be calculated according to the following possible cases:

– $\dot{y}_g < 0$, i.e., pile moving along the gap-opening path ($r_1 \rightarrow r_2$ in Figure IV.8);

– $\dot{y}_g > 0$, i.e., pile re-closing the gap (towards the origin $(y_g - y_g^r \to 0)$ – $r_2 \to r_3$, $r_4 \to r_0$);

– $\dot{y}_g = 0$, no force increment.

$$p_d = \begin{cases} (\dot{y}_g < 0) & (a) \\ p_d^r + \mathrm{sgn}(\dot{y}_g) \cdot \left[p_{u,d} - |p_d^r| \right] \left[1 - \mathrm{e}^{-\alpha \left| (y_g - y_g^r)/D \right|^m} \right] & \\ (\dot{y}_g > 0) & (b) \\ p_d^r + \mathrm{sgn}(\dot{y}_g) \cdot p_{u,d} \left[1 - \mathrm{e}^{\alpha_d^r \left| (y_g - y_g^r)/D \right|^m} \right] & \\ (\dot{y}_g = 0) & (c) \\ p_d & \end{cases} \tag{IV.23}$$

in which the internal variables p_d^r and y_g^r, represent the drag reaction and displacement at the last load reversal. Entering the gap from $y = y_{max}$ resets p_d^r and $y_g - y_g^r$ to zero (i.e., $y_g^r = y_g$). For $\dot{y}_g < 0$, the shape parameter α is replaced by α_d^r (< 0) as,

$$\alpha_d^r = \frac{\ln\left(1 - |p_d^r|/p_{u,d}\right)}{(|y_g^r|/D)^m}$$

which is updated when the displacement direction changes from $\dot{y}_g > 0$ to $\dot{y}_g < 0$ (i.e., instances r_2, r_4), following the simple procedure described in 5 to ensure that a nil drag reaction results (i.e., $p_d = 0$) when $(y_g - y_g^r) = 0$. This choice determines the specific path from r_4 to r_0 in Figure IV.8 – particularly, the use of α_d^r ensures that the drag spring is perfectly re-closed when the r_0 point is achieved).

3 .2. From gapping $p - y$ model performance to cyclic pile response

The cyclic performance of the complete gapping $p-y$ model is exemplified in Figures IV.9 and IV.10 with reference to force-controlled two-way and one-way cyclic loading, respectively. For the former case, the impact of the drag spring capacity is explored by setting $C_d = 0.1$ (Figures IV.9a-b-c) and $C_d = 0.25$ (Figure IV.9d-e-f), while all other parameters are identical regardless of C_d. Evidently, the particular repartition of the identical ultimate capacity (at the level of the whole gapping $p-y$ model) over the memory and the drag springs has a significant impact on the observed global response, particularly on the displacement accumulation behaviour (Figures IV.9c-IV.9f) – $p_{u,m} = 0.9p_u$, $p_{u,d} = 0.1p_u$ in Figure IV.9c, and $p_{u,m} = 0.75p_u$, $p_{u,d} = 0.25p_u$ in Figure IV.9f. It is expected that larger drag resistance should result in less displacement accumulation, since the work of the applied loads will be increasingly spent against the pile-soil drag resistance, rather than to enlarge the gap opening. The model

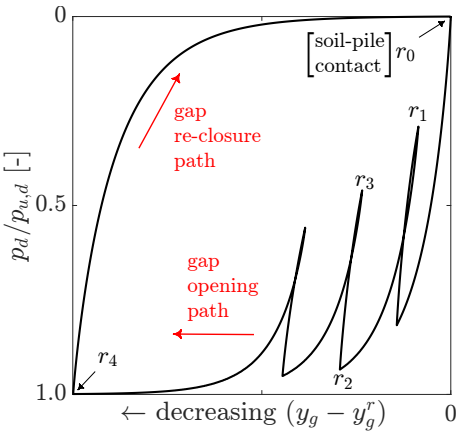

Figure IV.8: Response of the right drag spring component (for the left drag spring $y_g - y_g^r$ would also be zero upon pile-soil contact, though increasing towards the inner part of the gap) to cyclic loading – all relevant parameters (m, α, D) set as for Figure IV.2.

naturally captures this aspect through the influence of the drag coefficient C_d – in essence, a capacity repartition parameter – on the stress paths within the soil and gap springs.

For the case of one-way cyclic loading, the gapping $p-y$ response is illustrated in Figure IV.10, which displays the outcome of combining all the modelling features for gapping and ratcheting control described above. In Figure IV.10a the response of the soil springs can be observed (the separation springs are deactivated by setting $\alpha_{sp} = 0$, so that the soil springs reduce to the sole memory springs). In the same figure, a small contribution of the memory spring is shown for the left side of the pile, which would further decrease for larger α_{sp} values – cf. to Equation (IV.18). As a next step, Figure IV.10b illustrate the response of the global left and right $p-y$ springs: on the left side, the observed deformation is to be mainly attributed to the drag spring, since (i) the deformability of the soil spring is limited (cf. to Figure IV.10a), and (ii) within the gap spring, the closure spring opposes no resistance as $p_{c,L,max} = 0$. Finally, the global response of the whole gapping $p-y$ spring is depicted in Figure IV.10c.

The response to lateral cyclic loading of the tubular steel pile in Figure IV.11a was simulated through a 1D FE model endowed with the complete gapping $p-y$ model described in this section. The FE model set-up is identical to that presented in Section 2 .3 (Figure IV.3a) and, similarly, the assumed soil profile features a linearly increasing cone resistance $q_c = 5 + 2z$ [MPa] with a uniform distribution of the ratcheting parameter $\mu = 20$ along the depth z. The following additional parameters values were chosen to complete the calibration of the gapping $p-y$ model: $C_d = 0.1$, $\alpha_{sp} = 0$, $m_c = 0.5$, $\alpha_c = 10$. The transition from unsaturated to saturated soil conditions (i.e., location of the water table) was arbitrarily set at $z = 4$ m, and therefore gapping $p-y$ springs (on both sides of the pile) and non-gapping memory springs (on one side only) were distributed over the depth intervals $z = 0-4$ m and $z = 4-8$ m,

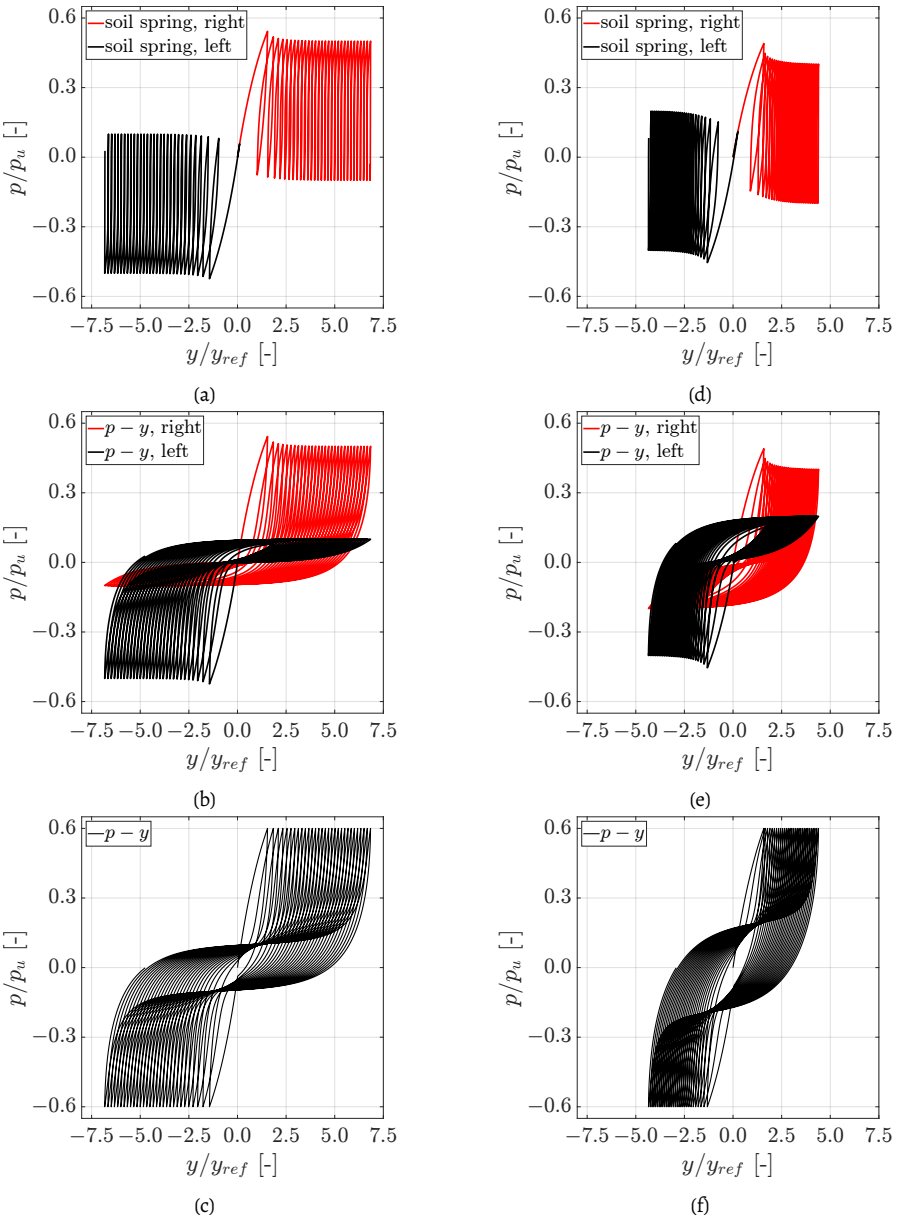

Figure IV.9: Force-displacement response to $N = 30$ force-controlled two-way cycles for (a-b-c) $C_d = 0.1$ and (d-e-f) $C_d = 0.25$. For both cases, the global $p-y$ response is presented in (c) and (f) after the soil sub-components (soil springs) in (a) and (d), and the global left and right components in (b) and (e). Black and red colours denote the responses of the left and right interaction elements in Figure IV.5. Relevant model parameters are the same as reported for Figure IV.2, along with: $C_d = 0.1/0.25$, $\alpha_{sp} = 0$, $\alpha_c = 5$, $m_c = 0.6$, $\mu_0 = 20$).

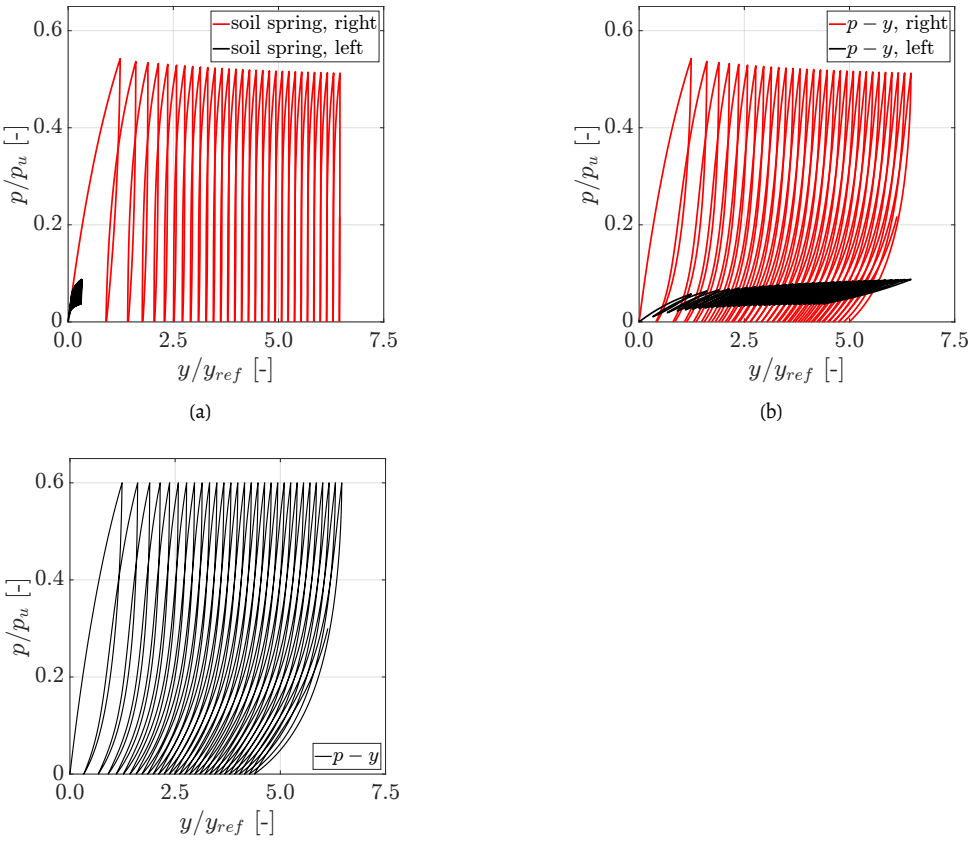

Figure IV.10: Force-displacement response to $N = 30$ force-controlled one-way cycles. The global $p - y$ response is presented in (c) after the soil sub-components (soil springs) in (a), and the global left and right components in (b). Black and red colours denote the responses of the left and right interaction elements in Figure IV.5. Relevant model parameters are the same as reported for Figure IV.2, along with: $C_d = 0.1$, $\alpha_{sp} = 0$, $\alpha_c = 5$, $m_c = 0.6$, $\mu_0 = 50$).

respectively. The resulting pile response is shown in Figure IV.11. The impact of the unsaturated zone on the lateral pile response (especially under 2-way loading) is very evident – cf. to Figures IV.11 and IV.3c). The calculated 1-way response compares well (qualitatively) with the field data presented in (Kementzetzidis et al., 2023a), and captures the data discussed in Section 4 for the reference impact-driven pile. For 2-way loading, the calculated response in Figure IV.11c can reproduce the global S-shaped response loops that are observed for piles in cohesive soils, and is largely consistent with the general experimental observations of Suzuki and Nakai, 1985. In this regard, it is also worth noting that the tangent stiffness associated with the pile head response tends to increase under cycling during stages of pile-soil contact as consequence of the ratcheting control mechanism, while the occurrence

		Test piles	Reaction pile
Total length	L	10 m	10 m
Embedded length	L_e	8 m	8 m
Outer diameter	D	0.762 m	1.6 m
Wall thickness	h	1.59 cm	2 cm

Table IV.3: Geometrical specifications for the reference test pile.

of gapping – and the gradual enlargement of the gap size – determine a reduction of the average (or secant) stiffness.

4 . Comparison to field measurements

In this section, the performance of the proposed $p-y$ formulation is evaluated against the results of a lateral pile loading field test performed on a 10m-long tubular steel pile – see all geometrical specifications in Table IV.3. The field measurements considered herein were recorded during the experimental campaign associated with the Gentle Driving of Piles (GDP) project (Metrikine et al., 2020; Tsetas et al., 2023), namely at the sandy site Maasvlakte II located at the port of Rotterdam. The reference pile was impact hammered on November 4 2019 down to a target depth of 8 m, and then laterally loaded on December 9 with an eccentricity $e = 1$ m above the ground surface. The lateral loading test was performed using a custom-built load frame in combination with a larger/stiffer reaction pile. The pile was instrumented with fiber Bragg grating (FBG) sensors at multiple locations, which enabled to obtain the bending moment profiles discussed later on. Further details regarding pile instrumentation, loading equipment, and test setup are provided by Kementzetzidis et al., 2023a; Tsetas et al., 2023. Prior to pile installation, a comprehensive site investigation was carried out (Tsetas et al., 2023), including borehole sampling and Seismic CPTu (SCPTu) tests (target depth: 10 m). The soil deposit was found to mainly comprise medium-dense to very dense sand ($D_r = 60-100\%$ – with an overall negative D_r depth-gradient), with a water table located about 4 m below the ground surface. Profiles at the reference pile location of cone resistance (q_c) and soil's relative density (D_r) (obtained based on Jamiolkowski et al., 2003) are shown in Figure IV.12a.

4 .1. Cyclic/dynamic lateral loading programme

The reference pile was subjected to the cyclic/dynamic loading programme illustrated in Figure IV.12b, which lasted approximately 40 hours and featured a total amount of loading cycles equal to $N = 82000$. Some of the cycles were applied with relatively large amplitude at constant/low frequency (black parcels in Figure IV.12b), with interleaved stages of small-amplitude loading at variable frequency (henceforth referred to as dynamic 'frequency sweeps' or 'f-sweeps' – grey parcels in Figure IV.12b). Each load parcel was defined by

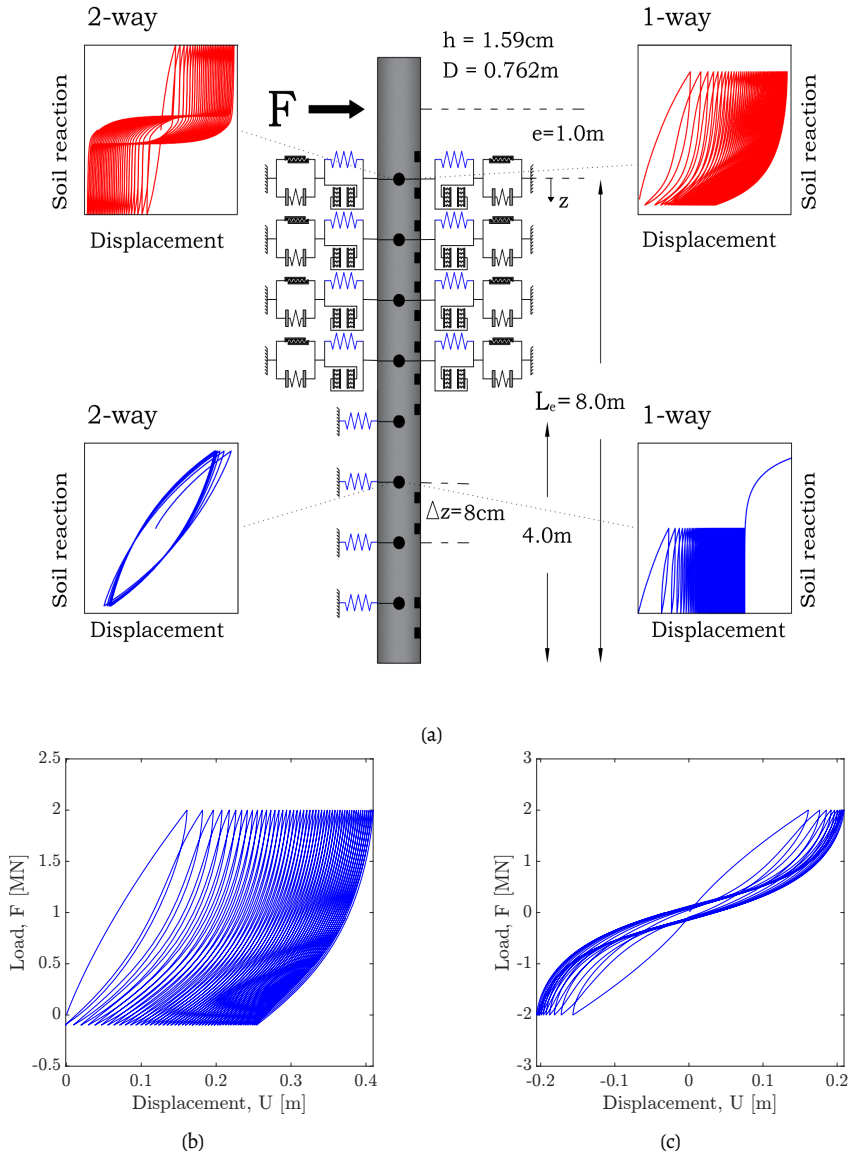

Figure IV.11: (a) Reference pile subjected to lateral cyclic loading: typical one-way vs two-way response of the soil reaction springs in agreement with the proposed gapping $p - y$ formulation with ratcheting control. The black rectangular symbols indicate the locations of the FBG sensors mentioned in Section 4 . Simulated load-displacement pile response at ground surface to (b) one-way and (c) two-way cyclic loading ($N = 50$ loading cycles) for the reference pile in (a).

superimposing a mono-harmonic excitation of amplitude F_{cyc} and frequency f onto an average load level F_{av}:

$$F(t) = F_{av} + F_{cyc} \times \sin(2\pi f t) \tag{IV.24}$$

In particular, each low-frequency cyclic parcel ($a-e$ in Figure IV.12b) comprised $N = 1000$ cycles; the 16 f-sweeps featured $N = 4800$ cycles applied at a constant/low amplitude of $F_{cyc} = 2.5$ kN, while the loading frequency was increased from 0.1 Hz to 4 Hz with increments of 0.1 Hz every 120 cycles. All the loading settings associated with Equation (IV.24) and Figure IV.12b are summarised in Table IV.4. All lateral loading parcels were applied with $F_{av} > F_{cyc}$, which corresponds with so-called 'one-way' loading (i.e., with no load sign reversals). The remainder of this work will focus on lateral pile-soil interaction under relatively large loading cycles (parcels $a-e$ in Figure IV.12b), under the assumption that the impact of small-amplitude vibrations on the lateral ratcheting and gapping of the pile may be disregarded as shown in (Kementzetzidis et al., 2023a).

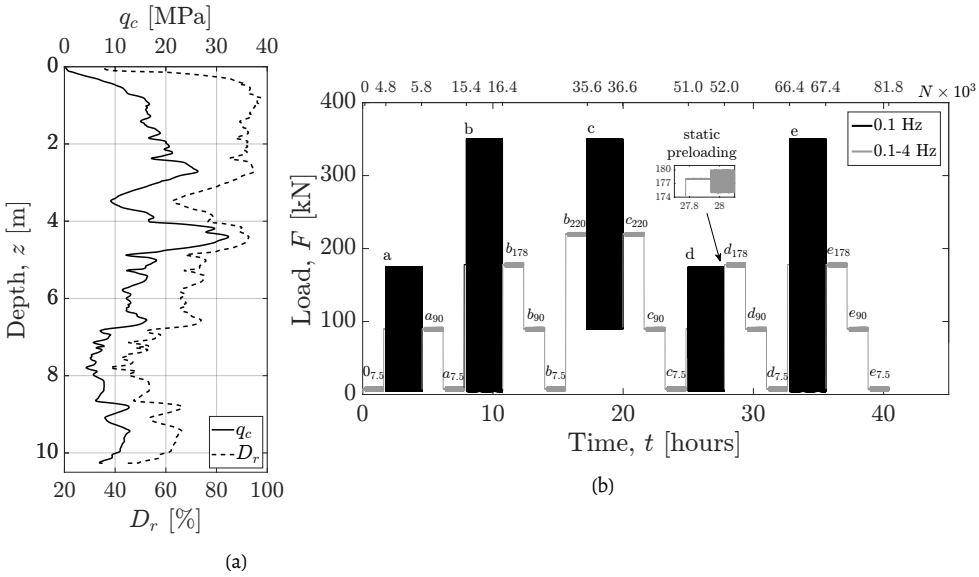

Figure IV.12: Profiles of cone resistance (q_c) and relative density (D_r) at the pile location in (a), and in (b) cyclic/dynamic loading programme. Load amplitudes are provided against time (bottom axis) and number of cycles (top axis). Cyclic load parcels ($a-e$, 1000 cycles per parcel) and dynamic f-sweeps ($a-e_{7.5,\ldots,220}$, 4800 cycles per sweep) are shown in black and grey, respectively – see loading specifications in Table IV.4.

4 .2. Impact of unsaturated soil conditions on cyclic pile response

Due to the frequent rainfalls in the Rotterdam area, the shallowest soil at the Maasvlakte II site was unsaturated, which had a clear impact on the recorded pile response in that it enabled pile-soil gapping under cyclic loading. In a related study, Kementzetzidis et al.,

-	F_{av} [kN]	F_{cyc} [kN]	f [Hz]	$N \times 10^3$
$0_{7.5}$	7.5	2.5	0.1-4	4.8
a	**90**	**85**	**0.1**	**1**
a_{90}	89.5	2.5	0.1-4	4.8
$a_{7.5}$	7.5	2.5	0.1-4	4.8
b	**177.5**	**172.5**	**0.1**	**1**
b_{178}	177.5	2.5	0.1-4	4.8
b_{90}	89.5	2.5	0.1-4	4.8
$b_{7.5}$	7.5	2.5	0.1-4	4.8
b_{220}	219.5	2.5	0.1-4	4.8
c	**220**	**130**	**0.1**	**1**
c_{220}	219.5	2.5	0.1-4	4.8
c_{90}	89.5	2.5	0.1-4	4.8
$c_{7.5}$	7.5	2.5	0.1-4	4.8
d	**90**	**85**	**0.1**	**1**
d_{178}	177.5	2.5	0.1-4	4.8
d_{90}	89.5	2.5	0.1-4	4.8
$d_{7.5}$	7.5	2.5	0.1-4	4.8
e	**177.5**	**172.5**	**0.1**	**1**
e_{178}	177.5	2.5	0.1-4	4.8
e_{90}	89.5	2.5	0.1-4	4.8
$e_{7.5}$	7.5	2.5	0.1-4	4.8

Table IV.4: Loading specifications for the cyclic/dynamic field tests – cf. to Figure IV.12b, Equation IV.24.

Type	Sylex FFA-01
Number of sensors	24 (12 per side)
Measurement range	±3000 m/m
Wavelength range	1510 nm - 1590 nm

Table IV.5: Technical specifications of FBG strain sensors.

2023a inferred a maximum gap depth of approximately 4 m (i.e, as deep as the water table) by examining the measured bending moment profiles. Qualitatively, the experimental one-way cyclic response of the test pile in Figure IV.13a recalls the simulated cyclic behaviour of a pile supported by the proposed gapping $p-y$ model – cf. to Figure IV.11, but note that the $p-y$ parameters initially assumed in Section 3 .2 are not representative of the specific soil conditions at the Maasvlakte II site. In both cases, the tangent stiffness (K_{tang}) is severely affected by the distance to the maximum lateral displacement ever experienced (which is an approximate measure of the gap opening), as typically observed for cyclically loaded piles in the presence of a gap. A detailed discussion of all field observations at the Maasvlakte II site may be found in Kementzetzidis et al., 2023a.

Additional light into the field response of the pile can be shed by analysing the lateral soil reactions back-calculated from axial strain measurements). Axial strains were measured via fiber Bragg grating (FBG) sensors – in-line and rosettes, installed at 13 different cross sections along the pile length (see specifications and locations in Tables IV.5-IV.6); at each depth, two sensors were installed at diametrically opposite locations on the external pile surface.

For slender piles, lateral $p-y$ reactions can be derived based on the standard Euler-Bernoulli beam theory – measured axial strains (ϵ_{zz}) can directly be converted into profiles of beam curvature and bending moment (M), which can then be used to obtain the evolution in time of the distributed soil reaction (p) and the corresponding pile deflection (y) at a

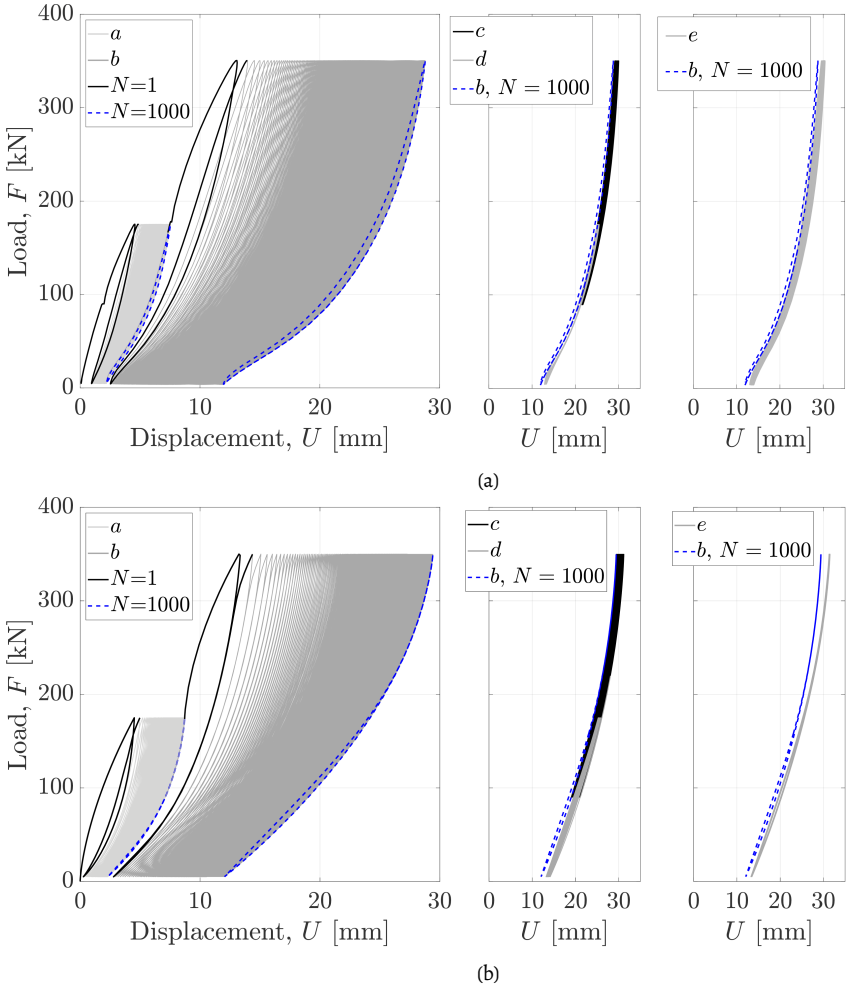

Figure IV.13: Measured (a) and simulated (b) force-displacement pile response at ground level to the load parcels $a-b$ (left), $c-d$ (middle), and e (right) associated with lateral loading programme in Figure IV.4. On the left, the solid black and dashed blue lines denote $N = 1$ and $N = 1000$, respectively; in the middle and right subfigures, the dashed blue lines indicate $N = 1000$ for parcel b.

certain depth. In the absence of inertial effects and axial loads, the following governing relationships hold:

$$M(z,t) = -EI\frac{\epsilon_{zz}(z,t)}{D/2} \tag{IV.25}$$

$$p(z,t) = -\frac{\partial^2 M(z,t)}{\partial z^2} \tag{IV.26}$$

z [m]	-0.37	0.23	0.77	1.30	1.78
	2.25	2.77	3.30	3.80	5.26
	5.77	7.00	7.50		

Table IV.6: FBG sensor locations along the pile length – cf. to Figure IV.11a. Except for the sensor installed at $z = -0.37$ m (rosette type), all sensors are of an in-line type.

$$y(z,t) = -\iint_L \frac{M(z,t)}{EI}\,\mathrm{d}z\,\mathrm{d}z \tag{IV.27}$$

where EI represents the flexural rigidity of the pile, $D/2$ is the distance of the FBG strain sensors from the neutral axis of the beam cross-section, and $p(z,t)$ is the soil reaction. For piles of low L/D ratio, such as that under consideration, the Timoshenko beam theory is known to be more suitable (Timoshenko, 1921) – due to the influence of shear deformations, the bending moment, M, does no longer relate directly to the beam curvature, but rather to the cross-sectional rotation, ϕ (Equation (IV.28)). In contrast, the following set of differential equations may be considered for a pile of uniform flexural (EI) and shear (GA) rigidities:

$$\frac{M(z,t)}{EI} = -\frac{\epsilon_{zz}(z,t)}{D/2} = -\frac{\partial\phi(z,t)}{\partial z} \tag{IV.28}$$

$$p(z,t) = EI\frac{\partial^3\phi(z,t)}{\partial z^3} \tag{IV.29}$$

$$\frac{\partial y(z,t)}{\partial z} = \phi(z,t) - \frac{EI}{\kappa GA}\frac{\partial^2\phi(z,t)}{\partial z^2} \tag{IV.30}$$

where ϕ is the local rotation angle of a given cross-section, and κ a section-specific shear deformation factor – $\kappa = 0.57$ for the thin-walled circular cross-section of the pile at hand (Table IV.3 (Hutchinson, 2001)). The following procedure was adopted to estimate local reaction-deflection responses at arbitrary pile locations, using a finite number of strain measurements along the pile and polynomial fitting of moment profiles:

1. profiles of lateral soil pressure were obtained via double differentiation (Equation (IV.29)) of the bending moment profiles (Equation (IV.28)). A low-order (3rd) polynomial function was adopted for fitting purposes, so as to avoid difficulties associated with the differentiation of higher-order polynomials;

2. the slope of the deformed pile axis, $\frac{\partial y(z,t)}{\partial z}$, was calculated via Equation (IV.30). At this point, a higher-order (5th) polynomial was used to re-fit the moment profiles, which were then integrated to obtain $\phi(z,t)$ (Equation (IV.28)). The necessary integration constant was determined for each loading step by solving an algebraic equation for $\phi(z_0,t)$ (Equation (IV.30)), which requires the measurement of the beam axis slope at a chosen location $z = z_0$, as well as the value of $\frac{\partial^2\phi(z_0,t)}{\partial z^2}$ (obtained via the previous step);

3. finally, soil displacement profiles were obtained by integrating $\frac{\partial y(z,t)}{\partial z}$, with the relevant integration constant obtained by enforcing the measured value of lateral displacement at the ground level.

The strain gauge configuration with a relatively wide spacing of 70 cm (approximately constant along the pile, (Tsetas et al., 2023), see Table IV.6 and Figure IV.11a) rendered the $p-y$ curve identification process quantitatively sensitive to the order of the polynomial fitting functions. Nevertheless, the qualitative features of the back-calculated $p-y$ curves are relatively unaltered by the specific interpolation choices, and are exemplified in Figure IV.14 for a pile location at a depth $z = 0.8$ m and the first 100 cycles of the loading parcel a in Figure IV.12b.

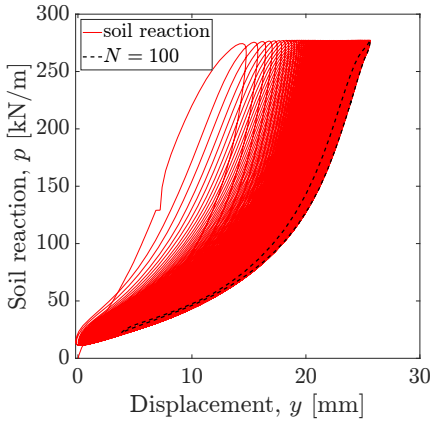

Figure IV.14: Back-calculated soil reaction at depth $z = 0.8$ m for the first $N = 100$ cycles of the loading parcel a in Figure IV.12b

4 .3. 1D modelling of cyclic pile response

The cyclic field response of the reference impact-driven pile was numerically simulated via the same 1D FE model illustrated in Figure IV.11a (previously set up in view of this final simulation exercise). Gapping $p-y$ springs were distributed along the pile from ground surface ($z = 0$ m) down to the estimated depth of the phreatic level ($z = 4$ m), while only memory springs (Section 2) were applied to the lower portion of the pile in saturated sand ($z = 4-8$ m). An inter-spring spacing of 0.08 m was found appropriate to capture the cone resistance profile in Figure IV.12a, as well as to accurately solve the 1D boundary value problem at hand. Since what follows focuses on the pile response to the cyclic/low-frequency parcels in Figure IV.12b (from a to e), inertial effects were deemed negligible. It should also be noted that no additional soil reaction mechanisms were considered in this 1D modelling study, such as distributed moment reactions associated with shear stresses along the pile shaft, and/or shear resistance and moment fixity at the pile base – cf. to the PISA method

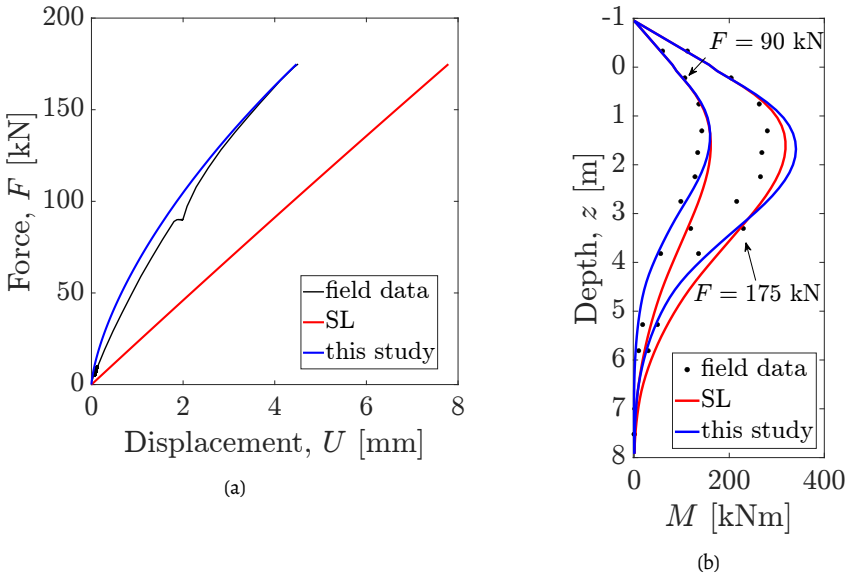

Figure IV.15: Comparison between simulated and measured pile response to the first monotonic loading branch associated with parcel *a* in Figure IV.12b: (a) force-displacement response at ground surface, and (b) moment profiles at two distinct load lateral levels – $F = 90$, 175 kN.

proposed for large-diameter offshore monopiles (Burd et al., 2020; Byrne et al., 2019). Such a choice was justified by (i) the relatively small diameter of the pile (D =0.762 m), (ii) its aspect ratio at the transition between flexible and rigid pile behaviour, and (iii) the lack of fully reliable $q_c \rightarrow D_r$ correlations for the high relative density characterising the shallowest sand layers at the Maasvlakte site (Figure IV.12a, Kementzetzidis et al., 2023a) – this factor would have added further uncertainty to the calibration of additional soil reaction mechanisms using the D_r-based PISA correlations (Burd et al., 2020).

To simulate the cyclic response of the reference test pile, all $p-y$ model parameters must be first calibrated. Although $p-y$ reaction curves back-calculated from measured strain data could ideally have supported such endeavour, the abovementioned uncertainties in the interpolation of moment profiles discouraged the use of strain data for quantitative parameter calibration.

An initial calibration trial was conducted by applying the CPT-based procedure by Suryasentana and Lehane, 2016 (Equation (IV.2)†) to the first monotonic pile response branch associated with parcel *a* in Figure IV.12b – i.e., with the lateral load F ranging from 0 to 175 kN. Using the suggested calibration procedure, both $p-y$ (for saturated sand) and memory springs were calibrated (only p_u, α, and m impact the monotonic pile response – also for the

† Soil stresses determined using γ_{sat} = 19.3 kN/m^3 and γ_{unsat} = 15.2 kN/m^3 for, respectively, the saturated and unsaturated unit weight of the soil – values representative of D_r = 70% were obtained from lab tests results reported in Tsetas et al., 2023.

gapping $p-y$ springs) prior to subjecting the pile to lateral monotonic loading. The measured pile deflection response (black line) and the corresponding moment profiles (black markers) at $F = 90$, 175 kN are compared in Figure IV.15 to the 1D simulation results based on the SL calibration procedure (red lines). While the simulated moment profiles are rather satisfactory, a prominent under-prediction of the lateral pile stiffness was obtained – due to using the SL calibration method outside the recommended range of applicability and, potentially, to disregarding other soil resistance contributions in addition to normal $p-y$ reactions. The measured pile deflection at ground surface equals $U = 4.45$ mm (i.e, $U/D = 5.8{\cdot}10^{-3}$) when F =175 kN, which is approximately half the minimum working threshold of $U/D \geq 10^{-2}$ ($U \geq 7.85$ mm) suggested by Suryasentana and Lehane, 2016 for monotonic loading up to ultimate capacity – indeed, the GDP loading programme was conceived to investigate the pile response to medium-low amplitude loading cycles. The poor agreement between field data and SL-based simulations motivated a re-calibration of the proposed $p-y$ model that led to fully satisfactory results – see blue lines in Figure IV.15. In particular, the following calibration guidelines were followed:

1. regarding the calibration of the memory (both in saturated and saturated soil), the shape parameter m (m=0.5 instead of 1.0) and the q_c-dependence of p_u in Equation (IV.2) was slightly modified (see Table IV.2) to best-fit the global lateral (monotonic) response of the pile as measured in the field (Figure IV.15);

2. the calibration of ratcheting (μ_0) and gap-related parameters was solely based on parcels *a* and *b* (initial 2000 cycles of high amplitude loading), with no further adjustments for parcels *c-d-e* (3000 cycles in total);

3. due to the dearth of detailed data for calibration, the complexity of the calibration procedure was herein reduced by setting $\alpha_{sp} = 0$ (Equation (IV.18)) and $C_d = 0$ (Equation (IV.21)), and therefore deactivating the separation and drag springs;

4. relevant shape parameters (m for the memory spring, m_c and α_c for the closure spring), were calibrated to match the global response of the pile upon unloading-reloading cycles. With reference to the closure spring, the global force-displacement response (Figure IV.13a) and the back-calculated $p-y$ reaction trends (Figure IV.14) generally suggested a gradual decrease in average soil reaction stiffness upon increasing pile deflection (Kementzetzidis et al., 2023a). This aspect was accommodated by setting $\alpha_c = -\frac{ln(0.15)}{(0.55)^{m_c=0.5}}$ – for clearer presentation, the reason for this setting is explained in 5 ;

5. the ratcheting-control parameter μ_0 was identified against the displacement accumulation trends measured at the ground surface, under the simplifying assumption of negligible influence of the degree of saturation (typically unknown and variable along the depth).

Regarding point 2, the deactivation of the separation and drag elements – which would in principle contribute to the flexibility of the $p-y$ model – was enforced in light of the following arguments:

- inhibiting the separation spring did not hinder the attainment of the sharp unloading stiffness, as it is anyhow achieved owing to the progressive stiffening of the memory spring (see also the previous discussion in Section 3 .1);
- the qualitative shape of the back-calculated soil reactions (Figure IV.14) indicated very weak influence of pile-soil drag , partly due to the one-way cyclic loading considered herein (the contribution of soil drag would be higher under two-way loading with load sign reversals).

As for the calibration of μ_0, it is well-reported in the literature that the accumulation of soil strains associated with cyclic ratcheting is substantially affected by the initial mean effective stress $\bar{\sigma}'_0$ – namely, lower $\bar{\sigma}'$ leads to higher/faster strain accumulation (Wichtmann et al., 2005). To heuristically incorporate this notion into the calibrated $p-y$ model, the following calibration relationship was introduced for μ_0:

$$\mu_0 = \mu_c \cdot \exp\left\{ C_p \cdot \left(\frac{\bar{\sigma}'_0}{\bar{\sigma}_{ref}} - 1 \right) \right\} \tag{IV.31}$$

where C_p and μ_c are scalar factors to be identified, while $\bar{\sigma}_{ref} = 100$ kPa is a reference pressure. Equation (IV.31) implies a depth-dependence of μ_0 through the in-situ $\bar{\sigma}'_0$ profile (calculated using an at-rest earth pressure coefficient equal to 0.5, and $\gamma_{sat} = 19.3$ kN/m^3 – $\gamma_{unsat} = 15.2$ kN/m^3), though with no attempt of capturing further expected dependencies on the pile geometry and the features of the cyclic loading programme (Wichtmann et al., 2005) – such dependencies are implicitly included in the selected values of C_p and μ_c, and would require additional studies to be described in detail. While such studies were beyond the scope of this work, the whole set of $p-y$ parameters identified to reproduce the response of the reference test pile are reported in Table IV.2.

4 .4. 1D simulation results

Following the set-up of the 1D FE pile model (Figure IV.11a) and the calibration of all $p-y$ parameters (Table IV.2), the response of the reference test pile to the cyclic load parcels $a-e$ in Figure IV.12b was numerically simulated. The comparison between measured and computed force-displacement responses (displacement recorded at the ground surface) is shown in Figure IV.13, while the corresponding displacement accumulation trends (ground level displacement vs number of loading cycles) are compared in Figure IV.16. Finally, simulated and measured bending moment profiles are reported in Figure IV.17 for six different times along the cyclic loading history.

Considering the lack of data for direct calibration (i.e., reliable $p-y$ curves obtained pile strain measurements), the global response of the pile seems to be overall well-captured by

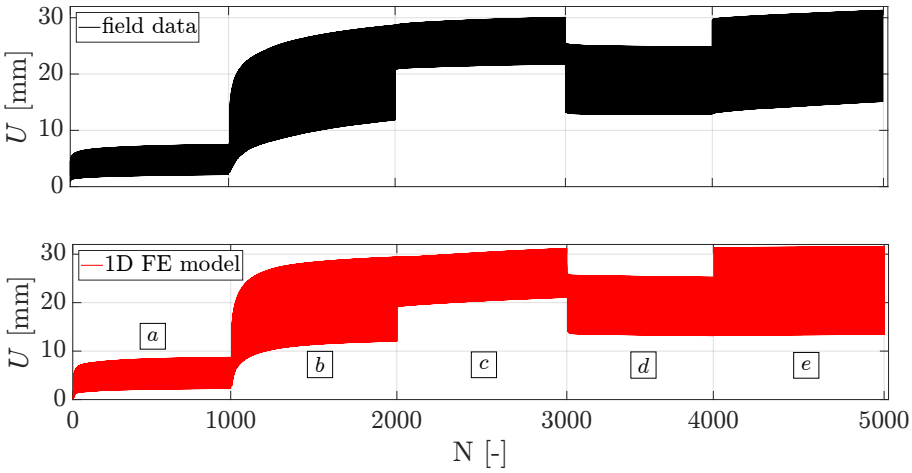

Figure IV.16: Measured (top) and calculated (bottom) evolution of the lateral pile displacement at ground level for parcels $a - e$.

the model in several respects. With particular regard to the force-displacement loops in Figure IV.13, it may be stated that:

- the response to the initial monotonic branches in the cyclic parcels a ($F = 0 - 175$ kN) and b ($F = 175 - 350$ kN) are very well-captured;
- the softening in the unloading-reloading response measured in the field, (compare $N = 1$ to $N = 1000$ for parcel b in Figures IV.13a and IV.13b) is also adequately captured owing to the gapping modelling features described above;
- cyclic hysteresis (area of force-displacement loops) is mostly well-reproduced, with the exception of the first few cycles of parcel b. Further improvement in this respect could be achieved, for instance, by activating/calibrating the dragging mechanism (here inhibited for simplicity).

The 1D model performance appears to be fully satisfactory also when assessed in terms of displacement accumulation trends (Figure IV.16). The evolution per cycle of the pile displacement minima and maxima (and therefore of the associated average cyclic stiffness $K_{cyc}^{av} = (U_{max} - U_{min})/(F_{max} - F_{min})$) are in satisfactory agreement with field measurements. In particular, the peculiar displacement relaxation observed during parcel d is spontaneously simulated by the model, which reflects well on the ability of capturing cyclic load redistribution along the pile (Kementzetzidis et al., 2023a)). Owing to the memory mechanism in the memory elements, the resulting $p - y$ formulation can also reproduce load history effects in the displacement accumulation rate – and particularly its drastic reduction under loading amplitudes that do not exceed the maximum load experienced by the pile in its previous loading history.

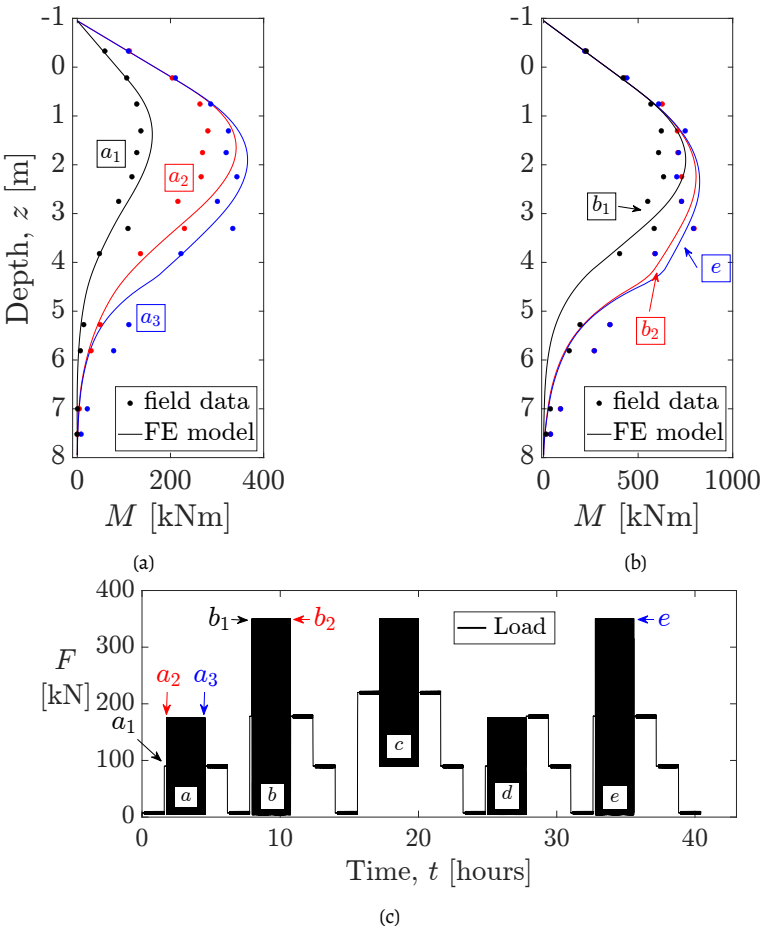

Figure IV.17: (a)-(b) Measured (dots) and calculated (solid lines) bending moment profiles; times at which bending moment profiles were measured/calculated along the reference loading programme – each cyclic parcel ($a - e$) features 1000 loading cycles.

As for the simulation of bending moment profiles (Figure IV.17), the following conclusions may be drawn:

- the evolution of the moment profiles along the loading history is reasonably well-captured, especially in the upper half of the embedded pile length;
- in agreement with field measurements, the 1D model simulates upon cycling a gradual increase in the maximum bending moment, as well as its slight shift towards deeper pile locations.

– the simulated bending moments along the deepest third of pile tend to be less accurate than in the upper portion of the pile, especially after the earliest a_1 and a_2 isochrones associated with parcel a (Figure IV.17b).

Better agreement between measurements and simulation results could be obtained by including additional moment fixity at the pile base – this probably played some role also for the reference test pile, which is was relatively stubby though still quite flexible. As previously mentioned, such addition was not pursued to limit the number of free model parameters with only limited independent data available for calibration. Further, a closer observation of the measured bending moments in Figure IV.17 suggests a possibly imperfect performance of some strain gauges, which would make the comparison between recorded and calculated moments somewhat less meaningful at those locations.

5 . Concluding remarks

The formulation, calibration, and application of a new $p-y$ model for cyclically loaded piles have been presented in this study. Particularly, the proposed model has been built to extend to cyclic loading conditions the previous monotonic, CPT-based $p-y$ formulation by Suryasentana and Lehane, 2016, with the inclusion of (i) a ratcheting control mechanism and (ii) additional soil reaction elements for the detailed modelling of pile-soil gapping effects. Owing to such features, the model can realistically simulate the ratcheting behaviour of the pile head under lateral cyclic loading, along with the peculiar variations in lateral stiffness induced by gapping. Importantly, the main component of the model – formulated in the framework of memory-enhanced bounding surface plasticity – can be calibrated against common CPT data, in a fashion inspired by Suryasentana and Lehane's approach.

The performance of the new $p-y$ model has been assessed against field data from a cyclic loading pile test. In order quantitatively capture the experimental data (both pile head deflection and bending moment profiles), some adjustments to Suryasentana and Lehane's CPT-based calibration procedure have been necessary, luckily due to a different range of pile deflection and the neglected influence of additional soil resistance mechanisms (e.g., distributed moments, base shear resistance and moment fixity) – the predictive capabilities of the SL model have already been demonstrated in (Anusic et al., 2019; Li et al., 2015; Suryasentana and Lehane, 2014a; Suryasentana and Lehane, 2016). Further, gap-related parameters had to be calibrated by trial-and-error, due to the lack of fully reliable information regarding real in-situ soil reactions.

Overall, the model has been shown to possess very promising predictive potential, as well as to enable efficient analyses of cyclically loaded piles. Future work on the subject will be devoted to three important aspects: (i) extension to clayey soils, featuring inherent cohesive behaviour even when fully saturated; (ii) inclusion of additional soil resisting mechanisms for more accurate analysis of stubby monopiles; (iii) development of a more comprehensive

CPT-based calibration procedure, based on additional experimental data and detailed 3D FE studies.

Appendix

Derivation of evolution laws for memory internal variables

Specific evolution laws for the memory internal variables, p_M and $p_{\alpha,M}$ in Equation (IV.13), were derived by adapting the same assumptions made by Liu et al., 2019a to the simpler case of a 1D soil reaction model. It is also worth recalling the following important assumption: the evolution laws that are first derived for virgin loading, are then held valid for any loading conditions (i.e., also for $p \neq \tilde{p}_M$).

Memory locus expansion

In order to enforce assumed constraints on the evolution of the memory locus ($F^M = 0$), the differential of the memory function F^M with respect to its independent variables is first obtained as follows:

$$\mathrm{d}F^M = \frac{\partial F^M}{\partial p}\mathrm{d}p + \frac{\partial F^M}{\partial p_{\alpha,M}}\mathrm{d}p_{\alpha,M} + \frac{\partial F^M}{\partial p_M}\mathrm{d}p_M = \\ \mathrm{sgn}(p - p_{\alpha,M}) \cdot \mathrm{d}p - \mathrm{sgn}(p - p_{\alpha,M}) \cdot \mathrm{d}p_{\alpha,M} - \mathrm{d}p_M \tag{IV.32}$$

During a virgin loading event (i.e., starting from $p = \tilde{p}_M$), the boundary of the memory locus that coincides with the current stress point (henceforth, point A) is considered to be dragged along the load increment while the opposite boundary (point B) is kept fixed. Analytically, this assumption translates into requiring $\mathrm{d}F^M(B) = 0$ with $\mathrm{d}p(B) = 0$, i.e., based on Equation (IV.32):

$$\mathrm{d}F^M(B) = 0 = -\mathrm{sgn}(p_B - p_{\alpha,M}) \cdot \mathrm{d}p_{\alpha,M} - \mathrm{d}p_M \tag{IV.33}$$

and therefore to the following increment of the memory locus size:

$$\mathrm{d}p_M = |\mathrm{d}p_{\alpha,M}| \tag{IV.34}$$

Memory locus translation

It has been shown in Section 2 .1 how the translation of the vanishing yield locus (i.e., with $\mathrm{d}p_\alpha \equiv \mathrm{d}p$) takes place along the direction of the plastic displacement increment (with $\mathrm{sgn}(\mathrm{d}y_p) \equiv \mathrm{sgn}(\mathrm{d}y) \equiv \mathrm{sgn}(\mathrm{d}p)$ in proportion to the distance $|\tilde{p}_u - p|$ – see Equations (IV.6), (IV.8), and (IV.10). Similarly, the memory locus is assumed to translate along the direction of $\mathrm{sgn}(\mathrm{d}p_{\alpha,M}) = \mathrm{sgn}(\mathrm{d}y)$ with incremental magnitude proportional to $|\tilde{p}_u - \tilde{p}_M|$. The expression of the associated 'dummy' hardening modulus $\tilde{H}_M$ in Equation (IV.16) can be first derived under virgin loading conditions – i.e., when $p \equiv \tilde{p}_M$ – in combination with the condition set by Equation (IV.34):

$$\mathrm{d}p = \mathrm{d}\bar{p}_M = \mathrm{d}p_{\alpha,M} + \mathrm{d}p_M \cdot \mathrm{sgn}(\mathrm{d}y) = 2\,\mathrm{d}p_{\alpha,M} \tag{IV.35}$$

Using Equation (IV.35) it is possible to relate the two translation rules for the memory locus (Equation (IV.16)) and the vanishing yield locus (Equations (IV.6), (IV.10)), which in turn leads to the following relationship between the 'dummy' and the 'real' hardening moduli:

$$\tilde{H}_M = \frac{1}{2} H_M \tag{IV.36}$$

Equation (IV.36), strictly applicable only to virgin loading, is finally extended to arbitrary loading conditions to enable the determination of $\mathrm{d}p_{\alpha,M}$ by combining Equations (IV.36)–(IV.16):

$$\tilde{H}_M = \frac{1}{2} \cdot \frac{\alpha \cdot m}{D} \cdot |\bar{p}_u - \bar{p}_M| \cdot \left| \frac{1}{\alpha} \ln\left(\frac{\bar{p}_u - \bar{p}_M}{\bar{p}_u - p_0} \right) \right|^{\frac{m-1}{m}} \tag{IV.37}$$

Calibration of the closure spring parameter α_c in Equation (IV.19)

The inspection of the field data shown in Section 4 (Figures IV.13a, IV.14) suggests an increasing displacement relaxation for increasing $|y_{max}|$, i.e., the minimum and the maximum pile head displacements evolve at substantially different rates (the former more slowly than the latter). This feature is incorporated in the model through the formulation of the closure spring, particularly by updating either α_c or m_c (shape parameters) upon each resetting of the gap configuration, i.e., upon unloading from the latest y_{max}. By rewriting Equation (IV.19) as:

$$\mathrm{B}p_{c,max} = p_{c,max} \times \exp\left\{-\alpha_c \mathrm{A}^{m_c}\right\} \tag{IV.38}$$

and solving for α_c

$$\mathrm{B} = \exp\left\{-\alpha_c (\mathrm{A})^{m_c}\right\} \Rightarrow a_c = -\frac{\ln \mathrm{B}}{\mathrm{A}^{m_c}} \tag{IV.39}$$

it possible to impose for every reconfiguration of the gap (unloading from the latest y_{max}), the deformation of the gap spring ($\Delta y_g = |y_g - y_{g,0}|$) required for the transition $p_{c,max} \rightarrow \mathrm{B}p_{c,max}$ ($0 < B < 1$), or backwards ($\mathrm{B}p_{c,max} \rightarrow p_{c,max}$). Setting $\Delta y_g = \mathrm{A}|y_{max}|$ enables the simulation of the observed enhancement in relaxation (decrease of the average stiffness $|p_{c,max} - \mathrm{B}p_{c,max}|/|\mathrm{A}y_{max}|$) with increasing y_{max} ($0 < A < 1$). In essence, the recalibration of α_c based on $|y_{max}|$ essentially tunes the average closure spring stiffness to fit the field data – $B = 0.15$ and $A = 0.55$ have been used throughout this work.

V

Paper IV

Gentle Driving of Piles (GDP) at a sandy site combining axial and torsional vibrations: quantifying the influence of pile installation method on lateral behaviour

---

Evangelos Kementzetzidis, Federico Pisanò, Athanasios Tsetas, Andrei V. Metrikine,
Journal of Geoenvironmental and Geotechnical Engineering, under review.

Abstract

Gentle Driving of Piles (GDP) is a new technology for the vibratory installation of tubular (mono)piles, which aims to achieve both efficient installation and low noise emission by combining axial and torsional vibrations. To provide a preliminary demonstration of the GDP concept, onshore medium-scale tests in sand were performed in late 2019 at the Maasvlakte II site in Rotterdam (Netherlands). Several piles were installed using both impact and vibratory driving methods (including GDP), with the twofold aim of comparatively assessing (i) the effectiveness of GDP-driving and (ii) the presence of installation effects in the pile response to lateral loading. This work focuses on the latter aspect and presents a quantitative analysis of the installation effects observed in the pile loading test data recorded in the field. Due to soil inhomogeneity across the field, a purely data-based analysis would have not supported objective conclusions, which led to adopt an alternative approach based on 1D numerical modelling. To this end, the recent cyclic $p-y$ model by (Kementzetzidis et al., 2022) is calibrated for the simulation of the reference pile loading tests, and the values of key parameters compared to infer quantitative information about relevant installation effects. The results presented herein support the excellent performance of the GDP method, particularly in comparison to traditional impact hammering: the GDP-installed piles are on average stiffer throughout the loading programme, while certain features of pile installation effects seem to gradually vanish as more loading cycles are applied.

1. Introduction

Since the installation in 1991 of the first 5MW offshore wind farm in Denmark, over 28 GW of offshore wind power have been developed in Europe (Komusanac et al., 2022), while a global capacity of 37 GW has been reported at the end of 2021 (Lee et al., 2021). In the coming thirty years, North America, Europe, and Asia will lead the way towards the installation of additional 560 GW, which is likely a lower bound estimate of the real growth that will take place (Lee et al., 2021). To support this unprecedented energy transition endeavour, considerable research efforts are being devoted to closing knowledge gaps and promoting innovation in all areas of offshore wind science and engineering. Among many others, such areas include the installation (and future decommissioning) of ever larger offshore wind turbines (OWTs), which are currently approaching/exceeding a power output of 15 MW (Gaertner et al., 2020). Therefore, the remarkable fabrication costs for these enormous steel structures may only be alleviated by optimising the design of the whole OWT-foundation system, particularly with respect to environmental cyclic loading conditions (Byrne et al., 2020a; Igwemezie et al., 2019; Pisanò et al., 2022a).

It is worth recalling that, to date, OWTs are most often founded on so-called monopiles, which are tubular steel piles featuring a large diameter (in the range from 5 to 11 m) and a low ratio between embedded length and diameter (typically between 3 and 6). Monopiles are most commonly installed through impact hammering, a technology that has substantially matured over years of intense offshore oil and gas developments (Kallehave et al., 2015a). However, while impact installation may sometimes slow down (or even abort) in the presence of very competent soils (Achmus et al., 2020; Rodger and Littlejohn, 1980), its execution inevitably produces significant underwater noise. Since such noise is known to be harmful to marine life, ocean management authorities have been enforcing strict regulations to limit its negative impact on the environment (Tsouvalas, 2020). A promising, less noisy alternative to impact piling is represented by vibratory pile driving technologies: their performance in different soil types, as well as their impact on post-installation pile behaviour, is being investigated by an increasing number of research teams (Achmus et al., 2020; Anusic et al., 2019; Heins and Grabe, 2017; Herwig and Gattermann, 2015; Labenski and Moormann, 2019; LeBlanc, 2014; Staubach, 2022).

This study presents some recent achievements related to the development and assessment of a new vibratory pile installation technology named Gentle Driving of Piles (GDP) (Metrikine et al., 2020). The GDP method replaces the high-amplitude blows of traditional impact hammering with silent axial and torsional vibrations, with the latter applied at substantially higher frequency than the former. First demonstration of the GDP technology has been recently accomplished through a field campaign at the Maasvlakte II site in Rotterdam (Netherlands). To enable a general comparison among different pile installation methods, identical tubular test piles (see specifications in Table V.1) were installed in sandy soil using three different driving technologies, namely impact hammering, traditional axial vibratory piling, and the new GDP method (Tsetas et al., 2023); subsequently, the same piles were subjected to lateral cyclic load parcels of varying amplitude, so as to enable a first assessment of GDP installation effects in comparison to existing technologies (Kementzetzidis et al., 2023a). Additionally, 'complementary' pile impact tests were also performed to confirm (or challenge) certain indications provided by the main cyclic loading experiments.

Regarding the post-installation cyclic tests, it is noted that the inhomogeneity of the site and the location of the water table (about 4 m below ground surface) had altogether a noticeable impact on the cyclic response of the test piles – largely due to the occurrence of pile-soil gapping in the shallow unsaturated sand. While 'onshore site effects' are also clearly visible in previously published field data (Byrne et al., 2020b; Li et al., 2015; Prendergast and Igoe, 2022), a model-based analysis of the GDP cyclic test results has been carried out in this work to try and decipher relevant installation effects in the lateral response of the test piles. To this end, the cyclic soil reaction model recently proposed by Kementzetzidis et al., 2022 was adopted to simulate cyclic ratcheting and gapping effects as observed at the Maasvlakte II site. Following a calibration of the model parameters largely based on SCPT

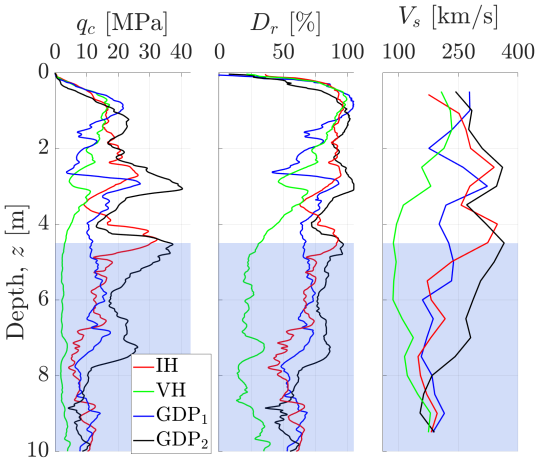

Figure V.1: Profiles of (left) cone resistance (q_c), (middle) relative density (D_r), and (right) S-wave velocity (V_s) obtained at the MTP locations through in-situ SCPTu tests. The blue-shaded areas indicate water-saturated soil.

data, the proposed analysis provides encouraging evidence regarding the lateral behaviour of GDP-driven piles.

2 . Field tests at the MAASVLAKTE II site

All GDP field tests were performed at the Maasvlakte II port site in Rotterdam, which comprises the North Sea sand that was used to create a reclaimed/compacted site. The experimental campaign was carried out over 6 months (June-December 2019) and included the execution of geotechnical site investigation, pile installation experiments, and cyclic lateral loading tests – with the addition of the abovementioned pile impact tests. After the conclusion of site investigation activities, nine tubular steel piles were installed at the test site in October/November 2019, namely eight test piles and one larger reaction pile (the latter to serve as a central 'fixed' point for the post-installation loading tests – Table V.1). Four of the test piles, henceforth referred to as *Main Test Piles* (MTPs), were extensively instrumented as reported by Tsetas et al., 2023; the other four *Auxiliary Test Piles* (ATPs) were installed uninstrumented for preliminary testing purposes. The remainder of this paper exclusively focuses on analysing the behaviour of the four MTPs, which were labelled after the corresponding installation method: IH (impact hammering), VH (axial vibro-hammering), and GDP$_{1,2}$ (two MTPs were GDP-driven).

2 .1. Geotechnical site investigation

Geotechnical investigation activities took place at the Maasvlakte II site between June and August 2019. A preliminary phase of site investigation was first carried out in June 2019 to support the selection of the test pile locations. To this end, 25 CPTu tests were performed

Table V.1: Geometrical specifications of the test and reaction piles.

		Test piles	Reaction pile
Length	L	10 m	10 m
Embedded length	L_e	8 m	8 m
Outer diameter	D	0.762 m	1.6 m
Wall thickness	h	0.0159 m	0.02 m

down to a target depth of 10 m, which also enabled the identification of the water table depth – on average, approximately 4 m below the ground surface. A more detailed site investigation programme was executed two months later, including the following tests at the MTP locations:

- four Seismic CPTu (SCPTu) tests – see Figure V.1;
- four hydro-profiling tests with mini-pump tests (HPT-MTP) around the piles (target depth: 15 m);
- borehole sampling around the piles, with a total of eight 10 m long boreholes (two per MTP) – resulting soil classification information is provided by Tsetas et al., 2023;

The main outcomes of the SCPTu tests are summarised in Figure V.1. The profiles of cone resistance (q_c), relative density (D_r, obtained following Jamiolkowski et al., 2003), and shear wave velocity (V_s) indicate somewhat inhomogeneous sand conditions, featuring a negative D_r gradient below a depth of approximately 1 m. Importantly, the soil profile at the VH pile location was found to be quite different from that at the IH/GDP$_{1,2}$ locations, with significantly looser sand below the water table.

2 .2. Installation of MTPs

During the first week of November 2019, all four MTPs were driven into the ground according to the following installation protocol: first, piles were driven down to a depth of 3 m, with each pile laterally restrained to ensure verticality; then, the lateral restraints were removed and the piles were finally driven down to the target penetration depth of 8 m. The pile driving settings are summarised in Table V.2 for each MTP, while the consumed energy for the vibratory-installed piles is presented in Figure V.2. When considering the specific soil profiles in Figure V.1, the driving performance of the GDP method, stands out both in terms of installation time and consumed energy to achieve the required target depth – comparing the driving records of piles GDP$_1$ and VH pile, the GDP-driven pile installed in a considerably more competent soil (Figure V.1) achieves the target depth faster, with almost equal energy consumption.

	IH	VH	GDP_1	GDP_2
			Axial	Torsional
Driving settings	E_b = 24.97 kJ N_b = 70 blows/min	me = 25 kg·m f_{ax} = 24.8 Hz	me = 15 kg·m f_{ax} = 16.3 Hz	me = 4 kg·m f_{tor} = 63 Hz
Driving duration	348 s	261 s	151 s	273 s

Table V.2: Driving settings and duration associated with the main pile driving phase (z = 3 – 8 m) for the four MTPs. E_b and N_b denote energy per blow and number of blows per minute for IH pile, while me and f indicate the eccentric moment and the driving frequency for the vibratory methods (both VH and GDP).

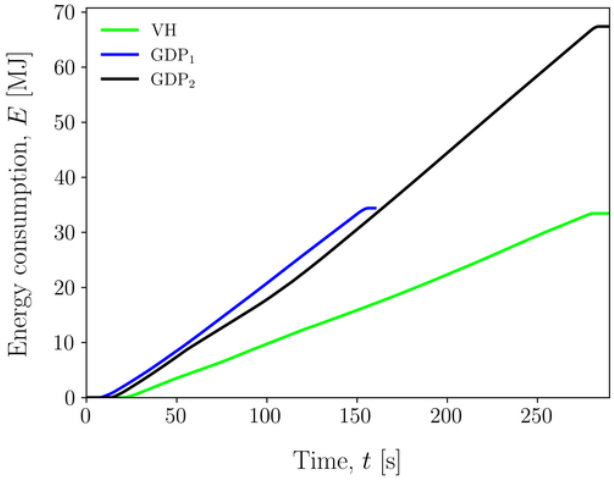

Figure V.2: Energy consumption over installation time during the final 5 m of pile driving (out of the total 8 m) for the axial and GDP vibro-driven piles.

2 .3. Cyclic lateral loading tests

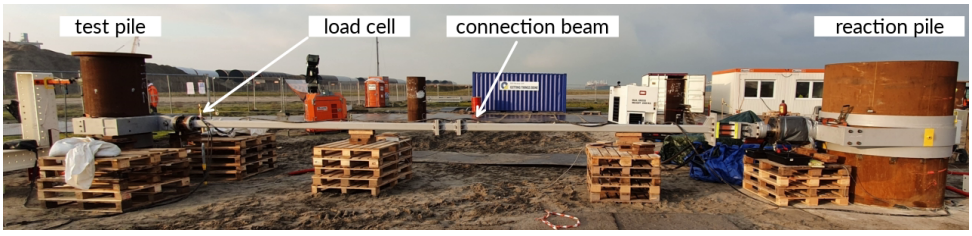

Figure V.3: The loading frame connecting a test pile (left) to the reaction pile (right).

The lateral loading tests, main subject of this paper, were performed using the loading frame shown in Figure V.3. Since all test piles were installed to a target depth of 8 m, the

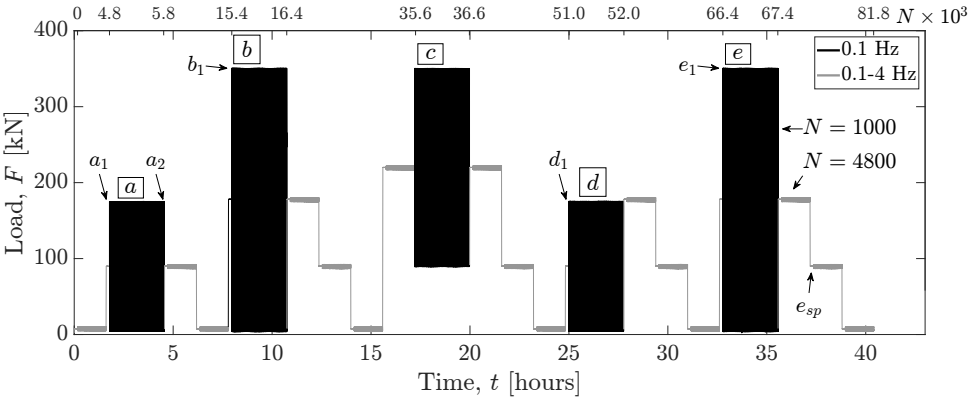

Figure V.4: Cyclic/dynamic loading programme. Load amplitudes are provided against time (bottom axis) and number of cycles (top axis). Cyclic load parcels ($a - e$, $N = 1000$ for each parcel) and dynamic frequency sweeps ($N = 4800$ per sweep) are shown in black and grey, respectively.

V

remaining pile length allowed lateral loading with an eccentricity $e = 1$ m above the ground surface. During lateral loading, the deflection of all test piles was sampled near the soil surface (shown in the following after low-pass filtering at 70 Hz) using dedicated displacement sensors (Gefran PY1, 100 mm stroke).

Figure V.4 illustrates the MTP loading programme, featuring a combination of cyclic and dynamic load parcels. 'Cyclic' parcels were applied with relatively large amplitude at a constant low frequency of 0.1 Hz (black parcels in Figure V.4, from *a* to *e*); each cyclic parcel comprised $N = 1000$ cycles, with a maximum applied load of 350 kN – an approximate reference lateral capacity of 1.5 MN was identified for the GDP-driven MTPs as a reasonable approximation (Kementzetzidis et al., 2023a). The grey parcels in Figure V.4 represent 'dynamic' load parcels, i.e., small-amplitude (5 kN) 'frequency sweeps' interleaved between consecutive cyclic parcels. Each sweep was set to span loading frequencies ranging from 0.1 to 4 Hz, in order to explore possible frequency-dependence features in the small-vibration response of the system (Kementzetzidis et al., 2021). In what follows, selected data from the GDP testing campaign are reported to summarise relevant features of MTPs' behaviour.

Figure V.5 reports the evolution in time of the lateral deflection measured for all MTPs under the loading programme in Figure V.4 (displacement values measured at the soil surface). Despite mild quantitative differences, all piles exhibited similar displacement accumulation patterns, with clear appearance of cyclic ratcheting behaviour. Interestingly, all load parcels except *d* induced displacement responses characterised by positive accumulation rates, while a gradual reduction in accumulated deflection was observed during parcel *d*. Such a mechanism, sometimes termed *self-healing*, *stabilisation* or *relaxation*, has been previously documented in relation to small-scale 1g tests on monopiles (Sturm et al., 2008; Theodoros et al., 2009). Figure V.5 also suggests that the low-amplitude frequency sweeps had negligible impact on the overall pile displacement trends. At the end of the loading

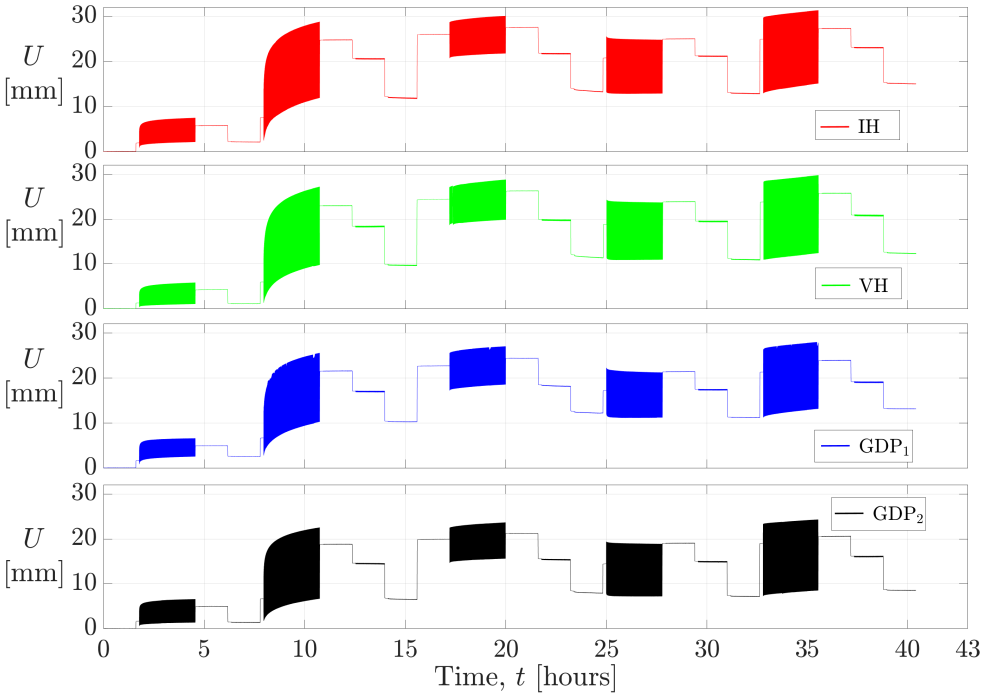

Figure V.5: Lateral deflection of all MTPs (soil surface level) under the loading programme in Figure V.4.

programme, the IH pile accumulated the most lateral deflection, followed by VH, GDP_1 and GDP_2, which may be also clearly observed in Figure V.6.

Figure V.6-left shows the cyclic force-displacement response of all MTPs (displacement measured at the soil surface) to the whole loading programme in Figure V.4. The shape of the measured cyclic responses indicates the occurrence of pile-soil separation (gapping) during the loading tests, which was likely enabled by the hydraulic suction, and the resulting 'apparent cohesion', in the shallow unsaturated sand above the water table (Fredlund, 2006) – note that this kind of response would not be expected for piles installed in either dry or fully saturated (uncemented) sand. The influence of gapping is more clearly illustrated in Figure V.6-right, which reports the response cycles measured for the IH pile under the first cycle ($N = 1$) of parcel *b* and the last cycle ($N = 1000$) of parcel *e* (cf. to Figure V.4): both the unloading and reloading branches of the response appear to be of a 'locking' type, with the tangent lateral stiffness increasing with the load level. This is a well-known consequence of the pile-soil re-engagement that occurs upon the gradual (re)closure of the gap (Kementzetzidis et al., 2023a). Visual pile-soil inspection further confirmed the alleged impact of gapping in the shallow unsaturated soil - see the pictures in Figure V.7 associated with (a) at rest (i.e., at the end of cycling) and (b) post-extraction conditions..

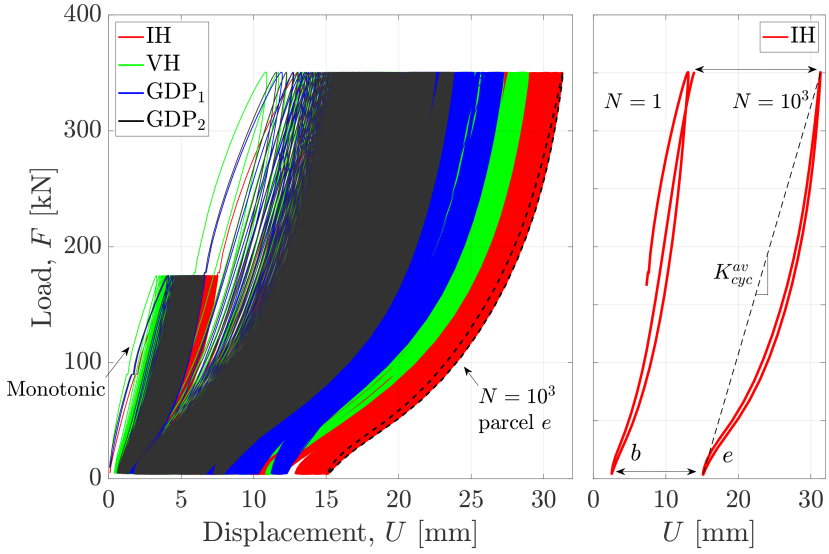

Figure V.6: (left) Force-displacement response of all MTPs (displacement measured at the soil surface) to the loading programme in Figure V.4 – the label 'Monotonic' refers to the first loading branch in parcel *a*; (right) IH pile response to the first cycle ($N = 1$) in parcel *b* and the last cycle ($N = 1000$) in parcel *e*, for which, the definition of cyclic secant stiffness K_{cyc}^{av} is visualised.

(a) (b)

Figure V.7: Evidence of pile-soil gapping (a) at the end of the cyclic loading programme and (b) after pile extraction.

Figure V.8-top reports the evolution of the cyclic secant stiffness $|K_{av}^{cyc}|$, (defined for each cycle as $K_{av}^{cyc} = \frac{F_{max}-F_{min}}{U_{max}-U_{min}}$, see Figure V.6 –right), for all MTPs during the loading programme in Figure V.4. Close inspection of the figure points out to some mild frequency-dependence during most frequency sweeps – such effects are discussed in detail by Kementzetzidis et al.,

2021, 2023a and are not further analysed herein. Importantly, the $|K_{av}^{cyc}|$ values measured for the four MPTs converge as the loading marches both for the frequency sweeps and the slow (0.1Hz) high amplitude loads. In Figure V.8-top, the range of measured $|K_{av}^{cyc}|$ for all MPTs is graphically presented via diamond-headed arrows. It is evident that ranges of $|K_{av}^{cyc}|$ measured between the initial and final application of a particular sweep (identical forcing) is significantly reduced for all the three presented cases, c.f., the black diamond-headed arrows (top figure) depict the range of $|K_{av}^{cyc}|$ measured during the first and the last application of the parcel with forcing $F = 5 + 2.5 \times \sin(2\pi f t)$, $f \sim 0.1 - 4$ Hz. Similar findings are reported in Figure V.8-middle, for the parcels of slower (0.1 Hz) and larger amplitude cyclic loading. Overall swift reductions in K_{av}^{cyc} are visible in the early stage of parcels a and b, arguably due to the gradual enlargement of the pile-soil gap as increasing load levels were experienced by the piles for the first time (Kementzetzidis et al., 2023a) – i.e., from 0 to 175 kN and from 175 kN to 350 kN for parcels a and b, respectively. Conversely, all pile responses to parcels d and e featured a modest increase in K_{av}^{cyc}, likely to be associated with fabric changes in the soil – including cyclic sand densification (Cuéllar et al., 2009; Kementzetzidis et al., 2023a; Liu et al., 2021). It should be noted that both GDP-driven piles responded to cyclic loading with (on average) the largest stiffness K_{av}^{cyc} among the four MTPs; at the same time, the experimental K_{av}^{cyc} trends in Figure V.8-middle appear to converge towards very similar values for all MTPs. Such convergence of the observed pile response indicates that the loading programme gradually homogenises certain features of the cyclic pile behaviour which are initially different due to the pre-installation soil conditions (Figure V.1) and any installation effects.

The remainder of this study exclusively focuses on the response of the MTPs to the five cyclic parcels (from a to e), which showed negligible impact of the interleaved frequency sweeps – see Figure V.5 and Kementzetzidis et al., 2023a. In an attempt to distinguish possible installation effects (by accounting for the site inhomogeneity and pile-soil gapping effects), the field data shown in Figures V.5, V.6, V.8-middle are interpreted in Section 4 .2 through 1D pile-soil analyses based on the recent $p-y$ model proposed by Kementzetzidis et al., 2022 (see Section 3).

2 .4. Complementary field tests

To complement the experimental evidence provided by the pile installation and loading tests, additional pile impact tests were performed (Tsetas et al., 2020). Pile impact tests are well-established in structural vibration testing (Brandt, 2011), and have been recently applied to the dynamic characterisation of pile-soil systems **prendergast2016comparison.** During the GDP campaign at the Maasvlakte II site, similar impact experiments were conducted to identify the frequency response properties of each MTP-soil system in its pre- and post-loading states (i.e., always after the pile driving phase). The tests were performed using an instrumented hammer to hit all piles at a point located 1.5 m above the ground surface (Tsetas et al., 2020). The resulting dynamic responses were recorded for each pile by two

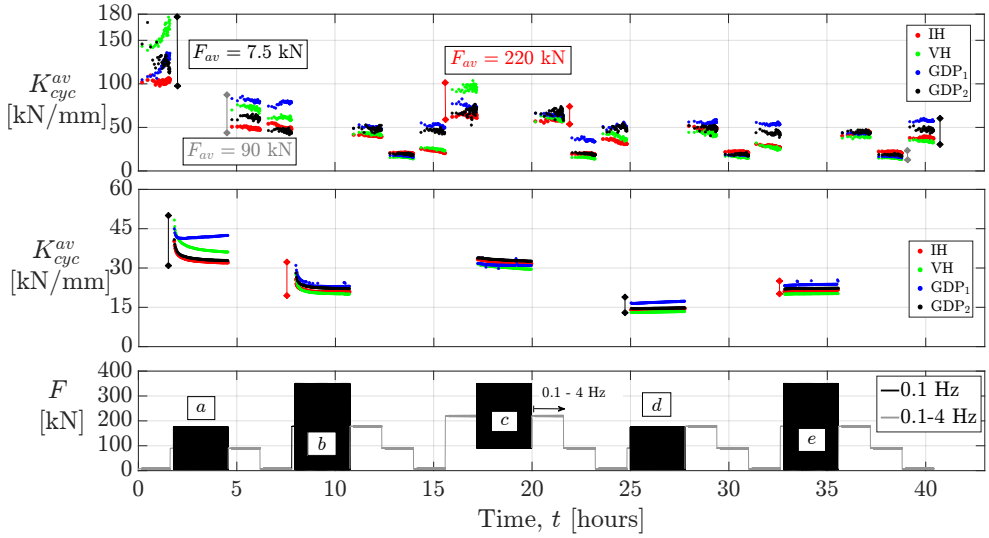

Figure V.8: Average cyclic stiffness $|K_{av}^{cyc}|$ vs time t for all MTPs during (top) dynamic frequency sweeping and (middle) cyclic loading of larger amplitude; (bottom) applied loading programme. Diamond-headed arrows (top, middle) indicate the range of measured $|K_{av}^{cyc}|$ for all the MPTs during the first and last application of a particular load parcel.

tri-axial MEMS accelerometers, symmetrically positioned with respect to the location of the impact point and set to sample at 16 kHz. Finally, the recorded signals were processed to obtain experimental frequency response functions (FRFs). It should be mentioned, however, that the pre-loading impact tests on the IH and GDP$_1$ piles returned 'corrupted' signals due to the defective installation of some accelerometers – therefore, such data were excluded from relevant analyses.

Based on the processing of the recorded signals, Figure V.9 shows, for instance, significant differences in amplitude between the pre-loading FRFs obtained for the VH and GDP$_1$ piles; such differences, however, turned out to be attenuated by the cyclic loading process, as is testified by the much closer post-loading values of the FRF amplitudes and peak frequencies. In this respect, the most notable feature is the response peak at a frequency lower than 40 Hz, which is similarly observed for all piles.

Overall, the impact test results in Figure V.9 indicate a sort of 'homogenising' effect of prolonged cyclic loading with respect to the combined influence of pile driving method and the soil profile features – at least for what concerns the post-cyclic dynamic response to small-amplitude perturbations (and in good agreement with the stiffness data in Figure V.8).

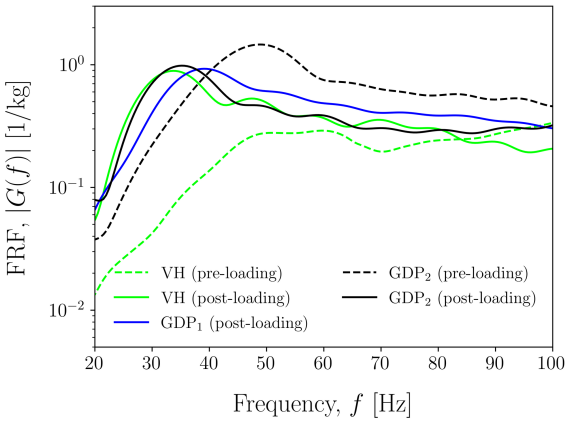

Figure V.9: Experimental frequency response functions identified for the MTP-soil systems in their pre- and post-loading states.

3 . Modelling of cyclic soil reactions

This section summarises the salient features of the cyclic $p-y$ model used in Section 4 to simulate the GDP field tests. Elasto-plastic modelling of drained soil reactions in water-saturated sand is carried out by combining in series a linear elastic spring and a non-linear hysterestic element – i.e., the lateral soil displacement (y) at the interface with the pile is interpreted as the sum of two distinct components, reversible/elastic (y_e) and irreversible/plastic (y_p). The resulting cyclic soil reaction model is embedded into a comprehensive 1D rheological model for detailed modelling of gapping effects in unsaturated sand.

3 .1. Elastic component

The mentioned linear elastic component is fully characterised by the corresponding value of the stiffness K_e. In agreement with recent studies (Delavinia, 2022; Wan et al., 2021), K_e is set to be directly proportional to the in-situ profile of soil's small-strain shear modulus G_0 Figure V.1:

$$K_e = 7G_0 \tag{V.1}$$

The influence of installation effects and cyclic loading on K_e is disregarded herein and will require further dedicated studies.

3 .2. Plastic component with cyclic ratcheting control

The following ingredients of Kementzetzidis et al., 2022's model enable accurate simulation of (drained) pile-soil interaction in either dry or water-saturated sand, i.e., with no relevant gapping effects.

Monotonic backbone

Under monotonic loading, the plastic component of the 1D model exactly replicates the empirical relationship by Suryasentana and Lehane, 2016 between soil reaction (p) and the irreversible/plastic displacement, y_p:

$$p = p_u \left[1 - e^{-\alpha (y_p/D)^m}\right] \tag{V.2}$$

where p_u represents the ultimate soil reaction force (per unit length), D is the pile diameter, while α and m are dimensionless model parameters.

Extension to cyclic loading

The irreversible response to unloading-reloading cycles (hysteretic behaviour) is reproduced via a standard kinematic hardening mechanism, resulting in the following form of the plastic modulus, K_p:

$$K_p = \frac{\alpha \cdot m}{D} \cdot |\bar{p}_u - p| \cdot \left| \frac{1}{\alpha} \ln\left(\frac{\bar{p}_u - p}{\bar{p}_u - p_0}\right)\right|^{\frac{m-1}{m}} \tag{V.3}$$

in which $\bar{p}_u = p_u \cdot \mathrm{sgn}(\mathrm{d}p)$ with $\mathrm{d}p$ denoting the soil reaction increment within the current calculation step; p_0 represents a projection centre that takes the current p value whenever a soil reaction reversal occurs (i.e., whenever $\mathrm{sgn}(\mathrm{d}p)$ changes). Equation (V.3) produces a mechanical response that, under monotonic loading, reduces exactly to that established by Equation (V.2) in the case of monotonic loading.

Ratcheting control mechanism

Excessive ratcheting in the elasto-plastic $p - y$ response under (asymmetric) cyclic loading is prevented by introducing a memory-enhancing mechanism, following previous constitutive modelling studies (Corti et al., 2016; Liu et al., 2019a). To this end, the model is endowed with an additional memory locus, whose size and location evolve depending on the cyclic loading history. The main role of the memory locus is to introduce an additional metric associated with the distance b_M between the current soil reaction and its projection onto the memory locus along the loading direction. b_M is exploited to enhance the definition of the plastic modulus in Equation (V.3) as follows:

$$K_{p,M} = K_p \cdot \exp\left\{\mu_0 \left(\frac{b_M}{b_{ref}}\right)^2\right\} \tag{V.4}$$

where μ_0 is a scalar ratcheting-control parameter, and $b_{ref} = 2p_u$ is introduced for normalisation purposes. Equation (V.4) returns either $K_{p,M} = K_p$ when $b_M = 0$ ('virgin' loading conditions, i.e., when the soil reaction point lies on the memory locus) or $K_{p,M} > K_p$ when $b_M > 0$ due to an expansion of the memory locus induced by the previous loading history. In the latter

case, the evolution of the tangent stiffness, and therefore the cyclic accumulation of lateral deflection, is controlled by the value of μ_0.

Recommendations for parameter calibration

The response resulting from the above constitutive equations depends on the calibration of four parameters, namely p_u, α, m and μ_0. While the ratcheting parameter μ_0 may be identified by trial-and-error against the results of cyclic pile loading tests or advanced 3D FE studies (Liu et al., 2021), p_u, α, and m may be set through the following CPT-based relationships inspired by the work of Suryasentana and Lehane, 2016:

$$\begin{cases} p_u = C_{pu}\sigma'_{v0}D\left(\dfrac{q_c}{\sigma'_{v0}}\right)^{0.67}\left(\dfrac{z}{D}\right)^{0.75} \leq q_c D \\ \alpha = 8.9\left(\dfrac{z}{D}\right)^{-1.25}\left(\dfrac{\sigma_{v0}-u_g}{\sigma'_{v0}}\right)^{0.5} \\ m = 1 \end{cases} \tag{V.5}$$

where $C_{pu} = 2.4$ is the value recommended by Suryasentana and Lehane, 2016, σ_{v0} and σ'_{v0} represent the in-situ total and effective vertical stresses at a depth z below the ground surface, and u_g is the hydrostatic pore water pressure at $z = 0$. Compliance with usual bounding surface modelling principles requires $m < 1$, which can be closely approximated by setting, e.g, $m = 0.9999$. The performance of the model under one-way cyclic loading is exemplified in Figure V.10 for different μ_0 values.

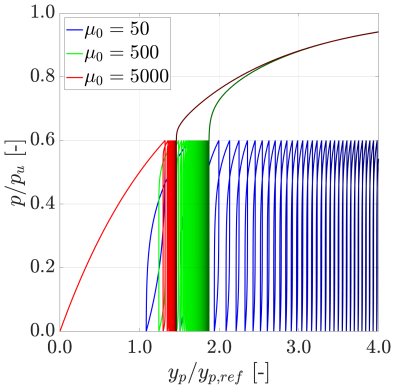

Figure V.10: Cyclic $p-y$ soil reactions (no gapping) under $N = 100$ cycles of one-way loading ($\mu_0 = 50,\ 500, 5000$). Other model parameters calibrated based on Equation (V.5) for a circular pile (diameter: $D = 0.762$ m) and a soil location characterised by: $z = 4$ m (soil depth), $q_c = 17$ MPa (cone resistance), $\gamma_{dry} = 16$ kN/m^3 (dry unit weight).

3 .3. Simulation of cyclic pile-soil gapping

In the presence of cohesive soil behaviour, an accurate $p-y$ formulation should be able to reproduce pile-soil gapping, usually resulting in S-shaped lateral soil reaction curves of

the kind shown in Figure V.11. Importantly, gapping effects under cyclic loading are inherently displacement-dependent, as are the evolution of the gap depth and the alternation of 'contact'-'no-contact' stages between the pile and the soil – more details about the mechanics of pile-soil gapping are provided, e.g., by Boulanger et al., 1999; Kementzetzidis et al., 2023a; Matlock et al., 1978; Suzuki and Nakai, 1985. As previously mentioned, gapping effects were clearly exhibited by all pile loading data recorded at the Maasvlakte II site (Figure V.6), due to the unsaturated soil above the water table.

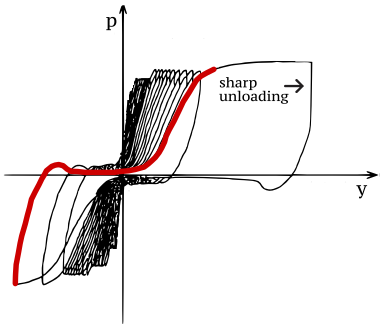

Figure V.11: Cyclic $p - y$ curves for cohesive soils – modified after (Randolph and Gourvenec, 2011), originally from (Bea et al., 1979). The red line highlights the mentioned S-shape of the last $p - y$ response cycle.

Following Kementzetzidis et al., 2022, lateral soil reactions in the upper unsaturated sand have been modelled by combining the above memory-enhanced $p - y$ model – the 'memory' spring – with additional rheological elements, namely the so-called 'separation', 'closure', and 'drag' springs. Figure V.12 illustrates (half of) the resulting pile-soil interaction scheme – note that the inherent asymmetry of the gapping mechanism requires the use of two distinct interaction elements on both sides of the pile.

Separation spring

The separation spring enables the simulation of the sharp unloading branch that originates at the onset of pile-soil separation (see Figure V.11). Due to lack of dedicated data for calibration, the separation spring is deactivated in the global pile-soil interaction scheme, and for brevity not further described herein – more details available in Kementzetzidis et al., 2022. For the pile loading cases considered in the following, the stiffening that is necessary to simulate the mentioned stiff unloading response is directly provided by the parallel memory mechanism (Figure V.12).

Closure spring

The inclusion of the so-called closure spring is required to simulate the peculiar shape (resembling a rotated S) of the $p - y$ response cycles in the presence of cohesive soil behaviour (Boulanger et al., 1999) (Figure V.11). To reproduce mathematically such a shape, the

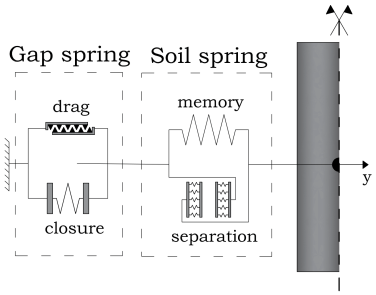

Figure V.12: 1D modelling scheme for the simulation of cyclic hysteresis with ratcheting control and pile-soil gapping (Kementzetzidis et al., 2022) – left-side only, a similar scheme is also applied to the right-side.

following function – similar to Equation V.2 – is adopted to relate, in finite terms, the reaction component in the closure spring (p_c) to the corresponding displacement (y_g, i.e., the displacement of the overall gap spring in Figure V.12):

$$p_c = p_{c,max}\left(\mathrm{e}^{-\alpha_c\left|\frac{y_g - y_{g,0}}{y_{max}}\right|^{m_c}}\right) \tag{V.6}$$

where m_c and α_c are dimensionless shape parameters, while $y_{g,0}$ assumes the current value of y_g every time the pile re-enters the gap from a new y_{max}.

The formulation of the closure spring was chosen to represent the shape of pile soil interactions when the pile moves inside the gap and ensures that upon unloading from $p_c = p_{c,max}$, the closure spring reaches a nil asymptote ($p_c = 0$) as fast as enabled by the selected pair of m_c-α_c values (shape parameters), so as to reproduce the desired S-shape of the $p-y$ response – more information on the impact of such parameters on the gapping soil reactions is available in Kementzetzidis et al., 2022. Values in the order of $m_c = 0.6$ and $\alpha_c = 20$ have been found to provide a reasonable gap-closing response for a sharp pile-soil separation, and are henceforth considered as a first-guess pair of calibrated parameters.

Combined memory and drag springs

A gapping $p-y$ model should also reproduce the frictional resistance offered by the side soil wall when normal contact is lost on either one or both sides of the pile. Frictional drag (side pile-soil friction, introduced via the drag spring) resists pile motion regardless of the pile location and displacement direction within the gap area. In the model of Kementzetzidis et al., 2022, the drag soil reaction component, p_d, is described as follows:

$$p_d = p_{u,d}\left(1 - \mathrm{e}^{-\alpha\frac{\left|y_g - y_g^r\right|}{D}^m}\right) \tag{V.7}$$

where $p_{u,d} = C_d p_u$, with C_d being a scalar parameter that can be tuned between 0 and 1 to modulate the relative contribution of the drag reaction to the total lateral soil resistance – therefore, to preserve the total ultimate soil resistance, the quota associated with the

memory spring is reduced to $p_{u,m} = (1 - C_d)\, p_u$. Additionally, $y_g^r = y_g$ is updated at every sign reversal of $\dot{y}_g$ (at the beginning of the analysis, the initialisation $y_g^r = y_g = 0$ is set). Equations (V.2) and (V.7) are identical for monotonic loading conditions, which allows the use of the CPT-calibration procedure by (Suryasentana and Lehane, 2016) also for the complete gapping $p - y$ model.

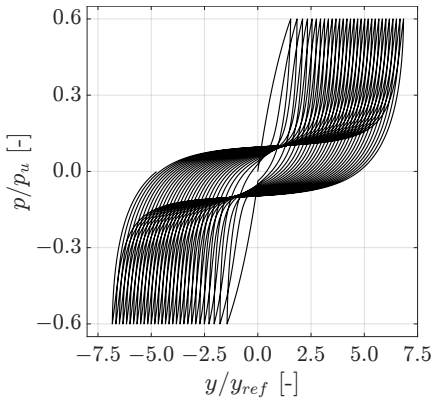

Figure V.13: Cyclic $p - y$ soil reactions (with gapping) under symmetric/two-way loading. Model parameters calibrated based on Equation (V.5) for a circular pile (diameter: $D = 0.762$ m) and a soil location characterised by: $z = 4$ m (soil depth), $q_c = 17$ MPa (cone resistance), $\gamma_{dry} = 16$ kN/m^3 (dry unit weight). Additionally: $\mu_0 = 20$, $\alpha_c = 5$, $m_c = 0.6$, and $C_d = 0.1$.

3 .4. 1D pile-soil model setup

In order to simulate the reference pile loading tests, 1D FE models were set up for the four MTPs using the OpenSees simulation platform (McKenna, 2011), in which the complete $p - y$ model described above has been previously implemented. To this end, the four identical piles were idealised as Timoshenko beams, with their embedded length (8 m below ground surface) set in contact with a sequence of gapping (upper 4 m, in the unsaturated soil) and non-gapping (lower 4 m) spring elements with a vertical spacing of 8 cm – see Figure V.14. The calibration of all soil reaction parameters is discussed in the following section along with the simulation of the four MTP loading tests.

4 . Comparative analysis of pile installation effects

In this section, the response all of MTPs to the cyclic loading programme in Figure V.4 is quantitatively analysed using the elasto-plastic $p - y$ model presented in Section 3 . Given the different soil profiles at the four pile locations (Figure V.1), such analysis aims to 'filter out' differences in lateral response features that are mainly related to pre-installation soil conditions.

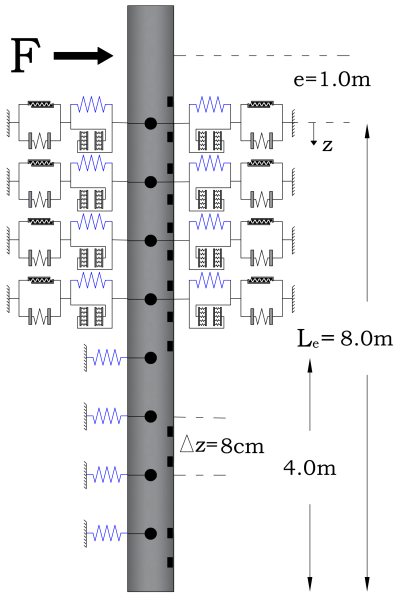

Figure V.14: Reference 1D pile model subjected to lateral cyclic loading. The ground water table depth ($z = 4$ m) marks the transition between unsaturated and saturated soil. The black rectangular symbols indicate the locations of the FBG axial strain sensors.

4 .1. General considerations

For each loading test, the first loading branch in parcel a (highlighted in Figure V.6) – from 0 to $F = 175$ kN – may be regarded as a post-installation stage of monotonic loading. The measured load-displacement curves are reported in Figure V.15 for all MTPs, along with their numerically simulated counterparts (dashed lines). It is possible to observe that, in absolute terms, the VH pile was the stiffest of all piles (although installed in the loosest/softest sand profile, cf. to Figure V.1), followed by the GDP-driven piles ($GDP_{1,2}$) and, finally, the IH pile (impact hammered). Quite surprisingly, GDP_1 and GDP_2 exhibited almost identical monotonic responses, despite the non-negligible differences in terms of pre-installation q_c profile at the respective locations.

The cyclic pile deflection trends presented in Figures V.5,V.6 seem to contradict the conclusions drawn on the sole basis of the monotonic response curves. Regarding the impact of the five cyclic parcels in Figure V.4 (5000 cycles in total), it may be stated that:

– while the VH pile was 'monotonically' the stiffest (which is seemingly in contradiction with the corresponding q_c profile), it accumulated the second largest cyclic deflection by the end of the cyclic loading sequence;

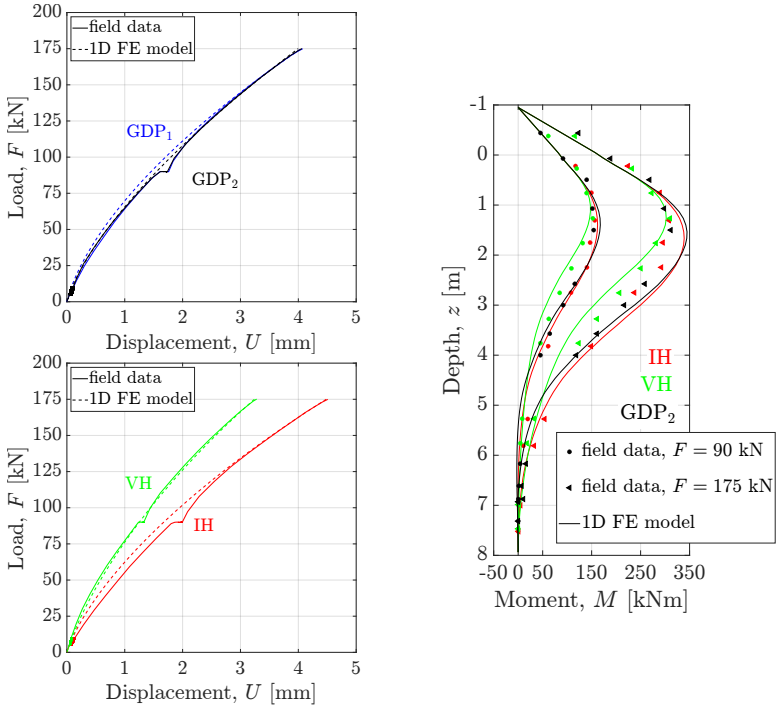

Figure V.15: Measured and calculated force-displacement responses and selected bending moment profiles (associated with $F = 90$ kN and $F = 175$ kN in parcel *a*, monotonic branch ($N = 1$) – see Figures V.4, V.6). GDP_1's bending moment profiles were deemed unreliable (sensor malfunctioning) and therefore omitted.

– cyclic deflection accumulation was lowest for the two GDP piles (see Figures V.5, V.6), in a fashion that is consistent with the respective pre-installation soil profiles (i.e., GDP_2 displaced less than GDP_1 with $q_c^{GDP_1}$ being on average lower than $q_c^{GDP_2}$;

– the IH pile experienced the largest lateral deflection, both monotonically (first segment of parcel *a*) and cyclically (over the whole loading programme).

In more detail,it is worth noting that the VH pile accumulated during parcel *a* the lowest lateral deflection at the ground surface, while it displaced more than both GDP-driven piles by the end of parcel *e*: this outcome is arguably the result of a complex interaction between initial soil conditions and pile installation effects, where the latter seem to be working differently depending on the pre-installation relative density profile – see also the previous studies of Bienen et al., 2021; Fan et al., 2021c,d; Staubach et al., 2020; Staubach, 2022. Since the VH pile was installed in substantially looser sand than the other MTPs, it is preferred to focus in what follows on the comparison between GDP-driven and impact-hammered

(IH) piles, which were all installed in medium-dense to dense sand – such an option was ultimately suggested by the modelling outcomes in Section 4 .2.

4 .2. Quantitative 1D FE studies

The measured differences in the lateral response of the otherwise identical MTPs may be attributed to differences in the installation procedures and the foundation soil. Relevant $p-y$ model parameters were calibrated, both for the saturated and the unsaturated soil layers, by first identifying those governing the monotonic lateral response (i.e., K_e, p_u, α, and m). The elastic component of the memory springs was calibrated as $K_e = 7G_0$, as obtained from the shear velocity profiles in Figure V.1. For p_u, α, and m a first calibration attempt was made by following the CPT-based procedure proposed by Suryasentana and Lehane, 2016 and reported in Equation (V.5). The resulting comparison between field data and first-trial simulations was rather unsatisfactory, probably due to the applied monotonic load being relatively low compared to the reference load range considered by Suryasentana and Lehane, 2016 – they examined monotonic pile responses up to the reference capacity $U = 0.2D$. The same calibration strategy described by Kementzetzidis et al., 2022 was applied to the four MTPs to improve the agreement between measured and simulated monotonic load-displacement curves. It was first found beneficial to reduce the value of m, from 1 to 0.5 for all piles; then, new C_{pu} values were re-calibrated as reported in Table V.3 (cf. to Equation (V.5)), with direct impact on the local ultimate resistance of each $p-y$ element. The re-tuned C_{pu} values produced the very satisfactory matches shown in Figure V.15 for all piles, both in terms of load-displacement curves and bending moment profiles at two distinct load levels (90 kN and 175 kN). Owing to the explicit q_c-dependence of p_u in (the first line of) Equation (V.5), it may be argued that C_{pu} is directly representative of pile installation effects – particularly for piles that are geometrically identical. In this respect, Table V.3 indicates that:

- in spite of quite different average cone resistance values ($q_{c,av}$) down the pile, almost identical C_{pu} values were identified for the GDP-driven piles, implying strong correlation of C_{pu} with the pile-driving technology;
- overall the response of piles installed in medium dense to dense sands was reproduced by similar C_{pu} values – c.f. $GDP_{1,2}$ and IH to VH. GDP-driven piles were found to be represented by C_{pu} values that are approximately 13% larger than for the impact hammered pile. This outcome establishes the same relationship between the respective soil resistance values (p_u), and would theoretically extend to the (very) ultimate pile capacity defined as $F_{ult}=\int_0^{Le} p_u\,dz$. Conversely, a slightly different capacity increment (+ 15%) is estimated later in Section 4 .3 for GDP and IH piles in the same soil profile by adopting a conventional definition of lateral capacity (i.e., the load inducing a lateral pile deflection $U = 0.1D$ at ground surface).

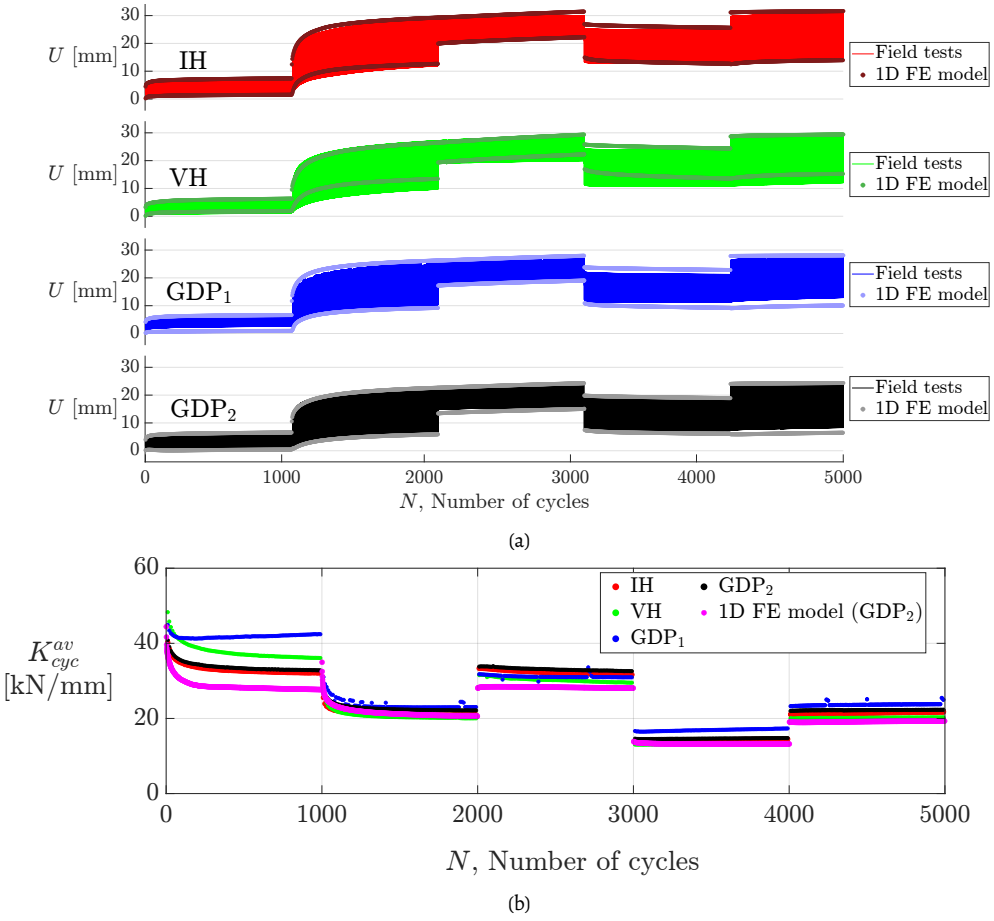

Figure V.16: (a) Cyclic pile deflection trends (deflection measured at the soil surface) and (b) evolution of K_{cyc}^{av} (defined in Figure V.6) induced by the cyclic load parcels ($a-e$) in Figure V.4 on the four MTPs. In (a), the $p-y$ simulation results (dotted lines indicate cyclic deflection bounds) are compared to measured data (solid lines). In (b), the K_{cyc}^{av} trend simulated for the GDP$_2$ pile is shown in magenta.

The same philosophy for analysing pile installation effects was also applied to the measured cyclic responses. To this end, additional $p-y$ model parameters had to be calibrated, namely μ_0 (ratcheting-control parameter), C_d (frictional drag resistance parameter), and the shape parameters α_c and m_c governing the behaviour of the closure spring (Figure V.12). Following Kementzetzidis et al., 2022, the values of $m_c = 0.5$, $\alpha_c = -\ln(0.15)/(0.55)^{m_c}$, and $C_d = 0.0$ were first set (equal for all piles). In a further attempt to reduce the calibration effort, the frictional drag mechanism (Section 3 .3) was inhibited by setting $C_d = 0.0$ – in fact, Kementzetzidis et al., 2022 have shown the modest impact of frictional drag for piles subjected to one-way cycling. Finally, the following CPT-based relationship was assumed for the calibration of μ_0:

Table V.3: Values of C_{pu} and C_{μ_0} (from Equations (V.5), (V.8)) set to fit the measured monotonic and cyclic lateral pile responses at the Maasvlakte II site – Figures V.15-V.16b. $q_{c,av}$ is the average q_c along the embedded length of each pile, c.f. to Figure V.1. The shaded column on the right highlights that VH data are considered less meaningful for comparison purposes (see discussion in Section 4).

	GDP_1	GDP_2	IH	VH
$q_{c,av}$ [MPa]	12.4	21.3	14.9	6.4
C_{pu} [-]	0.417	0.411	0.365	0.674
$C_{\mu 0}$ [-]	310	181	282	165

$$\mu_0 = C_{\mu_0} \cdot \left(\frac{q_c}{\sigma'_{v0}}\right)^{0.1} \left(\frac{\sigma'_{v0}}{\sigma'_{v,ref}}\right)^{0.75} \tag{V.8}$$

where C_{μ_0} is a scalar dimensionless parameter, and $\sigma'_{v,ref} = \gamma' z$ kPa (for $z = 1$ m, and γ' the effective unit weight of soil) serves as a reference vertical effective stress. According to Equation (V.8), μ_0 is assumed to depend both on q_c and z. The adopted z-dependence is similar to that considered for p_u in Equation (V.5), while the type of q_c-dependence was identified through trial-and-error to enable the simulation of all MTP responses using only C_{μ_0} as a location/installation-specific parameter. Since the same soil unit weight and pile geometry apply to all MTPs, it was not necessary to introduce additional factors in Equation (V.8) for the purposes of this study. The C_{μ_0} values in Table V.3 were identified for all piles to obtain a good match between experimental and simulated cyclic deflection trends at the ground surface – respectively, solid and dotted lines in Figure V.16a. Apparently, the numerical model reproduces very well the field measurements associated with all MTPs, including the peculiar displacement 'relaxation' observed during the fourth cyclic load parcel (*d*).

The same evolution trends of the average cyclic stiffness (K_{av}^{cyc}) discussed in Section 2 .3 are also compared in Figure V.16b – for clearer illustration, only those obtained for the GDP_2 pile (in magenta). Apart from the generally good agreement between measured and simulated trends, a closer inspection of relevant internal variables in the $p-y$ model confirmed some of the claims made by Kementzetzidis et al., 2023a on a purely experimental basis: (i) the drop in K_{av}^{cyc} during parcels *a*-*b* relates to the main gap-opening events; (ii) when an approximately steady size of the gap is maintained (here during parcels *d*-*e*), the model captures the gradual increases in cyclic stiffness through the expansion of the memory loci along the different $p-y$ springs (increase of b_M in Equation (V.4)).

The complete response of the main test piles to the whole cyclic loading programme is compared to the corresponding field data in Figures V.18, V.19, V.20, V.21 (load-displacement response). Bending moment profiles at selected loading instants (referred to as a_1, a_2, b_1, d_1, e_1 and e_{sp} in Figures V.4) are presented in Figure V.22, for brevity, only for the GDP_2 pile. The results obtained testify once again to the suitability of the adopted 1D modelling

framework, especially when considering the complexity introduced by multi-amplitude cycling and shallow unsaturated soil conditions.

Overall, the results presented in this section demonstrate the merits of the 1D FE model, as well as the consistency of a parameter calibration strategy that worked properly for all MTPs. It is thus possible to draw some final considerations suggested by the calibrated $c_{\mu 0}$ values in Table V.3 (the value calibrated for the VH pile is mostly regarded as an outlier, given the significantly lower density of the soil at that location):

- $c_{\mu 0}$ appears to be (negatively) correlated with the average cone resistance, $q_{c,av}$, rather than with the pile driving method – Figure V.17a. Indeed the above-mentioned finding is further supported by reploting the force-displacement response of the MPTs in Figure V.6, but now normalising the lateral displacement by the monotonic displacement attained for each pile at the onset of parcel a, in Figure V.17b. Apparently, such a normalisation highlights the mentioned correlation between cyclic ratcheting response and soil profile features (c.f. to Figure V.1) also suggested by 1D modelling results.

- at variance with what observed for post-installation monotonic responses (Figure V.15), prolonged lateral cycling seems to gradually erase/homogenise certain installation effects, in agreement with the observations of Staubach et al., 2020.

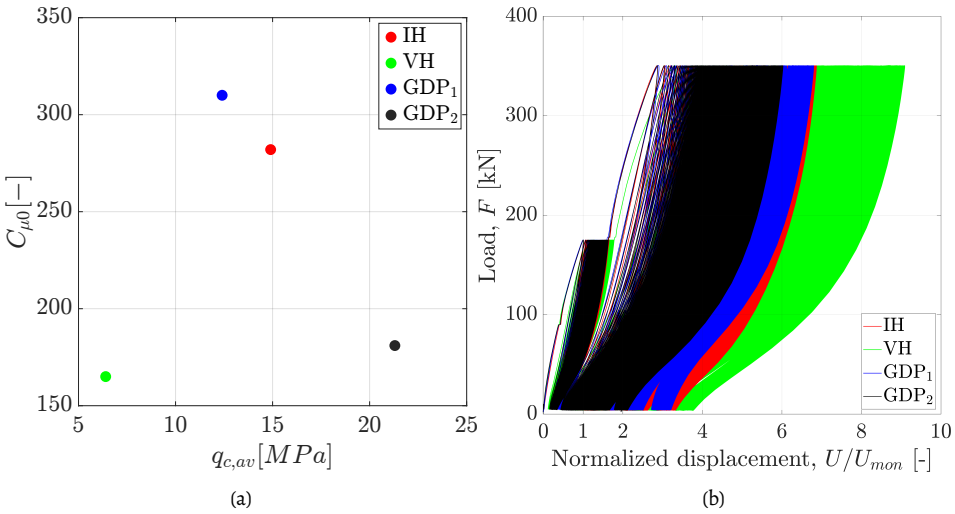

Figure V.17: (a) Values of $C_{\mu 0}$ versus $q_{c,v}$ (from Equation (V.8)) set to fit the measured monotonic and cyclic lateral pile responses at the Maasvlakte II site). The observed trend further supports that the VH data are less suitable for comparison purposes (see discussion in Section 4). (b) Force vs normalised displacement response of the MPTs under the cyclic loading programme in Figure V.4 – normalisation is by the value U_{mon} of lateral pile deflection at the end of the initial monotonic branch (i.e., prior to parcel a cycling).

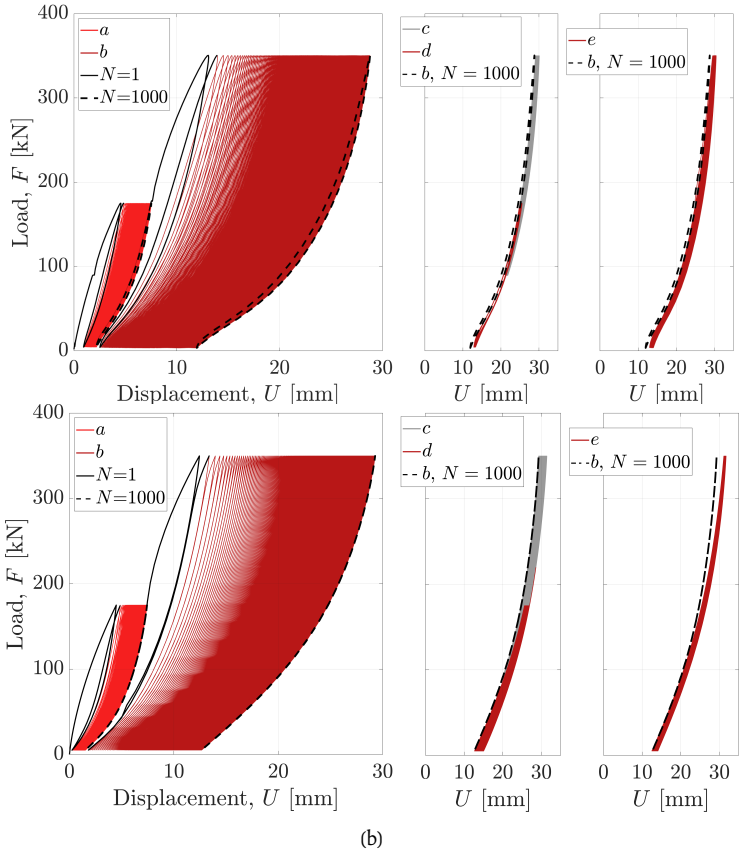

(b)

Figure V.18: IH: (a) measured and (b) calculated force-displacement pile responses to parcels $a - b$ (left), $c - d$ (middle), and e (right) (Figure V.4). In the left sub-plots, solid black and dashed lines denote, respectively, $N = 1$ and $N = 1000$; in the middle and right sub-plots, dashed lines are used for $N = 1000$ in parcel b.

4 .3. Predicted installation effects in a fictitious sand deposit

The analysis of both measured and simulated pile responses at the Maasvlakte II site in Sections 4 .1, 4 .2 highlight marked pile installation effects. Importantly, the trends of cyclic pile stiffness obtained from measured data exhibit a sort of homogenising tendency under prolonged cyclic loading (Figures V.9, V.16b). To reinforce the model-based interpretation of such installation effects, the same 1D FE model was used to simulate the lateral behaviour of two piles (identically sized as the MPTs – Table V.1) installed through impact hammering and GDP in a fictitious fully saturated sandy site – therefore, with no gapping effects under lateral loading. The fictitious site was charachterised by averaging the q_c and V_s profiles associated with the IH and GDP_1 pile locations (Figure V.1); then, 1D model parameters were calibrated for the two piles by setting $K_e = 7G_0$, while α, m, $\mu 0$ were obtained through correlation to the fictitious V_s and q_c profiles – $C_{\mu 0} = 296$ was determined as a representative

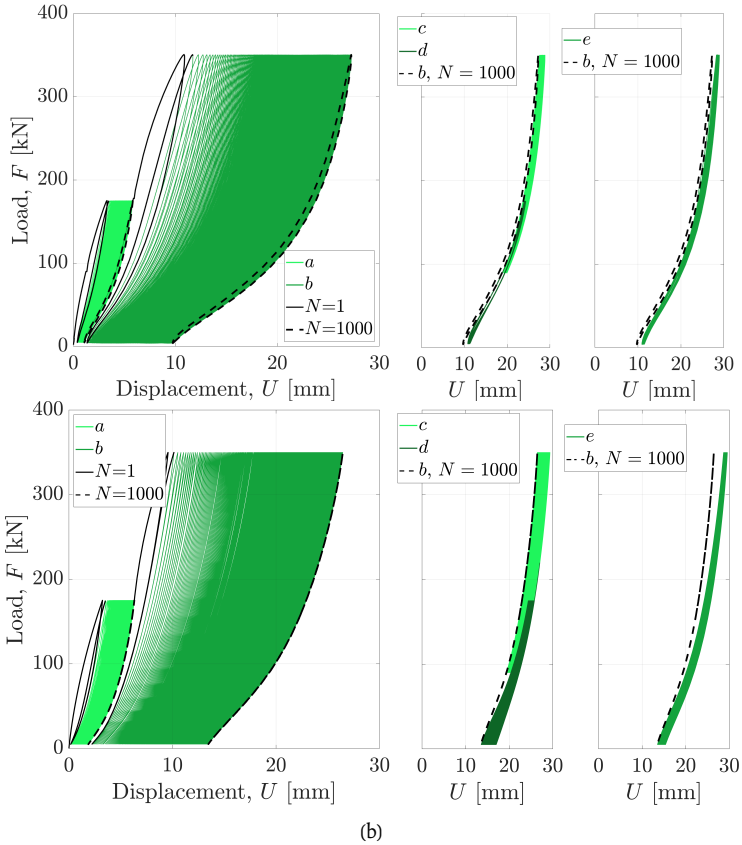

Figure V.19: VH: (a) measured and (b) calculated force-displacement pile responses to parcels $a - b$ (left), $c - d$ (middle), and e (right) (Figure V.4). In the left sub-plots, solid black and dashed lines denote, respectively, $N = 1$ and $N = 1000$; in the middle and right sub-plots, dashed lines are used for $N = 1000$ in parcel b.

value for the assumed average q_c profile (Figure V.17a). In agreement with the analysis in Section 4 .2, all installation effects were lumped into the calibrated p_u profiles, which ware determined using Equation V.5 with the C_{pu} values reported in Table V.3 – (an average $C_{pu} = 0.4135$ was selected for the GDP method). Both piles were monotonically loaded up to their conventional lateral capacity ($U = 0.1D = 0.762$ m); then, separate cyclic simulations were performed considering cyclic loading programme in Figure V.4.

The simulated monotonic behaviour of impact hammered and GDP-installed piles is shown in Figure V.23a. As expected, the differences in the corresponding p_u profiles determine a stiffer response of the GDP pile, with a larger load (conventional capacity) necessary to achieve a displacement at ground surface equal to $U = 0.1D$ – $F = 1740$ kN and $F = 1514$ kN for the GDP and the impact-driven piles, respectively. It is important to note that the ratio between such (conventional) capacities for the two piles ($1740/1514 \approx 1.15$) is slightly larger

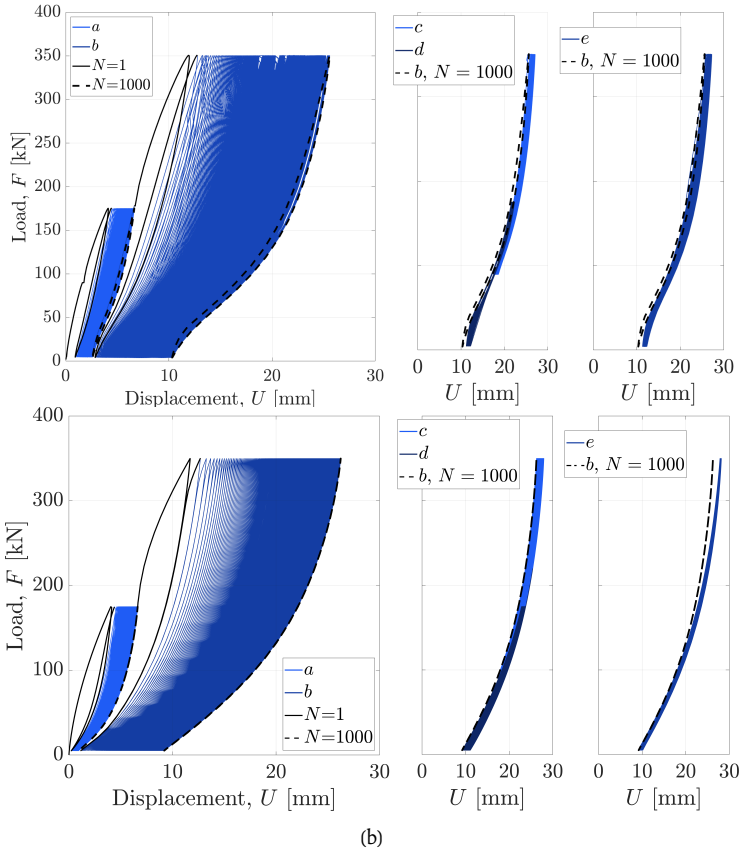

Figure V.20: GDP$_1$: (a) measured and (b) calculated force-displacement pile responses to parcels $a-b$ (left), $c-d$ (middle), and e (right) (Figure V.4). In the left sub-plots, solid black and dashed lines denote, respectively, $N = 1$ and $N = 1000$; in the middle and right sub-plots, dashed lines are used for $N = 1000$ in parcel b.

than the ratio between the respective values of the soil resistance parameter C_{pu} (see Section 4 .2).

As for the simulated cyclic response, the two piles are predicted to accumulate significantly different lateral deflection (see Figure V.23b). In particular, the final deflection associated with the impact driven pile is almost 30% larger at ground surface, notwithstanding the use of the same ratcheting-control parameter μ_0 (due to identical q_c profiles and C_{μ_0} values for the two piles – see also Equation V.8). Regarding the cyclic evolution of the K_{av}^{cyc} stiffness, the 1D model predicts a similar homogenisation effect of cyclic loading as suggested by the above field data. This statement is supported by Figure V.23c, which displays the evolving K_{av}^{cyc} ratio between the GDP and the impact-driven piles. According to the 1D model, while the cyclic stiffness of the GDP pile is initially $\approx 10\%$ larger, a tendency towards very small differences is obtained as more loading cycles are gradually applied –

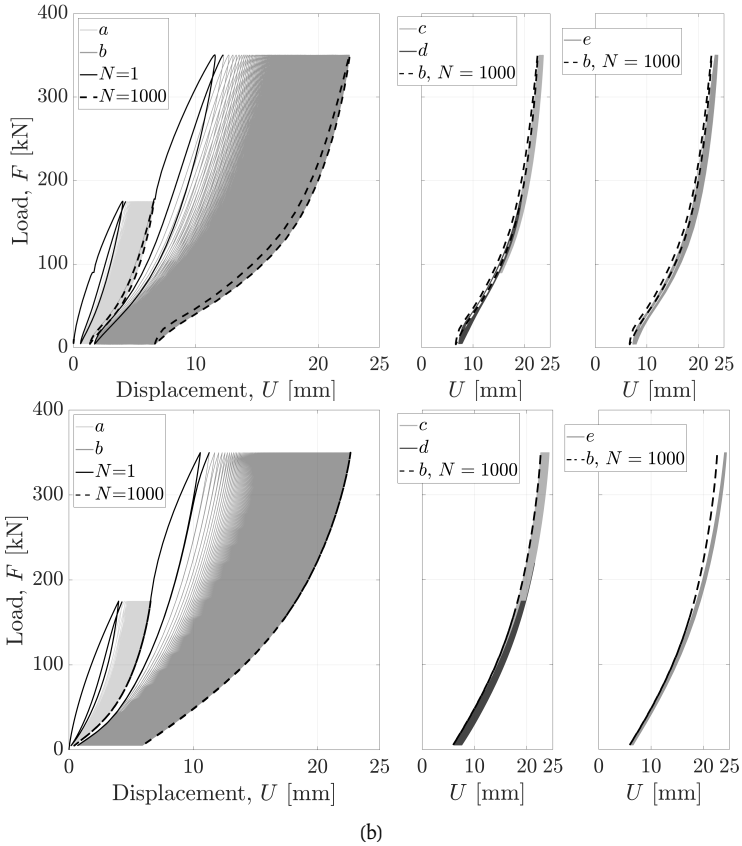

Figure V.21: GDP$_2$: (a) measured and (b) calculated force-displacement pile responses to parcels $a - b$ (left), $c - d$ (middle), and e (right) (Figure V.4). In the left sub-plots, solid black and dashed lines denote, respectively, $N = 1$ and $N = 1000$; in the middle and right sub-plots, dashed lines are used for $N = 1000$ in parcel b.

after a few thousands, an approximately steady difference of $\approx 3 - 4.5\%$ results for all load parcels.

5 . Conclusions

To compare the novel GDP driving method to more traditional approaches, four piles (MTPs) were driven in sandy soil via impact hammering (1 pile), axial vibro-driving (1 pile), and the GDP method (2 piles). In this study, the post-installation lateral loading test results from the GDP field campaign have been analysed/modelled in detail to assess the impact of the pile installation method.

All MTPs were subjected to the same complex cyclic loading programme comprising $N = 82000$ loading cycles in total, 5000 of which featuring low frequency (0.1 Hz) and relatively large amplitude – main focus of this study. The results of the first GDP field campaign

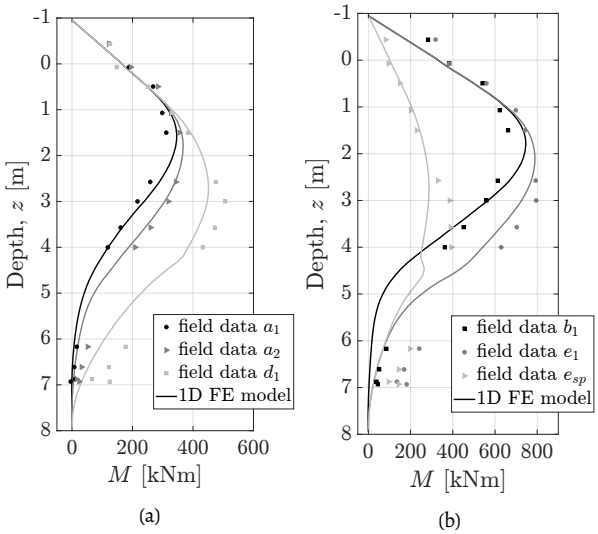

Figure V.22: GDP$_2$: (a)-(b) Measured (markers) and calculated (solid lines) bending moment profiles; the times at which bending moment profiles were measured/calculated along the loading programme (e.g. α_1, α_2, etc.) are indicated as in Figure V.4.

indicated that, overall, GDP-driven piles responded to cyclic loading better than the other IH- and VH-installed piles. At the same time, it was important to recognise the inevitable impact of unsaturated soil conditions (in the shallowest 4 m of the site) and geotechnical inhomogeneities, which altogether hindered a fair comparison of all measured pile responses on a pure data-analysis basis. To overcome this difficulty, pile performances were indirectly (but more fairly) compared through the parameters of an advanced cyclic $p-y$ model calibrated for each MTP, specifically accounting for the differences in cone resistance profile at the reference pile locations. Furthermore, by using the calibration same settings obtained by fitting the pile responses observed at the Maasvlakte II site, installation effects that could be found at a marine site (i.e., with no gapping effects in water-saturated soil) were re-evaluated for impact- and GDP-driven piles, based on the simulation of monotonic and cyclic lateral pile behaviour at fictitious sandy site.

The main findings regarding pile installation effects in the response to lateral loading may be summarised as follows:

– laterally loaded piles may exhibit significant installation effects during loading phases that are immediately post-installation, especially for relatively low lateral load amplitudes (say, less than 15% of the monotonic capacity), but also after application of many loading cycles, in that noticeable differences are present in the residual accumulated lateral deflection (Figures V.6, V.15).

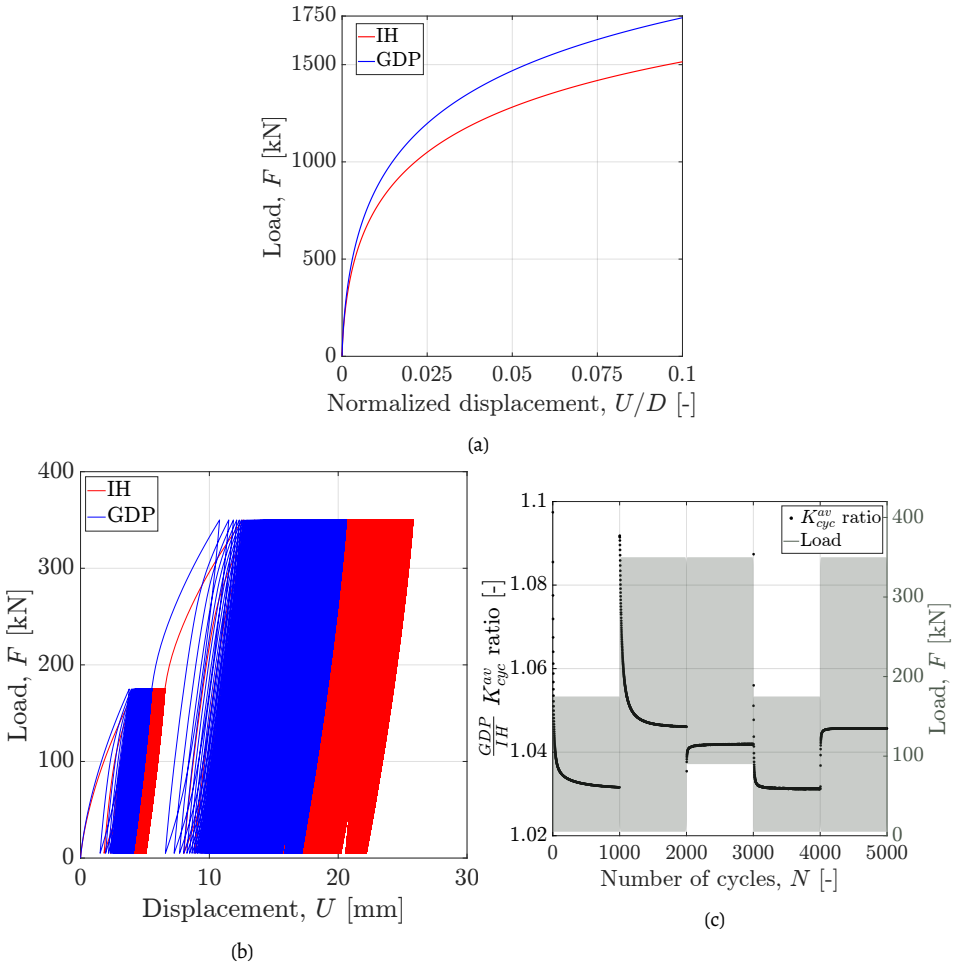

Figure V.23: Calculated force-displacement response of impact- and GDP-driven piles in a fictitious saturated sandy site (a) during monotonic loading to failure and (b) cyclic loading as in Figure V.4). In (c) the ratio of lateral cyclic average stiffness exhibited by the piles installed with different driving methods is presented (left) against the number of cycles during the forcing highlighted on the right.

– for piles installed in medium-dense to dense sand, the GDP method led to an estimated lateral capacity approximately 15% larger than for an impact-hammered pile at an identical soil location (conclusion supported by 1D FE calculations);

– after normalising the cyclic response of all MPTs by the maximum monotonic displacement attained prior to cyclic loading, the measured trends of cyclic deflection accumulation correlate altogether with soil profile features at the respective pile locations (c.f. Figure V.1 to V.17b). This finding is further supported by the identified parameters of the adopted 1D numerical model. Particularly, the ratcheting-control

parameter $c_{\mu 0}$ appears to be more strongly correlated with the average cone resistance $q_{c,av}$ (Figure V.17a), rather than the specific pile installation method;

– initial differences in lateral pile stiffness were attributed to the joint effect of the installation method and initial soil conditions. Such differences were both measured (field data) and simulated (1D FE model) to depend on the particular loading parcel applied and importantly to gradually vanish under the application of an increasing number of loading cycles. The two GDP-driven piles exhibited, on average, the largest cyclic lateral stiffness in comparison to the other MTPs.

The above conclusions do not include observations regarding the pile that was axially vibrated into substantially looser sand (VH). Describing the interaction between initial sand density and pile driving method will require additional experimental data and numerical modelling work. These and other open questions are currently being investigated in the framework of the SIMOX joint industry project.

VI

Conclusions

Since the construction of the first offshore wind turbine in Denmark (1991), the capacity to harvest offshore wind energy on Europe's coastline has increased by 28 GW. To foster the desired energy transition towards renewables, an additional 230-450 GW of offshore wind is required in Europe alone until 2050, while at the same time, 2000 GW of offshore wind energy is expected to be grid-connected worldwide (Lee et al., 2021). Such an unprecedented endeavor requires targeted academia-industry efforts to reduce the capital expenditure for investments in offshore wind by identifying and addressing existing knowledge gaps. In the same arena, this study attempts to bridge "costly" knowledge gaps, associated with the installation and operation of offshore wind turbines supported by the most prevalent foundation option in offshore wind, the large-diameter monopile.

In recent years, TU Delft has participated in two major experimental campaigns, each designed to address technical uncertainties associated with foundation monopiles. The DISSTINCT project (2014-2018) was designed to improve existing techniques for resonance frequency(-ies) identification, while the GDP project (2018-2022) was established to propose, engineer, and demonstrate a new monopile installation technology that remedies the installation-related challenges. Through the design of the experimental procedure (lateral load testing for the GDP field campaign), and with model-based interpretations of the available experimental measurements, this study was able to broaden the existing knowledge of soil-monopile interactions by bridging existing knowledge gaps. The main research achievements are presented in four journal papers, which at the time of writing are either published or under review. Following the structure of this thesis, the main conclusions are presented per chapter.

Frequency effects in the dynamic lateral stiffness of monopiles in sand: insight from field tests and 3D FE modelling*

Chapter II examines and interprets measurements from the DISSTINCT project, recorded on monopile MP45 (full-scale) and the surrounding sandy soil in the Dutch IJsselmeer lake. Test data revealed a substantially frequency-dependent lateral dynamic monopile stiffness at steady-state, featuring a three-fold reduction of $|K_{dyn}|$ (absolute value of the lateral dynamic stiffness of the monopile) at approximately 5.3 Hz (Figure II.6a), during the application of small amplitude lateral vibrations at the monopile head. To interpret such findings, 3D FE modelling was carried out in the OpenSees analysis platform (McKenna, 1997), by simulating the soil as a water-saturated, poroelastic† ($U-P$) medium (Zienkiewicz et al., 1999). The good agreement between experimental and numerical results (Figure II.13), enabled the interpretation of the experimental outcomes, and supported the following assertions:

- Linear elastic soil modelling is appropriate for geotechnical foundations under weak cyclic loading.
- Weak foundation vibrations can cause a buildup of pore pressures in sandy soils, which in turn can be successfully calculated with $U-P$ poroelastic FE modelling – Figure II.17.
- For the particular loading settings, the impact of hydraulic conductivity was found insignificant, even comparing the limit cases of drained and undrained conditions – Figure II.18.
- The FE-based interpretations indicated that the remarkable decrease in the lateral dynamic stiffness of the monopile, was caused by system (monopile-soil) resonance – Figures II.13-II.15.
- The examined resonance frequency of monopile foundations can be successfully identified using 3D FE modelling, even when soil properties are calibrated against commonly available geotechnical data (cone resistance from CPTs) – Figures II.2, II.9, II.12-II.14, II.17-II.18.
- Numerical eigenvalue analysis performed in the soil-monopile model, did not identify any particular natural frequency at the resonance peak at 5.5 Hz. The first observed and later calculated system resonance, was attributed to the added contribution of various participating modes in the vicinity of the excitation frequency – Figures II.12 - II.14.

* In 2022, this paper was awarded the prestigious David Hislop award from ICE, the Institution of Civil Engineers.
† Initial modelling attempts with the sophisticated SANISAND model (Dafalias and Manzari, 2004) revealed that the weak vibrations induced by the shaking device did not induce any meaningful plasticity in the soil.

– The foundation damping ratio was determined to be $\zeta = 16\%$ via 1dof fitting the measured response – Figure II.6b. Combined radiation and steel damping ($\zeta steel = 0.19\%$) in the 3D FE model, yielded similar, albeit lower foundation damping values. The reduced calculated dissipation was likely due to the disregard of hydrodynamic and soil damping (water table only at 4.4 m above the mudline and linear elastic soil) – Figure II.13.

Gentle Driving of Piles (GDP) at a sandy site combining axial and torsional vibrations: Part II - cyclic/dynamic lateral loading tests

Chapter III examines the lateral pile loading tests conducted for the GDP project, designed to compare installation technologies via the post-installation performance of piles. A total of nine piles were installed at a sandy site in the port of Rotterdam, consisting of eight test piles and one larger-diameter reaction pile. To facilitate the comparison of driving methods, four of the test piles (main test piles or MTPs) were first heavily instrumented and then installed in the soil with the GDP method – two piles, via impact piling – one pile, and vibratory driving – one pile. Post installation, the MPTs were loaded with the elaborate 82000-cycle, 42-hour loading programme shown in Figure III.7. The particular geotechnical conditions at the GDP site, i.e., site inhomogeneity (Figure III.3) and the 4 m deep unsaturated topsoil, hindered any attempt to compare directly the cyclic lateral performance of the main test piles. This study presents the lateral loading test procedure, along with the cyclicl lateral performance of the GDP-driven piles. The impact of unsaturated topsoil on the cyclic lateral pile behaviour is discussed in detail. Careful review of the experimental evidence in this study supports the following assertions:

– The unsaturated topsoil enabled the occurrence of pile-soil gapping, which manifested in the test results for instance, via locking-type force-displacement behaviour of the piles i.e., higher tangent stiffness with increasing lateral load – Figure III.9.

– During the cyclic loading programme, the maximum (pile-soil) gap depth (L_y) was calculated as deep as the unsaturated topsoil (4 m, or half the embedded pile length), inferred from measured pile bending moment profiles – Figures III.8, III.11b.

– Contrary to available experimental data from pile testing in dry sands (Abadie, 2015a; Klinkvort, 2012), the measured average lateral secant stiffness of the piles K_{av}^{cyc} decreased significantly during the first 2000 loading cycles. The stiffness drop was attributed on the abrupt widening of the pile-soil gap caused by the load increase during parcels $a-b$, later also re-confirmed via FE modelling in Chapter V – Figures III.14a, V.16b.

– Small-amplitude frequency sweeps (f-sweeps), had no observable impact on the overall cyclic performance of the piles, and were found to follow the locking-type backbone defined by the large amplitude cyclic loads (parcels $a-e$) – Figures III.16, III.17.

- In all instances the measured lateral stiffness during the small amplitude f-sweeps was higher compared to the tangent stiffness at equal forcing measured during the large amplitude cyclic loading –Figures III.16, III.17.
- In the range between 0.1-4 Hz, the frequency sweeps indicated a frequency-dependent lateral pile stiffness after parcel b (fully evolved gap), which was attributed to the reduced tangential stiffness caused by the observed locking-type behaviour around the particular forcing of the $(b-e)_{90}$ f-sweeps, with F_{av} = 90 kN – Figures III.17, III.18.
- Cyclic trends of lateral pile deflection have shown good compatibility with soil monitoring data, particularly with the variations in radial soil pressure that were recorded near the piles at different depths – Figure III.10.
- The normalized lateral performance of the GDP-driven piles on monotonic loading was found reasonably comparable to the DS4 and DM3 piles from the PISA project (McAdam et al., 2020) despite the differences in soil conditions and load eccentricity – Figure III.6b.
- The response of the four GDP-driven piles (two additional auxiliary piles were monotonically loaded) is remarkably similar at the onset of lateral loading despite differences in the soil profiles. This remark indicates a possible influence of the installation procedure on the lateral pile performance at low amplitudes immediately after pile installation – reconfirmed in Chapter V when compared to the other main test piles – Figures III.3, III.12, V.15.
- The response of the GDP-driven piles was found favorable compared to the impact- and axial vibro-driven piles, in that they displaced less (laterally) during the 82.000 load cycles – Figure III.10a.

A memory-enhanced $p-y$ model for piles in sand accounting for cyclic ratcheting and gapping effects

Chapter IV presents a CPT-based cyclic soil reaction model for $p-y$ soil-pile interactions in both unsaturated and saturated/dry soil conditions. This study takes further the previous work of Suryasentana and Lehane (Suryasentana and Lehane, 2016), who proposed a monotonic $p-y$ relationship for piles in sand along with a CPT-based parameter calibration procedure. To enable the simulation of cyclic soil-monopile interactions, the $p-y$ relationship was first reformulated as a bounding surface plasticity model with kinematic hardening (Dafalias, 1986), and later extended to include (i) a memory surface for the control of cyclic ratcheting (Corti et al., 2016; Liu et al., 2019b), and (ii) additional soil reaction elements (Figure IV.5) for the detailed modelling of pile-soil gapping effects. In this study, the cyclic $p-y$ model was implemented in the OpenSees analysis platform (McKenna, 1997) and used to simulate the behaviour of the impact-driven main test pile (Figure IV.11) in the

GDP lateral loading field tests, presented in Chapter III. The following statements can be derived from this work:

- The cyclic response of the impact-driven pile was successfully simulated with the proposed cyclic soil reaction model, despite the challenging geotechnical and test conditions i.e., the unsaturated topsoil and the elaborate cyclic loading programme in Figure IV.12b. The satisfactory calculation of cyclic deflection accumulation trends and bending moment profiles at selected instances is presented in Figures IV.13, IV.16, IV.17.

- Re-tuning the suggested settings from the CPT-based calibration procedure proposed in by Suryasentana and Lehane (Suryasentana and Lehane, 2016), was necessary to fit the monotonic pile performance in the GDP field – Figure IV.15.

- A calibration procedure for the ratcheting coefficient μ_0, based on the in-situ mean effective stress – Equation (IV.31), was proposed. Improved calibration strategies for both monotonic and cyclic parameters of the proposed model can only be achieved via a rich experimental dataset, currently pursued within the framework of the MIDAS project (Pisanò et al., 2022a).

Gentle Driving of Piles (GDP) at a sandy site combining axial and torsional vibrations: quantifying the influence of pile installation method on lateral behaviour

Chapter V presents a quantitative analysis of the installation effects observed in the pile test data recorded in the post-installation GDP field tests. Due to the inhomogeneity of the foundation soil and the added complexity from the occurrence of pile-soil gapping, a purely data-based comparison would not have been comprehensive and was initially avoided (in Chapter III). For these reasons, installation technologies were ultimately compared by employing the elasto-plastic cyclic soil reaction model presented in Chapter V – based on Kementzetzidis et al., 2022 with the addition of finite elastic stiffness. By simulating the response for each pile, relevant installation effects were quantitatively derived from the values of key $p-y$ calibration parameters. From this work, the following statements can be derived:

- The cyclic soil reaction model presented in Chapter IV combined with an elastic in-series spring, enabled the successful simulation of the cyclic pile performance in the GDP field tests – Figures V.16, V.18, V.19, V.20, V.21, V.22.

- laterally loaded piles may exhibit significant installation effects during loading phases that are immediately post-installation (re-confirming the findings in Chapter III, Figure III.12), especially for relatively low lateral load amplitudes (say, less than 15% of the monotonic capacity), but also after application of many loading cycles, in

that noticeable differences are present in the residual accumulated lateral deflection (Figures V.6, V.15).

– For the piles installed in medium-dense to dense sand, the GDP method led to an estimated lateral capacity ≈ 15% higher than for a pile hammered by impact at an identical soil location.

– by normalising the cyclic behaviour of the MPTs to their peak monotonic displacement during parcel a, the displacement accumulation trends assemble themselves in a manner that highlights a strong correlation to the soil profile features (Figure V.1, V.17b). This finding is further supported by the modeling calibration options, in that, when accounting for the installation effects identified by the monotonic pile behaviour (calibration of p_u), the $C_{\mu 0}$ values do not correlate well with the installation method but rather with the average cone resistance $q_{c,av}$ (Figure V.17a).

– initial differences in lateral pile stiffness were attributed to the joint effect of installation method and initial soil conditions. Such differences were found to asymptotically vanish (to a value reflecting the particular applied cyclic loads) under the application of an increasing number of loading cycles (Figures V.9, V.16b, V.23c). The two GDP-driven piles exhibited, on average, largest cyclic lateral stiffness in comparison to the other MTPs.

1. Future work

Chapters II-V contain in-depth analysis of soil-(mono)pile interactions targeted to resolve important engineering and technical challenges for offshore wind. Particularly, the presented work addresses uncertainties concerning the dynamic soil-(mono)pile interactions relevant to the resonance frequencies of offshore wind turbines, and the impact of installation technologies on the post-installation (mono)pile performance under long-term environmental loads. Adding to the soundness of the presented work, all the assertions made herein are based on experimental observations, interpreted via numerical modelling. Despite the above achievements, questions about certain aspects of monopile-soil interactions remain unanswered, while modelling tools could certainly further improve leaving room for future work:

– For the interpretation of the DISSTINCT field measurements, the soil was modelled as a poroelastic $U-P$ medium (Zienkiewicz et al., 1980). An improvement in the simulation accuracy would be achieved by modelling the soil as a $u-P-U$ medium, which also accounts for the relative acceleration between soil and fluid and naturally introduces velocity-proportional energy dissipation.

– Due to the very low amplitude of the applied cyclic loads, linear soil modelling was adopted in the simulation of the DISSTINCT field tests in Chapter II. The use of

cyclic plasticity models with zero elastic range (Dafalias and Taiebat, 2016; Pisanò and Jeremić, 2014) could potentially improve the simulation results.

– The DISSTINCT field tests in Chapter II were set to identify the resonance frequency of monopiles on small amplitude lateral vibrations on the monopile head. Similar tests could be repeated in the future with higher amplitude vibrations to detect changes in the resonance frequencies during storm events, previously simulated in (Kementzetzidis et al., 2019), which can be quite meaningful for the calculation of the fatigue life of OWTs.

– The unsaturated topsoil in the GDP field tests had a considerable impact on the test results both during pile driving and in the post-installation lateral pile behaviour. Similar test protocols in (more) uniform saturated sands at medium- and/or at full-scale, would have been more representative of offshore geotechnical conditions, and are currently explored within the framework of the SIMOX joint industry project.

– In the GDP field tests, the limitations of the loading frame permitted the application of one-way cyclic loads. Offshore monopiles are subjected to multi-directional loading conditions which can have an appreciable impact on the observed response (Richards et al., 2020), including the so-called 'self - healing' effects (Theodoros et al., 2009) – the progressive relaxation of accumulated displacements following strong loading events. Comprehensive numerical and experimental studies on the topic will reduce the engineering uncertainty for the long-term response of offshore wind turbines.

– The installation effects of piles in the GDP field were inferred from the measured response of the main test piles. Simulation of the installation process has already been demonstrated with FE or MPM simulations in Fan et al., 2021d; Martinelli and Galavi, 2022; Staubach et al., 2020, but was not pursued due to the additional complexity it would have brought (largely incompatible with the timing of the present doctoral study). Regardless, simulation of the installation process in the GDP field could close knowledge gaps on the impact of installation technologies, even in unsaturated soils.

– To enable the simulation of the GDP field experiments in Chapter V, some assumptions in the selection of constitutive parameters were necessary due to the lack of independent data for calibration. Future attempts should focus on providing improved CPT-based calibration procedures, particularly for parameters that enable the simulation of cyclic loading conditions in both marine and onshore environments. Such attempts are currently ongoing within the framework of the MIDAS project (Pisanò et al., 2022a), supported by elaborate centrifuge testing and 3D FE modelling with the SANISAND-MS model (Liu et al., 2019b).

– It is already established that modelling of lateral monopile-soil interactions requires the modelling of reaction mechanisms so far neglected in the simulation of flexible

beams i.e., the distributed moment caused by shear tractions along the pile shaft, and the base moment and shear reactions (Byrne et al., 2019; Davidson, 1982; Gerolymos and Gazetas, 2006; Lam and Martin, 1986). Precise modelling of the cyclic behaviour of such reactions would be very beneficial for the geo-community, a feature currently explored within the framework of the MIDAS project (Pisanò et al., 2022a).

– The widely adopted $p-y$ relationships are frequently updated to expand their range of application to include additional pile geometries and geotechnical/loading conditions. To a considerable extent, such updates are necessary due to the simplifying modelling assumption of locality i.e., soil reactions occur independently across the monopile length. Linear, non-local $p-y$ reactions have already been proposed in Versteijlen et al., 2017a, but extensions of such methods for nonlinear soil-monopile interactions would be considered an important step forward.

Nomenclature

Introduction

D	monopile diameter
F	applied load amplitude
f	frequency
L	monopile length
L_{emb}	embedded monopile depth
m	distributed moment soil reaction
N	number of cycles
p	lateral soil reaction
t	time
y	lateral pile displacement
θ	beam rotation angle
ϕ	peak sand friction angle

Paper I

A	amplification factor
C^{1dof}	viscous damping coefficient for the equivalent 1dof system
D	Soil stiffness tensor (D_{ijkl})
D_R	soil relative density
E	Young's modulus of elasticity
$\bar{E}$	1D (oedometer) stiffness modulus
F	applied load amplitude
f	frequency

f_s	CPT sleeve friction
f_n	n^{th} natural frequency of the soil deposit
f_{res}	resonance frequency
G	transfer function
g	Earth's gravity acceleration
H_w	water depth
K_{dyn}	lateral dynamic stiffness of the monopile
$\lvert K_{dyn}^{1dof} \rvert$	absolute value of the dynamic stiffness of the equivalent 1dof system
K_0^{1dof}	static stiffness of the equivalent 1dof system
K_f	fluid bulk modulus
K_s	soil grains bulk modulus
$k,\ k'$	soil permeability coefficients in the static and dynamic versions of Darcy law
L	monopile length
L_{emb}	embedded monopile length
M^{1dof}	mass of the equivalent 1dof system
M_{sh}	lumped shaker mass
m_e	rotating mass
n	soil porosity
p_w	pore water pressure
q_c	CPT cone resistance
R	lever arm
t	time
U	shaker displacement
u	soil displacement
$\bar{U}$	shaker steady-state displacement amplitude

$\bar{u}$	soil steady-state displacement amplitude
u_{inp}	bedrock steady-state displacement amplitude
u_{static}	static soil displacement
V_s	shear wave velocity
β, γ	Newmark's time integration parameters
Γ_i	modal participation factor associated with ith mode
Δp_w	pore water pressure variation
ε	axial strain
ζ^{1dof}	damping ratio of the equivalent 1dof system
ζ_{steel}	steel damping ratio
ν	soil Poisson's ratio
ρ	saturated mass density for sand
ρ_f	mass density of pore fluid
ρ_s	mass density of soil grains
σ, σ'	soil stress tensor (total and effective)
ϕ	phase difference/angle
Ω	angular excitation/loading frequency
ω_i	eigenfrequency associated with ith mode

Paper II

D	pile diameter
D_r	relative density
e	eccentricity
E_D	stored elastic energy
E_S	plastic work
$\tilde{F}$	normalised load amplitude
F	applied load amplitude

f	frequency
F_{av}	average load amplitude
F_{cyc}	cyclic load amplitude
f_{res}	resonance frequency
h	pile wall thickness
$\lvert K_{dyn} \rvert$	absolute value of the lateral dynamic stiffness
k_h	horizontal hydraulic conductivity
K_0	static stiffness
K_{cyc}^{av}	average secant lateral cyclic stiffness
K_{cyc}^{cg}	closed-gap tangential lateral cyclic stiffness
K_{cyc}^{og}	open-gap tangential lateral cyclic stiffness
K_{cyc}^{tan}	tangential lateral cyclic stiffness
L	pile length
L_e	embedded pile length
L_x	pile-soil gap breadth
L_y	pile-soil gap depth
$L_{x,max}$	maximum pile-soil gap breadth
M	bending pile moment
N	number of cycles
p_a	atmospheric pressure
p_w	pore water pressure
q_c	cone penetration resistance
t	time
$\tilde{U}$	normalised pile displacement
U	pile displacement
V_s	shear wave velocity

z	soil depth coordinate (under ground surface)
$\Delta\sigma_r$	variation of radial soil stress
Δp_w	variation of pore water pressure
γ'	soil's buoyant unit weight
σ_r	radial soil stress
ξ	damping ratio

Paper III

α, m	shape parameters – memory and drag springs
α_c, m_c	shape parameters – closure spring
α_d^r	shape parameter – drag spring
$\alpha_{sp}, M_{sp}, \beta_{sp}$	shape parameters – separation spring
b_M	distance between soil reaction and memory locus
b_{ref}	reference distance in soil reaction space
C_d	Scalar parameter for the modulation of $p_{u,d}$
C_p , μ_c	scalar parameters for the calibration of μ_0
D	pile diameter
D_r	sand relative density
$\mathrm{d}\lambda$	plastic multiplayer
$\mathrm{d}p_\alpha$	increment of back stress
$\mathrm{d}p$	lateral soil reaction increment
$\mathrm{d}y$	strain increment
$\mathrm{d}y_e$	elastic strain increment
$\mathrm{d}y_p$	plastic strain increment
E	Young's modulus of elasticity
F	applied load amplitude
f	frequency and yield function

F_{av}	average load amplitude
F_{cyc}	cyclic load amplitude
F_M	memory function
F_{max}	maximum load amplitude
F_{min}	minimum load amplitude
G	shear modulus
H	hardening modulus
h	pile wall thickness
H_M	memory enhanced hardening modulus
$\tilde{H}_M$	hardening modulus of the memory locus
I	moment of inertia
K	elastic spring stiffness
K_{av}^{cyc}	average secant lateral pile stiffness
K_{50}	Spring stiffness at 50% of $p_{u,m}$ – separation spring
k_{sp}	spring stiffness – separation spring
K_{tang}	tangent lateral pile stiffness
L	left spring component
L	pile length
L_e	embedded pile length
M	bending pile moment
μ_0	ratcheting parameter
N	number of cycles
p	lateral soil reaction
p_α	back stress
$p_{\alpha,M}$	memory back stress
$p_{c,max}$	maximum spring reaction – closure spring

p_c	spring reaction – closure spring
p_d	spring reaction – drag spring
p_M	size of memory locus
$\bar{p}_M$	projection of p_M along dp
p_M^{cur}	current size of the memory locus
$\tilde{p}_M$	projection of p on memory locus
p_s	spring reaction – soil spring
p_{sp}	spring reaction – separation spring
p_0	spring reaction at load reversal – memory spring
p_u	limit soil reaction
$p_{u,m}$	limit soil reaction – memory spring
$\bar{p}_u$	projection of p_u along dp – memory spring
$p_{u,d}$	limit spring reaction – drag spring
p_y	size of yield locus
q_c	CPT cone resistance
R	right spring component
t	time
U	pile displacement at the soil surface
u_g	hydrostatic pore pressure at ground surface
U_{max}	maximum pile displacement at soil surface
U_{min}	minimum pile displacement at soil surface
V_s	shear wave velocity
y	lateral pile displacement
y_{max}	maximum lateral pile displacement
y_{ref}	maximum pile displacement at monotonic loading
$\dot{y}$	lateral pile displacement increment

$y_g, y_{g,0}, y_g^r$	spring deflection and deflection history parameters – gap spring
$y_g, y_{g,0}, y_g^r$	spring deflection and deflection history parameters – gap spring
y_s	spring deflection – soil spring
$y_{s,max}$	maximum spring deflection – soil spring
z	depth
z_0	selected depth for measurement of beam slope
Δz	$p-y$ spring spacing
ϵ_{zz}	axial strain
ϕ	beam rotation angle
κ	shear coefficient for Timoshenko beams
ν	Poisson's ratio of steel
γ_{dry}	dry unit weight of soil
$\sigma_{v0}, \sigma'_{v0}$	in-situ total and effective vertical stress
$\bar{\sigma}'_0$	in-situ mean effective stress
$\bar{\sigma}_{ref}$	reference pressure

Paper IV

α, m	shape parameters – memory and drag springs
α_c, m_c	shape parameters – closure spring
b_M	distance between soil reaction and memory locus
b_{ref}	reference distance in soil reaction space
C_d	Scalar parameter for the modulation of $p_{u,d}$
$C_{\mu 0}$	CPT-based calibration parameter for μ_0
C_{pu}	CPT-based calibration parameter for p_u
D	pile diameter
D_r	sand relative density
$\mathrm{d}p$	lateral soil reaction increment

e	load eccentricity
E_b	consumed energy per blow – impact driving
F	applied load amplitude
f	frequency
f_{ax}	axial driving frequency – vibratory driving
f_{tor}	torsional driving frequency – GDP vibratory driving
F_{max}	maximum load amplitude
F_{min}	minimum load amplitude
F_{ult}	lateral pile capacity
G	frequency response function
H	hardening modulus
h	pile wall thickness
H_M	memory enhanced hardening modulus
K_{av}^{cyc}	average secant lateral pile stiffness
k_e	elastic spring stiffness
K_p	plastic modulus stiffness
$K_{p,M}$	plastic modulus of the memory enhanced spring
L	pile length
L_e	embedded pile length
M	bending pile moment
me	eccentric moment – vibratory driving
μ_0	ratcheting parameter
N	number of cycles
N_b	number of blows per minute – impact driving
p	lateral soil reaction
$p_{c,max}$	maximum spring reaction – closure spring

p_c	spring reaction – closure spring
p_0	spring reaction at load reversal – memory spring
p_u	limit soil reaction
$\bar{p_u}$	projection p_u along dp – memory spring
$p_{u,d}$	limit spring reaction – drag spring
q_c	CPT cone resistance
$q_{c,av}$	average CPT cone resistance for pile length
t	time
U	pile displacement at the soil surface
u_g	hydrostatic pore pressure at ground surface
U_{mon}	peak monotonic pile displacement at the soil surface
U_{max}	maximum pile displacement at soil surface
U_{min}	minimum pile displacement at soil surface
V_s	shear wave velocity
y	lateral pile displacement
y_{max}	maximum lateral pile displacement
y_{ref}	maximum lateral pile displacement at monotonic loading
$\dot{y}$	lateral pile displacement increment
Δz	$p-y$ spring spacing
γ_{dry}	dry unit weight of soil
$\sigma_{v0}, \sigma'_{v0}$	in-situ total and effective vertical stress
$\sigma'_{v,ref}$	reference effective vertical stress

Conclusions

F_{av}	average pile load
K_{av}^{cyc}	average secant lateral pile stiffness
L_y	pile-soil gap depth

q_c	CPT cone resistance
μ_0	ratcheting parameter
ζ	damping ratio
ζ_{steel}	steel damping ratio

Bibliography

References for Chapter I

Abadie, C. N. (2015a). *Cyclic lateral loading of monopile foundations in cohesionless soils* (DPhil thesis). University of Oxford. Oxford, UK.

Abdullahi, A., Bhattacharya, S., Li, C., Xiao, Y., & Wang, Y. (2022). Long term effect of operating loads on large monopile-supported offshore wind turbines in sand. *Ocean Engineering*, *245*, 110404.

Achmus, M., Schmoor, K. A., Herwig, V., & Matlock, B. (2020). Lateral bearing behaviour of vibro-and impact-driven large-diameter piles in dense sand. *geotechnik*, *43*(3), 147–159.

Albiker, J., Achmus, M., Frick, D., & Flindt, F. (2017). 1 g model tests on the displacement accumulation of large-diameter piles under cyclic lateral loading. *Geotechnical Testing Journal*, *40*(2), 173–184.

Anusic, I., Lehane, B., Eiksund, G., & Liingaard, M. (2019). Influence of installation method on static lateral response of displacement piles in sand. *Géotechnique Letters*, *9*(3), 193–197.

API, R. (2011). 2GEO (2011). *Recommended Practice for Geotechnical Foundation Design Consideration*.

Arany, L., Bhattacharya, S., Macdonald, J., & Hogan, S. (2017b). Design of monopiles for offshore wind turbines in 10 steps. *Soil Dynamics and Earthquake Engineering*, *92*, 126–152.

Barkan, D. Developments in soil dynamics. In: In *International Symposium on Wave Propagation and Dynamic Properties of Earth Materials, Univ. of New Mexico Press*. Albuquerque, New Mexico, 1967, 599–606.

Beuckelaers, W., Burd, H., Houlsby, G., McAdam, R., & Byrne, B. (2020). A generalised Winkler model for the hysteretic and ratcheting behaviour of monopiles in clay and sand. In Z. Westgate (Ed.), *In Frontiers in Offshore Geotechnics IV: Proceedings of the 4th International Symposium on Frontiers in Offshore Geotechnics (ISFOG 2021)*. Houston, TX, USA (pp. 1263–1272). Leiden, the Netherlands: CRC Press/Balkema.

Byrne, B. W., Aghakouchak, A., Buckley, R. M., Burd, H. J., Gengenbach, J., Houlsby, G. T., McAdam, R. A., Martin, C. M., Schranz, F., Sheil, B. B., & Suryasentana, S. K. (2020a). PICASO: Cyclic lateral loading of offshore wind turbine monopiles. In Z. Westgate (Ed.), *Frontiers in Offshore Geotechnics IV: Proceedings of the 4th International Symposium on Frontiers in Offshore Geotechnics (ISFOG 2021)*. Houston, TX, USA (pp. 1526–1535). Leiden, the Netherlands: CRC Press/Balkema.

Byrne, B. W., Burd, H. J., Zdravkovic, L., Abadie, C. N., Houlsby, G. T., Jardine, R. J., Martin, C. M., McAdam, R. A., Pacheco Andrade, M., Pedro, A. M., et al. PISA Design Methods for Offshore Wind Turbine Monopiles. In: In *Offshore Technology Conference*. Houston, TX, USA. 2019, paper OTC-29373–MS.

Byrne, B. W., McAdam, R. A., Beuckelaers, W. J., Burd, H. J., Gavin, K., Houlsby, G. T., Igoe, D. J. P., Jardine, R., Martin, C. M., et al. (2020b). Cyclic laterally loaded medium scale field pile testing for the PISA project. In Z. Westgate (Ed.), *Frontiers in Offshore Geotechnics IV: Proceedings of the 4th International Symposium on Frontiers in Offshore Geotechnics (ISFOG 2021)*. Austin, TX, USA (pp. 1323–1332). Leiden, the Netherlands: CRC Press/Balkema.

Choi, J. I., Kim, M. M., & Brandenberg, S. J. (2015). Cyclic p-y Plasticity Model Applied to Pile Foundations in Sand. *Journal of Geotechnical and Geoenvironmental Engineering*, *141*(5), 04015013.

Corti, R., Diambra, A., Wood, D. M., Escribano, D. E., & Nash, D. F. (2016). Memory surface hardening model for granular soils under repeated loading conditions. *Journal of Engineering Mechanics*, *142*(12), 04016102.

Dafalias, Y. F., & Manzari, M. T. (2004). Simple plasticity sand model accounting for fabric change effects. *Journal of Engineering mechanics*, *130*(6), 622–634.

Davidson, H. (1982). *Laterally loaded drilled pier research. Volume 1: design methodology. Final report.[PADLL]* (tech. rep.). GAI Consultants, Inc., Monroeville, PA (USA).

Dıaz, H., & Soares, C. G. (2020). Review of the current status, technology and future trends of offshore wind farms. *Ocean Engineering*, *209*, 107381.

DNVGL (Det Norske Veritas GL). (2016). *DNVGL-ST-0126: Support structures for wind turbines*. DNV GL Group. Høvik, Norway.

Dyson, G., & Randolph, M. Installation effects on lateral load-transfer curves in calcareous sands. Tokyo, Japan. In: In *Centrifuge 98*. Tokyo, Japan: Brookfield, VT, USA/Rotterdam, the Netherlands: A.A. Balkema, 1998, 545–550.

Esteban, M. D., Diez, J. J., López, J. S., & Negro, V. (2011). Why offshore wind energy? *Renewable Energy*, *36*(2), 444–450.

Etheridge, D., Steele, L., Langenfelds, R., Francey, R., Barnola, J., & Morgan, V. (1998). Historical CO2 records from the Law Dome DE08, DE08-2, and DSS ice cores. *Trends: a compendium of data on global change*, 351–364.

Fan, S., Bienen, B., & Randolph, M. F. (2021a). Centrifuge study on effect of installation method on lateral response of monopiles in sand. *International Journal of Physical Modelling in Geotechnics*, *21*(1), 40–52.

Feinstein, C. H. (1998). Pessimism perpetuated: real wages and the standard of living in Britain during and after the industrial revolution. *The Journal of Economic History*, *58*(3), 625–658.

Fischer, H., Wahlen, M., Smith, J., Mastroianni, D., & Deck, B. (1999). Ice core records of atmospheric CO2 around the last three glacial terminations. *Science*, *283*(5408), 1712–1714.

Frick, D., & Achmus, M. (2019). Model Tests on the Displacement Accumulation of Monopiles Subjected to General Cyclic Loading. In N. Goseberg & T. Schlurmann (Eds.), *Proceedings of Coastal Structures 2019, Karlsruhe: Bundesanstalt für Wasserbau* (pp. 913–922).

Gaertner, E., Rinker, J., Sethuraman, L., Zahle, F., Anderson, B., Barter, G. E., Abbas, N. J., Meng, F., Bortolotti, P., Skrzypinski, W., et al. (2020). *IEA wind TCP task 37: definition of the IEA 15-megawatt offshore reference wind turbine* (tech. rep.). National Renewable Energy Lab.(NREL), Golden, CO (United States).

Gerolymos, N., & Gazetas, G. (2006). Development of Winkler model for static and dynamic response of caisson foundations with soil and interface nonlinearities. *Soil Dynamics and Earthquake Engineering*, *26*(5), 363–376.

Heins, E., & Grabe, J. (2017). Class-A-prediction of lateral pile deformation with respect to vibratory and impact pile driving. *Computers and Geotechnics*, *86*, 108–119.

Herwig, V., & Gattermann, J. (2015). VIBRO-Project–Vergleich der lateralen Tragfähigkeit von vibrierten und geschlagenen Stahlpfählen in sandigen Böden. *Pfahl-Symposium*, *19*(20.02), 2015.

(IMF), I. M. F. (2000). The world economy in the twentieth century: Striking developments and policy lessons. *World Economic Outlook*, 149–180.

Indermühle, A., Monnin, E., Stauffer, B., Stocker, T. F., & Wahlen, M. (2000). Atmospheric CO2 concentration from 60 to 20 kyr BP from the Taylor Dome ice core, Antarctica. *Geophysical Research Letters*, *27*(5), 735–738.

Kallehave, D., Byrne, B. W., LeBlanc Thilsted, C., & Mikkelsen, K. K. (2015a). Optimization of monopiles for offshore wind turbines. *Philosophical Transactions of the Royal Society A: Mathematical, Physical and Engineering Sciences*, *373*(2035), 20140100.

Kallehave, D., Thilsted, C., & Troya, A. (2015b). Observed variations of monopile foundation stiffness. In M. Vaughan (Ed.), *Frontiers in Offshore Geotechnics III: Proceedings of the 3rd International Symposium on Frontiers in Offshore Geotechnics (ISFOG 2015)*. Austin, TX, USA (pp. 717–722). Leiden, the Netherlands: CRC Press/Balkema.

Keeling, C., & Whorf, T. (1994). Atmospheric CO2 records from sites in the SIO air sampling network. *Trends*, *93*, 16–26.

Kementzetzidis, E., Corciulo, S., Versteijlen, W. G., & Pisanò, F. (2019). Geotechnical aspects of offshore wind turbine dynamics from 3D non-linear soil-structure simulations. *Soil Dynamics and Earthquake Engineering*, *120*, 181–199.

Kementzetzidis, E., Metrikine, A. V., Versteijlen, W. G., & Pisanò, F. (2021). Frequency effects in the dynamic lateral stiffness of monopiles in sand: insight from field tests and 3D FE modelling. *Géotechnique*, *71*(9), 812–825.

Kementzetzidis, E., Pisanò, F., Elkadi, A. S., Tsouvalas, A., & Metrikine, A. V. (2023a). Gentle Driving of Piles (GDP) at a sandy site combining axial and torsional vibrations: Part II - cyclic/dynamic lateral loading tests. *Ocean Engineering*, *270*, 113452.

Kementzetzidis, E., Pisanò, F., & Metrikine, A. V. (2022). A memory-enhanced $p - y$ model for piles in sand accounting for cyclic ratcheting and gapping effects. *Computers and Geotechnics*, *148*, 104810.

Kementzetzidis, E., Pisanò, F., Tsetas, A., & Metrikine, A. V. (2023b). Gentle Driving of Piles (GDP) at a sandy site combining axial and torsional vibrations: quantifying the influence of pile installation method on lateral behaviour. *Journal of Geoenvironmental and Geotechnical Engineering, under review*, –, 0–0.

Kementzetzidis, E., Versteijlen, W. G., Nernheim, A., & Pisanò, F. (2018). 3D FE dynamic modelling of offshore wind turbines in sand: Natural frequency evolution in the pre-to after-storm transition. In A. S. Cardoso, J. L. Borges, P. A. Costa, A. T. Gomez, J. C. Marques & C. S. Vieira (Eds.), *Numerical Methods in Geotechnical Engineering IX, Volume 2*. Porto, Portugal (pp. 1477–1484). Florida, USA: CRC Press.

Klinkvort, R. T. (2012). *Centrifuge modelling of drained lateral pile-soil response* (Doctoral dissertation). The Technical University of Denmark, DTU Civil Engineering. Lyngby, Denmark.

Klinkvort, R. T., Leth, C. T., & Hededal, O. (2010). Centrifuge modelling of a laterally cyclic loaded pile. In S. Springman, J. Laue & L. Steward (Eds.), *Proceedings of the 7th International Conference on Physical Modelling in Geotechnics (ICPMG 2010)*. Zurich, Switzerland (pp. 959–964). London, UK: Taylor & Francis London.

Komusanac, I., Brindley, G., Fraile, D., & Ramirez, R. (2022). Wind energy in Europe: 2021 Statistics and the outlook for 2022-2026. *WindEurope*.

Labenski, J., & Moormann, C. (2019). Lateral bearing behaviour of vibratory-driven monopiles: a modified py approach based on experimental observations of scaled model tests. Reykjavik, Iceland. In M. Hamza, M. Shahien & Y. El-Mossallamy (Eds.), *Proc. of 17th European Conf. on Soil Mechanics and Geotechnical Engineering*. Amsterdam, the Netherlands: IOS Press BV.

Lam, I., & Martin, G. (1986). *Seismic Design of High-Way Bridge Foundations. US Department of Transportation* (tech. rep.). Report No. FHWA/RD-86/102.

Lammertz, P. (2003). Field studies on bearing capacity of vibratory and impact driven piles. *International Young Geotechnical Engineers' Conference (IYGEC)*. Mamaia, Romania.

LeBlanc, C. (2014). Vibro-Driving Monopiles — A Feasible Installation Concept for the Future? *Danish Geotechnical Society Seminar, Gentofte, Denmark, April*, *1*.

LeBlanc, C., Houlsby, G., & Byrne, B. (2010). Response of stiff piles in sand to long-term cyclic lateral loading. *Géotechnique*, *60*(2), 79–90.

Lee, J., Zhao, F., & Dutton. (2021). Global Offshore Wind Report 2021. *GWEC (Global Wind Energy Council)*.

Li, W., Igoe, D., & Gavin, K. (2014). Evaluation of CPT-based P–y models for laterally loaded piles in siliceous sand. *Géotechnique Letters*, *4*(2), 110–117.

Li, W., Igoe, D., & Gavin, K. (2015). Field tests to investigate the cyclic response of monopiles in sand. *Proceedings of the Institution of Civil Engineers - Geotechnical Engineering*, *168*(5), 407–421. https://doi.org/10.1680/jgeen.14.00104.

Liu, H. (2020). *Constitutive modelling of cyclic sand behaviour for offshore foundations* (Doctoral dissertation). Delft University of Technology. Delft, the Netherlands.

Liu, H. Y., Abell, J. A., Diambra, A., & Pisanò, F. (2019b). Modelling the cyclic ratcheting of sands through memory-enhanced bounding surface plasticity. *Géotechnique*, *69*(9), 783–800.

Liu, H.-y., & Kaynia, A. M. (2022). Monopile responses to monotonic and cyclic loading in undrained sand using 3D FE with SANISAND-MSu. *Water Science and Engineering*, *15*(1), 69–77.

Liu, H., Kementzetzidis, E., Abell, J. A., & Pisanò, F. (2021). From cyclic sand ratcheting to tilt accumulation of offshore monopiles: 3D FE modelling using SANISAND-MS. *Géotechnique*, 1–16.

Liu, H., Pisanò, F., Jostad, H. P., & Sivasithamparam, N. (2022). Impact of cyclic strain accumulation on the tilting behaviour of monopiles in sand: An assessment of the Miner's rule based on SANISAND-MS 3D FE modelling. *Ocean Engineering*, *250*, 110579.

Loucks, D. P. (2021). Impacts of climate change on economies, ecosystems, energy, environments, and human equity: A systems perspective. In *The Impacts of Climate Change* (pp. 19–50). Elsevier.

Lüthi, D., Le Floch, M., Bereiter, B., Blunier, T., Barnola, J.-M., Siegenthaler, U., Raynaud, D., Jouzel, J., Fischer, H., Kawamura, K., et al. (2008). High-resolution carbon dioxide concentration record 650,000–800,000 years before present. *nature*, *453*(7193), 379–382.

Mazza, N., & Holeyman, A. (2019). Frequency-Penetration Response Spectrum on Vibratory Amplitude Matching of Monopiles. In P. Bullock, G. Verbeek, D. Tara & S. Paikowsky (Eds.), *10th International Conference on Stress Wave Theory and Testing Methods for Deep Foundations*. San Diego, California, USA.

Metrikine, A., Tsouvalas, A., Segeren, M., Elkadi, A., Tehrani, F., Gómez, S., Atkinson, R., Pisanò, F., Kementzetzidis, E., Tsetas, A., Molenkamp, T., van Beek, K., & P, D. (2020). GDP: a new technology for Gentle Driving of (mono)Piles. In Z. Westgate (Ed.), *Frontiers in Offshore Geotechnics IV: Proceedings of the 4th International Symposium on Frontiers in Offshore Geotechnics (ISFOG 2021)*. Austin, TX, USA (pp. 736–745). Leiden, the Netherlands: CRC Press/Balkema.

Mosher, R. L. (1987). *Comparison of Axial Capacity of Vibratory-Driven Piles to Impact-Driven Piles.* (tech. rep.). Engineer Research and Development Center (ERDC).

Mosher, R. L. (1990). Axial capacity of vibratory-driven piles versus impact-driven piles. *Transportation Research Record*, (1277).

Niemunis, A., Wichtmann, T., & Triantafyllidis, T. (2005). A high-cycle accumulation model for sand. *Computers and geotechnics*, *32*(4), 245–263.

Nijsse, F. (2018). CC BY-SA 3.0 <https://creativecommons.org/licenses/by-sa/3.0>, via Wikimedia Commons.

Norén-Cosgriff, K., & Kaynia, A. M. (2021). Estimation of natural frequencies and damping using dynamic field data from an offshore wind turbine. *Marine Structures*, *76*, 102915.

Novello, E. (1999). From static to cyclic py data in calcareous sediments. In K. Al-Shafei (Ed.), *Proc. 2nd Int. Conf. on Engineering for Calcareous Sediments.* Bahrain (pp. 17–24). Rotterdam, the Netherlands: Balkema.

Pisanò, F., Askarinejad, A., Wang, H., Maghsoodi, S., Gavin, K. G., Segeren, M. L. A., Elkadi, A. S. K., de Lange, D., & Konstadinou, M. (2022a). MIDAS: Monopile Improved Design through Advanced cyclic Soil modelling. *Proceedings of 20th International Conference on Soil Mechanics and Geotechnical Engineering (ICSMGE2022)*. Sydney, Australia.

Ramırez, L., Fraile, D., & Brindley, G. (2021). Offshore wind in Europe: Key trends and statistics 2020. *WindEurope*.

Richards, I., Bransby, M., Byrne, B., Gaudin, C., & Houlsby, G. (2021). Effect of stress level on response of model monopile to cyclic lateral loading in sand. *Journal of Geotechnical and Geoenvironmental Engineering*, *147*(3), 04021002.

Richards, I. (2019). *Monopile foundations under complex cyclic lateral loadings* (DPhil thesis). University of Oxford. Oxford, UK.

Rodger, A., & Littlejohn, G. (1980). A study of vibratory driving in granular soils. *Géotechnique*, *30*(3), 269–293.

Rudolph, C., Bienen, B., & Grabe, J. (2014). Effect of variation of the loading direction on the displacement accumulation of large-diameter piles under cyclic lateral loading in sand. *Canadian Geotechnical Journal*, *51*(10), 1196–1206.

Staubach, P., & Machaček, J. (2019). Influence of relative acceleration in saturated sand: Analytical approach and simulation of vibratory pile driving tests. *Computers and Geotechnics*, *112*, 173–184.

Staubach, P., Machaček, J., Moscoso, M., & Wichtmann, T. (2020). Impact of the installation on the long-term cyclic behaviour of piles in sand: A numerical study. *Soil Dynamics and Earthquake Engineering*, *138*, 106223.

Staubach, P., & Wichtmann, T. (2020). Long-term deformations of monopile foundations for offshore wind turbines studied with a high-cycle accumulation model. *Computers and Geotechnics*, *124*, 103553.

Staubach, P. (2022). *Contributions to the numerical modelling of pile installation processes and high-cyclic loading of soils* (Doctoral dissertation) [ruhr-unibochum.de]. Ruhr-Universität Bochum. Bochum, Germany.

Stehly, T. J., & Duffy, P. (2021). *2020 Cost of Wind Energy Review* (tech. rep.). National Renewable Energy Lab.(NREL), Golden, CO (United States).

Suryasentana, S. K., & Lehane, B. M. (2016). Updated CPT-based p–y formulation for laterally loaded piles in cohesionless soil under static loading. *Géotechnique*, *66*(6), 445–453.

Truong, P., Lehane, B., Zania, V., & Klinkvort, R. T. (2019). Empirical approach based on centrifuge testing for cyclic deformations of laterally loaded piles in sand. *Géotechnique*, *69*(2), 133–145.

Tsetas, A., Gómez, S. S., Tsouvalas, A., van Beek, K., Tehrani, F. S., Kementzetzidis, E., Pisanò, F., Elkadi, A., Segeren, M., Molenkamp, T., & Metrikine, A. V. (2020). Experimental identification of the dynamic behaviour of pile-soil system installed by means of three different pile-driving techniques. In M. Papadrakakis, M. Fragiadakis & C. Papadimitriou (Eds.), *Proceedings of the XI International Conference on Structural Dynamics, EURODYN 2020*. Athens, Greece (pp. 3005–3015).

Tsetas, A., Tsouvalas, A., Gómez, S. S., Pisanò, F., Kementzetzidis, E., Molenkamp, T., Elkadi, A. S., & Metrikine, A. V. (2023). Gentle Driving of Piles (GDP) at a sandy site combining axial and torsional vibrations: Part I - installation tests. *Ocean Engineering*, *270*, 113453.

Tsouvalas, A. (2020). Underwater Noise Emission Due to Offshore Pile Installation: A Review. *Energies*, *13*(12), 3037.

Tsouvalas, A., & Metrikine, A. V. (2016b). Structure-borne wave radiation by impact and vibratory piling in offshore installations: From sound prediction to auditory damage. *Journal of Marine Science and Engineering*, *4*(3), 44.

Versteijlen, W. G., Metrikine, A. V., & van Dalen, K. N. (2016a). A method for identification of an effective Winkler foundation for large-diameter offshore wind turbine support structures based on in-situ measured small-strain soil response and 3D modelling. *Engineering Structures*, *124*, 221–236.

Versteijlen, W. (2018). *Identification of effective 1D soil models for large-diameter offshore wind turbine foundations based on in-situ seismic measurements and 3D modelling* (Doctoral dissertation). Delft University of Technology. Delft, the Netherlands.

Versteijlen, W., Metrikine, A., & van Dalen, K. (2016b). A method for identification of an effective Winkler foundation for large-diameter offshore wind turbine support structures based on in-situ measured small-strain soil response and 3D modelling. *Engineering Structures*, *124*, 221–236.

Versteijlen, W., Renting, F., van der Valk, P., Bongers, J., van Dalen, K., & Metrikine, A. (2017a). Effective soil-stiffness validation: Shaker excitation of an in-situ monopile foundation. *Soil Dynamics and Earthquake Engineering*, *102*, 241–262.

Wang, H., van Zanten D, V., de Lange, D., Pisanò, F., Gavin, K., & Askarinejad, A. (2022). Centrifuge study on the CPT based $p - y$ models for the monopiles. In G. Gottardi & L. Tonni (Eds.), *The 5th International Symposium on Cone Penetration Testing (CPT'22)*. Bologna, Italy. Florida, USA: CRC Press.

Wang, L., Wang, H., Zhu, B., & Hong, Y. (2018a). Comparison of monotonic and cyclic lateral response between monopod and tripod bucket foundations in medium dense sand. *Ocean Engineering*, *155*, 88–105.

White, D., Doherty, J., Guevara, M., & Watson, P. (2022). A cyclic py model for the whole-life response of piles in soft clay. *Computers and Geotechnics*, *141*, 104519.

WindEurope. (2019). Our energy, our future. *WindEurope*.

Zhu, B., Li, T., Xiong, G., & Liu, J. C. (2016). Centrifuge model tests on laterally loaded piles in sand. *International Journal of Physical Modelling in Geotechnics*, *16*(4), 160–172.

References for Chapter II

Angelides, D. C., & Roesset, J. M. (1981). Nonlinear lateral dynamic stiffness of piles. *Journal of Geotechnical and Geoenvironmental Engineering*, *107*.

Anusic, I., Eiksund, G. R., Meissl, S., & Liingaard, M. A. (2017). Study of a new installation technique for large diameter monopiles. In W. Lee, J. S. Lee, H. K. Kim & D. S. Kim (Eds.), *Proceedings of 19th International Conference on Soil Mechanics and Geotechnical Engineering (ICSMGE2017)*. Seoul, South Korea (pp. 2261–2264). Seoul, Korea: International Society of Soil Mechanics and Geotechnical Engineering.

Arany, L., & Bhattacharya, S. (2018). Simplified load estimation and sizing of suction anchors for spar buoy type floating offshore wind turbines. *Ocean Engineering*, *159*, 348–357.

Archer, C., Simão, H., Kempton, W., Powell, W., & Dvorak, M. (2017). The challenge of integrating offshore wind power in the US electric grid. Part I: Wind forecast error. *Renewable energy*, *103*, 346–360.

Berger, E., Mahi, S. A., Pyke, R., et al. (1977). Simplified method for evaluating soil-pile-structure interaction effects. *Proceedings of 9th Offshore Technology Conference.* Houston, TX, USA, 589–598.

Bienen, B., Klinkvort, R. T., O'Loughlin, C., Zhu, F., & Byrne, B. (2018). Suction caissons in dense sand, part II: vertical cyclic loading into tension. *Géotechnique*, 1–15.

Biot, M. (1956). Theory of elastic waves in a fluid-saturated porous solid. 1. Low frequency range. *J. Acoust. Soc. Am.*, *28*, 168–178.

BS EN. (1991). 1-4: 2005 Eurocode 1: Actions on structures - General actions - Wind actions.

Byrne, B. W., Burd, H. J., Zdravkovic, L., Abadie, C. N., Houlsby, G. T., Jardine, R. J., Martin, C. M., McAdam, R. A., Pacheco Andrade, M., Pedro, A. M., et al. PISA Design Methods for Offshore Wind Turbine Monopiles. In: In *Offshore Technology Conference.* Houston, TX, USA. 2019, paper OTC-29373–MS.

Chan, A. H.-C. (1988). *A unified finite element solution to static and dynamic problems of geomechanics* (Doctoral dissertation). Swansea University. Swansea, Wales.

Chancham, C., Waewsak, J., & Gagnon, Y. (2017). Offshore wind resource assessment and wind power plant optimization in the Gulf of Thailand. *Energy*, *139*, 706–731.

Corciulo, S., Zanoli, O., & Pisanò, F. (2017). Transient response of offshore wind turbines on monopiles in sand: role of cyclic hydro–mechanical soil behaviour. *Computers and Geotechnics*, *83*, 221–238.

Dobry, R., & Gazetas, G. (1988). Simple method for dynamic stiffness and damping of floating pile groups. *Geotechnique*, *38*(4), 557–574.

Doherty, P., & Gavin, K. (2012). Laterally loaded monopile design for offshore wind farms. *Proceedings of the Institution of Civil Engineers - Energy*, *165*(1), 7–17.

Dutch Ministry of Economic Affairs. (2016). *Energy report: transition to sustainable energy* (tech. rep.). Ministry of Economic Affairs, The Netherlands. https://www.government.nl/documents/reports/2016/04/28/energy-report-transition-tot-sustainable-energy

Elgamal, A., Yang, Z., & Parra, E. (2002). Computational modeling of cyclic mobility and post-liquefaction site response. *Soil Dynamics and Earthquake Engineering*, *22*(4), 259–271.

Fan, S., Bienen, B., & Randolph, M. F. (2021b). Centrifuge study on effect of installation method on lateral response of monopiles in sand. *International Journal of Physical Modelling in Geotechnics*, *21*(1), 40–52.

Galavi, V., Beuth, L., Coelho, B. Z., Tehrani, F. S., Hölscher, P., & Van Tol, F. (2017). Numerical simulation of pile installation in saturated sand using material point method. *Procedia Engineering*, *175*, 72–79.

Gazetas, G. (1983). Analysis of machine foundation vibrations: state of the art. *International Journal of Soil Dynamics and Earthquake Engineering*, *2*(1), 2–42.

Gazetas, G., & Dobry, R. (1984a). Horizontal response of piles in layered soils. *Journal of Geotechnical engineering*, *110*(1), 20–40.

Gazetas, G., & Dobry, R. (1984b). Simple radiation damping model for piles and footings. *Journal of Engineering Mechanics*, *110*(6), 937–956.

Graff, K. F. (2012). *Wave motion in elastic solids*. New York, NY, USA: Dover.

Han, B., Zdravkovic, L., & Kontoe, S. (2016). Numerical and analytical investigation of compressional wave propagation in saturated soils. *Computers and Geotechnics*, *75*, 93–102.

He, R., Kaynia, A. M., & Zhang, J. (2019). A poroelastic solution for dynamics of laterally loaded offshore monopiles. *Ocean Engineering*, *179*, 337–350.

Houlsby, G., Kelly, R., Huxtable, J., & Byrne, B. (2005). Field trials of suction caissons in clay for offshore wind turbine foundations. *Géotechnique*, *55*(4), 287–296.

Houlsby, G., Kelly, R., Huxtable, J., & Byrne, B. (2006). Field trials of suction caissons in sand for offshore wind turbine foundations. *Géotechnique*, *56*(1), 3–10.

Hughes, T. J. R. (1987). *The Finite Element Method: linear static and dynamic finite element analysis*. Englewood Cliffs, NJ, USA: Prentice-Hall.

Kagawa, T., & Kraft, L. M. (1980). Lateral load-deflection relationships of piles subjected to dynamic loadings. *Soils and Foundations*, *20*(4), 19–36.

Kallehave, D., Thilsted, C. L., & Liingaard, M. Modification of the API $p - y$ formulation of initial stiffness of sand. In: In *Offshore site investigation and geotechnics: integrated technologies-present and future*. Society of Underwater Technology. London, UK, 2012, 465–472.

Kallehave, D., Byrne, B. W., LeBlanc Thilsted, C., & Mikkelsen, K. K. (2015a). Optimization of monopiles for offshore wind turbines. *Philosophical Transactions of the Royal Society A: Mathematical, Physical and Engineering Sciences*, *373*(2035), 20140100.

Kementzetzidis, E., Corciulo, S., Versteijlen, W. G., & Pisanò, F. (2019). Geotechnical aspects of offshore wind turbine dynamics from 3D non-linear soil-structure simulations. *Soil Dynamics and Earthquake Engineering*, *120*, 181–199.

Kementzetzidis, E., Versteijlen, W. G., Nernheim, A., & Pisanò, F. (2018). 3D FE dynamic modelling of offshore wind turbines in sand: Natural frequency evolution in the pre-to after-storm transition. In A. S. Cardoso, J. L. Borges, P. A. Costa, A. T. Gomez, J. C. Marques & C. S. Vieira (Eds.), *Numerical Methods in Geotechnical Engineering IX, Volume 2*. Porto, Portugal (pp. 1477–1484). Florida, USA: CRC Press.

Kontoe, S., Zdravkovic, L., & Potts, D. M. (2008). An assessment of time integration schemes for dynamic geotechnical problems. *Computers and geotechnics*, *35*(2), 253–264.

Kuhlemeyer, R. L. (1979). Static and dynamic laterally loaded floating piles. *Journal of Geotechnical and Geoenvironmental Engineering*, *105*(ASCE 14394).

Liu, H. Y., Abell, J. A., Diambra, A., & Pisanò, F. (2019a). Modelling the cyclic ratcheting of sands through memory- enhanced bounding surface plasticity. *Géotechnique*, *69*(9), 783–800.

Lysmer, J., & Kuhlemeyer, R. L. (1969). Finite dynamic model for infinite media. *Journal of the Engineering Mechanics Division*, *95*(4), 859–878.

Mattar, C., & Borvarán, D. (2016). Offshore wind power simulation by using WRF in the central coast of Chile. *Renewable Energy*, *94*, 22–31.

McGann, C. R., Arduino, P., & Mackenzie-Helnwein, P. (2015). A stabilized single-point finite element formulation for three-dimensional dynamic analysis of saturated soils. *Computers and Geotechnics*, *66*, 126–141.

McKenna, F. T. (1997). *Object-oriented finite element programming: frameworks for analysis, algorithms and parallel computing* (Doctoral dissertation). University of California, Berkeley.

Mylonakis, G., & Gazetas, G. (1999). Lateral vibration and internal forces of grouped piles in layered soil. *Journal of Geotechnical and Geoenvironmental Engineering*, *125*(1), 16–25.

Newman, J. N. (1977). *Marine hydrodynamics*. MIT press.

Novak, M. (1974). Dynamic stiffness and damping of piles. *Canadian Geotechnical Journal*, *11*(4), 574–598.

Novak, M., Aboul-Ella, F., & Nogami, T. (1978). Dynamic soil reactions for plane strain case. *Journal of the Engineering Mechanics Division*, *104*(4), 953–959.

O'Rourke, M. J., & Dobry, R. (1982). Spring and dashpot coefficients for machine foundations on piles. *Special Publication*, *78*, 177–198.

Paulsen, B. T., de Sonneville, B., van der Meulen, M., & Jacobsen, N. G. (2019). Probability of wave slamming and the magnitude of slamming loads on offshore wind turbine foundations. *Coastal Engineering*, *143*, 76–95.

Pisanò, F. (2019). Input of advanced geotechnical modelling to the design of offshore wind turbine foundations. In H. Sigursteinsson, S. Erlingsson & B. Bessason (Eds.), *Proceedings of 17th European Conference on Soil Mechanics and Geotechnical Engineering (ECSMGE2019)*. Rík, Iceland (pp. 272–297). London, UK: International Society of Soil Mechanics; Geotechnical Engineering (ISSMGE).

Pisanò, F., & Gavin, K. G. (2017). General report for TC209 - Offshore Geotechnics. *Proceedings of 19th International Conference on Soil Mechanics and Geotechnical Engineering (ICSMGE2017). Seoul, South Korea*.

Pisanò, F., & Pastor, M. (2011). 1D wave propagation in saturated viscous geomaterials: improvement and validation of a fractional step Taylor–Galerkin finite element algorithm. *Computer methods in applied mechanics and engineering*, *200*(47-48), 3341–3357.

Shadlou, M., & Bhattacharya, S. (2014). Dynamic stiffness of pile in a layered elastic continuum. *Geotechnique*, *64*(4), 303.

Shadlou, M., & Bhattacharya, S. (2016). Dynamic stiffness of monopiles supporting offshore wind turbine generators. *Soil Dynamics and Earthquake Engineering*, *88*, 15–32.

Skau, K. S., Page, A. M., Kaynia, A. M., Løvholt, F., Norén-Cosgriff, K., Sturm, H., Andersen, H., Nygard, T., Jostad, H. P., Eiksund, G., et al. (2018). REDWIN–REDucing cost in offshore WINd by integrated structural and geotechnical design. *Journal of Physics: Conference Series*, *1104*(1), 012029.

Tehrani, F. S., Nguyen, P., Brinkgreve, R. B., & van Tol, A. F. (2016). Comparison of Press-Replace Method and Material Point Method for analysis of jacked piles. *Computers and Geotechnics*, *78*, 38–53.

Tsai, Y.-C., Huang, Y.-F., & Yang, J.-T. (2016). Strategies for the development of offshore wind technology for far-east countries–A point of view from patent analysis. *Renewable and Sustainable Energy Reviews*, *60*, 182–194.

Versteijlen, W. (2018). *Identification of effective 1D soil models for large-diameter offshore wind turbine foundations based on in-situ seismic measurements and 3D modelling* (Doctoral dissertation). Delft University of Technology. Delft, the Netherlands.

Versteijlen, W., Renting, F., van der Valk, P., Bongers, J., van Dalen, K., & Metrikine, A. (2017a). Effective soil-stiffness validation: Shaker excitation of an in-situ monopile foundation. *Soil Dynamics and Earthquake Engineering*, *102*, 241–262.

Versteijlen, W., Renting, F., van der Valk, P., Bongers, J., van Dalen, K., & Metrikine, A. (2017b). Effective soil-stiffness validation: shaker excitation of an in-situ monopile foundation. *Soil Dynamics and Earthquake Engineering*, *102*, 241–262.

Wang, X., Zeng, X., Li, J., Yang, X., & Wang, H. (2018b). A review on recent advancements of substructures for offshore wind turbines. *Energy conversion and management*, *158*, 103–119.

Watanabe, K., Pisanò, F., & Jeremić, B. (2017). Discretization effects in the finite element simulation of seismic waves in elastic and elastic-plastic media. *Engineering with Computers*, *33*(3), 519–545.

Zienkiewicz, O. C., Chan, A. H. C., Pastor, M., Schrefler, B. A., & Shiomi, T. (1999). *Computational geomechanics*. Chichester,UK:

Zienkiewicz, O. C., Chang, C. T., & Bettess, P. (1980). Drained, undrained, consolidating and dynamic behaviour assumptions in soils. *Géotechnique*, *30*(4), 385–395.

References for Chapter III

Abadie, C. N., Byrne, B. W., & Houlsby, G. T. (2019). Rigid pile response to cyclic lateral loading: laboratory tests. *Géotechnique*, *69*(10), 863–876.

Abadie, C. N. (2015b). Cyclic lateral loading of monopile foundations in cohesionless soils. *DPhil thesis, University of Oxford*.

Achmus, M., Schmoor, K. A., Herwig, V., & Matlock, B. (2020). Lateral bearing behaviour of vibro-and impact-driven large-diameter piles in dense sand. *geotechnik*, *43*(3), 147–159.

Albiker, J., Achmus, M., Frick, D., & Flindt, F. (2017). 1 g model tests on the displacement accumulation of large-diameter piles under cyclic lateral loading. *Geotechnical Testing Journal*, *40*(2), 173–184.

Angelides, D. C., & Roesset, J. M. (1981). Nonlinear lateral dynamic stiffness of piles. *Journal of Geotechnical and Geoenvironmental Engineering*, *107*.

Anusic, I., Lehane, B., Eiksund, G., & Liingaard, M. (2019). Influence of installation method on static lateral response of displacement piles in sand. *Géotechnique Letters*, *9*(3), 193–197.

Arany, L., Bhattacharya, S., Macdonald, J., & Hogan, S. (2017b). Design of monopiles for offshore wind turbines in 10 steps. *Soil Dynamics and Earthquake Engineering*, *92*, 126–152.

Barkan, D. Developments in soil dynamics. In: In *International Symposium on Wave Propagation and Dynamic Properties of Earth Materials, Univ. of New Mexico Press*. Albuquerque, New Mexico, 1967, 599–606.

Bea, R. G., Audibert, J. M., & Akky, M. R. (1979). Earthquake response of offshore platforms. *J. Struct. Div., Am. Soc. Civ. Eng.; (United States)*, *105*. https://www.osti.gov/biblio/5581003

Buckley, R. M., Byrne, B. W., Martin, S. C., McAdam, R. A., Sheil, B. B., Aghakouchak, A., & Lindeboom, R. (2020). LARGE DIAMETER PILE TESTING FOR OFFSHORE WIND APPLICATIONS WITH A FOCUS ON CYCLIC LATERAL LOADING AND RATE EFFECTS. *Frontiers in Offshore Geotechnics IV: Proceedings of the 4th International Symposium on Frontiers in Offshore Geotechnics (ISFOG 2021)*.

Byrne, B. W., Aghakouchak, A., Buckley, R. M., Burd, H. J., Gengenbach, J., Houlsby, G. T., McAdam, R. A., Martin, C. M., Schranz, F., Sheil, B. B., & Suryasentana, S. K. (2020a). PICASO: Cyclic lateral loading of offshore wind turbine monopiles. In Z. Westgate (Ed.), *Frontiers in Offshore Geotechnics IV: Proceedings of the 4th International Symposium on Frontiers in Offshore Geotechnics (ISFOG 2021)*. Houston, TX, USA (pp. 1526–1535). Leiden, the Netherlands: CRC Press/Balkema.

Byrne, B. W., Burd, H. J., Zdravkovic, L., Abadie, C. N., Houlsby, G. T., Jardine, R. J., Martin, C. M., McAdam, R. A., Pacheco Andrade, M., Pedro, A. M., et al. PISA Design Methods for Offshore Wind Turbine Monopiles. In: In *Offshore Technology Conference.* Houston, TX, USA. 2019, paper OTC-29373–MS.

Byrne, B. W., McAdam, R. A., Beuckelaers, W. J., Burd, H. J., Gavin, K., Houlsby, G. T., Igoe, D. J. P., Jardine, R., Martin, C. M., et al. (2020b). Cyclic laterally loaded medium scale field pile testing for the PISA project. In Z. Westgate (Ed.), *Frontiers in Offshore Geotechnics IV: Proceedings of the 4th International Symposium on Frontiers in Offshore Geotechnics (ISFOG 2021)*. Austin, TX, USA (pp. 1323–1332). Leiden, the Netherlands: CRC Press/Balkema.

Chopra, A. K. (1995). *Dynamics of Structures* (Vol. 3). Prentice Hall New Jersey.

Ciavaglia, F., Carey, J., & Diambra, A. (2017). Monotonic and cyclic lateral tests on driven piles in Chalk. *Proceedings of the Institution of Civil Engineers-Geotechnical Engineering*, *170*(4), 353–366.

Cuéllar, P., Baeßler, M., & Rücker, W. (2009). Ratcheting convective cells of sand grains around offshore piles under cyclic lateral loads. *Granular Matter*, *11*(6), 379.

De Nicola, A., & Randolph, M. F. (1993). Tensile and compressive shaft capacity of piles in sand. *Journal of Geotechnical Engineering*, *119*(12), 1952–1973.

Dobry, R., & Gazetas, G. (1988). Simple method for dynamic stiffness and damping of floating pile groups. *Geotechnique*, *38*(4), 557–574.

Dutch Goverment. (2022). Offshore wind energy [[Online; accessed Oct-2022]].

Esteban, M. D., Diez, J. J., López, J. S., & Negro, V. (2011). Why offshore wind energy? *Renewable Energy*, *36*(2), 444–450.

European Commission. (2020). Offshore Renewable Energy Strategy.

Fredlund, D. G. (2006). Unsaturated soil mechanics in engineering practice. *Journal of Geotechnical and Geoenvironmental Engineering*, *132*(3), 286–321.

Frick, D., & Achmus, M. (2019). Model Tests on the Displacement Accumulation of Monopiles Subjected to General Cyclic Loading. In N. Goseberg & T. Schlurmann (Eds.), *Proceedings of Coastal Structures 2019, Karlsruhe: Bundesanstalt für Wasserbau* (pp. 913–922).

Gazetas, G., & Dobry, R. (1984a). Horizontal response of piles in layered soils. *Journal of Geotechnical engineering*, *110*(1), 20–40.

He, R., Kaynia, A. M., & Zhang, J. (2019). A poroelastic solution for dynamics of laterally loaded offshore monopiles. *Ocean Engineering*, *179*, 337–350.

Jacobsen, L. S. (1960). Damping in composite structures. *Proceedings of the second World Conference on Earthquake Engineering. Japan, Tokyo*, *2*, 1029–1044.

Jamiolkowski, M., Lo Presti, D., & Manassero, M. (2003). Evaluation of relative density and shear strength of sands from CPT and DMT. *Soil behavior and soft ground construction*, ASCE Geotechnical Special Publication 119, *7*(119), 201–238.

Kagawa, T., & Kraft, L. M. (1980). Lateral load-deflection relationships of piles subjected to dynamic loadings. *Soils and Foundations*, *20*(4), 19–36.

Kallehave, D., Byrne, B. W., LeBlanc Thilsted, C., & Mikkelsen, K. K. (2015a). Optimization of monopiles for offshore wind turbines. *Philosophical Transactions of the Royal Society A: Mathematical, Physical and Engineering Sciences*, *373*(2035), 20140100.

Kementzetzidis, E., Corciulo, S., Versteijlen, W. G., & Pisanò, F. (2019). Geotechnical aspects of offshore wind turbine dynamics from 3D non-linear soil-structure simulations. *Soil Dynamics and Earthquake Engineering*, *120*, 181–199.

Kementzetzidis, E., Metrikine, A. V., Versteijlen, W. G., & Pisanò, F. (2021). Frequency effects in the dynamic lateral stiffness of monopiles in sand: insight from field tests and 3D FE modelling. *Géotechnique*, *71*(9), 812–825.

Kementzetzidis, E., Pisanò, F., & Metrikine, A. V. (2022). A memory-enhanced $p - y$ model for piles in sand accounting for cyclic ratcheting and gapping effects. *Computers and Geotechnics*, *148*, 104810.

Klinkvort, R. T. (2012). *Centrifuge modelling of drained lateral pile-soil response* (Doctoral dissertation). The Technical University of Denmark, DTU Civil Engineering. Lyngby, Denmark.

Klinkvort, R. T., Leth, C. T., & Hededal, O. (2010). Centrifuge modelling of a laterally cyclic loaded pile. In S. Springman, J. Laue & L. Steward (Eds.), *Proceedings of the 7th International Conference on Physical Modelling in Geotechnics (ICPMG 2010)*. Zurich, Switzerland (pp. 959–964). London, UK: Taylor & Francis London.

Koschinski, S., & Lüdemann, K. (2013). Development of noise mitigation measures in offshore wind farm construction. *Commissioned by the Federal Agency for Nature Conservation*, 1–102.

Lammertz, P. (2003). Field studies on bearing capacity of vibratory and impact driven piles. *International Young Geotechnical Engineers' Conference (IYGEC)*. Mamaia, Romania.

Lazari, M., Sanavia, L., di Prisco, C., & Pisanò, F. (2019). Predictive potential of Perzyna viscoplastic modelling for granular geomaterials. *International Journal for Numerical and Analytical Methods in Geomechanics*, *43*(2), 544–567.

LeBlanc, C., Houlsby, G., & Byrne, B. (2010). Response of stiff piles in sand to long-term cyclic lateral loading. *Géotechnique*, *60*(2), 79–90.

Li, W., Igoe, D., & Gavin, K. (2015). Field tests to investigate the cyclic response of monopiles in sand. *Proceedings of the Institution of Civil Engineers - Geotechnical Engineering*, *168*(5), 407–421. https://doi.org/10.1680/jgeen.14.00104.

Liu, H., Kementzetzidis, E., Abell, J. A., & Pisanò, F. (2021). From cyclic sand ratcheting to tilt accumulation of offshore monopiles: 3D FE modelling using SANISAND-MS. *Géotechnique*, 1–16.

Matlock, H. (1970a). Correlations for design of laterally loaded piles in soft clay. *Offshore Technology in Civil Engineering's Hall of Fame Papers from the Early Years*, 77–94.

Matlock, H., Foo, S., & Bryant, L. (1978). Simulation of lateral pile behavior. *Proceedings of the ASCE Geotechnical Engineering Division Specialty Conference.* Pasadena, CA, USA, *1*, 600–619.

Matlock, H., & Reese, L. C. (1962). Generalized solutions for laterally loaded piles. *Transactions of the American Society of Civil Engineers*, *127*(1), 1220–1247.

Mazza, N., & Holeyman, A. (2019). Frequency-Penetration Response Spectrum on Vibratory Amplitude Matching of Monopiles. In P. Bullock, G. Verbeek, D. Tara & S. Paikowsky (Eds.), *10th International Conference on Stress Wave Theory and Testing Methods for Deep Foundations.* San Diego, California, USA.

McAdam, R. A., Byrne, B. W., Houlsby, G. T., Beuckelaers, W. J., Burd, H. J., Gavin, K. G., Igoe, D. J., Jardine, R. J., Martin, C. M., Muir Wood, A., et al. (2020). Monotonic laterally loaded pile testing in a dense marine sand at Dunkirk. *Géotechnique*, *70*(11), 986–998.

McClelland, B., et al. (1956). Soil modulus for laterally loaded piles. *Journal of the Soil Mechanics and Foundations Division*, *82*(4), 1–22.

Meijers, P., Tsouvalas, A., & Metrikine, A. (2018). A non-collocated method to quantify plastic deformation caused by impact pile driving. *International Journal of Mechanical Sciences*, *148*, 1–8.

Metrikine, A., Tsouvalas, A., Segeren, M., Elkadi, A., Tehrani, F., Gómez, S., Atkinson, R., Pisanò, F., Kementzetzidis, E., Tsetas, A., Molenkamp, T., van Beek, K., & P, D. (2020). GDP: a new technology for Gentle Driving of (mono)Piles. In Z. Westgate (Ed.), *Frontiers in Offshore Geotechnics IV: Proceedings of the 4th International Symposium on Frontiers in Offshore Geotechnics (ISFOG 2021)*. Austin, TX, USA (pp. 736–745). Leiden, the Netherlands: CRC Press/Balkema.

Minister of Economic Affairs and Climate Policy. (2020). Offshore Wind Energy Roadmap 2030.

Mosher, R. L. (1987). *Comparison of Axial Capacity of Vibratory-Driven Piles to Impact-Driven Piles.* (tech. rep.). Engineer Research and Development Center (ERDC).

Mosher, R. L. (1990). Axial capacity of vibratory-driven piles versus impact-driven piles. *Transportation Research Record*, (1277).

Mylonakis, G., & Gazetas, G. (1999). Lateral vibration and internal forces of grouped piles in layered soil. *Journal of Geotechnical and Geoenvironmental Engineering*, *125*(1), 16–25.

Novak, M. (1974). Dynamic stiffness and damping of piles. *Canadian Geotechnical Journal*, *11*(4), 574–598.

OpenStreetMap contributors. (2017). Planet dump retrieved from https://planet.osm.org.

Page, A. M., Norén-Cosgriff, K., Skau, K. S., & Kaynia, A. M. (2019). REDWIN Foundation Models for Integrated Dynamic Analyses of Offshore Wind Turbines. *International Conference on Offshore Mechanics and Arctic Engineering*, *58899*, V010T09A073.

Pisanò, F., Askarinejad, A., Wang, H., Maghsoodi, S., Gavin, K. G., Segeren, M. L. A., Elkadi, A. S. K., de Lange, D., & Konstadinou, M. (2022a). MIDAS: Monopile Improved Design through Advanced cyclic Soil modelling. *Proceedings of 20th International Conference on Soil Mechanics and Geotechnical Engineering (ICSMGE2022)*. Sydney, Australia.

Poulos, H. G. (1971). Closure of "Behavior of Laterally Loaded Piles: I-Single Piles". *Journal of the Soil Mechanics and Foundations Division*, *98*, 1269–1271.

Poulos, H. G., & Davis, E. H. (1980). *Pile foundation analysis and design*.

Ramırez, L., Fraile, D., & Brindley, G. (2021). Offshore wind in Europe: Key trends and statistics 2020. *WindEurope*.

Reese, L. C., Cox, W. R., Koop, F. D., et al. (1975). Field testing and analysis of laterally loaded piles om stiff clay. *Offshore Technology Conference*.

Richards, I., Bransby, M., Byrne, B., Gaudin, C., & Houlsby, G. (2021). Effect of stress level on response of model monopile to cyclic lateral loading in sand. *Journal of Geotechnical and Geoenvironmental Engineering*, *147*(3), 04021002.

Richards, I. (2019). *Monopile foundations under complex cyclic lateral loadings* (DPhil thesis). University of Oxford. Oxford, UK.

Rodger, A., & Littlejohn, G. (1980). A study of vibratory driving in granular soils. *Géotechnique*, *30*(3), 269–293.

Rudolph, C., Bienen, B., & Grabe, J. (2014). Effect of variation of the loading direction on the displacement accumulation of large-diameter piles under cyclic lateral loading in sand. *Canadian Geotechnical Journal*, *51*(10), 1196–1206.

Shadlou, M., & Bhattacharya, S. (2014). Dynamic stiffness of pile in a layered elastic continuum. *Geotechnique*, *64*(4), 303.

Shadlou, M., & Bhattacharya, S. (2016). Dynamic stiffness of monopiles supporting offshore wind turbine generators. *Soil Dynamics and Earthquake Engineering*, *88*, 15–32.

Solf, O., Kudella, P., & Triantafyllidis, T. (2010). Investigation of the self-healing effect of monopile foundations. In S. Springman, J. Laue & L. Seward (Eds.), *International Conference on Physical Modelling in Geotechnics ICPMG*. Zurich, Switzerland (pp. 1003–1008). London, UK: CRC Press.

Staubach, P., Machaček, J., Bienen, B., & Wichtmann, T. (2022). Long-Term Response of Piles to Cyclic Lateral Loading Following Vibratory and Impact Driving in Water-Saturated Sand. *Journal of Geotechnical and Geoenvironmental Engineering*, *148*(11), 04022097.

Stehly, T. J., & Beiter, P. C. (2020). *2018 Cost of Wind Energy Review* (tech. rep.). National Renewable Energy Lab.(NREL), Golden, CO (United States).

Sturm, H., Solf, O., & Kudella, P. (2008). Self-healing effects of shallow foundations for offshore wind turbine structures. In Z. Mlynarek (Ed.), *11th Baltic Sea Geotechnical*

Conference:" Geotechnics in Maritime Engineering". Gdansk, Poland (pp. 301–308). London, UK: CRC Press.

Truong, P., Lehane, B., Zania, V., & Klinkvort, R. T. (2019). Empirical approach based on centrifuge testing for cyclic deformations of laterally loaded piles in sand. *Géotechnique*, *69*(2), 133–145.

Tsetas, A., Gómez, S. S., Tsouvalas, A., van Beek, K., Tehrani, F. S., Kementzetzidis, E., Pisanò, F., Elkadi, A., Segeren, M., Molenkamp, T., & Metrikine, A. V. (2020). Experimental identification of the dynamic behaviour of pile-soil system installed by means of three different pile-driving techniques. In M. Papadrakakis, M. Fragiadakis & C. Papadimitriou (Eds.), *Proceedings of the XI International Conference on Structural Dynamics, EURODYN 2020*. Athens, Greece (pp. 3005–3015).

Tsetas, A., Tsouvalas, A., Gómez, S. S., Pisanò, F., Kementzetzidis, E., Molenkamp, T., Elkadi, A. S., & Metrikine, A. V. (2023). Gentle Driving of Piles (GDP) at a sandy site combining axial and torsional vibrations: Part I - installation tests. *Ocean Engineering*, *270*, 113453.

Tsouvalas, A., & Metrikine, A. (2016a). Noise reduction by the application of an air-bubble curtain in offshore pile driving. *Journal of Sound and Vibration*, *371*, 150–170.

Tsouvalas, A. (2020). Underwater Noise Emission Due to Offshore Pile Installation: A Review. *Energies*, *13*(12), 3037.

Tsouvalas, A., & Metrikine, A. V. (2016b). Structure-borne wave radiation by impact and vibratory piling in offshore installations: From sound prediction to auditory damage. *Journal of Marine Science and Engineering*, *4*(3), 44.

Versteijlen, W., Renting, F., van der Valk, P., Bongers, J., van Dalen, K., & Metrikine, A. (2017a). Effective soil-stiffness validation: Shaker excitation of an in-situ monopile foundation. *Soil Dynamics and Earthquake Engineering*, *102*, 241–262.

Vos, P. (2015). *Origin of the Dutch coastal landscape: long-term landscape evolution of the Netherlands during the Holocene, described and visualized in national, regional and local palaeogeographical map series*. Barkhuis.

Wang, L., Wang, H., Zhu, B., & Hong, Y. (2018a). Comparison of monotonic and cyclic lateral response between monopod and tripod bucket foundations in medium dense sand. *Ocean Engineering*, *155*, 88–105.

Wu, X., Hu, Y., Li, Y., Yang, J., Duan, L., Wang, T., Adcock, T., Jiang, Z., Gao, Z., Lin, Z., et al. (2019). Foundations of offshore wind turbines: A review. *Renewable and Sustainable Energy Reviews*, *104*, 379–393.

Yang, H., Sinha, S. K., Feng, Y., McCallen, D. B., & Jeremić, B. (2018). Energy dissipation analysis of elastic–plastic materials. *Computer Methods in Applied Mechanics and Engineering*, *331*, 309–326.

Zhu, B., Li, T., Xiong, G., & Liu, J. C. (2016). Centrifuge model tests on laterally loaded piles in sand. *International Journal of Physical Modelling in Geotechnics*, *16*(4), 160–172.

References for Chapter IV

Abadie, C. N., Byrne, B. W., & Houlsby, G. T. (2019). Rigid pile response to cyclic lateral loading: laboratory tests. *Géotechnique*, *69*(10), 863–876.

Abadie, C. N. (2015b). Cyclic lateral loading of monopile foundations in cohesionless soils. *DPhil thesis, University of Oxford*.

Achmus, M., Kuo, Y.-S., & Abdel-Rahman, K. (2009). Behavior of monopile foundations under cyclic lateral load. *Computers and Geotechnics*, *36*(5), 725–735.

Albiker, J., Achmus, M., Frick, D., & Flindt, F. (2017). 1 g model tests on the displacement accumulation of large-diameter piles under cyclic lateral loading. *Geotechnical Testing Journal*, *40*(2), 173–184.

Anusic, I., Lehane, B., Eiksund, G., & Liingaard, M. (2019). Influence of installation method on static lateral response of displacement piles in sand. *Géotechnique Letters*, *9*(3), 193–197.

API, R. (2011). 2GEO (2011). *Recommended Practice for Geotechnical Foundation Design Consideration*.

Arany, L., Bhattacharya, S., Macdonald, J., & Hogan, S. (2017a). Design of monopiles for offshore wind turbines in 10 steps. *Soil Dynamics and Earthquake Engineering*, *92*, 126–152.

Bea, R. G., Audibert, J. M., & Akky, M. R. (1979). Earthquake response of offshore platforms. *J. Struct. Div., Am. Soc. Civ. Eng.; (United States)*, *105*. https://www.osti.gov/biblio/5581003

Beuckelaers, W., Burd, H., Houlsby, G., McAdam, R., & Byrne, B. (2020). A generalised Winkler model for the hysteretic and ratcheting behaviour of monopiles in clay and sand. In Z. Westgate (Ed.), *In Frontiers in Offshore Geotechnics IV: Proceedings of the 4th International Symposium on Frontiers in Offshore Geotechnics (ISFOG 2021)*. Houston, TX, USA (pp. 1263–1272). Leiden, the Netherlands: CRC Press/Balkema.

Borja, R. I., & Amies, A. P. (1994). Multiaxial cyclic plasticity model for clays. *Journal of geotechnical engineering*, *120*(6), 1051–1070.

Boulanger, R. W., Curras, C. J., Kutter, B. L., Wilson, D. W., & Abghari, A. (1999). Seismic soil-pile-structure interaction experiments and analyses. *Journal of geotechnical and geoenvironmental engineering*, *125*(9), 750–759.

Boulanger, R. W., Kutter, B. L., & Wilson, D. W. (1998). *Pile foundations in liquefied and laterally spreading ground during earthquakes: centrifuge experiments & analyses* (tech. rep.). University of California, Davis, Center for Geotechnical Modeling, Department of Civil and Environmental Engineering.

Brandenberg, S. J., Zhao, M., Boulanger, R. W., & Wilson, D. W. (2013). p-y plasticity model for nonlinear dynamic analysis of piles in liquefiable soil. *Journal of geotechnical and geoenvironmental engineering*, *139*(8), 1262–1274.

Burd, H. J., Taborda, D. M., Zdravković, L., Abadie, C. N., Byrne, B. W., Houlsby, G. T., Gavin, K. G., Igoe, D. J., Jardine, R. J., Martin, C. M., et al. (2020). PISA design model

for monopiles for offshore wind turbines: application to a marine sand. *Géotechnique*, *70*(11), 1048–1066.

Byrne, B. W., Aghakouchak, A., Buckley, R. M., Burd, H. J., Gengenbach, J., Houlsby, G. T., McAdam, R. A., Martin, C. M., Schranz, F., Sheil, B. B., & Suryasentana, S. K. (2020a). PICASO: Cyclic lateral loading of offshore wind turbine monopiles. In Z. Westgate (Ed.), *Frontiers in Offshore Geotechnics IV: Proceedings of the 4th International Symposium on Frontiers in Offshore Geotechnics (ISFOG 2021)*. Houston, TX, USA (pp. 1526–1535). Leiden, the Netherlands: CRC Press/Balkema.

Byrne, B. W., Burd, H. J., Zdravkovic, L., Abadie, C. N., Houlsby, G. T., Jardine, R. J., Martin, C. M., McAdam, R. A., Pacheco Andrade, M., Pedro, A. M., et al. PISA Design Methods for Offshore Wind Turbine Monopiles. In: In *Offshore Technology Conference.* Houston, TX, USA. 2019, paper OTC-29373–MS.

Byrne, B. W., McAdam, R. A., Beuckelaers, W. J., Burd, H. J., Gavin, K., Houlsby, G. T., Igoe, D. J. P., Jardine, R., Martin, C. M., et al. (2020b). Cyclic laterally loaded medium scale field pile testing for the PISA project. In Z. Westgate (Ed.), *Frontiers in Offshore Geotechnics IV: Proceedings of the 4th International Symposium on Frontiers in Offshore Geotechnics (ISFOG 2021)*. Austin, TX, USA (pp. 1323–1332). Leiden, the Netherlands: CRC Press/Balkema.

Choi, J. I., Kim, M. M., & Brandenberg, S. J. (2015). Cyclic p-y Plasticity Model Applied to Pile Foundations in Sand. *Journal of Geotechnical and Geoenvironmental Engineering*, *141*(5), 04015013.

Corti, R., Diambra, A., Wood, D. M., Escribano, D. E., & Nash, D. F. (2016). Memory surface hardening model for granular soils under repeated loading conditions. *Journal of Engineering Mechanics*, *142*(12), 04016102.

Cuéllar, P., Baeßler, M., & Rücker, W. (2009). Ratcheting convective cells of sand grains around offshore piles under cyclic lateral loads. *Granular Matter*, *11*(6), 379.

Cuéllar, P., Georgi, S., Baeßler, M., & Rücker, W. (2012). On the quasi-static granular convective flow and sand densification around pile foundations under cyclic lateral loading. *Granular Matter*, *14*(1), 11–25.

Dafalias, Y. F. (1986). Bounding surface plasticity. I: Mathematical foundation and hypoplasticity. *Journal of engineering mechanics*, *112*(9), 966–987.

Dafalias, Y. F., & Popov, E. P. (1977). Cyclic loading for materials with a vanishing elastic region. *Nuclear engineering and design*, *41*(2), 293–302.

Dafalias, Y., & Taiebat, M. (2016). SANISAND-Z: zero elastic range sand plasticity model. *Géotechnique*, *66*(12), 999–1013.

Davidson, H. (1982). *Laterally loaded drilled pier research. Volume 1: design methodology. Final report.[PADLL]* (tech. rep.). GAI Consultants, Inc., Monroeville, PA (USA).

DNV. (2014). DNV-OS-J101 Offshore Standard: Design of Offshore Wind Turbine Structures. *DNV AS, Høvik, Norway*.

Dyson, G., & Randolph, M. (2001). Monotonic lateral loading of piles in calcareous sand. *Journal of Geotechnical and Geoenvironmental Engineering*, *127*(4), 346–352.

Fredlund, D. G. (2006). Unsaturated soil mechanics in engineering practice. *Journal of Geotechnical and Geoenvironmental Engineering*, *132*(3), 286–321.

Frick, D., & Achmus, M. (2019). Model Tests on the Displacement Accumulation of Monopiles Subjected to General Cyclic Loading. In N. Goseberg & T. Schlurmann (Eds.), *Proceedings of Coastal Structures 2019, Karlsruhe: Bundesanstalt für Wasserbau* (pp. 913–922).

Gerolymos, N., & Gazetas, G. (2005a). Constitutive model for 1-D cyclic soil behaviour applied to seismic analysis of layered deposits. *Soils and Foundations*, *45*(3), 147–159.

Gerolymos, N., & Gazetas, G. (2005b). Phenomenological model applied to inelastic response of soil-pile interaction systems. *Soils and Foundations*, *45*(4), 119–132.

Gerolymos, N., & Gazetas, G. (2006). Development of Winkler model for static and dynamic response of caisson foundations with soil and interface nonlinearities. *Soil Dynamics and Earthquake Engineering*, *26*(5), 363–376.

Hededal, O., Klinkvort, R. T., et al. (2010). A new elasto-plastic spring element for cyclic loading of piles using the py curve concept. In T. Benz & S. Nordal (Eds.), *Numerical Methods in Geotechnical Engineering: NUMGE 2010*. Trondheim, Norway (pp. 883–888). Florida, USA: CRC Press.

Heidari, M., El Naggar, H., Jahanandish, M., & Ghahramani, A. (2014). Generalized cyclic p–y curve modeling for analysis of laterally loaded piles. *Soil Dynamics and Earthquake Engineering*, *63*, 138–149.

Hutchinson, J. (2001). Shear coefficients for Timoshenko beam theory. *J. Appl. Mech.*, *68*(1), 87–92.

Jamiolkowski, M., Lo Presti, D., & Manassero, M. (2003). Evaluation of relative density and shear strength of sands from CPT and DMT. *Soil behavior and soft ground construction,* ASCE Geotechnical Special Publication 119, *7*(119), 201–238.

Jostad, H., Grimstad, G., Andersen, K., Saue, M., Shin, Y., & You, D. (2014). A FE procedure for foundation design of offshore structures–applied to study a potential OWT monopile foundation in the Korean Western Sea. *Geotechnical Engineering Journal of the SEAGS &AGSSEA*, *45*(4), 63–72.

Kaynia, A. M. (2021). *Analysis of Pile Foundations Subject to Static and Dynamic Loading*. Leiden, the Netherlads: CRC Press.

Kementzetzidis, E., Corciulo, S., Versteijlen, W. G., & Pisanò, F. (2019). Geotechnical aspects of offshore wind turbine dynamics from 3D non-linear soil-structure simulations. *Soil Dynamics and Earthquake Engineering*, *120*, 181–199.

Kementzetzidis, E., Metrikine, A. V., Versteijlen, W. G., & Pisanò, F. (2021). Frequency effects in the dynamic lateral stiffness of monopiles in sand: insight from field tests and 3D FE modelling. *Géotechnique*, *71*(9), 812–825.

Kementzetzidis, E., Pisanò, F., Elkadi, A. S., Tsouvalas, A., & Metrikine, A. V. (2023a). Gentle Driving of Piles (GDP) at a sandy site combining axial and torsional vibrations: Part II - cyclic/dynamic lateral loading tests. *Ocean Engineering*, *270*, 113452.

Kementzetzidis, E., Versteijlen, W. G., Nernheim, A., & Pisanò, F. (2018). 3D FE dynamic modelling of offshore wind turbines in sand: Natural frequency evolution in the pre-to after-storm transition. In A. S. Cardoso, J. L. Borges, P. A. Costa, A. T. Gomez, J. C. Marques & C. S. Vieira (Eds.), *Numerical Methods in Geotechnical Engineering IX, Volume 2*. Porto, Portugal (pp. 1477–1484). Florida, USA: CRC Press.

Klinkvort, R. T. (2012). *Centrifuge modelling of drained lateral pile-soil response* (Doctoral dissertation). The Technical University of Denmark, DTU Civil Engineering. Lyngby, Denmark.

Klinkvort, R. T., Leth, C. T., & Hededal, O. (2010). Centrifuge modelling of a laterally cyclic loaded pile. In S. Springman, J. Laue & L. Steward (Eds.), *Proceedings of the 7th International Conference on Physical Modelling in Geotechnics (ICPMG 2010)*. Zurich, Switzerland (pp. 959–964). London, UK: Taylor & Francis London.

Lam, I., & Martin, G. (1986). *Seismic Design of High-Way Bridge Foundations. US Department of Transportation* (tech. rep.). Report No. FHWA/RD-86/102.

LeBlanc, C., Houlsby, G., & Byrne, B. (2010). Response of stiff piles in sand to long-term cyclic lateral loading. *Géotechnique*, *60*(2), 79–90.

Li, W., Igoe, D., & Gavin, K. (2014). Evaluation of CPT-based P–y models for laterally loaded piles in siliceous sand. *Géotechnique Letters*, *4*(2), 110–117.

Li, W., Igoe, D., & Gavin, K. (2015). Field tests to investigate the cyclic response of monopiles in sand. *Proceedings of the Institution of Civil Engineers - Geotechnical Engineering*, *168*(5), 407–421. https://doi.org/10.1680/jgeen.14.00104.

Liu, H. Y., Abell, J. A., Diambra, A., & Pisanò, F. (2019a). Modelling the cyclic ratcheting of sands through memory- enhanced bounding surface plasticity. *Géotechnique*, *69*(9), 783–800.

Liu, H. Y., Abell, J. A., Diambra, A., & Pisanò, F. (2019b). Modelling the cyclic ratcheting of sands through memory-enhanced bounding surface plasticity. *Géotechnique*, *69*(9), 783–800.

Liu, H., Kementzetzidis, E., Abell, J. A., & Pisanò, F. (2021). From cyclic sand ratcheting to tilt accumulation of offshore monopiles: 3D FE modelling using SANISAND-MS. *Géotechnique*, 1–16.

Liu, H., Pisanò, F., Jostad, H. P., & Sivasithamparam, N. (2022). Impact of cyclic strain accumulation on the tilting behaviour of monopiles in sand: An assessment of the Miner's rule based on SANISAND-MS 3D FE modelling. *Ocean Engineering*, *250*, 110579.

Matlock, H. (1970b). Correlations for design of laterally loaded piles in soft clay. *Proceedings of 2nd Offshore technology conference,* Houston, TX, USA, *1*, 577–594.

Matlock, H., Foo, S., & Bryant, L. (1978). Simulation of lateral pile behavior. *Proceedings of the ASCE Geotechnical Engineering Division Specialty Conference.* Pasadena, CA, USA, *1*, 600–619.

McKenna, F. (2011). OpenSees: a framework for earthquake engineering simulation. *Computing in Science & Engineering*, *13*(4), 58–66.

Metrikine, A., Tsouvalas, A., Segeren, M., Elkadi, A., Tehrani, F., Gómez, S., Atkinson, R., Pisanò, F., Kementzetzidis, E., Tsetas, A., Molenkamp, T., van Beek, K., & P, D. (2020). GDP: a new technology for Gentle Driving of (mono)Piles. In Z. Westgate (Ed.), *Frontiers in Offshore Geotechnics IV: Proceedings of the 4th International Symposium on Frontiers in Offshore Geotechnics (ISFOG 2021)*. Austin, TX, USA (pp. 736–745). Leiden, the Netherlands: CRC Press/Balkema.

Niemunis, A., Wichtmann, T., & Triantafyllidis, T. (2005). A high-cycle accumulation model for sand. *Computers and geotechnics*, *32*(4), 245–263.

Nogami, T., Otani, J., Konagai, K., & Chen, H.-L. (1992). Nonlinear soil-pile interaction model for dynamic lateral motion. *Journal of Geotechnical Engineering*, *118*(1), 89–106.

Novello, E. (1999). From static to cyclic py data in calcareous sediments. In K. Al-Shafei (Ed.), *Proc. 2nd Int. Conf. on Engineering for Calcareous Sediments.* Bahrain (pp. 17–24). Rotterdam, the Netherlands: Balkema.

Pisanò, F. (2019). Input of advanced geotechnical modelling to the design of offshore wind turbine foundations. In H. Sigursteinsson, S. Erlingsson & B. Bessason (Eds.), *Proceedings of 17th European Conference on Soil Mechanics and Geotechnical Engineering (ECSMGE2019)*. Rík, Iceland (pp. 272–297). London, UK: International Society of Soil Mechanics; Geotechnical Engineering (ISSMGE).

Pisanò, F., Askarinejad, A., Wang, H., Maghsoodi, S., Gavin, K. G., Segeren, M. L. A., Elkadi, A. S. K., de Lange, D., & Konstadinou, M. (2022a). MIDAS: Monopile Improved Design through Advanced cyclic Soil modelling. *Proceedings of 20th International Conference on Soil Mechanics and Geotechnical Engineering (ICSMGE2022)*. Sydney, Australia.

Pisanò, F., & Jeremić, B. (2014). Simulating stiffness degradation and damping in soils via a simple visco-elastic–plastic model. *Soil Dynamics and Earthquake Engineering*, *63*, 98–109.

Pyke, R. M. (1979). Nonlinear soil models for irregular cyclic loadings. *Journal of the Geotechnical Engineering Division*, *105*(6), 715–726.

Randolph, M. F., & Gourvenec, S. (2011). *Offshore Geotechnical Engineering*. Oxford, UK: CRC Press, Taylor & Francis Group.

Richards, I., Bransby, M., Byrne, B., Gaudin, C., & Houlsby, G. (2021). Effect of stress level on response of model monopile to cyclic lateral loading in sand. *Journal of Geotechnical and Geoenvironmental Engineering*, *147*(3), 04021002.

Richards, I. (2019). *Monopile foundations under complex cyclic lateral loadings* (DPhil thesis). University of Oxford. Oxford, UK.

Rudolph, C., Bienen, B., & Grabe, J. (2014). Effect of variation of the loading direction on the displacement accumulation of large-diameter piles under cyclic lateral loading in sand. *Canadian Geotechnical Journal*, *51*(10), 1196–1206.

Sloan, S. W., Abbo, A. J., & Sheng, D. (2001). Refined explicit integration of elastoplastic models with automatic error control. *Engineering Computations*.

Staubach, P., & Wichtmann, T. (2020). Long-term deformations of monopile foundations for offshore wind turbines studied with a high-cycle accumulation model. *Computers and Geotechnics*, *124*, 103553.

Suryasentana, S., & Lehane, B. (2014a). Verification of numerically derived CPT based py curves for piles in sand. *Proceedings of 3rd International Symposium on Cone Penetration Testing*. Las Vegas, NV, USA, 3–29.

Suryasentana, S. K., & Lehane, B. M. (2014b). Numerical derivation of CPT-based p–y curves for piles in sand. *Géotechnique*, *64*(3), 186–194.

Suryasentana, S. K., & Lehane, B. M. (2016). Updated CPT-based p–y formulation for laterally loaded piles in cohesionless soil under static loading. *Géotechnique*, *66*(6), 445–453.

Suzuki, Y., & Nakai, S. (1985). Behavior of a pile under horizontal cyclic loading. *Proceedings of 11th International conference on soil mechanics and foundation engineering*. San Francisco, CA, USA, *3*, 1413–1416.

Timoshenko, S. P. (1921). LXVI. On the correction for shear of the differential equation for transverse vibrations of prismatic bars. *The London, Edinburgh, and Dublin Philosophical Magazine and Journal of Science*, *41*(245), 744–746.

Truong, P., Lehane, B., Zania, V., & Klinkvort, R. T. (2019). Empirical approach based on centrifuge testing for cyclic deformations of laterally loaded piles in sand. *Géotechnique*, *69*(2), 133–145.

Tsetas, A., Tsouvalas, A., Gómez, S. S., Pisanò, F., Kementzetzidis, E., Molenkamp, T., Elkadi, A. S., & Metrikine, A. V. (2023). Gentle Driving of Piles (GDP) at a sandy site combining axial and torsional vibrations: Part I - installation tests. *Ocean Engineering*, *270*, 113453.

Wang, H., van Zanten D, V., de Lange, D., Pisanò, F., Gavin, K., & Askarinejad, A. (2022). Centrifuge study on the CPT based $p - y$ models for the monopiles. In G. Gottardi & L. Tonni (Eds.), *The 5th International Symposium on Cone Penetration Testing (CPT'22)*. Bologna, Italy. Florida, USA: CRC Press.

Wang, L., Wang, H., Zhu, B., & Hong, Y. (2018a). Comparison of monotonic and cyclic lateral response between monopod and tripod bucket foundations in medium dense sand. *Ocean Engineering*, *155*, 88–105.

Wichtmann, T., Niemunis, A., & Triantafyllidis, T. (2005). Strain accumulation in sand due to cyclic loading: drained triaxial tests. *Soil Dynamics and Earthquake Engineering*, *25*(12), 967–979.

Wichtmann, T., Niemunis, A., & Triantafyllidis, T. (2010). Strain accumulation in sand due to drained cyclic loading: on the effect of monotonic and cyclic preloading (Miner's rule). *Soil Dynamics and Earthquake Engineering*, *30*(8), 736–745.

Winkler, E. (1867). *Die Lehre von der Elasticitaet und Festigkeit: mit besonderer Rücksicht auf ihre Anwendung in der Technik, für polytechnische Schulen, Bauakademien, Ingenieure, Maschinenbauer, Architecten, etc*. H. Dominicus.

Zhu, B., Li, T., Xiong, G., & Liu, J. C. (2016). Centrifuge model tests on laterally loaded piles in sand. *International Journal of Physical Modelling in Geotechnics*, *16*(4), 160–172.

References for Chapter V

Achmus, M., Schmoor, K. A., Herwig, V., & Matlock, B. (2020). Lateral bearing behaviour of vibro-and impact-driven large-diameter piles in dense sand. *geotechnik*, *43*(3), 147–159.

Anusic, I., Lehane, B., Eiksund, G., & Liingaard, M. (2019). Influence of installation method on static lateral response of displacement piles in sand. *Géotechnique Letters*, *9*(3), 193–197.

Bea, R. G., Audibert, J. M., & Akky, M. R. (1979). Earthquake response of offshore platforms. *J. Struct. Div., Am. Soc. Civ. Eng.; (United States)*, *105*. https://www.osti.gov/biblio/5581003

Bienen, B., Fan, S., Schröder, M., & Randolph, M. F. (2021). Effect of the installation process on monopile lateral response. *Proceedings of the Institution of Civil Engineers-Geotechnical Engineering*, *174*(5), 530–548.

Boulanger, R. W., Curras, C. J., Kutter, B. L., Wilson, D. W., & Abghari, A. (1999). Seismic soil-pile-structure interaction experiments and analyses. *Journal of geotechnical and geoenvironmental engineering*, *125*(9), 750–759.

Brandt, A. (2011). *Noise and vibration analysis: signal analysis and experimental procedures*. John Wiley & Sons.

Byrne, B. W., Aghakouchak, A., Buckley, R. M., Burd, H. J., Gengenbach, J., Houlsby, G. T., McAdam, R. A., Martin, C. M., Schranz, F., Sheil, B. B., & Suryasentana, S. K. (2020a). PICASO: Cyclic lateral loading of offshore wind turbine monopiles. In Z. Westgate (Ed.), *Frontiers in Offshore Geotechnics IV: Proceedings of the 4th International Symposium on Frontiers in Offshore Geotechnics (ISFOG 2021)*. Houston, TX, USA (pp. 1526–1535). Leiden, the Netherlands: CRC Press/Balkema.

Byrne, B. W., McAdam, R. A., Beuckelaers, W. J., Burd, H. J., Gavin, K., Houlsby, G. T., Igoe, D. J. P., Jardine, R., Martin, C. M., et al. (2020b). Cyclic laterally loaded medium scale field pile testing for the PISA project. In Z. Westgate (Ed.), *Frontiers in Offshore Geotechnics IV: Proceedings of the 4th International Symposium on Frontiers in Offshore Geotechnics (ISFOG 2021)*. Austin, TX, USA (pp. 1323–1332). Leiden, the Netherlands: CRC Press/Balkema.

Corti, R., Diambra, A., Wood, D. M., Escribano, D. E., & Nash, D. F. (2016). Memory surface hardening model for granular soils under repeated loading conditions. *Journal of Engineering Mechanics*, *142*(12), 04016102.

Cuéllar, P., Baeßler, M., & Rücker, W. (2009). Ratcheting convective cells of sand grains around offshore piles under cyclic lateral loads. *Granular Matter*, *11*(6), 379.

Delavinia, D. (2022). *Seismic response of monopile foundations for offshore wind turbines: from 3D to 1D modelling of soil-foundation interaction* (M.S. thesis). Delft University of Technology. The Netherlands. http://resolver.tudelft.nl/uuid:96ab302d-9ecb-496f-bcae-b44e29bc9ffb

Fan, S., Bienen, B., & Randolph, M. F. (2021c). Effects of monopile installation on subsequent lateral response in sand. I: Pile installation. *Journal of Geotechnical and Geoenvironmental Engineering*, *147*(5), 04021021.

Fan, S., Bienen, B., & Randolph, M. F. (2021d). Effects of Monopile Installation on Subsequent Lateral Response in Sand. II: Lateral Loading. *Journal of Geotechnical and Geoenvironmental Engineering*, *147*(5), 04021022.

Fredlund, D. G. (2006). Unsaturated soil mechanics in engineering practice. *Journal of Geotechnical and Geoenvironmental Engineering*, *132*(3), 286–321.

Gaertner, E., Rinker, J., Sethuraman, L., Zahle, F., Anderson, B., Barter, G. E., Abbas, N. J., Meng, F., Bortolotti, P., Skrzypinski, W., et al. (2020). *IEA wind TCP task 37: definition of the IEA 15-megawatt offshore reference wind turbine* (tech. rep.). National Renewable Energy Lab.(NREL), Golden, CO (United States).

Heins, E., & Grabe, J. (2017). Class-A-prediction of lateral pile deformation with respect to vibratory and impact pile driving. *Computers and Geotechnics*, *86*, 108–119.

Herwig, V., & Gattermann, J. (2015). VIBRO-Project–Vergleich der lateralen Tragfähigkeit von vibrierten und geschlagenen Stahlpfählen in sandigen Böden. *Pfahl-Symposium*, *19*(20.02), 2015.

Igwemezie, V., Mehmanparast, A., & Kolios, A. (2019). Current trend in offshore wind energy sector and material requirements for fatigue resistance improvement in large wind turbine support structures–A review. *Renewable and Sustainable Energy Reviews*, *101*, 181–196.

Jamiolkowski, M., Lo Presti, D., & Manassero, M. (2003). Evaluation of relative density and shear strength of sands from CPT and DMT. *Soil behavior and soft ground construction*, ASCE Geotechnical Special Publication 119, *7*(119), 201–238.

Kallehave, D., Byrne, B. W., LeBlanc Thilsted, C., & Mikkelsen, K. K. (2015a). Optimization of monopiles for offshore wind turbines. *Philosophical Transactions of the Royal Society A: Mathematical, Physical and Engineering Sciences*, *373*(2035), 20140100.

Kementzetzidis, E., Metrikine, A. V., Versteijlen, W. G., & Pisanò, F. (2021). Frequency effects in the dynamic lateral stiffness of monopiles in sand: insight from field tests and 3D FE modelling. *Géotechnique*, *71*(9), 812–825.

Kementzetzidis, E., Pisanò, F., Elkadi, A. S., Tsouvalas, A., & Metrikine, A. V. (2023a). Gentle Driving of Piles (GDP) at a sandy site combining axial and torsional vibrations: Part II - cyclic/dynamic lateral loading tests. *Ocean Engineering*, *270*, 113452.

Kementzetzidis, E., Pisanò, F., & Metrikine, A. V. (2022). A memory-enhanced $p - y$ model for piles in sand accounting for cyclic ratcheting and gapping effects. *Computers and Geotechnics*, *148*, 104810.

Komusanac, I., Brindley, G., Fraile, D., & Ramirez, R. (2022). Wind energy in Europe: 2021 Statistics and the outlook for 2022-2026. *WindEurope*.

Labenski, J., & Moormann, C. (2019). Lateral bearing behaviour of vibratory-driven monopiles: a modified py approach based on experimental observations of scaled model tests. Reykjavik, Iceland. In M. Hamza, M. Shahien & Y. El-Mossallamy (Eds.), *Proc. of 17th European Conf. on Soil Mechanics and Geotechnical Engineering*. Amsterdam, the Netherlands: IOS Press BV.

LeBlanc, C. (2014). Vibro-Driving Monopiles — A Feasible Installation Concept for the Future? *Danish Geotechnical Society Seminar, Gentofte, Denmark, April*, *1*.

Lee, J., Zhao, F., & Dutton. (2021). Global Offshore Wind Report 2021. *GWEC (Global Wind Energy Council)*.

Li, W., Igoe, D., & Gavin, K. (2015). Field tests to investigate the cyclic response of monopiles in sand. *Proceedings of the Institution of Civil Engineers - Geotechnical Engineering*, *168*(5), 407–421. https://doi.org/10.1680/jgeen.14.00104.

Liu, H. Y., Abell, J. A., Diambra, A., & Pisanò, F. (2019a). Modelling the cyclic ratcheting of sands through memory- enhanced bounding surface plasticity. *Géotechnique*, *69*(9), 783–800.

Liu, H., Kementzetzidis, E., Abell, J. A., & Pisanò, F. (2021). From cyclic sand ratcheting to tilt accumulation of offshore monopiles: 3D FE modelling using SANISAND-MS. *Géotechnique*, 1–16.

Matlock, H., Foo, S., & Bryant, L. (1978). Simulation of lateral pile behavior. *Proceedings of the ASCE Geotechnical Engineering Division Specialty Conference.* Pasadena, CA, USA, *1*, 600–619.

McKenna, F. (2011). OpenSees: a framework for earthquake engineering simulation. *Computing in Science & Engineering*, *13*(4), 58–66.

Metrikine, A., Tsouvalas, A., Segeren, M., Elkadi, A., Tehrani, F., Gómez, S., Atkinson, R., Pisanò, F., Kementzetzidis, E., Tsetas, A., Molenkamp, T., van Beek, K., & P, D. (2020). GDP: a new technology for Gentle Driving of (mono)Piles. In Z. Westgate (Ed.), *Frontiers in Offshore Geotechnics IV: Proceedings of the 4th International Symposium on Frontiers in Offshore Geotechnics (ISFOG 2021)*. Austin, TX, USA (pp. 736–745). Leiden, the Netherlands: CRC Press/Balkema.

Pisanò, F., Askarinejad, A., Wang, H., Maghsoodi, S., Gavin, K. G., Segeren, M. L. A., Elkadi, A. S. K., de Lange, D., & Konstadinou, M. (2022a). MIDAS: Monopile Improved Design through Advanced cyclic Soil modelling. *Proceedings of 20th International Conference on Soil Mechanics and Geotechnical Engineering (ICSMGE2022)*. Sydney, Australia.

Prendergast, L., & Igoe, D. (2022). Examination of the reduction in natural frequency of laterally loaded piles due to strain-dependence of soil shear modulus. *Ocean Engineering*, *258*, 111614.

Randolph, M. F., & Gourvenec, S. (2011). *Offshore Geotechnical Engineering*. Oxford, UK: CRC Press, Taylor & Francis Group.

Rodger, A., & Littlejohn, G. (1980). A study of vibratory driving in granular soils. *Géotechnique*, *30*(3), 269–293.

Staubach, P., Machaček, J., Moscoso, M., & Wichtmann, T. (2020). Impact of the installation on the long-term cyclic behaviour of piles in sand: A numerical study. *Soil Dynamics and Earthquake Engineering*, *138*, 106223.

Staubach, P. (2022). *Contributions to the numerical modelling of pile installation processes and high-cyclic loading of soils* (Doctoral dissertation) [ruhr-unibochum.de]. Ruhr-Universität Bochum. Bochum, Germany.

Sturm, H., Solf, O., & Kudella, P. (2008). Self-healing effects of shallow foundations for offshore wind turbine structures. In Z. Mlynarek (Ed.), *11th Baltic Sea Geotechnical Conference:" Geotechnics in Maritime Engineering"*. Gdansk, Poland (pp. 301–308). London, UK: CRC Press.

Suryasentana, S. K., & Lehane, B. M. (2016). Updated CPT-based p–y formulation for laterally loaded piles in cohesionless soil under static loading. *Géotechnique*, *66*(6), 445–453.

Suzuki, Y., & Nakai, S. (1985). Behavior of a pile under horizontal cyclic loading. *Proceedings of 11th International conference on soil mechanics and foundation engineering*. San Francisco, CA, USA, *3*, 1413–1416.

Theodoros, T., Peter, K., & Torsten, W. (2009). Geotechnical Robustness and Deformation Recovery Effects of Offshore Wind Turbine Foundations. *Proceedings of 3rd science days on the utilization of offshore wind energy.* Oldenburg, Germany.

Tsetas, A., Gómez, S. S., Tsouvalas, A., van Beek, K., Tehrani, F. S., Kementzetzidis, E., Pisanò, F., Elkadi, A., Segeren, M., Molenkamp, T., & Metrikine, A. V. (2020). Experimental identification of the dynamic behaviour of pile-soil system installed by means of three different pile-driving techniques. In M. Papadrakakis, M. Fragiadakis & C. Papadimitriou (Eds.), *Proceedings of the XI International Conference on Structural Dynamics, EURODYN 2020*. Athens, Greece (pp. 3005–3015).

Tsetas, A., Tsouvalas, A., Gómez, S. S., Pisanò, F., Kementzetzidis, E., Molenkamp, T., Elkadi, A. S., & Metrikine, A. V. (2023). Gentle Driving of Piles (GDP) at a sandy site combining axial and torsional vibrations: Part I - installation tests. *Ocean Engineering*, *270*, 113453.

Tsouvalas, A. (2020). Underwater Noise Emission Due to Offshore Pile Installation: A Review. *Energies*, *13*(12), 3037.

Wan, X., Doherty, J. P., & Randolph, M. F. (2021). Relationships between lateral and rotational load transfer stiffnesses and soil modulus for the elastic response of monopiles. *Computers and Geotechnics*, *137*, 104256.

References for Chapter VI

Abadie, C. N. (2015a). *Cyclic lateral loading of monopile foundations in cohesionless soils* (DPhil thesis). University of Oxford. Oxford, UK.

Byrne, B. W., Burd, H. J., Zdravkovic, L., Abadie, C. N., Houlsby, G. T., Jardine, R. J., Martin, C. M., McAdam, R. A., Pacheco Andrade, M., Pedro, A. M., et al. PISA Design Methods for Offshore Wind Turbine Monopiles. In: In *Offshore Technology Conference*. Houston, TX, USA. 2019, paper OTC-29373–MS.

Corti, R., Diambra, A., Wood, D. M., Escribano, D. E., & Nash, D. F. (2016). Memory surface hardening model for granular soils under repeated loading conditions. *Journal of Engineering Mechanics*, *142*(12), 04016102.

Dafalias, Y. F. (1986). Bounding surface plasticity. I: Mathematical foundation and hypoplasticity. *Journal of engineering mechanics*, *112*(9), 966–987.

Dafalias, Y. F., & Manzari, M. T. (2004). Simple plasticity sand model accounting for fabric change effects. *Journal of Engineering mechanics*, *130*(6), 622–634.

Dafalias, Y., & Taiebat, M. (2016). SANISAND-Z: zero elastic range sand plasticity model. *Géotechnique*, *66*(12), 999–1013.

Davidson, H. (1982). *Laterally loaded drilled pier research. Volume 1: design methodology. Final report.[PADLL]* (tech. rep.). GAI Consultants, Inc., Monroeville, PA (USA).

Fan, S., Bienen, B., & Randolph, M. F. (2021d). Effects of Monopile Installation on Subsequent Lateral Response in Sand. II: Lateral Loading. *Journal of Geotechnical and Geoenvironmental Engineering*, *147*(5), 04021022.

Gerolymos, N., & Gazetas, G. (2006). Development of Winkler model for static and dynamic response of caisson foundations with soil and interface nonlinearities. *Soil Dynamics and Earthquake Engineering*, *26*(5), 363–376.

Kementzetzidis, E., Corciulo, S., Versteijlen, W. G., & Pisanò, F. (2019). Geotechnical aspects of offshore wind turbine dynamics from 3D non-linear soil-structure simulations. *Soil Dynamics and Earthquake Engineering*, *120*, 181–199.

Kementzetzidis, E., Pisanò, F., & Metrikine, A. V. (2022). A memory-enhanced $p - y$ model for piles in sand accounting for cyclic ratcheting and gapping effects. *Computers and Geotechnics*, *148*, 104810.

Klinkvort, R. T. (2012). *Centrifuge modelling of drained lateral pile-soil response* (Doctoral dissertation). The Technical University of Denmark, DTU Civil Engineering. Lyngby, Denmark.

Lam, I., & Martin, G. (1986). *Seismic Design of High-Way Bridge Foundations. US Department of Transportation* (tech. rep.). Report No. FHWA/RD-86/102.

Lee, J., Zhao, F., & Dutton. (2021). Global Offshore Wind Report 2021. *GWEC (Global Wind Energy Council)*.

Liu, H. Y., Abell, J. A., Diambra, A., & Pisanò, F. (2019b). Modelling the cyclic ratcheting of sands through memory-enhanced bounding surface plasticity. *Géotechnique*, *69*(9), 783–800.

Martinelli, M., & Galavi, V. (2022). An explicit coupled MPM formulation to simulate penetration problems in soils using quadrilateral elements. *Computers and Geotechnics*, *145*, 104697.

McAdam, R. A., Byrne, B. W., Houlsby, G. T., Beuckelaers, W. J., Burd, H. J., Gavin, K. G., Igoe, D. J., Jardine, R. J., Martin, C. M., Muir Wood, A., et al. (2020). Monotonic laterally loaded pile testing in a dense marine sand at Dunkirk. *Géotechnique*, *70*(11), 986–998.

McKenna, F. T. (1997). *Object-oriented finite element programming: frameworks for analysis, algorithms and parallel computing* (Doctoral dissertation). University of California, Berkeley.

Pisanò, F., Askarinejad, A., Wang, H., Maghsoodi, S., Gavin, K. G., Segeren, M. L. A., Elkadi, A. S. K., de Lange, D., & Konstadinou, M. (2022a). MIDAS: Monopile Improved Design through Advanced cyclic Soil modelling. *Proceedings of 20th International Conference on Soil Mechanics and Geotechnical Engineering (ICSMGE2022)*. Sydney, Australia.

Pisanò, F., & Jeremić, B. (2014). Simulating stiffness degradation and damping in soils via a simple visco-elastic–plastic model. *Soil Dynamics and Earthquake Engineering*, *63*, 98–109.

Richards, I. A., Byrne, B. W., & Houlsby, G. T. (2020). Monopile rotation under complex cyclic lateral loading in sand. *Géotechnique*, *70*(10), 916–930.

Staubach, P., Machaček, J., Moscoso, M., & Wichtmann, T. (2020). Impact of the installation on the long-term cyclic behaviour of piles in sand: A numerical study. *Soil Dynamics and Earthquake Engineering*, *138*, 106223.

Suryasentana, S. K., & Lehane, B. M. (2016). Updated CPT-based p–y formulation for laterally loaded piles in cohesionless soil under static loading. *Géotechnique*, *66*(6), 445–453.

Theodoros, T., Peter, K., & Torsten, W. (2009). Geotechnical Robustness and Deformation Recovery Effects of Offshore Wind Turbine Foundations. *Proceedings of 3rd science days on the utilization of offshore wind energy.* Oldenburg, Germany.

Versteijlen, W., Renting, F., van der Valk, P., Bongers, J., van Dalen, K., & Metrikine, A. (2017a). Effective soil-stiffness validation: Shaker excitation of an in-situ monopile foundation. *Soil Dynamics and Earthquake Engineering*, *102*, 241–262.

Zienkiewicz, O. C., Chan, A. H. C., Pastor, M., Schrefler, B. A., & Shiomi, T. (1999). *Computational geomechanics*. Chichester,UK:

Zienkiewicz, O. C., Chang, C. T., & Bettess, P. (1980). Drained, undrained, consolidating and dynamic behaviour assumptions in soils. *Géotechnique*, *30*(4), 385–395.

Curriculum Vitæ

Evangelos Kementzetzidis

03-05-1989 Born in Thessaloniki, Greece

Academic development

2008–2014 Master of Engineering
University of Thessaly, Greece
Thesis: Seismic behaviour of buildings with large lightly reinfornced shear walls
Supervisor: Dr. M. Moretti

2015–2017 Master of Science
Delft University of Technology
Thesis: Geotechnical aspects of offshore wind turbine dynamics emerging from 3D sand-monopile non-linear simulations
Supervisor: Dr. F. Pisanò

2018–2022 Ph.D. research
Delft University of Technology
Thesis: Geotechnical aspects of offshore wind turbine dynamics emerging from 3D sand-monopile non-linear simulations
Promotor: Prof.dr. A. V. Metrikine
Copromotor: Dr. F. Pisanò

2019	Visiting researcher
May–August	Universidad de los Andes, Chile
	Supervisor: José A. M. Abell

2022–	University lecturer
	Delft University of Technology

Publications

Journal publications

7. Kementzetzidis, E., Pisanò, F., Tsetas, A., & Metrikine, A. V. (2023). Gentle Driving of Piles (GDP) at a sandy site combining axial and torsional vibrations: quantifying the influence of pile installation method on lateral behaviour. *Journal of Geoenvironmental and Geotechnical Engineering, under review*, –, 0–0

6. Kementzetzidis, E., Pisanò, F., Elkadi, A. S., Tsouvalas, A., & Metrikine, A. V. (2023). Gentle Driving of Piles (GDP) at a sandy site combining axial and torsional vibrations: Part II - cyclic/dynamic lateral loading tests. *Ocean Engineering*, *270*, 113452

5. Tsetas, A., Tsouvalas, A., Gómez, S. S., Pisanò, F., Kementzetzidis, E., Molenkamp, T., Elkadi, A. S., & Metrikine, A. V. (2023). Gentle Driving of Piles (GDP) at a sandy site combining axial and torsional vibrations: Part I - installation tests. *Ocean Engineering*, *270*, 113453

4. Kementzetzidis, E., Pisanò, F., & Metrikine, A. V. (2022). A memory-enhanced $p - y$ model for piles in sand accounting for cyclic ratcheting and gapping effects. *Computers and Geotechnics*, *148*, 104810

3. Liu, H., Kementzetzidis, E., Abell, J. A., & Pisanò, F. (2021). From cyclic sand ratcheting to tilt accumulation of offshore monopiles: 3D FE modelling using SANISAND-MS. *Géotechnique*, 1–16

2. Kementzetzidis, E., Metrikine, A. V., Versteijlen, W. G., & Pisanò, F. (2021). Frequency effects in the dynamic lateral stiffness of monopiles in sand: insight from field tests and 3D FE modelling. *Géotechnique*, *71*(9), 812–825

1. Kementzetzidis, E., Corciulo, S., Versteijlen, W. G., & Pisanò, F. (2019). Geotechnical aspects of offshore wind turbine dynamics from 3D non-linear soil-structure simulations. *Soil Dynamics and Earthquake Engineering*, *120*, 181–199

Conference publications

5. Pisanò, F., Liu, H., & Kementzetzidis, E. (2022). Geotechnical modelling framework for the tilting analysis of offshore monopiles under environmental cyclic loading. In K. Sharman, A. Myers & D. Roddier (Eds.), *Proceedings of the ASME 2022 International Offshore Wind Technical Conference (IOWTC2022)*. Boston, MA, USA (pp. 0–0)

4. Tsetas, A., Gómez, S. S., Tsouvalas, A., van Beek, K., Tehrani, F. S., Kementzetzidis, E., Pisanò, F., Elkadi, A., Segeren, M., Molenkamp, T., & Metrikine, A. V. (2020). Experimental identification of the dynamic behaviour of pile-soil system installed by means of three different pile-driving techniques. M. Papadrakakis, M. Fragiadakis & C. Papadimitriou (Eds.), *Proceedings of the XI International Conference on Structural Dynamics, EURODYN 2020*. Athens, Greece (pp. 3005–3015)

3. Metrikine, A., Tsouvalas, A., Segeren, M., Elkadi, A., Tehrani, F., Gómez, S., Atkinson, R., Pisanò, F., Kementzetzidis, E., Tsetas, A., Molenkamp, T., van Beek, K., & P, D. (2020). GDP: a new technology for Gentle Driving of (mono)Piles. Z. Westgate (Ed.), *Frontiers in Offshore Geotechnics IV: Proceedings of the 4th International Symposium on Frontiers in Offshore Geotechnics (ISFOG 2021)*. Austin, TX, USA (pp. 736–745). Leiden, the Netherlands: CRC Press/Balkema

2. Vacareanu, V., Kementzetzidis, E., & Pisanò, F. (2019). 3D FE seismic analysis of a monopile-supported offshore wind turbine in a non-liquefiable soil deposit. G. Gazetas & I. Anastasopoulos (Eds.), *Proceedings of 2nd International Conference on Natural Hazards & Infrastructure (ICONHIC2019)*, Chania, Crete, Greece (pp. 23–26)

1. Kementzetzidis, E., Versteijlen, W. G., Nernheim, A., & Pisanò, F. (2018). 3D FE dynamic modelling of offshore wind turbines in sand: Natural frequency evolution in the pre-to after-storm transition. A. S. Cardoso, J. L. Borges, P. A. Costa, A. T. Gomez, J. C. Marques & C. S. Vieira (Eds.), *Numerical Methods in Geotechnical Engineering IX, Volume 2*. Porto, Portugal (pp. 1477–1484). Florida, USA: CRC Press